5-1-2015

High Pressure Behavior of Mullite-Type Oxides: Phase Transitions, Amorphization, Negative Linear Compressibility and Microstructural Implications

Patricia Kalita
University of Nevada, Las Vegas, kalitap@unlv.nevada.edu

Repository Citation

Kalita, Patricia, "High Pressure Behavior of Mullite-Type Oxides: Phase Transitions, Amorphization, Negative Linear Compressibility and Microstructural Implications" (2015). *UNLV Theses, Dissertations, Professional Papers, and Capstones*. 2369.
https://digitalscholarship.unlv.edu/thesesdissertations/2369

HIGH PRESSURE BEHAVIOR OF MULLITE-TYPE OXIDES: PHASE TRANSITIONS, AMORPHIZATION, NEGATIVE LINEAR COMPRESSIBILITY AND MICROSTRUCTURAL IMPLICATIONS

by

Patricia E. Kalita

Bachelor of Sciences in Physics
University of Nevada Las Vegas
2006

Master of Sciences in Physics
University of Nevada Las Vegas
2008

A dissertation submitted in partial fulfillment
of the requirements for the

Doctor of Philosophy – Physics

Department of Physics and Astronomy
College of Sciences
Graduate College

University of Nevada, Las Vegas
May 2015

We recommend the dissertation prepared under our supervision by

Patricia E. Kalita

entitled

High Pressure Behavior of Mullite-Type Oxides: Phase Transitions, Amorphization, Negative Linear Compressibility and Microstructural Implications

is approved in partial fulfillment of the requirements for the degree of

Doctor of Philosophy - Physics
Department of Physics and Astronomy

Andrew Cornelius, Ph.D., Committee Chair

Yusheng Zhao, Ph.D., Committee Member

Leonard Zane, Ph.D., Committee Member

Stanislav Sinogeikin, Ph.D., Committee Member

Hartmut Schneider, Ph.D., Committee Member

Wanda Taylor, Ph.D., Graduate College Representative

Kathryn Hausbeck Korgan, Ph.D., Interim Dean of the Graduate College

May 2015

ABSTRACT

Even though mullite occurs rarely in nature, it is perhaps one of the most important phases in both traditional and advanced ceramics. Existing and emerging applications of mullite and mullite-type materials include: high-temperature composites, aerospace materials, ballistic shielding for military applications and even non-linear optical materials. There are many uncertainties regarding the basic physical properties of mullite-type materials, particularly in terms of their high-pressure structural stability and mechanical behavior that are important to address for emerging applications of mullites as engineering materials. This work is the first reported comprehensive investigation of the high –pressure structural behavior of several different mullites and synthetic mullite-type oxides. The materials investigated are representatives of different structural and chemistry branches of the mullite family. The goal is to elucidate how the most fundamental building blocks of mullite oxides accommodate high pressure compression. Mullites and mullite-type oxides are investigated at extreme pressures using synchrotron x-ray diffraction and laser Raman spectroscopy. These experiments enable the extraction of the materials' structure and its modifications in a function of increasing pressure: deformation of polyhedra, phase transitions, formation and breaking of bonds. The experimental techniques used here are ideally suited to provide a synergical interplay in the study of oxides under high-pressure conditions: Raman spectroscopy is a technique for investigating short range order phenomena while x-ray diffraction accesses structural changes occurring at the long range order. The following phenomena are discussed: phase transitions, equations of state, pressure-driven amorphization, and the very rare effect of negative linear compressibility. The unprecedented discovery of negative linear compressibility in mullite-type oxides presented here opens the door to military applications as incompressible optical materials.

ACKNOWLEDGEMENTS

I would like to express my deepest appreciation to my outstanding committee chair and advisor, Prof. Andrew Cornelius for continuously supporting my research endeavors and giving me independence in taking the research project in new directions.

I would also like to express my deepest gratitude to Dr. Stanislav Sinogeikin for being an extraordinary mentor in my research at the Advanced Photon Source.

In addition a big thank you goes to Prof. Hartmut Schneider for introducing me to the fascinating world of mullite materials.

Many heartfelt thanks go to my entire committee: Prof. Andrew Cornelius, Dr. Stanislav Sinogeikin, Prof. Hartmut Schneider, Prof. Wanda Taylor, Prof. Leonard Zane, and Prof. Yusheng Zhao.

Work at UNLV is supported by DOE award no. DEFG36-05GO08502. UNLV HiPSEC is supported by the US DOE, NNSA, under Agreement DEFC08- 01NV14049. Portions of this work were performed at HPCAT (Sector 16), Advanced Photon Source (APS), Argonne National Laboratory. HPCAT operations are supported by DOE-NNSA under Award No. DE-NA0001974 and DOE-BES under Award No. DE-FG02-99ER45775, with partial instrumentation funding by NSF. APS is supported by DOE-BES, under Contract No. DE-AC02-06CH11357. Use of the APS was supported by DOE-BES, Contract W-31-109-ENG-38.).

FAME-Tech Labs, UNLV are supported by DOEEERE under Award No. DE-FG 3606GO8636 and Award No. EE-0000269.

The author acknowledges the use of the gas-loading facility of GSECARS–COMPRESS.

DEDICATION

I dedicate this dissertation work to my family and friends for their encouragements, cheerleading and all the support throughout the process. I special feeling of gratitude goes to Prof. Kris Lipinska who has the attitude and the substance of a genius: she continually and convincingly conveyed a spirit of adventure and excitement in regard to research and scholarship and in doing so made it possible for me to successfully complete this endeavor.

TABLE OF CONTENTS

ABSTRACT III
ACKNOWLEDGEMENTS IV
DEDICATION V
TABLE OF CONTENTS VI
LIST OF TABLES IX
LIST OF FIGURES X
CHAPTER 1 - INTRODUCTION 1
CHAPTER 2 – BACKGROUND 4
2.1. DESCRIPTION OF MULLITES AND THEIR APPLICATIONS 4
2.1.1. Alumino-Silicate Mullites 4
  2.1.1.1. Objectives of high-pressure studies of alumino-silicate mullites. 5
  2.1.1.2. Previous studies of aluminosilicate mullites and of sillimanite. 5
2.1.2. Boron Mullite 6
2.1.3. $PbMBO_4$ Synthetic Mullites 8
2.1.4. How Do the Investigated Materials Relate to Each Other? 9
2.2. RAMAN SPECTROSCOPY 11
2.2.1. A Brief History of the Raman Effect 12
2.2.2. What is the Raman Effect? 14
2.2.3. Limitations of Raman Spectroscopy 16
2.2.4. States of a System – Vibration of a Diatomic Molecule 17
2.2.5. Classical Light Scattering - Rayleigh Theory 22
2.2.6. Theory of Raman Scattering - Overview 24
  2.2.6.1. Theory of Raman and Rayleigh Scattering – Classical Treatment 25
  2.2.6.2. Theory of Raman Scattering – Quantum Mechanical Treatment 30
2.2.7. Selection Rules 37
2.2.8. Raman Spectroscopy at Ambient and High Pressures 38
2.3. X-RAY DIFFRACTION 39
2.3.1. Production of X-Rays 40
2.3.2. The Bragg Equation 41
2.3.3. Theory of X-Ray Diffraction 42
  2.3.3.1. The Reciprocal Space 43
  2.3.3.2. The Laue condition 44
  2.3.3.3. The Bragg Equation 46
  2.3.3.4. Atomic scattering factor 47
  2.3.3.5. The Structure Factor 48
  2.3.3.6. Temperature Factor 50
2.4. HIGH-PRESSURE MATERIALS PHYSICS 51
2.4.1. Overview 51
2.4.2. Diversification of High-Pressure Research 52
2.4.3. The Effect of Pressure on Matter 53
2.4.4. The Diamond Anvil Cell 54
2.4.5. Measuring Pressure in a Diamond Anvil Cell 56
2.5. SYNCHROTRON X-RAY DIFFRACTION 57
2.5.1. History of Synchrotrons 57
2.5.2. Bending Magnets, Undulators, Wigglers 58
2.5.3. The Advanced Photon Source at Argonne National Laboratory 59

CHAPTER 3 - EXPERIMENTAL 62
3.1. SAMPLES 62
3.1.1. Alumino-Silicate Mullite and Sillimanite 62
3.1.2. Boron Mullites 62
3.1.3. $PbAlBO_4$, $PbFeBO_4$ and $PbMnBO_4$ Mullites 63
3.2. RAMAN SPECTROSCOPY AT AMBIENT AND HIGH PRESSURE 63
3.2.1. Alumino-Silicate Mullites and Sillimanite 65
3.2.2. $PbAlBO_4$ Mullite 66
3.2.3. $PbFeBO_4$ Mullite 66
3.3. HIGH PRESSURE XRD AT THE ADVANCED PHOTON SOURCE, ARGONNE NATIONAL LABORATORY 67
3.3.1. Experimental Conditions 67
3.3.2. Alumino-Silicate Mullite and Sillimanite 69
3.3.3. Boron Mullite 70
3.3.4. $PbMBO_4$ Mullites 70
3.3.5. Ambient Pressure X-ray Diffraction 71
CHAPTER 4 – RESULTS AND DISCUSSION 72
4.1. CRYSTAL STRUCTURE OF CRYSTAL STRUCTURES OF MULLITES 72
4.1.1. Crystal Structure of Alumino-Silicate Mullite 72
4.1.2. Crystal Structure of Boron Mullite 74
4.1.3. Crystal Structure of $PbMBO_4$ Synthetic Mullites 76
4.2. HIGH-PRESSURE BEHAVIOR OF ALUMINO-SILICATE MULLITES AND SILLIMANITE 79
4.2.1. High-Pressure Synchrotron XRD 79
  4.2.1.1. Compression Mechanisms 85
  4.2.1.2. Equation of State of Alumino-Silicate Mullites and Sillimanite 89
4.2.2. Laser Raman Spectroscopy at High Pressures 91
4.2.3. High-Pressure Raman Spectroscopy of Mullites and of Sillimanite 91
  4.2.3.1. Predicting Vibrations using Group Theory 91
  4.2.3.2. Raman Spectra at High Pressures 101
  4.2.3.3. Mode Grüneisen Parameters 104
  4.2.3.4. Comparison of Pressure Evolution. 108
4.3. HIGH-PRESSURE SYNCHROTRON XRD OF BORON MULLITES 112
4.3.1. Compression Mechanisms 117
4.3.2. Mechanisms of Pressure-Induced Amorphization 122
4.3.3. Equation of State and Axial Compressibilities 126
4.4. HIGH-PRESSURE BEHAVIOR OF $PBMBO_4$ SYNTHETIC MULLITES 129
4.4.1. High-Pressure Synchrotron XRD of $PbFeBO_4$ 129
4.4.2. High-Pressure Synchrotron XRD of $PbAlBO_4$ 132
4.4.3. High-Pressure Raman Spectroscopy of $PbFeBO_4$ 136
4.4.4. High-Pressure Raman Spectroscopy of $PbAlBO_4$ 141
4.4.5. Phase transition in $PbMBO_4$ 146
  4.4.5.1. Structural Phase Transition in $PFeBO_4$ 146
  4.4.5.2. Two Structural Phase Transitions in $PAlBO_4$ 149
4.4.6. The Influence of LEP on High-Pressure Behavior of $PbMBO_4$ 153
4.4.7. Bond Valence Model and Eccentricity Parameter 159
4.4.8. Large Negative Linear Compressibility in $PbMBO_4$ 161
  4.4.8.1. Implications of the Large NLC Effect in $PbMBO_4$ Compounds 166
4.4.9. Equation of State 168
CHAPTER 5 – CONCLUSIONS 172
5.1. ALUMINO-SILICATE MULLITES AND SILLIMANITE 172

5.2. BORON MULLITES 174
5.3. PBMBO$_4$ SYNTHETIC MULLITES 175
5.4. GLOBAL CONCLUSIONS 178
REFERENCES........ 180
CURRICULUM VITAE 189

LIST OF TABLES

Table 1. Comparison of: bulk moduli for mullites and for sillimanite. 90
Table 2. Atomic sites and atomic parameters for sillimanite. 93
Table 3. Site correlation for space group #62, D_{2h}^{16} 94
Table 4. Finding Factor Group, Site Group and Point Group Symmetries for Sillimanite 94
Table 5. Expected number of vibrational modes for sillimanite. 95
Table 6. Filling out the Site Group → Factor Group Correlation Table for Al1 in sillimanite. 96
Table 7. Site Group → Factor Group Correlation Table for Al1 in sillimanite. 96
Table 8. Site Group → Factor Group Correlation Table for Al2..97
Table 9. Factor Group Correlation Table for O2 97
Table 10. Correlation Table for SiO_4 Tetrahedron – Internal Modes. 98
Table 11. Correlation table for internal modes of SiO_4 tetrahedron. 99
Table 12. Correlation table for external modes of SiO_4 tetrahedron. 99
Table 13. Complete Character Table and Correlation Scheme 100
Table 14. Raman modes and Grüneisen parameters for 2:1 mullite and sillimanite below 350cm^{-1}. 106
Table 15. Raman modes and Grüneisen parameters for 2:1 mullite and sillimanite above 350cm^{-1}. 107
Table 16. Correspondence of sillimanite and mullite Raman modes and Grüneisen parameters. 111
Table 17. Results of Rietveld structural refinements of B-Mullite and 7:4 mullite from Figure 36. 115
Table 18. Bulk moduli of various mullites. 127
Table 19. Axial compressibilities of various mullites. 128
Table 20. Raman modes for $PbFeBO_4$ and its mode Grüneisen parameters. 140
Table 21. Raman modes for $PbAlBO_4$ and its mode Grüneisen parameters. 145
Table 22. Results of Rietveld structural refinements of $PbFeBO_4$ at high pressures. 148
Table 23. Calculations of bond valence sums for $PbFeBO_4$ and $PbAlBO_4$. 160
Table 24. About 20 materials known to possess negative linear compressibility. 163
Table 25. Comparison of bulk moduli for $PbMBO_4$. 169

LIST OF FIGURES

Figure 1. The Bärnighausen tree [42] illustrating the relations in the family of mullite-type compounds. 10
Figure 2. Number of articles published on the topic of Raman spectroscopy between 1946 and 2014. 13
Figure 3. Classification of spectroscopies by the amount of energy transferred in the process. 16
Figure 4. Vibrations of a diatomic molecule. 18
Figure 5. Potential energy curve or Morse potential for a diatomic molecule. 20
Figure 6. Schematic of the classical light scattering process. 23
Figure 7. Polarization of a diatomic molecule in an external electric field. 25
Figure 8. Energy levels of a diatomic molecule. 26
Figure 9. Dipole moment of a molecule and its relation to the induced dipole moment. 27
Figure 10. Interaction of a molecule’s vibration with incoming radiation. 29
Figure 11. Possible consequences of a photon-molecule interaction. 31
Figure 12. Schematic illustrating the principle of Bragg’s law. 41
Figure 13. Schematic of a reciprocal lattice with (hkl)’s marking some of the reciprocal planes. 45
Figure 14. Set of crystal lattice plains in real space. 46
Figure 15. Schematic illustrating the decomposition of the position vector r. 47
Figure 16. Schematic of the inside of a diamond anvil cell (DAC). 55
Figure 17. Aerial view of the Advanced Photon Source (APS). 60
Figure 18. Overview of the experimental Raman setup at FAME-Tech Labs, UNLV. 64
Figure 19. Sketch of the optical setup of the experimental Raman at FAME-Tech Labs, UNLV. 64
Figure 20. Setup for in-situ high-pressure synchrotron x-ray diffraction experiments in a DAC. 68
Figure 21. Comparison of the structures of sillimanite (a) and of mullite (b). 73
Figure 22. Ambient pressure crystal structures of mullite [103] and B-substituted mullite. [29] 75
Figure 23. The ambient pressure and temperature crystal structure of $PbAlBO_4$. 76
Figure 24. The ambient pressure and temperature crystal structure of $PbFeBO_4$. 77
Figure 25. The first coordination sphere of the Pb^{2+} cation. 78
Figure 26. Selected high pressure XRD patterns of: (a) sillimanite, (b) 3:2- and (c) 2:1-mullite. 80
Figure 27. High-pressure XRD patterns of 2:1-mullite and sillimanite on decompression. 81
Figure 28. Cell parameters *vs*. pressure. 82
Figure 29. Fractional pressure evolution cell parameters. 83
Figure 30. Zoom on the fractional pressure-evolution of the *c* lattice parameter. 84
Figure 31. Comparison of Raman spectra of 2:1 mullite and sillimanite at ambient pressure. 101
Figure 32. Pressure-driven evolution of Raman spectra of sillimanite measured in the DAC. 102
Figure 33. Pressure-driven evolution of Raman spectra of 2:1 mullite measured in the DAC. 103
Figure 34. Pressure-evolution of experimental vibrational modes of 2:1 mullite and sillimanite. 108
Figure 35. 7:4 mullite and B-mullite X-ray diffraction at high-pressures. 113
Figure 36. Rietveld refinements of 7:4 mullite and B-mullite. 114
Figure 37. Pressure-driven change of unit cell parameters. 116
Figure 38. The crystal structure of B-mullite at different pressures. 118
Figure 39. Indices of distortion in in 7:4 mullite and B-mullite. 120
Figure 40. Bond lengths in 7:4 mullite and B-mullite. 121
Figure 41. Decompression of 7:4 mullite and B-mullite. 125
Figure 42. Pressure-volume plot and equation of state fits for 7:4 mullite and B-mullite. 126

Figure 43. High-pressure ADXRD patterns of the mullite-type $PbFeBO_4$. 130
Figure 44. Pressure-driven evolution of unit cell parameters and volume of $PbFeBO_4$. 131
Figure 45. Pressure-driven fractional change of unit cell parameters in $PbFeBO_4$. 132
Figure 46. High-pressure ADXRD patterns of the mullite-type $PbAlBO_4$. 133
Figure 47: Pressure-driven evolution of unit cell parameters and volume of $PbAlBO_4$. 134
Figure 48: Pressure-driven fractional change of unit cell parameters in $PbAlBO_4$. 135
Figure 49. Selected Raman spectra of $PbFeBO_4$ measured as a function of increasing pressure. 137
Figure 50. Pressure-dependence of Raman modes of $PbFeBO_4$. 138
Figure 51. Raman spectra of $PbAlBO_4$ measured as a function of pressure from ambient and 88 GPa. 142
Figure 52. Pressure-dependence of Raman modes of $PbAlBO_4$. 143
Figure 53. Crystal structure of $PbFeBO_4$ at 0.0001GPa and ~14 GPa. 147
Figure 54 Example of Rietveld refinements: the low-pressure structure of $PbFeBO_4$ at ~9.7GPa. 149
Figure 55. Example of Rietveld refinements: the high-pressure structure of $PbFeBO_4$ at ~14GPa. 149
Figure 56. Crystal structure of $PbAlBO_4$ at 0.0001GPa and ~14 GPa. 150
Figure 57. Example of Rietveld refinements: the low-pressure structure of $PbAlBO_4$ at ~9.7GPa. 151
Figure 58. Example of Rietveld refinements: the high-pressure structure of $PbAlBO_4$ at ~14GPa. 151
Figure 59. Supercell of $PbFeBO_4$ at ambient pressure..156
Figure 60. Supercell of $PbFeBO_4$ at 14 GPa. 156
Figure 61. Synergical interplay of factors leading to negative linear compressibility along *b*. 165
Figure 62. Pressure-driven change of unit cell volume in $PbFeBO_4$. 168
Figure 63. Pressure-driven change of unit cell volume in $PbAlBO_4$. 169
Figure 64. Correlation between bulk moduli of $PbMBO_4$ and of other mullite materials. 170

CHAPTER 1 - INTRODUCTION

Even though mullite occurs rarely in natural rocks, it is perhaps one of the most important phases in both traditional and advanced ceramics and thus one of the most widely studied ceramic phases. The outstanding position of mullite in ceramics is due to its overall properties, like low density, high temperature stability even in severe oxidizing environments, favorable mechanical properties, low thermal expansion and associated very good thermal shock behavior, low thermal and electrical conductivity, excellent creep resistance, and transmittance to electro-magnetic (visible and near infrared) radiation.

There many uncertainties regarding the basic physical properties of alumino-silicate mullite, particularly in terms of its high-pressure phase stability and mechanical behavior that are important to address for applications of mullite as an engineering material. The knowledge of the high-pressure behavior of materials does offer a sensitive probe to detect their structural instabilities and possible phase transitions. This is why this work was begun with the examination of several alumino-silicate mullites at high-pressures. Another branch of the mullite family that is investigated here are lead-metal-borate mullites. These mullites are negative thermal expansion materials (NTE). From a physics point of view it is rational to search for unusual pressure-dependent behavior in NTE materials. Further, the strong *anisotropy* of the Pb^{2+} coordination, due to its lone electron pair, affects not only the geometry, but is often the origin of interesting physical properties, while its open structures makes them predisposed to pressure-driven phase transitions.

In the past 30 years it has become possible to achieve, in the laboratory, extremely high-pressures (superior to what can be achieved with the temperature parameter). The multimegabar pressures now achievable correspond to a volume compression in excess of an order of magnitude, which can reveal a wealth of information about molecular materials.

The pressure-volume work (free energy change) can be of up to 10 eV which exceeds the strongest molecular bonds. Among the effects of such extreme compression there are: changes in bonding patterns, phase transitions, chemical reactions, quantum effects, changes in chemical properties, changes in physical properties. Pressure also modifies chemical affinities and hence reactivties, and in this way new materials with unusual combination of physical and chemical properties can be formed. High-pressure Raman spectroscopy and high-pressure x-ray diffraction studies of materials (bulk- and nano-structures) are critical to identifying new equilibrium and metastable states that can be accessed, as these materials are compressed to very small volumes.

Furthermore the two techniques used in this work are ideally suited to provide a synergical interplay in the study of mullites in high-pressure compression: Raman spectroscopy is a technique for investigating short range order phenomena while x-ray diffraction accesses phenomena occurring at the long range order.

The presented Doctor of Philosophy in Physics Dissertation is structured in five chapters as outlined below.

Chapter 2 introduces all the conceptual elements involved in the present research. Since the materials investigated belong to the mullite family, an overview of mullites is presented, including structural relationships, properties and applications and relevant previous studies. The physical foundations and the technique of Raman spectroscopy is presented in detail including history, classical and quantum mechanical treatments, strength and applications to materials at high pressures. Subsequently the technique of X-ray diffraction is presented including the production of X-rays as well as elements of crystallography. The object of this work is the study of various mullites to extreme pressures (up to 1 Mbar or 100 GPa). Thus Chapter 2 also outlines the effects of high-pressures on materials, with specifics on how high-pressures are achieved in the laboratory and how materials under high-pressures are investigated. Finally, since X-ray diffraction studies at high-pressures require very bright and highly focused radiation, synchrotron radiation is introduced with production of X-rays as well as the synchrotron storage ring where the present studies were carried out.

Chapter 3 presents the samples investigated and the experimental approaches used for their studies. First, *in situ* high-pressure Rama spectroscopy is presented. High-pressure X-ray diffraction studies are described next, with details of the synchrotron radiation-based experiments.

Chapter 4 outlines the results and presents the discussion of high-pressure investigations of three families of mullite materials. First structural transformations in 2:1, 3:2 mullite and sillimanite are discussed in view of high-pressure x-ray diffraction results and high-pressure Raman spectroscopy results. Next structural transformations in B-mullite and isostructural 7:4 mullite are presented. In both materials' families structural changes leading towards a theorized phase transition and the pressure-driven amorphization are discussed. Structural transformations in two $PbMBO_4$ (M=metal) mullites are introduced next. Three new phase transitions are proposed in view of high-pressure x-ray diffraction results and high-pressure Raman spectroscopy results. The role of Pb^{2+} lone electron pairs on the structural behavior under pressure is discussed. The very rare effect of negative linear compressibility is demonstrated and discussed and an explanation is offered. Finally for all investigated materials, mechanical properties and vibrational properties are analyzed in relevant sub-sections, using specific mathematical formalism (equations of state and mode-Grüneisen parameters). Finally the key conclusions of this doctoral dissertation are presented.

CHAPTER 2 – BACKGROUND

2.1. Description of Mullites and Their Applications

2.1.1. Alumino-Silicate Mullites

Sillimanite, andalusite and kyanite, the three polymorphs of Al_2SiO_5 form at moderate and high pressure, respectively, while mullite ($3Al_2O_3·2SiO_2$), the stable crystalline phase in the Al_2O_3-SiO_2 system at ambient conditions, is known as a high temperature material. [1] Even though mullite occurs rarely in natural rocks, it is perhaps one of the most important phases in both traditional and advanced ceramics [1] and thus one of the most widely studied ceramic phases. The outstanding position of mullite in ceramics is due to its overall properties, like low density, high temperature stability even in severe oxidizing environments, favorable mechanical properties, low thermal expansion and associated very good thermal shock behavior, low thermal and electrical conductivity, excellent creep resistance, and transmittance to electro-magnetic (visible and near infrared) radiation. [1] Because of these technologically important properties mullite has become a major compound in a large number of conventional ceramics (e.g., porcelains and refractories), but also in various advanced ceramics (e.g.: heat exchangers, catalysator convertors, filters, optical devices, electronic packaging). For a review of mullite materials see Schneider *et al.* [1] [2] Mullite is also an important constituent of thermal and environmental barrier coatings, oxide fibers and oxide-based ceramic matrix composites, the latter having a high potential as insulating materials in combustors of aircraft and stationary gas turbine engines. [1, 2] Interestingly, one of the most promising armor materials with high ballistic performance are alumina-mullite ceramics with a coexisting alkali-aluminosilicate glassy phase. [3]

2.1.1.1. Objectives of high-pressure studies of alumino-silicate mullites.

There remain many uncertainties regarding the basic physical properties of mullite, particularly in terms of its high-pressure phase stability and mechanical behavior. These are important to address for applications of mullite as an engineering material. The knowledge of the high-pressure behavior of materials does offer a sensitive probe to detect their structural instabilities and possible phase transitions. Moreover, pressure-induced structural changes of mullite will also contribute to the in-depth fundamental understanding of the crystal chemistry of mullite-type alumino-silicates. Because of their close structural similarities, it is interesting to compare the pressure-induced behavior of different compounds of the mullite-type $Al_{4+2x}Si_{2-2x}O_{10-x}$ phases: sillimanite and different mullites. Therefore this study includes investigations of 2:1-mullite (x = 0.4, or 0.4 oxygen vacancy per unit cell), 3:2-mullite and (x = 0.25 or 0.25 vacancy per unit cell), sillimanite (x = 0, no oxygen vacancy), with the goal being the understanding of the role of oxygen vacancies on the high pressure behavior of the mullite-type alumino silicates. To the best of the author's knowledge the present is the first report of in situ static-pressure compression of alumino silicate mullites.

2.1.1.2. Previous studies of aluminosilicate mullites and of sillimanite.

The thermo-elastic behavior of sillimanite and of alumino-silicate mullites have been studied extensively by:

(i) Neutron or x-ray diffraction: Brace *et al.* (compressibility of sillimanite); [4] Winter and Ghose (thermal expansion of sillimanite); [5] Schneider and Eberhard (thermal expansion of mullite); [6] Balzar and Ledbetter (compressibility of mullite); [7] Brunauer *et al.* (high-temperature structure and thermal expansion of mullite); [8, 9]

(ii) Brillouin spectroscopy: Vaughan and Weidner (elasticity and structure of sillimanite); [10]

(iii) Acoustic resonance spectroscopy: Hildmann *et al.* (elastic constants of mullite and sillimanite); [11]

(iv) Resonant ultrasound spectroscopy: Schreuer *et al.* (elastic constants of mullite at high temperature); [12]

(v) Dilatometry: Schreuer *et al.* (single crystal derived thermal expansion of mullite); [12]

(vi) Vickers indentation as well as ball milling: Schmucker et al. (amorphization of mullite); [13, 14]

(vii) Simulation of thermo-elastic behavior: Oganov *et al.* (compression of sillimanite) [15] and by Winkler at al. (elastic constants of sillimanite). [16]

No in situ static high-pressure compression studies of mullite exist, where pressure and pressure-distribution are controlled. Static high-pressure compression of sillimanite was carried out previously up to 5.3 GPa by Yang *et al.;* [17] up to 46 GPa by Friedrich *et al.;* [18] and up to 8.5 GPa by Burt *et al.* [19] Shock-compression studies were performed by Schneider *et al.* (andalusite and kyanite), [20] Schneider and Horneman (andalusite).[21] A shock-compression study by Kawai *et al.* [22] reports a disproportionation of mullite to corundum and stishovite at ~30 GPa, while a work by Braue *et al.* [23] reported shock-wave induced amorphization of mullite above 35 GPa.

2.1.2. Boron Mullite

Boron is used in an extensive range of industrial applications including glasses, ceramics, glass-ceramics, metallurgy and more.[24] Boron forms preferentially covalent bonds due to its high ionization potential and it has a high affinity for oxygen. Also, boron has many similarities to silicon and carbon, and when associated with oxygen it has a similar structural chemistry to Si. This similarity suggests that in an alumino-silicate mullite, where Si is tetrahedrally coordinated to O, it should be possible to substitute some of the Si with B. The groups BO_3, BO_4, and SiO_4, are all predisposed to polymerize leading to great structural complexity.

After alumino-silicate mullites, a second category of ceramics, important from the technological point of view, are aluminum borates (e.g. $Al_{18}B_4O_{33}$) with mullite-type crystal structure. Industrial applications include the reinforcement of aluminum alloys by incorporation of aluminum borate whiskers and incorporation in refractory linings due to the good corrosion resistance of aluminum borates against molten glasses containing boron. [25] Therefore successful combination of alumino-silicate mullite with alumino-borate with mullite-type structure in one material would offer great promise to design technologically important, high-performance materials with on-demand properties.

The existence of a solid-solution between 3:2 mullite ($Al_{4.5}Si_{1.5}O_{9.75}$) and $Al_{18}B_4O_{33}$ by substitution of boron for silicon was first suggested by Dietzel and Scholze. [26] The term "boron-mullite" or "B-mullite" was introduced by Werding and Schreyer [27] in order to describe a compositional range between mullite solution series and Al_5BO_9 with mullite structure and $AlBO_3$ with calcite structure. It was recently shown [28, 29] that that there is no complete solid solution series between alumino-silicate mullite and mullite-type aluminum-borates.

Boron-doping of mullite results in significant changes of lattice parameters *b* and *c*, with a linear relationship between *c* and the boron-content. [29, 30] In contrast, no significant changes are observed for the lattice parameter *a*, which, in B-free mullite, is linearly correlated with the Al/Si ratio.[31] Furthermore, the incorporation of B results in a strong reduction of the mean thermal expansion coefficient of 15%, which makes the material interesting, e.g., for substrates resistant to thermal shock up to 1000°C. [32] The crystal structure of B-mullite has recently been solved from neutron diffraction data and ^{11}B MAS NMR spectroscopy of a series of sol-gel derived B-mullites with various compositions synthesized at 1200°C. [33]

The knowledge of crystal structure, boron incorporation mechanism,[30] composition and properties is very important to address for applications of boron-doped mullites as engineering materials. The response of mullite-type materials to high-pressure offers a sensitive probe of their structural integrity, structural instabilities and possible phase transitions. Moreover, investigations of pressure-induced structural changes in mullites will also contribute to the in-depth fundamental understanding of their crystal chemistry.

2.1.3. $PbMBO_4$ Synthetic Mullites

The sillimanite group contains a number of $PbMBO_4$ phases with M = Al^{3+}, Ga^{3+}, Fe^{3+}, Cr^{3+} and Mn^{3+} and it has been classified in space group setting *Pnam* to better understand the physical properties of these materials while guaranteeing the conformity to the mullite family members. [34, 35, 36, 37, 38] Their identical symmetry was the reason for their categorization in the sillimanite group, even though the structural details of sillimanite, Al_2SiO_5, and the $PbMBO_4$ phases differ considerably. In $PbMBO_4$ mullite, the octahedral chains are cross-linked by BO_3 groups and the four-coordinated Pb atoms form the vertex of a pyramid with four oxygens, this anisotropy stemming from the fact that the Pb^{2+} lone electron pair is stereochemically active. Because of the transition metal, the octahedral chains of $PbMBO_4$ display one-dimensional magnetic behavior. [39] The chromium and iron compounds are characterized by intra-chain antiferromagnetism, whereas the manganese compound shows ferromagnetic coupling. Inter-chain correlations are always ferromagnetic, which means that these phases belong to the class of insulating ferromagnets.

In particular $PbFeBO_4$ has drawn attention due to its diverse crystal chemical aspects. To describe the magnetic properties of $PbFeBO_4$, where the dominant spin exchange interaction is antiferromagnetic, its edge-sharing FeO_6 octahedra have been considered as a Heisenberg one-dimensional uniform chain model. [40] The nonlinear optical (NLO) properties of $PbFeBO_4$ seem to be promising from two points of view. First, according to the anionic group theory of NLO, [41] the planar ionic groups with π-conjugated systems such as trigonal planar BO_3 are responsible for large second harmonic generation (SHG) effects. Second, distortion from the stereochemically active LEP effect on the Pb^{2+} cation can give rise to non-centrosymmetric building units such as PbO_4 leading to SHG. These two non-centrosymmetric local factors in $PbFeBO_4$ may overcome the centrosymmetric constraint for NLO properties. The thermal expansion behavior ultimately determines the usefulness of many mullite ceramics and mullite refractory materials. [1] The thermal behavior of borates mainly stems from their unique B–O bonding strength as either isolated BO_x-polyhedra or bridging BO_x polyhedral unit.

2.1.4. How Do the Investigated Materials Relate to Each Other?

Typically mullite-type structures are characterized by their linear chains of edge-sharing MO6- octahedra with M representing a variety of di- and trivalent cations in the extended mullite family. 1 Following the classification of Baur & Fischer (2000) for zeolite-type frameworks, mullite materials are classified in a hierarchical order according to their crystallographic group-subgroup relationships (Figure 1).

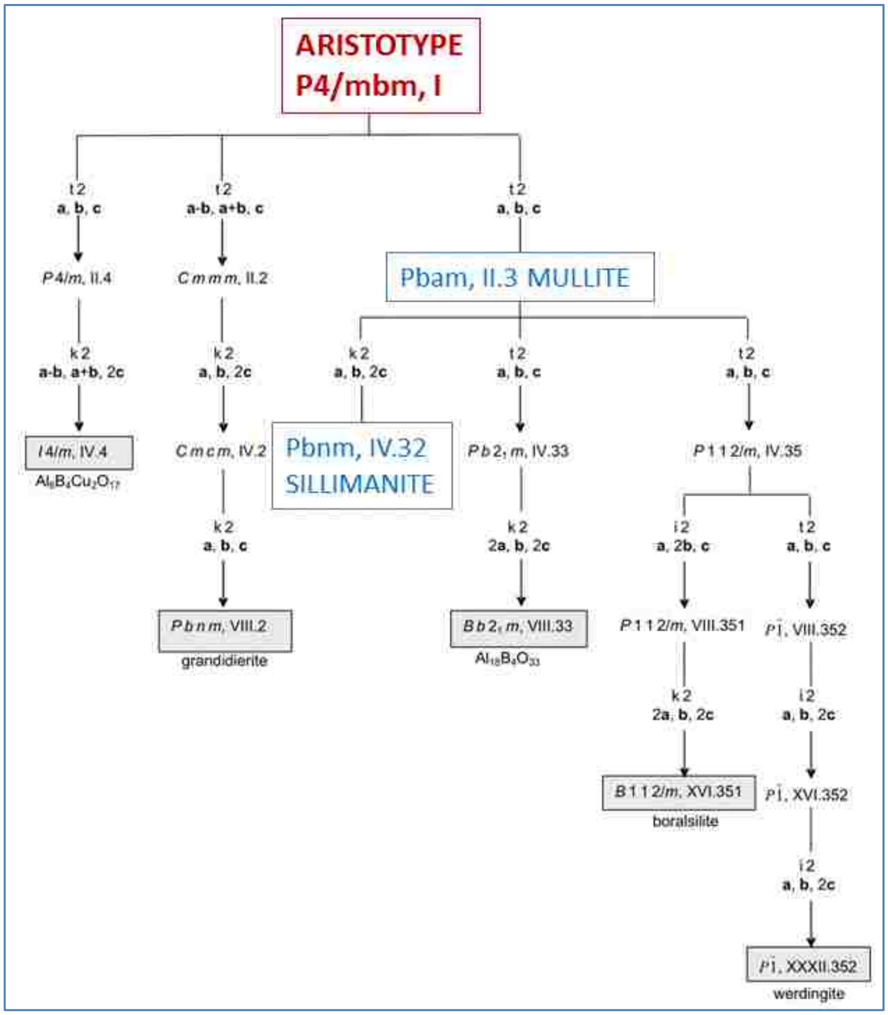

(i)

Figure 1. The Bärnighausen tree [42] illustrating the relations in the family of mullite-type compounds. After Bärnighausen, 1980. Figure prepared after [39] and [1]. The symbol *t* stands for "translationengleich", *k* for "klassengleich", *i* for "isomorphic". Unit-cell transformations are given by the corresponding expressions for the basis vectors. The numbers after this symbol represent the index of symmetry reduction for the respective step. Roman numerals represent the index of symmetry reduction relative to the aristotype. Group symbols in grey fields refer to observed compounds, the others are needed as intermediate steps for the symmetry reductions.

A material must meet the following benchmarks [1] to be classified in the mullite-type family:

(ii) The space group of a mullite-type compound must be a subgroup of $P4/mbm$ representing the highest possible symmetry of the hypothetical aristotype (so cubic, hexagonal, or trigonal structures are excluded from mullite family).

(iii) The edge-sharing MO_6 octahedra arranged in chains must be linear representing single Einer-chains in their highest topological symmetry in space group $P4/mbm$.

(iv) If an axis is drawn through the non-edge-sharing atoms of the octahedra such axis must point towards the edges of adjacent octahedral chains. This can also be expresses as the inclination angle ω which should have values $30^\circ \leqq \omega \leqq 90^\circ$.

(v) The chain structure should resemble the orthogonal metric of the aristotype perpendicular to the chain direction as closely as possible The approach to orthogonality is given by the angle γ between the projections of the basis vectors (in mullite these are the a and b axes) of the unit-cell onto the plane perpendicular to the chain axes ($\gamma = 90 \pm 5°$).

2.2. Raman Spectroscopy

Spectroscopic investigations give us most of our knowledge about the structure of atoms and molecules. Thus spectroscopy has made an outstanding contribution to the present state of atomic and molecular physics, to chemistry, and to molecular biology.

The primary object of Raman spectroscopy is the determination of molecular energy levels and transition probabilities connected with molecular transitions that are not accessible to infrared spectroscopy. Linear laser Raman spectroscopy, CARS, and hyper-Raman scattering have very successfully collected many spectroscopic data that could not have been obtained with other techniques. Besides these basic applications to molecular spectroscopy there are, however, a number of scientific and technical applications of Raman spectroscopy to other fields, which have become feasible with the new methods. [43, 44, 45, 46, 47]

Today Raman spectroscopy is used in many and wide-ranging applications such as: physics and chemistry, materials science and engineering, geosciences, biology, forensics, environmental sciences, pharmaceuticals, food analysis, cosmetics, corrosion, archeology and conservation science.

2.2.1. A Brief History of the Raman Effect

The origins of the Raman effect date back to the 1920's when the hot topic in research was scattering of electromagnetic radiation by charged particles. 1923 saw the discovery of the Compton effect or the quantum mechanical interpretation of the scattering of X-ray photons by electrons and their change in wavelength. Shortly after it was predicted that inelastic light scattering will occur in molecules just like in the Compton effect (Smekal, Germany). In 1925 Kramers and Heisenberg predicted the same in terms of electromagnetic theory. In 1928 the experiments followed theoretical predictions when C.V. Raman (India) reported a "feeble fluorescence" or "New Radiation".[48] Almost at the same time the effect was also reported by Landsberg and Mandelstam [49] (Moscow), and shortly after confirmed by R. W. Woods (USA), who was close to this discovery as well. The almost immediate award of the Nobel Prize in Physics to C.V. Raman in 1930, illustrated the prominence of this new phenomenon, which since then has been called Raman scattering, the Raman effect or Raman spectroscopy. [43, 44, 45, 46, 47]

In spite of early successes in 1940's with Raman spectroscopy, owing to instrumentation being similar to already exiting atomic spectroscopy, the technique was overshadowed in the 1950's and 1960's by the commercial development of IR spectrometers. Raman remained hindered by experimental difficulties and there were few experts (this can also be seen through the slow evolution of the number of publications on the topic in that time frame). [43, 44, 45, 46, 47]

A true revolution in Raman spectroscopy was brought, in the mid-1960's by: (i) the development of the first continuous wavelength lasers (He-Ne) to serve as incident radiation instead of high-pressure mercury arcs; as well as by the development of (ii) diffraction gratings, (for dispersion of scattered light), (iii)photomultipliers and photon counting equipment (for detection of scatterers light).

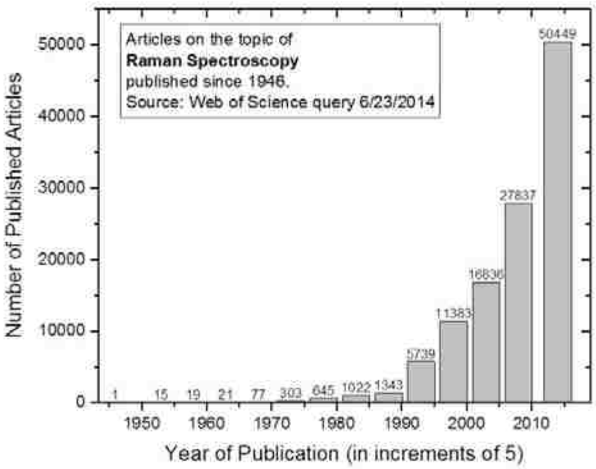

Figure 2. Number of articles published on the topic of Raman spectroscopy between 1946 and 2014. Source, Web of Science (query on 6/23/2014). Note the rapid increase starting in the 1980's.

These instruments were in widespread use by the 1970's. The new holographic grating developed in the 1970's opened the door for low-frequency Raman studies by eliminating many of the artifacts that afflicted early instruments. The next important milestone was the introduction of Ar^+ continuous lasers (514.532nm), which contributed in a dual way to the advancement of Raman spectroscopy: it increased the intensity of probing radiation by more than one order of magnitude while at the same time making the spectroscopic region of the Raman effect move to the green wavelength region, where incidentally the photomultipliers were much more effective. Lasers have greatly improved the sensitivity of spontaneous Raman spectroscopy. Lasers have also opened the door to new spectroscopic techniques, based on the stimulated Raman effect, such as coherent anti-Stokes Raman scattering (CARS) or hyper-Raman spectroscopy. [43, 44, 45, 46, 47]

Until ~ 1986, the Raman literature was composed mostly of physical and structural investigations, with few reports of Raman spectroscopy in chemistry. The barriers to entry in to the chemistry research were both fundamental and technical: weak intensity, fluorescence interference, and inefficient light collection and detection. In 1986 the introduction of charge-coupled devices (CCDs), Fourier transform (FT)-Raman, small computers, and near-infrared lasers opened the door for routine chemical analysis and created a period of Raman renaissance. [43, 44, 45, 46, 47] The development of instrumentation rendered Raman spectroscopy, which is inherently a difficult technique, much more accessible. This is also illustrated by the evolution of the number of publication on this topic which increased exponentially following instrumental advances (Figure 2). [43, 44, 45, 46, 47]

2.2.2. What is the Raman Effect?

When incoming light interacts with matter it can be either absorbed or scattered. The absorption process requires that the energy of the incident photon matches the energy gap between the ground state of a molecule and the excited state. Many spectroscopic techniques use this process (ex. IR Absorption). On the other hand scattering occurs independently of whether there is or there is not a suitable pair of energy levels to absorb the incoming radiation.

The Raman effect is a light-scattering effect, where an incident monochromatic beam interacts with a material and a small percentage of this light undergoes a change in frequency (either decrease or increase). The change in frequency is the outcome of coupling between the incident radiation and vibrational energy levels of molecules. Raman scattering is well well-known also from electronic and rotational energy levels. The most common spectroscopic region where the Raman effect is observed is the visible (with incident radiation being also in the visible). However both UV and near-IR Raman have also many applications.

Today, in many cases Raman spectroscopy is preferred to its cousin, IR spectroscopy, since measurements can be carried out in situ, property-related information can be obtained in samples in any physical state (solid, liquid, gas), dynamic investigations can be carried out and finally it is easily applied to aqueous solutions (IR spectroscopy is not), which is very useful for biological applications. The progress in diagnostic applications of Raman, which now overshadows IR spectroscopy, is connected to several crucial features of this technique: (i) the technique is non-destructive; (ii) very small samples can yield spectra, and with the addition of a microscope samples on the order of a micron can be studied (single crystals, grains, filaments, nano-liters of liquids can be studied without sample preparation); (iii) aqueous solutions can be readily investigated, since Raman scattering form water is very weak (as opposed to IR); (iv) high/low temperature stages and high-pressure cells allow for studies of materials in situ while P or T is being modified.

It is worth underlining that Raman spectroscopy offers the option to investigate the entire vibrational spectrum:

- Low-frequency modes, < 200cm^{-1}: lattice, torsional, chain modes; this region is still under-utilized; also triple-grating monochromators are usually required to access this very low frequency region;
- Mid-frequency, between 200cm^{-1} and ~1600 cm^{-1} (the actual upper limit depends on the type of molecular units investigated ex. inorganic vs organic): the so called “fingerprinting” modes that allow the identification of chemical species;
- High-frequency: fundamental modes;

2.2.3. Limitations of Raman Spectroscopy.

Raman scattering is inherently a very weak effect. Further, when one considers the energy transfer region of the Raman effect (Figure 3) it can be seen that Raman overlaps with fluorescence. If the incoming energy is enough to excite both luminescence and Raman then the luminescence phenomenon, which is 10^6-10^8 times stronger will overpower any present Raman signal. Trace impurities can often be enough to cause fluorescence.

Figure 3. Classification of spectroscopies by the amount of energy transferred in the process. Types of spectroscopy are indicated.

In such cases a different laser wavelength is required, for example UV or IR. If a tunable visible laser is available it can often be enough to choose a blue or a red wavelength to get away from the excitation of valence electrons of the impurities and hence to minimize or avoid fluorescence. To eliminate background fluorescence a classical approach is the irradiation of the sample with the laser for an extended period of time, just prior to a Raman measurement, which results in the photobleaching of the luminescent impurity. Finally, since the Raman effect arises on a much shorter time scale than fluorescence, this distinction can be used to separate the two although it requires a more intricate experimental setup.

Another issue which arises due to the use of intense, focused laser beams is that a sample can absorb this light, and heating and black-body radiation phenomena can overpower any present Raman signal, rendering it undetectable. Thermal decomposition or photochemistry can also be an issue. Besides reducing the power of the excitation beam, samples can be mixed with a fine metallic powder or dispersed in KBr, which will help in dissipating the absorbed heat.

2.2.4. States of a System – Vibration of a Diatomic Molecule

Consider the vibrations of a diatomic molecule in which two atoms are connected by a chemical bond. As indicated in Figure 4, r_1 +r_2 is the equilibrium distance and x1 and x2 are the displacements of atoms form their equilibrium positions. The conservation of the center of gravity requires that:

$$m_1 r_1 = m_2 r_2$$

or with the atoms moving from their equilibrium position that:

$$m_1(r_1 + x_1) = m_2(r_2 + x_2)$$

The above equations are combined to get:

$$x_2 = \left(\frac{m_1}{m_2}\right) x_1 \qquad \text{or} \qquad x_1 = \left(\frac{m_2}{m_1}\right) x_2$$

Classically the chemical bond is considered to be as a spring following Hooke's law where the restoring force *f* and the force constant *K* are related as:

$$f = -K(x_1 + x_2)$$

Combining the above two equations:

$$f = -K\left(\frac{m_1+m_2}{m_2}\right)x_1 = -K\left(\frac{m_1+m_2}{m_1}\right)x_2$$

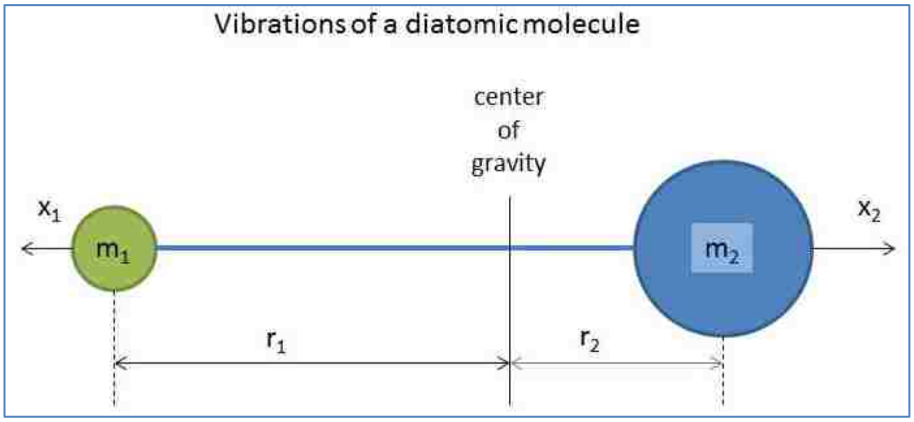

Figure 4. Vibrations of a diatomic molecule.

We can then write Newton's equation of motion for atom 1 and atom 2 (*f*=*ma*):

$$m_1\frac{d^2x_1}{dt^2} = -K\left(\frac{m_1+m_2}{m_2}\right)x_1 \qquad \text{and} \qquad m_2\frac{d^2x_2}{dt^2} = -K\left(\frac{m_1+m_2}{m_1}\right)x_2$$

By combining the above equations we obtain:

$$\frac{m_1m_2}{m_1+m_2}\left(\frac{d^2x_1}{dt^2}+\frac{d^2x_2}{dt^2}\right) = -K(x_1+x_2)$$

This can be rewritten as:

$$\mu\frac{d^2q}{dt^2} = -Kq$$

Where μ is the reduced mass and q is the displacement. This differential equation is solved with a sin function:

$$q = q_0 sin(2\pi v_0 t+\varphi) = q_0 sin(\omega t+\varphi)$$

Where q_0 is the maximum displacement and φ is the phase constant, which varies according to initial conditions. v_0 is the classical vibrational frequency:

$$v_0 = \frac{1}{2\pi}\sqrt{\frac{K}{\mu}} \qquad \rightarrow K = \mu(2\pi v_0)^2$$

The potential energy for the two atoms is:

$$f = -\frac{dV}{dq} \quad \rightarrow \quad dV = -f dq = Kq dq \quad \rightarrow \quad V = \frac{1}{2}Kq^2$$

$$V = \frac{1}{2}Kq_0^2 sin^2(2\pi v_0 t + \varphi)$$

And replacing K the potential energy is:

$$V = \frac{1}{2}Kq_0^2 sin^2(2\pi v_0 t + \varphi)$$

$$V = 2\mu\pi^2 v_0^2 q_0^2 sin^2(2\pi v_0 t + \varphi)$$

Next the expression for kinetic energy is:

$$T = \frac{1}{2}m_1\left(\frac{dx_1}{dt}\right)^2 + \frac{1}{2}m_2\left(\frac{dx_2}{dt}\right)^2 = \frac{1}{2}\mu\left(\frac{dq}{dt}\right)^2$$

$$T = 2\mu\pi^2 v_0^2 q_0^2 cos^2(2\pi v_0 t + \varphi)$$

Then we write the total energy:

$$E = T + V = \ 2\mu\pi^2 v_0^2 q_0^2 = constant$$

The potential V has a parabolic shape and in the classical point of view the two oscillating atoms constitute a harmonic oscillator.

In the quantum mechanical approach the vibration of the two atoms can be considered as motion of a single particle of mass u with potential energy again being:

$$V = \frac{1}{2}Kq^2$$

We can then write the Schrödinger equation for this system:

$$\frac{d^2\psi}{dq^2} + \frac{8\pi^2\mu}{h^2}\left(E - \frac{1}{2}Kq^2\right)\psi = 0$$

The condition for ψ is that it should be single valued, continuous and finite. The eigenvalues and the frequencies of vibration are:

$$E_v = hv\left(v + \frac{1}{2}\right) = hc\tilde{v}\left(v + \frac{1}{2}\right)$$

$$v = \frac{1}{2\pi}\sqrt{\frac{K}{\mu}} \qquad \text{and} \qquad \tilde{v} = \frac{1}{2\pi c}\sqrt{\frac{K}{\mu}}$$

In the above equation v is the vibrational quantum number with values 0, 1, 2, 3, 4. The quantum mechanical frequency is the same as the classical frequency.

In a given molecule there exists a series of electronic states, each of which contains a multiple vibrational and rotational states. When inter-nuclear separations are big, the atoms are basically unconstrained, but with decreasing distance (such as the application of pressure) they are attracted to one another and a bond is eventually formed (Figure 5).

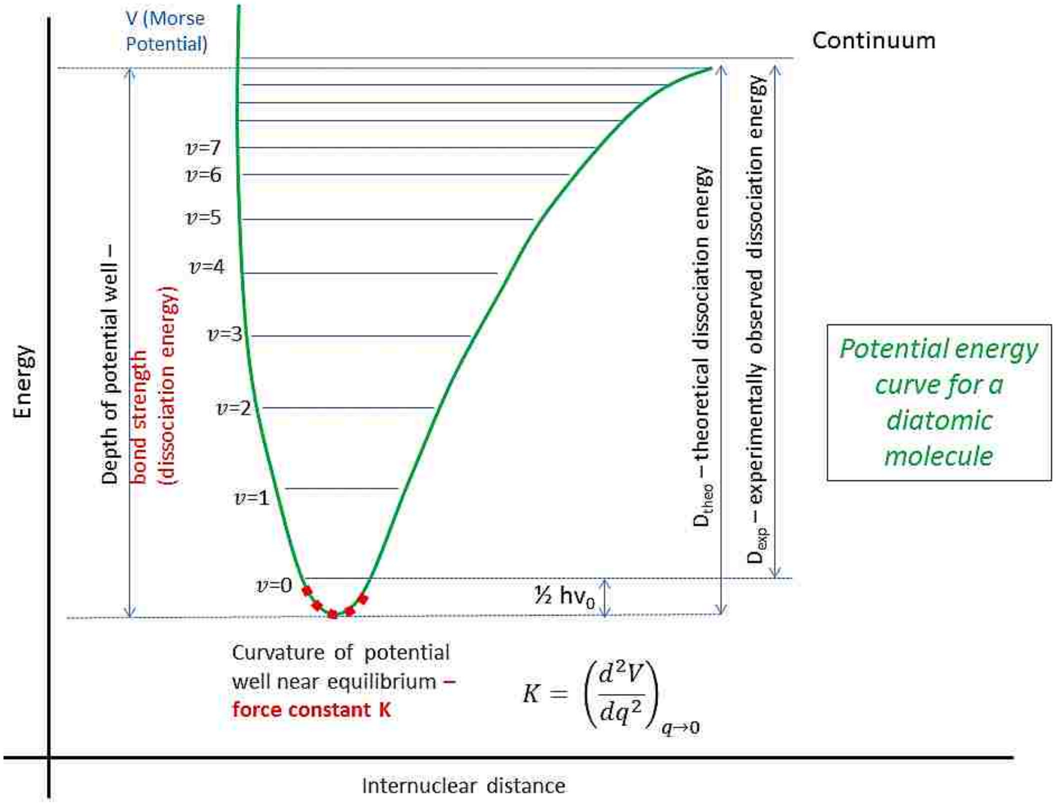

Figure 5. Potential energy curve or Morse potential for a diatomic molecule.

If the distance becomes too small however, nuclear repulsion begins to act and there is a sharp increase in energy of the molecule. The length of the bond corresponds to the internuclear distance with the lowest energy for the molecule. Due to the quantization of the vibrational energies of the molecule, only discrete energies are allowed in the potential energy curve. [45]

Compared to the time of nuclear movement, the phenomenon of Raman scattering is fast, so the nuclear separation does not have time to change noticeably during scattering and therefore there is no change in the internuclear distance (Figure 5). [45] To obtain a simple schematic, the energy states of a molecule are drawn as horizontal lines while modifications in energy of the molecule are drawn as vertical lines leading to a simplified energy level diagram, such as that in Figure 8.

For each vibrational quantum number v there is a corresponding eigenfunction:

$$\psi_v = \frac{(\alpha/\pi)^{1/4}}{\sqrt{2^v v!}} e^{-\alpha q^2/2} H_v\left(\sqrt{q\alpha}\right)$$

with $\alpha = 2\pi\sqrt{\mu K/h} = 4\pi^2 \mu\, v/h$

and with $H_v\left(\sqrt{q\alpha}\right)$ being Hermite polynomials of v^{th} degree. The eigenvalues and eigenfunctions are:

$v = 0$ and $E_0 = \frac{1}{2}hv$ and $\psi_0 = (\alpha/\pi)^{1/4} e^{-\alpha q^2/2}$

$v = 1$ and $E_1 = \frac{3}{2}hv$ and $\psi_1 = (\alpha/\pi)^{1/4} 2^{1/2} e^{-\alpha q^2/2}$

and so on.

What are the differences between classical and quantum mechanical descriptions of the vibrations of a diatomic molecule? Classically the lowest energy state for $q=0$ is $E=0$ but quantum mechanically the zero point energy is $E_0 = \frac{1}{2}hv$ (from Heisenberg's uncertainty principle). In the quantum mechanical treatment the energy changes in units of hv whereas classically the energy can change continuously. Finally due to the tunnel effect in quantum mechanics it is possible to find q outside of the parabola whereas in classical mechanics q is confined to the parabola.

In reality the molecular potential is better approximated by the Morse potential Figure 5:

$$V = D_e\left(1 - e^{-\beta q}\right)^2$$

where D_e is the dissociation energy, β is a measure of the curvature of at the bottom of the potential well. The solution to the Schrödinger equation with the Morse potential is: [47]

$$E_v = hc\omega_e\left(v + \frac{1}{2}\right) - hc\chi_e\omega_e\left(v + \frac{1}{2}\right)^2 + \cdots$$

where ω_e is the wavenumber corrected for anharmonicity and $\chi_e\omega_e$ is the magnitude of anharmonicity. The separation between energy levels is not equidistant (as for a harmonic oscillator) but it decreases for increasing energy levels v (Figure 5). In quantum mechanics, for a harmonic oscillator only transitions of $\Delta v = \pm 1$ are allowed. For anharmonic vibration transitions of $\Delta v = \pm 2, \pm 3, \cdots$ called overtones can be weakly allowed by selection rules. Out of the many $\Delta v = \pm 1$ allowed transitions, the strongest one is the $v = 0 \rightarrow 1$ called the fundamental transition is the strongest in IR and Raman spectroscopy.

When considering the vibrational frequency $\tilde{\nu} = \frac{1}{2\pi c}\sqrt{\frac{K}{\mu}}$ we see that $\tilde{\nu}$ is proportional to $\sqrt{K}$ referred to as the force constant effect and inversely proportional to $\sqrt{\mu}$ called the mass effect. However a large force constant does not necessarily indicate a strong bond, because the force constant is actually the curvature of the potential well near the equilibrium $K = \left(\frac{d^2V}{dq^2}\right)_{q\rightarrow 0}$ (so a large K means a sharp curvature near the bottom of the well) while bond strength or dissociation energy is the depth of the potential well.

2.2.5. Classical Light Scattering - Rayleigh Theory

The following derives the theory of light scattering from a small particle.[43, 44] Light, or electromagnetic radiation is described as a function of time:

$$E_z = E_0 \cos\omega t = E_0 \cos\left(\frac{2\pi ct}{\lambda}\right) \qquad / \ldots \left\{\nu = \frac{c}{\lambda} = \frac{\omega}{2\pi}\right\}$$

where E_0 is the amplitude of the electric field, c is the speed of light, and λ is the wavelength of light and E_z indicates plane polarized light along the z axis. An incident beam of light polarized in the z direction is shown in Figure 6. If the particle is polarizable, the incident electric field will induce a dipole moment in that particle. The polarizability α_p indicates the magnitude of the dipole moment in respect to the incident field. The dipole moment is:

$$p = \alpha_p E_0 cos\left(\frac{2\pi ct}{\lambda}\right) = \alpha_p E_0 cos(2\pi \nu t) = \alpha_p E_0 cos(\omega t)$$

The induced dipole moment will radiate light in all directions. Let's observe the scattered light at a distance *r* from the origin along a line that makes an angle θ_z with the *z* axis.

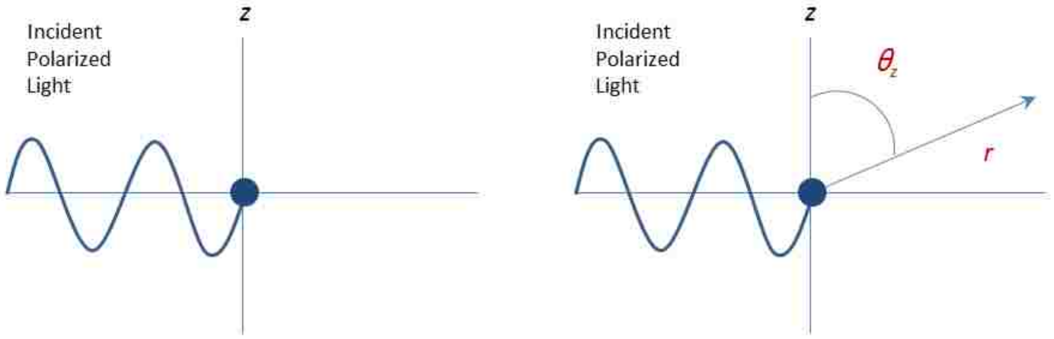

Figure 6. Schematic of the classical light scattering process.
Left: plane polarized light polarized in the *z* direction and incident on a small particle. Right: light scatters off the particle at an angle θ and it is observed a t a distance *r*.

Then we can write the electric field for light scattered in the θ_z direction:

$$E_S = \frac{1}{r}\frac{1}{c^2}\frac{d^2p}{dt^2} = -\left[\frac{1}{r}\frac{\omega^2}{c^2}\alpha_p E_0 sin(\theta_z)\right] cos(\omega t) = -\left[\frac{1}{r}\frac{4\pi^2}{\lambda^2}\alpha_p E_0 sin(\theta_z)\right] cos(\omega t)$$

The scattered light field will be proportional to $\frac{1}{c^2}\frac{d^2p}{dt^2}$ because the second derivative of p is the acceleration of the charge on the dipole moment. To include spatial effects, since electromagnetic fields decrease as $1/r$ the scattered light is also proportional to $1/r$, and finally the term $sin(\theta_z)$ accounts for the projection of the dipole moment along the direction of observation.

Measurements of scattered light are usually done through measurements of intensity. The intensity is obtained by squaring the amplitude of E_s:

$$I_{Scattered} = I_S = I_{0z}\alpha_p^2 \frac{\omega^4}{r^2c^2} sin^2(\theta_z) = I_{0z}\alpha_p^2 \frac{16\pi^4}{r^2\lambda^4} sin^2(\theta_z)$$

Where $I_0 = E_0^2$ is the intensity of the z polarized incident light. These results are for incident light polarized in the z direction. Experiments, however, are usually done with unpolarized light. We can account for unpolarized incident light by summing the intensity of equal parts of incident light polarized in both the z direction and the y direction:

$$I_0 = \frac{1}{2}I_{0z} + \frac{1}{2}I_{0y}$$

$$I_S = \frac{1}{2}I_{S,z} + \frac{1}{2}I_{S,y} = I_{0z}\alpha_p^2\frac{\omega^4}{2r^2c^2}\left[sin^2(\theta_z) + sin^2(\theta_y)\right] = I_{0z}\alpha_p^2\frac{8\pi^4}{r^2\lambda^4}\left[sin^2(\theta_z) + sin^2(\theta_y)\right]$$

where θ_y is the angle the observation direction makes with the y axis.

By geometry the θ_z and θ_y terms can be related to the angle θ_x that the observation direction makes with the x axis (Figure 6). This angle will simply be referred to as θ. Since direction cosines add up to 1:

$$cos^2\theta_x + cos^2\theta_y + cos^2\theta_z = 1$$

$$cos^2\theta_y + cos^2\theta_z = 1 + cos^2\theta$$

We now have the scattered light intensity for scattering off a single particle:

$$I_S = \frac{1}{2}I_{S,z} + \frac{1}{2}I_{S,y} = I_{0z}\alpha_p^2\frac{\omega^4}{2r^2c^2}[1 + cos^2\theta] = I_{0z}\alpha_p^2\frac{8\pi^4}{r^2\lambda^4}[1 + cos^2\theta]$$

2.2.6. Theory of Raman Scattering - Overview

When Incoming light of a specific energy encounters a molecule it can scatter from it either without change in energy (Rayleigh scattering), or with a decreased or increased energy (Raman). The physics of Raman scattering can be approached in two ways: the *classical wave interpretation* or the *quantum particle interpretation*. In the *classical wave interpretation* of Raman, electromagnetic radiation comprises an oscillating electric field which interacts with a molecule through the molecule's polarizability. Polarizability is the ability of the electron cloud to interact with an electric field. For example, soft molecules, such as benzene, tend to be strong Raman scatterers while harder molecules, like water, tend to be fairly weak scatterers. In the *quantum particle interpretation* of Raman, a photon reaches a molecule and then scatters inelastically. The number of scattered photons is proportional to the size of the bond. Reprising the previous example, molecules with large π bonds, such as benzene, tend to scatter lots of photons, while water, with small single bonds, tends to be a very weak Raman scatterer.

2.2.6.1. Theory of Raman and Rayleigh Scattering – Classical Treatment

In any spectroscopy there is a mechanism through which incident radiation interacts with molecular energy levels. Raman spectroscopy originates from the general phenomenon of light scattering where light (electromagnetic radiation) interacts with *a pulsating, deformable/polarizable electron cloud*.

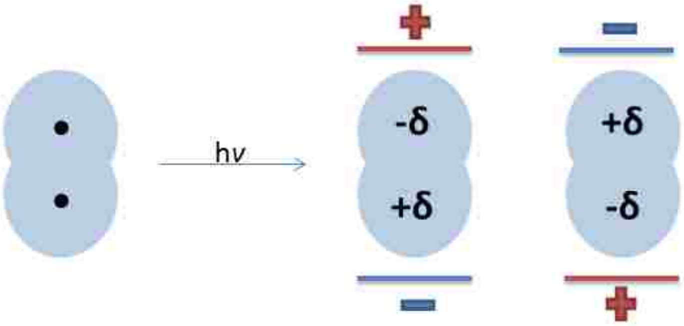

Figure 7. Polarization of a diatomic molecule in an external electric field.

In the case of Raman phenomenon, the above interaction is controlled by molecular vibrations and causes an *induced dipole moment*. In IR absorption spectroscopy the mechanism of interaction of radiation with molecular vibrational energy levels is the *change in permanent dipole moment* during the vibration. [44, 46]

When electromagnetic radiation strikes a (spherical) polarizable sample (Figure 7) this causes the electron cloud to oscillate, driven by the frequency of incident radiation. A pulsating electron cloud will radiate in all directions (scattered light). Now any molecule consists of a series of electronic states, each of which contains a large number of vibrational and rotational states (Figure 8). Vibrational transitions appear in the $10^4 \sim 10^2 \text{cm}^{-1}$ region and these are observed in Raman and IR spectra.

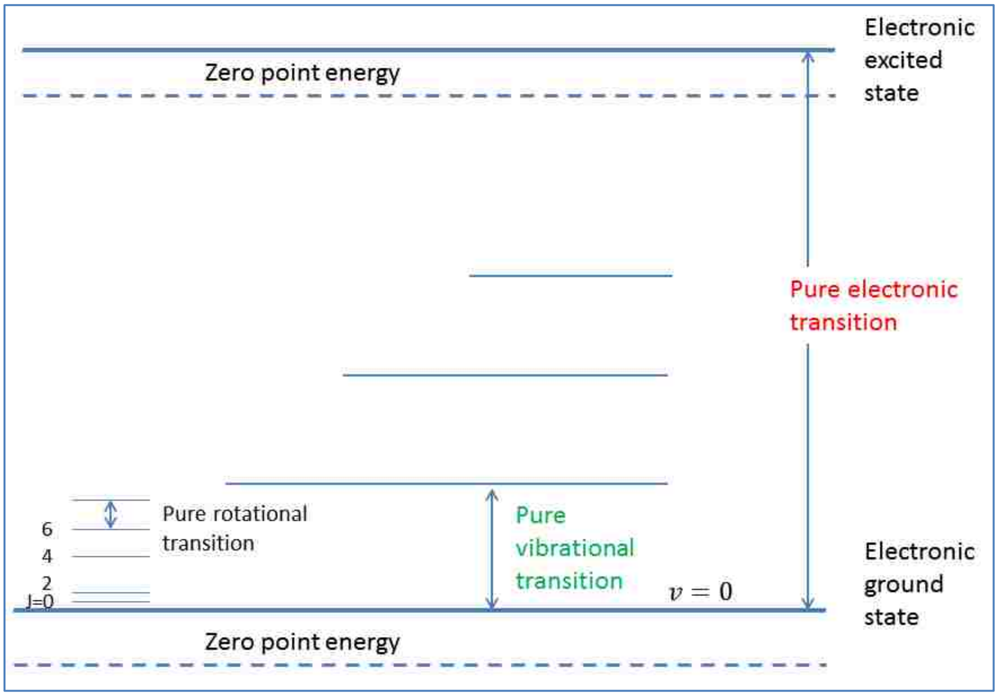

Figure 8. Energy levels of a diatomic molecule.

Assume the incident electromagnetic radiation is represented by its electric field:

$$\overrightarrow{E} = E_0 \cos \omega t = E_0 \cos\left(\frac{2\pi ct}{\lambda}\right) \qquad / \ldots \left\{v = \frac{c}{\lambda} = \frac{\omega}{2\pi}\right\} \qquad \text{Eq. 1}$$

A classical description of the vibrational Raman effect was developed first by Placzek,[50] and states the following relation:

$$\vec{p} = \overrightarrow{\mu_0} + \tilde{\alpha}\vec{E} \qquad \text{Eq. 2}$$

Connecting the incoming radiation with the dipole moment $\vec{p}$ of a molecule; $\overrightarrow{\mu_0}$ is a *possible permanent dipole moment*, and $\tilde{\alpha}\vec{E}$ is the *induced dipole moment* (Figure 9). Polarizability $\tilde{\alpha}$ is usually a tensor of rank 2, and it together with dipole moment are functions of the coordinates of nuclei and electrons. However as long as frequency of incident light is far off resonance (with electronic or vibrational transitions), the nuclear displacement induced by the polarization of the electron cloud are small.

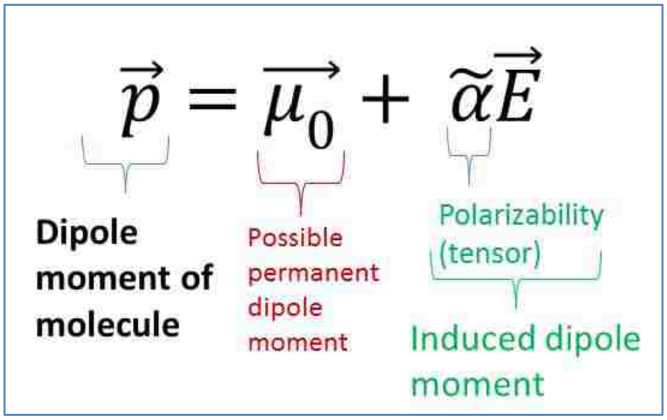

Figure 9. Dipole moment of a molecule and its relation to the induced dipole moment.

So we need to consider that the scattering body (a molecule in fact) is not just a polarizable sphere, but has vibrational modes of its own, or *normal modes q*. (The complex vibration that a molecule is making is really a superposition of a number of much simpler basic vibrations called "normal modes" q[1]). For small vibrational amplitudes the normal coordinates $q_n(t)$ of the vibrating molecule can be approximated by:

$$q_n(t) = q_{n0}\cos(\omega_n t) \qquad \text{Eq. (3)}$$

Since the electronic charge distribution is determined by the nuclear positions and adjusts "instantaneously" to changes in these positions, we can expand the *dipole moment* and *polarizability* into Taylor series in the normal coordinates q_n of the nuclear displacements:

---

[1] In general a normal mode of an oscillating system is a pattern of motion in which all parts of the system move sinusoidally with the same frequency and with a fixed phase relation. The motion described by the normal modes is called resonance. The frequencies of the normal modes of a system are known as its natural frequencies or resonant frequencies. A physical object, such as a building, bridge or molecule, has a set of normal modes that depend on its structure, materials and boundary conditions. The most general motion of a system is a superposition of its normal modes. The modes are normal in the sense that they can move independently, that is to say that an excitation of one mode will never cause motion of a different mode. In mathematical terms, normal modes are orthogonal to each other.

$$\vec{\mu} = \vec{\mu}(0) + \left(\frac{\partial \vec{\mu}}{\partial q_n}\right)_0 q_n + \cdots \qquad \text{Eq. (4)}$$

$$\alpha_{ij}(q) = \alpha_{ij}(0) + \left(\frac{\partial \alpha_{ij}}{\partial q_n}\right)_0 q_n + \cdots \qquad \text{Eq. (5)}$$

where $\boldsymbol{\mu}(0) = \boldsymbol{\mu}_0$ is the dipole moment and α_{ij} (0) is the polarizability at the equilibrium configuration $q_n = 0$. By combining Eq.(1) with Eq.(4) and Eq.(5) we can obtain a description of the dipole moment of a molecule:

$$\vec{p} = \overrightarrow{\mu_0} + \tilde{\alpha}\vec{E} = \left[\overrightarrow{\mu_0} + \left(\frac{\partial \vec{\mu}}{\partial q_n}\right)_0 q_n\right] + \left[\alpha_{ij}(0) + \left(\frac{\partial \alpha_{ij}}{\partial q_n}\right)_0 q_n\right] E_0 \cos \omega t \qquad \text{Eq.(6)}$$

And by inserting Eq. (3) we get:

$$\vec{p} = \left[\overrightarrow{\mu_0} + \left(\frac{\partial \vec{\mu}}{\partial q_n}\right)_0 q_{n0} \cos(\omega_n t)\right] + \left[\alpha_{ij}(0) + \left(\frac{\partial \alpha_{ij}}{\partial q_n}\right)_0 q_{n0} \cos(\omega_n t)\right] E_0 \cos \omega t \quad \text{Eq.(7)}$$

$$\vec{p} = \overrightarrow{\mu_0} + \left(\frac{\partial \vec{\mu}}{\partial q_n}\right)_0 q_{n0} \cos(\omega_n t) + \alpha_{ij}(0) E_0 \cos \omega t + \left(\frac{\partial \alpha_{ij}}{\partial q_n}\right)_0 q_{n0} \cos(\omega_n t)\, E_0 \cos \omega t$$

Eq.(8)

Finally by applying a trigonometric identity to the last term:

$$\vec{p} = \overrightarrow{\mu_0} + \left\{\left(\frac{\partial \vec{\mu}}{\partial q_n}\right)_0 q_{n0} \cos(\omega_n t)\right\} + \cdots$$

(→ **Infrared** Spectrum)

$$\cdots + \left\{\alpha_{ij}(0) E_0 \cos \omega t\right\} + \cdots$$

(→ **Rayleigh** elastic scattering; oscillating dipole that radiates light at frequency ω)

$$\cdots + \frac{1}{2} E_0 \left(\frac{\partial \alpha_{ij}}{\partial q_n}\right)_0 q_{n0} [\cos(\omega - \omega_n)t + \cos(\omega + \omega_n)t] \qquad \text{Eq.(9)}$$

(→ **Raman** scattering: inelastic Stokes and superelastic anti-Stokes)

The above expression was written for one vibrational mode of a molecule q_n with, but in fact a molecule with N nuclei has Q = 3N - 6 (or 3N-5 for linear) number of normal vibrational modes, which means that Eq.(4) and (5) should be re-written as a summation over all the Q vibrational modes:

$$\vec{\mu} = \vec{\mu}(0) + \sum_{n=1}^{Q} \left(\frac{\partial \vec{\mu}}{\partial q_n}\right)_0 q_n + \cdots \qquad \text{Eq. (10)}$$

$$\alpha_{ij}(q) = \alpha_{ij}(0) + \sum_{n=1}^{Q} \left(\frac{\partial \alpha_{ij}}{\partial q_n}\right)_0 q_n + \cdots \qquad \text{Eq. (11)}$$

And by adding the summation sign to Eq.(9) the complete description of the interaction of a molecule's vibrational modes with incoming radiation becomes:

$$\vec{p} = \overrightarrow{\mu_0} + \sum_{n=1}^{Q} \left\{ \left(\frac{\partial \vec{\mu}}{\partial q_n}\right)_0 q_{n0} \cos(\omega_n t) \right\} + \alpha_{ij}(0) E_0 \cos \omega t + \frac{1}{2} E_0 \sum_{n=1}^{Q} \left\{ \left(\frac{\partial \alpha_{ij}}{\partial q_n}\right)_0 q_{n0} [\cos(\omega - \omega_n)t + \cos(\omega + \omega_n)t] \right\} \qquad \text{Eq. (12)}$$

The complete description of the interaction of a molecule's vibrational modes with incoming radiation is also illustrated in Figure 10.

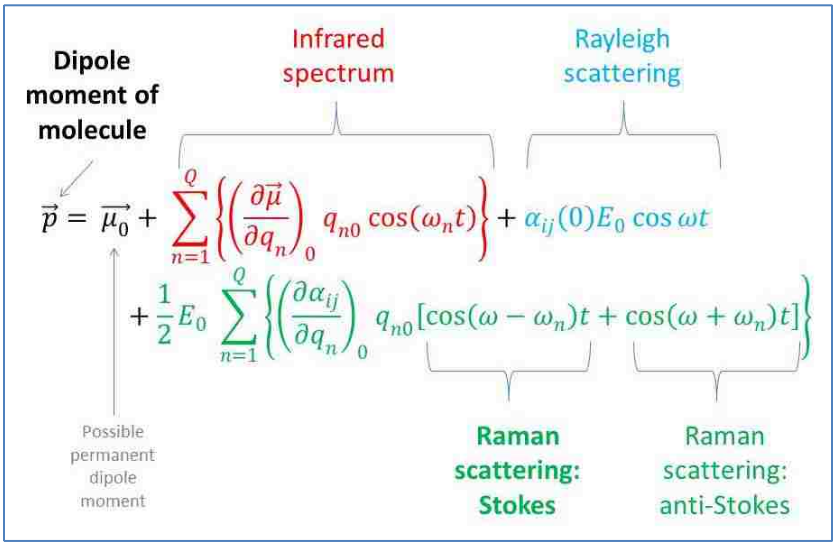

Figure 10. Interaction of a molecule's vibration with incoming radiation.
The complete description of the interaction of a molecule's vibrational modes with incoming radiation.

From the above equation we see that what determines whether a vibrational mode will be IR or Raman active is the non-zero rate of change of the dipole moment or of the polarizability (respectively) during normal vibrations of a molecule. An example can be seen below for the case of a CO_2 molecule. The polarizability change is $\partial\alpha/\partial q \neq 0$ only for the symmetric stretch ν_1, which is therefore called "Raman active." The permanent dipole moment change $\partial\mu/\partial q \neq 0$ for the bending vibration ν_2 and for the asymmetric stretch ν_3 which are then called "infrared active" vibrations.

An oscillating dipole moment is a source of new waves generated at each molecule. The microscopic contributions from each molecule add up to macroscopic waves with intensities that depend on the population $N(E_i)$ of the molecules in the initial level E_i, on the intensity of the incident radiation, and on the expression $(\partial\alpha_{ij}/\partial q_n)q_n$, which describes the dependence of the polarizability components on the nuclear displacements.

The classical description of Raman spectroscopy predicts a simple linear dependence of Raman scattering on incident beam intensity and sample concentration, which is in accordance with experimental observations. The frequencies $\omega \pm \omega_n$ are correctly predicted, and so are the relative intensities of Rayleigh and Raman scattering: it is expected that $\Sigma\partial\alpha_{ij}/\partial q_n$ will be much smaller than $\alpha_{ij}(0)$ implying that Raman scattering is in fact much smaller than Rayleigh. However the classical description does not yield absolute intensities of Raman modes, which brings about the need for a quantum mechanical treatment. The older classical treatment of Raman scattering is based on the wave theory of light and it's weakness lies in the fact that it does not account for the quantized nature of vibrations and it cannot explain as much about the relationship between Raman scattering and molecular properties as the quantum treatment can.

2.2.6.2. Theory of Raman Scattering – Quantum Mechanical Treatment

An incoming light wave may interact with a molecule, and because this light wave is a propagating oscillating dipole, it can then distort the electron cloud of the molecule. As a result of this interaction the energy is scattered or released again in the form of radiation (light). The incoming light is much larger than the molecule, since visible light has wavelengths between 400-700 nm, while a small molecule is a few angstroms (~0.5 nm). If the interaction between the propagating oscillating dipole (light wave) and the molecule takes place at all, the electrons of the molecule become polarized and move to a higher energy state. As that happens the light wave's energy is reassigned to the molecule.

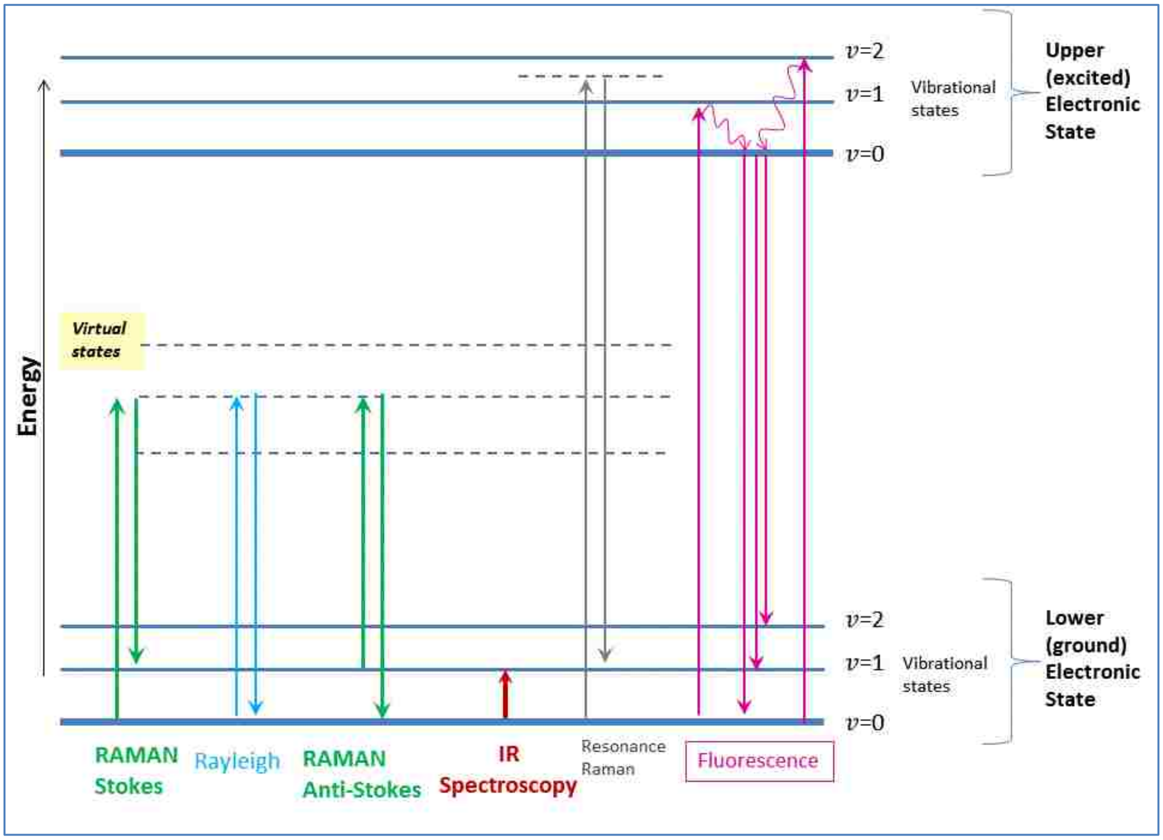

Figure 11. Possible consequences of a photon-molecule interaction.

The transfer of energy form light wave to molecule can be viewed as the creation of a very short-lived *composite* (also commonly referred to as a "virtual state" by chemists, Figure 11) between the electrons in the molecule and the light energy. In that very short time the nuclei do not move in a significant way. [45] The molecule assumes a high energy form with different electron geometry, but nuclear movement is not significant. The light is actually released immediately as scattered radiation since the above defined *composite* between the light and the molecule is unstable. The nuclei have no time to reach new equilibrium geometry, in response to the new, distorted electronic geometry of the molecule. Since the new electron arrangement cannot be illustrated by any of the electronic states of the molecule the very short-lived *composite* carries the label of "virtual state". Hence the "*virtual state*" is a real state of the *short-lived composite* formed between the light energy and the electrons in the molecule. The wavelength of the laser used thus the energy imparted to the molecule to create the virtual state determines the shape of the distorted electron geometry. So the energy of the virtual state and the amount of the distortion of the electron geometry is regulated by the excitation source used in the Raman experiment. [45]

How is scattering different from absorption? The electrons of the molecule are not promoted to any one excited state. In fact the states of the distorted *composite* between the light energy and the electrons in the molecule is made by involving and mixing - to varying degrees - all states of the static molecule. The excitation source determines the energy of the distorted *composite.* The electronic properties of the molecule, together with the energy of the excitation source determine the degree of distortion of the electron geometry.

In comparison to absorption processes, the lifetime of the excited state in Raman scattering is very short. The radiation is not lost by energy transfer within a molecule or emitted at a lower energy, but it is scattered as a sphere**.** The polarization of the exciting (laser) and scattered (Raman) phonons are related, which can be of value in distinguishing and assigning the scattering to particular vibrations.

Intensity is a characteristic feature of the two processes in scattering, Rayleigh and Raman scattering. Raman, with only one in 10^6-10^8 of the photons scattered is a very rare event. [45] The nuclei begin to move at the same time as the light and electrons of the molecule interact, but because they are so much heavier than electrons, the energy of the molecule changes to either a lower or higher energy depending whether the process begins with a molecule in the ground state or with a molecule in a vibrationally excited state (Figure 11). The first process is called anti-Stokes Raman (from a vibrationally excited state to the ground state) and the second Stokes Raman (from the ground state to a vibrationally excited state). Since Raman scattering is so rare, the overwhelming majority of scattered photons goes to Rayleigh scattering, with the electron cloud relaxing without any nuclear movement and without any change in energy (elastic scattering).

Most of the Raman effect is Stokes scattering (Figure 11) since most molecules will be initially in the ground vibrational state, while only a minority will be in an excited vibrational level *prior to* interaction with light. The Boltzmann equation gives the ratio of intensities of the Stokes and anti-Stokes scattering which is a function of the number of molecules in the ground and excited vibrational levels: [43]

$$\frac{N_n}{N_m} = \frac{g_n}{g_m} exp\left[\frac{-(E_n - E_m)}{kT}\right] \qquad \text{Eq. (13)}$$

where *n* and *m* are different vibrational states of the ground electronic state, g is the degeneracy of the levels n and m, N_n is the number of molecules in the excited vibrational level (*n*), N_m is the number of molecules in the ground vibrational level (*m*), E_n-E_m is the difference in energy between vibrational levels. The degeneracy *g* indicates the number of vibrations that can occur in more than one way (through symmetry) but with the same energies, so that individual components cannot be separated; for most vibrational states *g*=1 but for degenerate vibrations *g*=2 or 3. [45]

The expectation value of the component α_{ij} of the polarizability tensor is given by:

$$\langle\alpha_{ij}\rangle_{ab} = \int u_b^*(q)\, \alpha_{ij} u_a(q) dq \qquad \text{Eq.(14)}$$

where:

- the function $u_a(q)$ represent the *molecular eigenfunction* in the initial level a
- and the function $u_b(q)$ represent the *molecular eigenfunction* final level b.

The integration extends over all nuclear coordinates. The expectation value of the component α_{ij} of the polarizability tensor shows that a computation of the intensities of Raman lines is based on the knowledge of the molecular wave functions of the initial and final states. For vibrational–rotational Raman scattering these are the rotational–vibrational eigenfunctions of the electronic ground state.

Assuming small displacements q_n, the molecular potential can be approximated by a harmonic potential, where the coupling between the different normal vibrational modes can be neglected (it was mentioned before that normal vibrational modes are independent of each other or orthogonal to each other). The functions u(q) can then be written as a product:

$$u(q) = \prod_{n=1}^{Q} w_n(q_n, v_n) \qquad \text{Eq.(15)}$$

of vibrational eigenfunction of the n^{th} normal mode with v_n vibrational quanta. Using the orthogonality relation:

$$\int w_n w_m dq = \delta_{nm} \qquad \text{Eq.(16)}$$

of the functions $w_n(q_n)$, we get from Eq.(14) and Eq.(11)

$$\left\{\alpha_{ij}(q) = \alpha_{ij}(0) + \sum_{n=1}^{Q} \left(\frac{\partial \alpha_{ij}}{\partial q_n}\right)_0 q_n + \cdots \right\}$$

$$\langle \alpha_{ij} \rangle_{ab} = (\alpha_{ij})_0 + \sum_{n=1}^{Q} \left(\frac{\partial \alpha_{ij}}{\partial q_n}\right)_0 \int w_n(q_n, v_a)\ q_n\ w_n(q_n, v_a) dq_n \qquad \text{Eq.(17)}$$

The first term represents Rayleigh scattering and it is a constant.

For nondegenerate vibrations the integrals in the second term vanish unless $v_a = v_b \pm 1$. In these cases it has the value $\left[\frac{1}{2}(v_a + 1)\right]^{1/2}$. Hence the basic intensity parameter of vibrational Raman spectroscopy is the derivative ($\partial\alpha_{ij}/\partial q$), which can be determined from Raman spectra.

The intensity I_s of a Raman line at the Stokes or anti-Stokes frequency $\omega_s = \omega \pm \omega_n$ is determined by:

- the population density $N_i(E_i)$ in the initial level $E_i(v, J)$,
- by the intensity I_L of the incident pump laser,
- and by the Raman scattering cross section $\sigma_R(i \rightarrow f)$ for the Raman transition $E_i \rightarrow E_f$:

$$I_s = N_i(E_i)\sigma_R(i \rightarrow f)I_L \qquad \text{Eq.(18)}$$

At thermal equilibrium the population density $N_i(E_i)$ follows the Boltzmann distribution:

$$N_i(E_i, v, J) = \frac{N}{Z} g_i e^{-E_i/kT}, \text{ where } N = \sum N_i \qquad \text{Eq.(19)}$$

The statistical weight factors g_i depend on the vibrational state $v = (n_1 v_1, n_2 v_{2,\dots})$ the rotational state with the rotational quantum number J, the projection K onto the symmetry axis in the case of a symmetric top, and furthermore on the nuclear spins I of the N nuclei. The partition function Z is a normalization factor, which makes $\sum N_i(v, J) = N$ (to check insert Eq.(20) into Eq. (19)):

$$Z = \sum_i g_i e^{-E_i/kT} \qquad \text{Eq.(20)}$$

For anti-Stokes radiation the molecules may have initially some excitation energy, while for Stokes radiation the initial state of the molecules may be the vibrational ground state. Because of the lower population density in the excited levels, the intensity of the anti-Stokes lines is lower by $\exp(-\hbar\omega_v/kT)$.

The scattering cross section is:

$$\sigma_R(i \rightarrow f) = \frac{8\pi\omega_S^4}{9\hbar c^4} \left| \sum_j \frac{\langle \alpha_{ij} \rangle \widehat{\boldsymbol{e_L}} \, \langle \alpha_{jf} \rangle \widehat{\boldsymbol{e_S}}}{\omega_{ij} - \omega_L - i\gamma_j} + \frac{\langle \alpha_{ji} \rangle \widehat{\boldsymbol{e_L}} \, \langle \alpha_{jf} \rangle \widehat{\boldsymbol{e_S}}}{\omega_{jf} - \omega_L - i\gamma_j} \right|^2 \qquad \text{Eq.(21)}$$

where $\widehat{\boldsymbol{e_L}}$ and $\widehat{\boldsymbol{e_S}}$ are unit vectors representing the polarization of the incident laser beam and the scattered light. The scattering cross section depends on the matrix element of the polarizability tensor and depends on frequency as ω^4 analogously to what was derived in the chapter about Rayleigh Theory. The sum extends over all molecular levels j with homogeneous width γ_j accessible by single-photon transitions from the initial state i.

From Eq.(21) it can be seen that the initial and final states are connected by two-photon transitions, which implies that both states have the same parity. For example, the vibrational transitions in homonuclear diatomic molecules, which are forbidden for single-photon infrared transitions, are accessible to Raman transitions. The matrix elements α_{ij} depend on the symmetry characteristics of, the molecular states. While the theoretical evaluation of the magnitude of α_{ij} demands a knowledge of the corresponding wave functions, the question whether α_{ij} is zero or not depends on the symmetry properties of the molecular wave functions for the states $|i\rangle$ and $|f\rangle$ and can therefore be answered by group theory without explicitly calculating the matrix elements.

The intensity of the Raman lines is proportional to the product of the Raman scattering cross section σ_R, which depends according to Eq. (21) on the matrix elements α_{ij} of the polarizability tensor and the density Ni of molecules in the initial state. If the cross sections σ_R have been determined elsewhere, the intensity of the Raman lines can be used for measurements of the population densities N(v, J). Assuming a Boltzmann distribution Eq.(19) the temperature T of the sample can be derived from measured values of N(v, J). This is frequently used for the determination of unknown temperature profiles in flames or of unknown density profiles in liquid or gaseous flows at a known temperature.

According to Eq.(21) the Raman scattering cross section increases considerably if the laser frequency ω_L matches a transition frequency ω_{ij} of the molecule, and this is called the Resonance Raman effect. The enhanced sensitivity of resonant Raman scattering can be utilized for measurements of micro-samples or of very small concentrations of molecules in solutions, where the absorption of the pump wave is small in spite of resonance with a molecular transition. If the frequency difference $\omega_L - \omega_s$ corresponds to an electronic transition of the molecule, we speak of Electronic Raman scattering, which gives complementary information to electronic-absorption spectroscopy. This is because the initial and final states must have the same parity, and therefore a direct dipole-allowed electronic transition . $|i\rangle \rightarrow |f\rangle$ is not possible.

2.2.7. Selection Rules

The basic selection rule is that Raman scattering originates from a change in the polarizability of a molecule. This implies that symmetric vibrations will give the most intense Raman scattering. On the other hand in infrared absorption a dipole change in the molecule implies that asymmetric vibrations will be the most intense.

In the previous section we obtained an expression for the intensity of Raman scattering, but that expression does not show whether the key terms, the α_{ij}'s are non-zero for a particular vibrational mode. Group theory allows to predict whether these terms can be non-zero, with information about the symmetry of a molecule (crystal). In each case *group theory* predicts whether a *transition moment integral* can be non-zero. These integrals contain the product of three terms – the wavefunctions for the ground and excited states, and the operator (in this case the components of the polarizability derivatives) that connects these two states. For a transition to occur the product of these three terms must be totally symmetric, which means it must leave the original molecule totally unchanged. Molecules of high symmetry are needed in both IR and Raman spectroscopy to observe vibrational modes. The best known selection rule is the "Rule of Mutual Exclusion" which states that if a molecule has a center of symmetry, vibrations cannot be active in both IR and Raman spectroscopy. In general vibrations that do not distort the molecule or symmetric vibrations are intense in Raman while those that distort a molecule a lot are most intense in IR spectroscopy. If the atoms constituting these vibrations are highly polarizable then the

Raman intensity is high. Further there are four main generalizations [51] about intensities of Raman spectra:

- Stretching vibrations associated with chemical bonds should be more intense than deformation vibrations
- Multiple chemical bonds should give rise to intense stretching modes
- Bonds involving atoms of large atomic mass are expected to give rise to stretching vibrations of high Raman intensity.
- Raman features arising from normal coordinates involving two in-phase bond stretching motions are more intense than those involving a 180° phase difference. Similarly for cyclic compounds the in-phase breathing mode is usually the most intense.

2.2.8. Raman Spectroscopy at Ambient and High Pressures

Raman spectroscopy is a fantastic technique mainly because it can deliver - very quickly - a lot of easily analyzable information. Finger-printing of materials and phases – both their composition and their state - can be done thanks to the very sensitive discrimination of Raman phonons: lattice and molecular vibrations. The measurement of elementary excitations can be used to characterize the related elastic, vibrational, electronic, or magnetic structures. Raman activity of phonon modes is directed by vibrational selection rules, as a function of their symmetry and the wave vector. Therefore vibrational selection rules yield information about crystal structure. Vibrational states give access to electronic and magnetic excitations. The electronic and magnetic states can be accessed through coupling to vibrational states.

Changing the pressure variable will influence the spectra of elemental excitation, so that Raman spectra can be used to examine the changes in elastic, vibrational, electronic, or magnetic structures in function of pressure. Raman spectroscopy under pressure can be used to study phase transformations (including melting), changes in the energy of the vibrational excitations (from which we can get mode Grüneisen parameters), magnetic and electronic transitions, chemical reactivity. Raman spectroscopy is also very useful to measure accurately pressure at very low and very high temperatures. [52]

2.3. X-Ray Diffraction

With today's state of the art high-resolution electron or atomic force microscopes atomic structures of crystals can be imaged directly, which could hypothetically render obsolete the idea of indirect imaging through diffraction. [53] In reality, however, diffraction yields more information regarding an unknown structure or structural parameters, because it is optimally sensitive to the periodic nature of the crystal. Diffraction experiments can be carried out using X-rays, neutrons for the bulk and electrons and atoms –primarily for the surface - all of which have different (elastic or inelastic) interactions with a solid. Diffraction can be described quasi-classically since the only quantum mechanical idea is that a beam of X-rays or neutrons possesses the wave-particle dual nature. [53]

Diffraction is the constructive and destructive interference of radiation caused by an object in the path of the radiation and of size comparable to the wavelength of radiation. [53, 54, 55] Since the intensity of electromagnetic radiation is proportional to the square of the amplitude of the waves, regions of constructive interference appear as having an enhanced intensity. The spacing of atoms in a crystal is on the order of one to a few Å, therefore the appropriate wavelength to study their structure through diffraction falls in the X-ray region. X-rays range from "soft" just above the Carbon K edge to hard X-rays in the 100 keV range. These limits, however, are not very well defined and differ slightly depending on the scientific community.[56] The most common X-ray radiation wavelengths used are those of CuK_α (1.54056 Å) as well as the sub-angstrom wavelengths of synchrotron radiation. The depth of penetration of an x-ray beam depends on the solid and on the photon energy but a typical depth is about 1 cm.[54]

2.3.1. Production of X-Rays

In the laboratory, X-rays are generated by accelerating electrons through a potential difference, and bombarding a metal target with these high-energy electrons (~keVs).[57] Typical anode materials in X-ray tubes are: chromium, iron, cobalt, nickel, copper, molybdenum, silver and tungsten.[58] The collision with a metal target decelerates the electrons and the difference in energy is emitted as a continuous range of wavelengths, or Bremsstrahlung radiation. If some electrons have just the right amount of energy for ionization, they will collide and remove an electron from the K-shell of the target metal. The thus created vacancy will be immediately filled by an electron from the L or M-shell. (It is also possible, but less probable, that the vacancy will be filled with an electron from outside of the atom.) As the electron falls into a lower energy shell it will emit the excess energy as an X-ray photon called K_α and K_β radiation, depending on whether it originates from the L- or the M-shells, respectively. The radiation will be in the X-ray range because the energy difference between the L and K-shells in a high-Z metal is of several thousands of keVs.[57] Vacancies are also created in higher shells (M, N and up) but the energy differences between the levels are much smaller and the emitted radiation appears as part of the continuous radiation (Bremsstrahlung).

2.3.2. The Bragg Equation

The foundation of almost all modern crystallography lies in the work of William Henry Bragg and his son William Lawrence Bragg which took place in 1913 and brought the pair a Nobel prize almost instantly, in 1915. [57] Let's consider the crystal to be a set of parallel lattice planes separated by a distance *d*, and acting like a mirror for incoming X-rays. It is then straightforward to derive the condition on the angle between the lattice plane and the incident X-rays necessary for constructive interference.

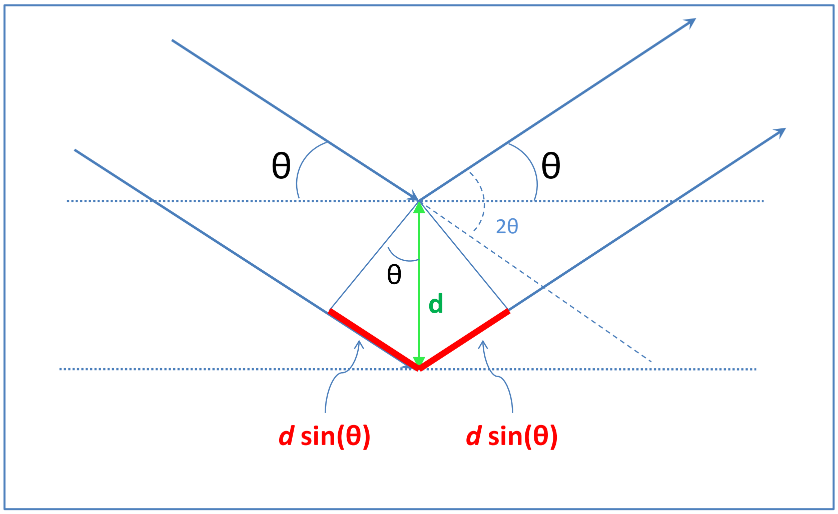

Figure 12. Schematic illustrating the principle of Bragg's law.
In order for the two waves to be in phase after they reflect from the two parallel planes, the path difference between the two waves must be equal to an integer number of wavelengths.

The difference of the length of the path of two X-rays diffracting from two planes separated by *d* must be an entire number of wavelengths λ. The condition on the path difference is called the Bragg law (Figure 12) and is:

$$\boldsymbol{n\lambda = 2\ d\ sin\theta}$$

Here *n* indicated the order of the reflection (or intense beam arising from constructive interference). In modern X-ray diffraction *n* is combined with d and hence the *n*th order reflection is considered as originating from the (*nh nk nl*) plane.

For a known angle, the *d*-spacing of a set of planes may be calculated. Once *d* is known then if the reflections can be indexed - that is ascribed (*hkl*) values - then one can obtain the lattice parameters *a*, *b*, and *c* of the unit cell. The key to solving a structure is then indexing. [53] Once the crystal structure is known, the parameters describing it, such as atom position and unit cell dimensions are adjusted (Rietveld refinement) until the calculated pattern (from the model of the structure) best matches the experimental pattern. [53] This can often be problematic for low symmetry system with a lot of reflections and for cases where there is more than one probable structure that differs very little. Finally, the next major step after refinement of the structure at ambient pressure is uncovering of possible phase transitions and the structural refinement when the pressure variable is introduced in the experiment. Such is the procedure followed in the presented work.

2.3.3. Theory of X-Ray Diffraction

W. L. Bragg's explanation for the diffracted beams from a periodic crystal structure assumed a mirror like behavior of the material. The Bragg equation is beautiful in its simplicity however it is convincing only [54] because it reproduces the correct result. Below is a more rigorous derivation of the condition of diffraction. [53, 54]

In order to describe diffraction one must start from a few basic assumptions. One assumption is that an incoming wave of X-rays, for example, will undergo single scattering and thus emit spherical waves from all points of an atom. If the waves are being emitted from a sufficiently distant source, they can be considered as plane waves at the site of an atom of the considered solid. Also we need to assume coherent scattering – a fixed phase between the incoming wave and the scattered spherical waves. Let the scattering center be located at a point P and the observation point to be labeled B. The amplitude of X-rays at point P can be expressed as:

$$A_P = A_o e^{i\vec{k}_o\cdot(\vec{R}+\vec{r})-i\omega t}$$

After scattering occurs, spherical waves are emitted from the sample and their amplitude and phase relative to the incident wave are described by the complex scattering density ρ(r). At the detection point B the spherical waves can be therefore expressed as:

$$A_B(r,t) = A_P\rho(\overrightarrow{r})\ \frac{e^{ik|\overrightarrow{R\prime}-\vec{r}|}}{|\overrightarrow{R\prime}-\vec{r}|}$$

And since the vector $\vec{k}$ is in the direction of $\overrightarrow{R'} - \vec{r}$ and further R’>>r:

$$A_B(r,t) = A_P\rho(\vec{r})\ \frac{e^{i\overrightarrow{k}\cdot\left(\overrightarrow{R'}-\vec{r}\right)}}{R'} = \frac{A_o}{R'} e^{i(\vec{k}_o\cdot\vec{R}+\vec{k}\cdot\overrightarrow{R'})} e^{-i\omega_o t}\rho(\vec{r})\ e^{i(\overrightarrow{k_o}-\vec{k})\cdot\vec{r}}$$

In order to obtain the total scattering amplitude one must integrate over the entire scattering region:

$$A_B^{total}(t) \propto e^{-i\omega_o t}\int \rho(\vec{r})\ e^{i(\overrightarrow{k_o}-\vec{k})\cdot\vec{r}}d\vec{r}$$

Since in diffraction we measure the intensity of the scattered waves and the intensity being proportional to the square of the amplitude we have:

$$I(\vec{K}) \propto \left|A_B^{total}(t)\right|^2 \propto \left|\int \rho(\vec{r})\ e^{i(\overrightarrow{k_o}-\vec{k})\cdot\vec{r}}d\vec{r}\right|^2$$

Where the scattering vector is defined as: $\vec{K} = \vec{k} - \vec{k}_o$

2.3.3.1. The Reciprocal Space

If we consider a crystal, which is a structure with translational symmetry, its electron density is periodic, so $\rho(x) = \rho(x + na)$ where n=0, 1, 2… and *a* is the lattice parameter (in 1D). [53, 54] Expanding in a Fourier series we have:

$$\rho(x) = \sum_n \rho_n e^{i\left(\frac{2\pi n}{a}\right)x}$$

In 3D the position $\vec{r}$ is described by three lattice vectors

$$\vec{r}_n = n_1\vec{a}_1 + n_2\vec{a}_2 + n_3\vec{a}_3$$

Then the electron density in 3D is written:

$$\rho(\vec{r}) = \sum_{\vec{G}} \rho_G e^{i\vec{G}\cdot\vec{r}}$$

where the vector $\vec{\boldsymbol{G}}$ is defined with basis vectors and intereger multipliers:

$$\vec{\boldsymbol{G}} = \boldsymbol{h}\vec{\boldsymbol{g}}_{\mathbf{1}} + \boldsymbol{k}\vec{\boldsymbol{g}}_{\mathbf{2}} + \boldsymbol{l}\vec{\boldsymbol{g}}_{\mathbf{3}}$$

In order for electron density to remain a periodic function, we need to impose a set of conditions on the vector $\vec{\boldsymbol{G}}$:

$$\vec{\boldsymbol{G}} \cdot \vec{\boldsymbol{r}}_{\boldsymbol{n}} = \mathbf{2}\boldsymbol{\pi m}$$

For example if n2=n3=0 then $(\boldsymbol{h}\vec{\boldsymbol{g}}_{\mathbf{1}} + \boldsymbol{k}\vec{\boldsymbol{g}}_{\mathbf{2}} + \boldsymbol{l}\vec{\boldsymbol{g}}_{\mathbf{3}})\boldsymbol{n}_{\mathbf{1}}\overrightarrow{\boldsymbol{a}_{\mathbf{1}}} = \mathbf{2}\boldsymbol{\pi m}$, which can be insured if $\vec{\boldsymbol{g}}_{\mathbf{1}} \cdot \vec{\boldsymbol{a}}_{\mathbf{1}} = \mathbf{2}\boldsymbol{\pi}$ and $\vec{\boldsymbol{g}}_{\mathbf{2}} \cdot \vec{\boldsymbol{a}}_{\mathbf{1}} = \mathbf{0}$ and $\vec{\boldsymbol{g}}_{\mathbf{3}} \cdot \vec{\boldsymbol{a}}_{\mathbf{1}} = \mathbf{0}$ which is equivalent to writing:

$$\vec{\boldsymbol{g}}_{\boldsymbol{i}} \cdot \vec{\boldsymbol{a}}_{\boldsymbol{j}} = \mathbf{2}\boldsymbol{\pi}\boldsymbol{\delta}_{\boldsymbol{ij}}$$

The three $\vec{\boldsymbol{g}}_{\boldsymbol{i}}$ vectors span the reciprocal space and the three values *h*, *k* and *l* are the reciprocals of points where the plane intersects the *a*, *b*, and *c* axis of the unit cell, respectively.

The above equation indicates that, for example, vector $\vec{\boldsymbol{g}}_{\mathbf{1}}$ is perpendicular to $\vec{\boldsymbol{a}}_{\mathbf{2}}$ and $\vec{\boldsymbol{a}}_{\mathbf{3}}$ (and hence to the plane formed by them), and that its length is $\mathbf{2}\boldsymbol{\pi}/(\boldsymbol{a}\ \boldsymbol{cos\varphi})$ where $\boldsymbol{\varphi}$ is the angle between $\vec{\boldsymbol{g}}_{\mathbf{1}}$ and $\vec{\boldsymbol{a}}_{\mathbf{1}}$. This can also be expressed by:

$$\vec{\boldsymbol{g}}_{\mathbf{1}} = \mathbf{2}\boldsymbol{\pi}\frac{\vec{\boldsymbol{a}}_{\mathbf{2}} \times \vec{\boldsymbol{a}}_{\mathbf{3}}}{\vec{\boldsymbol{a}}_{\mathbf{1}} \cdot (\vec{\boldsymbol{a}}_{\mathbf{2}} \times \vec{\boldsymbol{a}}_{\mathbf{3}})}$$

where the other vectors can be obtained by cyclic permutation.

2.3.3.2. The Laue condition

Let's return to $\boldsymbol{I}(\vec{\boldsymbol{K}}) \propto \left|\int \boldsymbol{\rho}(\vec{\boldsymbol{r}})\ \boldsymbol{e}^{\boldsymbol{i}(\overrightarrow{\boldsymbol{k}_{\boldsymbol{o}}} - \vec{\boldsymbol{k}}) \cdot \vec{\boldsymbol{r}}} \boldsymbol{d}\vec{\boldsymbol{r}}\right|^{\mathbf{2}}$ and insert the expression for $(\vec{\boldsymbol{r}}) = \sum_{\vec{\boldsymbol{G}}} \boldsymbol{\rho}_{\boldsymbol{G}} \boldsymbol{e}^{\boldsymbol{i}\vec{\boldsymbol{G}} \cdot \vec{\boldsymbol{r}}}$:

$$\boldsymbol{I}(\vec{\boldsymbol{K}}) \propto \frac{|\boldsymbol{A}_{\boldsymbol{o}}|^{\mathbf{2}}}{\boldsymbol{R}'^{\mathbf{2}}} \left|\sum_{\vec{\boldsymbol{G}}} \boldsymbol{\rho}_{\boldsymbol{G}} \int \boldsymbol{e}^{\boldsymbol{i}(\vec{\boldsymbol{G}} - \vec{\boldsymbol{K}}) \cdot \vec{\boldsymbol{r}}}\right|.$$

It can be shown that, in fact, the above sum is negligibly small when $\vec{\boldsymbol{K}}$ differs significantly from $\vec{\boldsymbol{G}}$. If the integral was expressed in components then for an infinite volume it would be a representation of respective δ-functions. We then have:

$$\int \boldsymbol{e}^{\boldsymbol{i}(\vec{\boldsymbol{G}} - \vec{\boldsymbol{K}}) \cdot \vec{\boldsymbol{r}}} \boldsymbol{d}\vec{\boldsymbol{r}} = \begin{cases} \textbf{the scattering volume } \boldsymbol{V}\ \boldsymbol{for}\ \vec{\boldsymbol{G}} = \vec{\boldsymbol{K}} \\ \sim\mathbf{0} \textbf{ otherwise} \end{cases}$$

The Laue condition [53, 54] states that scattering from periodic structures will lead to diffraction if the difference between the $\vec{k}$ vectors of scattered and incident wave corresponds to $\vec{G}$ (Figure 13) or:

$$\vec{G} = \vec{K}$$

Then the intensity that can be measured in a diffraction experiments is:

$$I_{\text{measured}}(\vec{K} = \vec{G}) \propto \frac{|A_o|^2}{R'^2} \left|\rho_{\vec{G}}\right|^2 V^2$$

The vector G is uniquely defined in the basis $\vec{g}_i$ of the reciprocal lattice by its three coordinates *h*, *k* and *l*. These indices can also be used to label the diffraction beams or reflections since a specific plane has a unique set of coordinates and it gives rise to one reflection which appears a peak in the diffraction pattern (Figure 13).

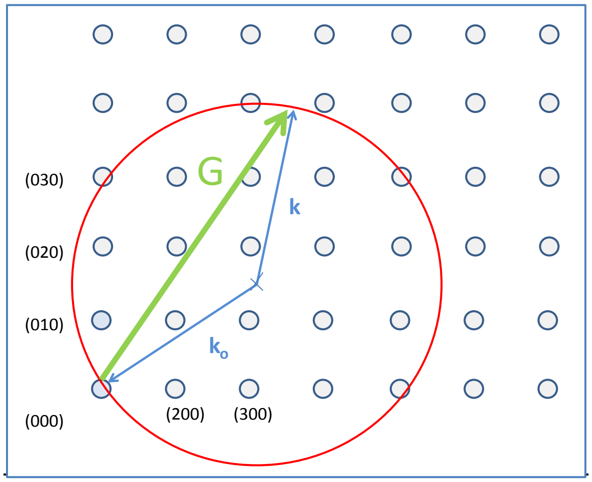

Figure 13. Schematic of a reciprocal lattice with (hkl)'s marking some of the reciprocal planes. The (reciprocal) c axis points out of the page. The circle represents the Ewald sphere of the reciprocal lattice illustrating the Laue condition $\vec{\mathbf{G}} = \vec{\mathbf{K}} = \vec{\mathbf{k}} - \vec{\mathbf{k}}_{\mathbf{o}}$. A diffracted beam will be produced whenever a reciprocal lattice point coincides with the surface of the sphere.

Let's consider one lattice plane in a periodic crystal structure: we can label the three points where the plane intersects with the coordinate axis as m, n and o and call the reciprocals of these numbers *h'*=1/*m*, *k'*=1/*n* and *l'*=1/*o* (Figure 14). In order to avoid dealing with fractions one can multiply *h'*, *k'* and *l'* by and integer *p* and obtain a set of three integers: *h*, *k*, *l* which are the coordinates of G. A given $\vec{G}_{hkl}$ is perpendicular to the corresponding (*hkl*) plane (Figure 14).

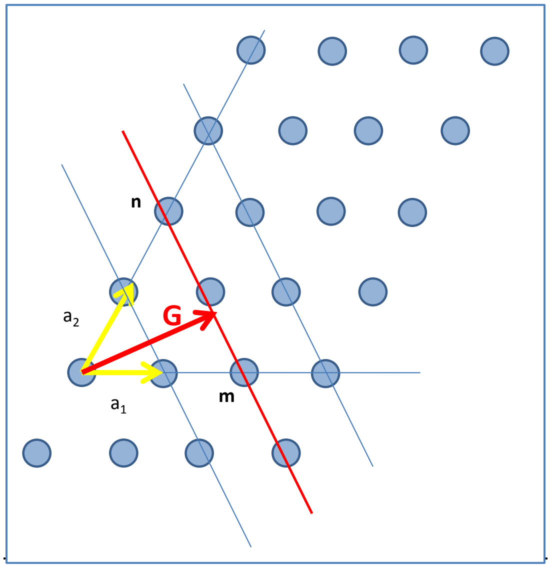

Figure 14. Set of crystal lattice plains in real space.
The plane in red intersects the axis at (2, 2, ∞) so the plane's (hkl)'s are 2*(1/2, 1/2, 0) which is (110). All planes parallel to this plane are equivalent, because they contain the same density of atoms.

2.3.3.3. The Bragg Equation

The distance from the origin of the lattice to a (hkl) plane is:

$$d'_{hkl} = \frac{a_1}{h'}\cos(\varphi) = \frac{a_1}{h'}\left(\frac{\vec{a}_1 \cdot \vec{G}_{hkl}}{a_1 G_{hkl}}\right) = \frac{1}{h'}\frac{2\pi h}{G_{hkl}} = \frac{2\pi}{G_{hkl}}\frac{h}{h'} = \frac{2\pi}{G_{hkl}}p$$

The distance to the nearest plane is then:

$$d_{hkl} = \frac{d'_{hkl}}{p} = \frac{2\pi}{G_{hkl}}$$

The Laue condition is the condition for scattering so one should be able to obtain the Bragg equation from it:

$$|\vec{G}| = |\vec{k} - \vec{k}_o|$$

$$G_{hkl} = \frac{2\pi}{d_{hkl}} = 2k_o \sin\theta \qquad \text{(Eq. 22)}$$

$$\frac{2\pi}{d_{hkl}} = 2\frac{2\pi}{\lambda}\sin\theta$$

$$\lambda = 2d_{hkl}sin\theta$$

In this way we obtain the Bragg equation, [53, 54] which says that the path difference between waves scattering from two parallel adjacent planes should be equal to the wavelength (or an integer of wavelengths) in order to produce constructive interference and hence a reflection (Figure 12).

2.3.3.4. Atomic scattering factor

How much of incoming X-rays will be scattered by an atom, that is the intensity of a reflection, depends on the electron density or in equation form: $I_{hkl} \propto |\rho_{hkl}|^2$ where $(\vec{r}) = \sum_{\vec{G}} \rho_G e^{i\vec{G}\cdot\vec{r}}$. The coefficients of the Fourier series of the scattering density are:

$$\rho_{hkl} = \frac{1}{V_c}\int_{\substack{unit\\cell}} \rho(\vec{r})e^{-i\vec{G}\cdot\vec{r}}d\vec{r}$$

In an element, the core electrons are concentrated in a small region around the atom (except for light elements, which are also ones that are least appropriate for investigation by X-rays). In comparison to core electrons, scattering from valence electrons is negligible.

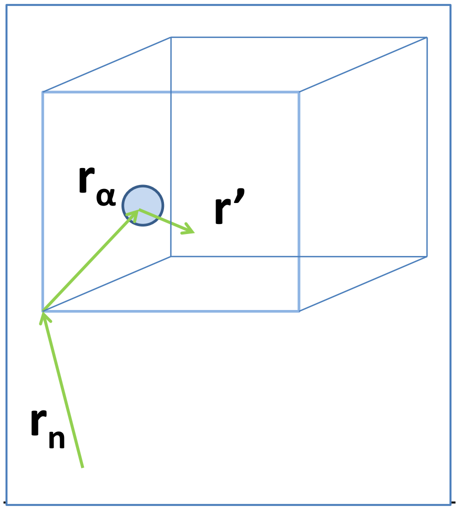

Figure 15. Schematic illustrating the decomposition of the position vector **r**.
r is decomposed into three vectors where $\mathbf{r} = \vec{r}_n + \vec{r}_\alpha + \vec{r}'$. The box represents a unit cell from a crystal lattice.

So we can consider the total scattering density of a crystal lattice as a sum of scattering densities of component atoms. Let $\vec{r}_n$ be the origin of the nth unit cell, $\vec{r}_\alpha$ be the position of of each atom in the unit cell and $\vec{r}'$ be a position vector pointing away from the center of each atom (Figure 15) so that $r = \vec{r}_n + \vec{r}_\alpha + \vec{r}'$.

Then the scattering density of a single atom is:

$$\rho_{hkl}^{\substack{single\\atom}} = \frac{1}{V_c} \sum_\alpha e^{-i\vec{G}\cdot\overrightarrow{r_\alpha}} \int_\alpha^{\cdot} \rho_\alpha\left(\overrightarrow{r'}\right) e^{-i\vec{G}\cdot\overrightarrow{r'}} \overrightarrow{dr'}$$

where we can define the atomic scattering factor or form factor (De):

$$f_\alpha = \int_\alpha^{\cdot} \rho_\alpha\left(\overrightarrow{r'}\right) e^{-i\vec{G}\cdot\overrightarrow{r'}} \overrightarrow{dr'}$$

Switching from Cartesian to polar coordinates:

$$f_\alpha = \int_\alpha^{\cdot} \rho_\alpha\left(\overrightarrow{r'}\right) e^{-i\vec{G}\cdot\overrightarrow{r'}} \overrightarrow{dr'} = -\iiint \rho_\alpha(r') e^{-iGr'cos\theta} r'^2 d\, r' \sin\theta \, d\varphi$$

$$f_\alpha = 4\pi \int \rho_\alpha(r')\, r'^2 \frac{\sin(Gr')}{Gr'} dr'$$

Now since the diffraction angle between $\vec{k}$ and $\vec{k}_o$ is 2Θ, the using Eq. 22 we have the final definition of atomic scattering factor or form factor:

$$f_\alpha = 4\pi \int \rho_\alpha(r')\, r'^2 \frac{\sin[4\pi r' \sin\left(\frac{\theta}{\lambda}\right)]}{4\pi r' \sin\left(\frac{\theta}{\lambda}\right)} dr'$$

The maximum of the atomic scattering factor occurs for Θ=0 where the integral becomes equal to the scattering density, which in turn is proportional to the total number of electrons per atom.

2.3.3.5. The Structure Factor

If we consider again all the atoms of a unit cell then we arrive at the definition of the structure factor:

$$F_{hkl} = \sum_\alpha f_\alpha e^{-i\vec{G}_{hkl}\cdot\vec{r}_\alpha}$$

where the summation is over the atoms in the unit cell (see Figure 15). So finally the scattering density is expressed as:

$$\boldsymbol{\rho}_{\boldsymbol{hkl}}^{\substack{\boldsymbol{single}\\ \boldsymbol{atom}}} = \frac{\boldsymbol{S_{hkl}}}{\boldsymbol{V_c}}$$

The intensity of diffraction lines is proportional to the square of the wave amplitude or of the structure factor:

$$\boldsymbol{I_{hkl} \propto F_{hkl}^{*} F_{hkl}}$$

And if we consider for example that there are two different atoms in the unit cell then we have:

$$\boldsymbol{I_{hkl} \propto F_{hkl}^{*} F_{hkl} = \left(f_1 e^{-i\vec{G}_{hkl}\cdot\vec{r}_1} + f_2 e^{-i\vec{G}_{hkl}\cdot\vec{r}_2}\right)^{*} \left(f_1 e^{-i\vec{G}_{hkl}\cdot\vec{r}_1} + f_2 e^{-i\vec{G}_{hkl}\cdot\vec{r}_2}\right) =}$$

$$\boldsymbol{\left(f_1 e^{+i\vec{G}_{hkl}\cdot\vec{r}_1} + f_2 e^{+i\vec{G}_{hkl}\cdot\vec{r}_2}\right)\left(f_1 e^{-i\vec{G}_{hkl}\cdot\vec{r}_1} + f_2 e^{-i\vec{G}_{hkl}\cdot\vec{r}_2}\right) = f_1^2 + f_1 f_2 \left(e^{+i\vec{G}_{hkl}\cdot\vec{r}_1 - i\vec{G}_{hkl}\cdot\vec{r}_2} +\right.}$$

$$\boldsymbol{\left. e^{+i\vec{G}_{hkl}\cdot\vec{r}_2 - i\vec{G}_{hkl}\cdot\vec{r}_1}\right) + f_2^2 = f_1^2 + f_2^2(2\cos(\phi_{hkl}))}$$

Finally we have a simple expression for the intensity of diffracted X-rays:

$$\boldsymbol{I_{hkl} \propto F_{hkl}^{*} F_{hkl} = f_1^2 + f_2^2 + 2 f_1 f_2 \cos(\phi_{hkl})}$$

The intensities of reflections are altered by the presence of other atoms in the cell and this can sometimes lead to characteristic extinctions of certain reflections (if two different atoms have the same Z and their scattered waves are 180° out of phase).

In conclusion the Bragg reflections' positions provide information about the shape and the dimensions of the unit cell, whereas the intensities of those reflections yield insight into the type of atoms present in the unit cell.

When it is desired to investigate the structure of a solid on the atomic scale then the wavelength used should be at least on the order of the lattice constant. We can only measure the intensity of the diffracted radiation, so we do not obtain any information about phases. If one could actually measure the amplitude of the scattering radiation, then the scattering density could be obtained by inverse Fourier transform of the amplitude. The lack of information about phases leads to the necessity of trying out different model structures (and varying their parameters which can be extremely time-intensive) and determining which one fits the experimental diffraction pattern best.

2.3.3.6. Temperature Factor

The Debye-Waller factor (DWF, after Peter Debye and Ivar Waller) is used to describe the attenuation of X-ray scattering (and also neutron) scattering caused by thermal motion or quenched disorder. It gives the fraction of elastic scattering. Assuming a solid is a classical harmonic oscillator the Debye-Waller factor is given by the exponential factor in the expression:

$$\boldsymbol{I(hkl) = I_o e^{\left(-\frac{1}{3}\langle u^2\rangle G^2\right)} = I_o e^{\left(-\frac{k_B T G^2}{M\omega^2}\right)}}$$

where $\langle \boldsymbol{u^2} \rangle$ is the mean square displacement of an atom, M is the mass of the atom, ω is the frequency of the oscillator.[54] This classical result approximates well experimental data at high temperatures. At low temperatures one must use quantum considerations. At T=0, the is the mean square displacement $\langle \boldsymbol{u^2} \rangle$of an atom does not vanish due to zero point motion and the scattered intensity is:

$$\boldsymbol{I(hkl) = I_o e^{\left(-\frac{\hbar G^2}{2M\omega}\right)}}$$

which gives about 90% of elastic scattering when typical numbers are substituted.[59]

The Debye-Waller factor was first called the temperature factor because Peter Debye (1913) and Ivar Waller (1923) were the first to understand and formulate the effect that thermal vibrations would have on the intensity of X-ray scattering. Since then it has become obvious that static displacements produce a similar effect on the scattered intensities of X-rays therefore the use of the term 'temperature factor' is formally discouraged, as stated by the 1996 IUCR Commission on Crystallographic Nomenclature.[59] What are the key components of static displacement? First is the displacement arising from atomic vibrations due to motion of molecules or molecular fragments or, in a crystal, due to internal vibrations, such as bond stretching and bending. All of these motions are temperature-dependent, unless the temperature is very low. Besides temperature effects there are other effective displacements from the mean position which are due to a variety of possible types of disorder. Disorder includes small deviations from ideal periodicity, present in all real crystals; orientational disorder, present in many molecular crystals; density and displacement modulations; and short- and long-range displacive correlations. Besides decreasing the intensity of diffraction lines, many types of disorder also give rise to diffuse scattering.

2.4. High-Pressure Materials Physics

2.4.1. Overview

Pressure and temperature are the key parameters in the thermodynamic study of materials. Materials at high-pressures are found in nature in oceans (0.1 GPa) and inside the Earth (center at 360 GPa) as well as within planets, stars, and the universe. [60] The static high-pressure range in nature and in the universe spans about 60 orders of magnitude and is hence larger than for any other physical variable. [61] Nowadays, pressures superior to those found at the center of the earth can be replicated in the laboratory environment. The pressure variable can be applied in a very controlled manner to samples of the order of few microns to a few centimeters cubed, by using either a diamond anvil cell or for the latter, a large volume press. A wealth of information can be obtained when molecular materials are subjected to very high-pressures. In fact, pressure allows for tuning of electronic, magnetic, structural and vibrational properties. Another application in fundamental science is the possibility to tune interatomic bonds for the purpose of testing theories.[60]

In summary, high-pressure research enables a better understanding of structural properties of materials, of chemical reactions, and of materials synthesis. Phase transitions, phase diagrams and equations of state have been determined for countless systems with the use of pressure and temperature combined with *in situ* X-ray diffraction.[62] [37, 38, 63, 64, 65, 66, 67, 68, 69, 70, 71, 72, 73, 74, 75]

2.4.2. Diversification of High-Pressure Research

As the 35th anniversary of high-pressure diffraction took place in 2012, synchrotron sources, pressure cells and data acquisition and analysis systems are continuously being modified and improved in the search for better, faster and more efficient experiments. [62] Synchrotron radiation was used for the first time in combination with X-ray diffraction 30 years ago, in 1977. [76] High-pressure X-ray diffraction studies involving synchrotron radiation were first reported in 1977 as well. [76] The key advantages of synchrotron X-rays, as applied to high-pressure studies, were the tunable wavelength, improved resolution, low noise and excellent statistics. On the other hand, high-pressure created new constraints due to the extremely small sample size and absorption and scattering due to small angular range.

High-pressure techniques have been steadily advancing since the eighties, with development accelerating in the past few years. Accompanied by the parallel development in new synchrotron techniques (diffraction, spectroscopy, from X-ray to infrared region) all these developments allowed high-pressure research to flourish into an interdisciplinary tool spanning geosciences, different domains of physics, materials science and even biology.

High-pressure research has shown an unprecedented wave of growth across research areas in the last 20 years.[60] The developments that contributed to making high-pressure the thriving research field it is today, are the evolution of diamond anvil cells and the arrival of 3rd generation synchrotron sources with the parallel advances in synchrotron techniques. Today the pressure limit achievable in the laboratory is ~5 Mbars.

2.4.3. The Effect of Pressure on Matter

What is the effect of pressure [60, 77] on a solid? [8, 12] As interatomic distances are reduced under pressure, the material becomes denser. It is then relevant to examine what are the mechanisms for increasing the density of a material. As the crystal lattice is reduced and atoms are drawn closer, compression acts on the energetics of electrons. The energy of electrons is composed of kinetic, coulomb, exchange and correlation contributions. From the point of view of density functional theory, the kinetic energy of electrons is proportional to electron density to the 5/3 power. Therefore, the kinetic energy increases fast under compression. [77] Electrons tend towards states of lower kinetic energy. As a consequence intramolecular bonds are destabilized. Already in the 1930s it was postulated that at pressures sufficiently high molecular systems will transition to close-packed structures before, or in concert with, the formation of a fully metallic phase ("metallic or valence states") [78] and ultimately form a plasma in which the chemical description of bonding does not hold anymore. In fact, as atoms are brought together, changes in hybridization occur, because of covalent interactions. On compression it is possible for different types of bonds (van der Waals, ionic, covalent, metallic and hydrogen) to compete among each other.

Since it is possible to achieve, in the laboratory, pressures high enough to reduce the unit cell volume by more than a factor of 2, the resulting changes in inter-atomic bonding can be immense and hence the properties of high-pressure phases can differ greatly from the ambient pressure and temperature phase. [60] As a result of compression the atomic arrangement can suddenly change. As the Gibbs free energy of different arrangements of atoms varies under pressure, it may become more energetically favorable for the material to change this arrangement in which case a solid-solid phase transition occurs. This change in atomic arrangement can either be discontinuous or continuous and accompanied by a change in crystal symmetry.

Under high-pressures some materials adopt high-symmetry structures of increasing coordination number. However, some materials can first transition into lower symmetry structures at intermediate pressures and only at higher pressures they transform into higher-symmetry structures.

So what is the bottom line result of compression? Unexpected, intermediate states can be formed at high-pressures as molecular bonds evolve before being annihilated. Pressure can induce auto-ionization as well as molecular bonding. New materials can be produced by chemical reactions or mechanisms very different from those at ambient conditions and their kinetics maybe either accelerated or slowed down depending on the activation volume. High-pressures can lead to materials with technological implications such as super hard materials, nonlinear optical materials or high temperature superconductors. Pressure can also induce loss of long-range order or material amorphization, where glassy materials can be obtained below their regular glass transition temperature. [77]

2.4.4. The Diamond Anvil Cell

The reliable and controlled replication of high-pressures in the laboratory begins with “the Bridgman” era as referred to by Jayaraman. [79] From 1910 to 1950 P.W. Bridgman invented and developed the Bridgman anvil and the piston cylinder device for electrical resistance and compressibility measurements (up to 100 kbar = 10 GPa). The diamond anvil cell (DAC) was first developed by Jamieson, Lawson, and Nachtrieb [80] and Weir et al. [81] The principle of operation of any high-pressure device is based on the fact that a large force F applied to a small area A generates a large pressure p=F/A (Figure 16). The smaller the area, the large will be the pressure created on the sample. The limit is the deformation and eventual fracture of the diamond under very high loads. Diamond is ideal for high-pressure applications because it combines the highest bulk modulus and hardness among all known materials.

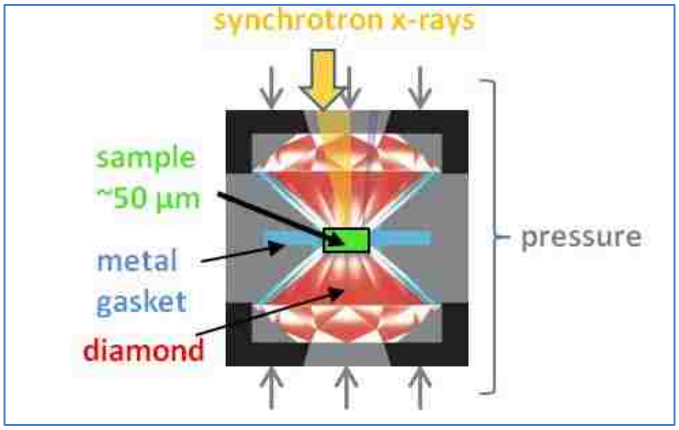

Figure 16. Schematic of the inside of a diamond anvil cell (DAC).
Typical sizes are: 1/3 carat for the diamond with a culet of ~300 μm; the sample chamber is usually 100 μm or less.

In the DAC, a small amount of material is placed between the flat faces or culets of two brilliant-cut diamonds.[82, 83] The culets are separated by a thin metallic foil which serves as gasket. An initial compression of the gasket creates a indentation in the foil and in the middle of the indentation a micron-size hole is drilled. This hole constitutes the sample chamber, where the desired sample is placed together with a pressure standard as well as a pressurizing fluid medium to insure (quasi-) hydrostaticity and homogeneous conditions. The diamond culets can have dimensions between 100 μm and 1000 μm, the metallic gasket has a thickness between 300 μm and as little as 100 μm (in the case of X-ray Raman) with the indented area being anywhere between 80 to 30 μm. The ideally circular hole centered in the indentation can have a diameter between 50 and 200 μm. Exact dimensions will depend on the diamond culets, type of experiment and target pressure. Due to the small dimensions involved, as well as the need for perfect centering of various elements and high precision, all manipulations are carried out under a high-magnification optical microscope. The chief reason for using diamonds, besides their exceptional hardness, is also their wide window of transparency, between the near ultraviolet (~5.5 eV) up to hard X-rays (>10 keV), which allows for a multitude of scattering and diffraction techniques. Diamond anvil cells have been the key limiting factor in high-pressure research, in terms of optical access and signal exit (through diamonds, through the gasket material), extent of attainable pressure, and integration with various experimental techniques.

2.4.5. Measuring Pressure in a Diamond Anvil Cell

Static pressure P is the force excreted per unit area. The force applied on a DAC is transmitted to the sample in a very complex way (especially above 10 GPa) due to the friction and deformation of the materials of the cell, so the generated pressure depends not only on the force but also on the mechanical properties of the materials.[82, 83] In that case instead of modeling how pressure is transmitted to the sample chamber, it is much more practical to use transferable pressure scales. Here pressure measurements are based on the equation of state (P(V) isotherms) reference materials.

Primary pressure scales are based on materials such as Au, Pt, Ag, Cu or NaCl, for which the equations of state, which were established from a combination of ultrasonic data and shock-wave experiments, show a good degree of consistency. In a typical X-ray diffraction compression experiment the lattice parameters of a primary pressure scale are accurately measured and the pressure is obtained through the corresponding equation of state.

Another possibility is the use of a secondary scale, calibrated against a primary pressure scale, and which may be easier to use in a high-pressure experiment. In fact, at very high-pressure, the accurate determination of the lattice parameters of a reference material becomes difficult. One such secondary scales is the very popular ruby ($Al_2O_3:Cr^{3+}$) scale, which has a fluorescence line (R_1) which shifts with pressure almost linearly up to 10 GPa, with dp/dλ=0.2746 GPa Å-1, and with a small deviation at higher pressures, according to the empirical equation [84] :

$$P(GPa) = \frac{1904}{B}\left[\left(1 + \frac{\Delta\lambda}{\lambda_o}\right)^B - 1\right]$$

where B=7.665 for quasi-hydrostatic conditions and B=5.0 for non-hydrostatic conditions. The R_1 fluorescence line is also dependent on temperature with dλ/dT=0.068 Å K-1, so that an increase in temperature of 10 K corresponds to an increase in pressure of 0.187 GPa →0.2 GPa.

$(0.2746 \text{ GPa Å}^{-1}) * (0.068 \text{ Å K}^{-1}) * (10 \text{ K}) = 0.187 \text{ GPa}$

In most of the presented studies in the experimental part of this Dissertation both a primary and a secondary pressure scale was used.

2.5. Synchrotron X-ray Diffraction

2.5.1. History of Synchrotrons

Synchrotron radiation got off to a “poor” start at electron accelerators where it was seen as a nuisance since it represented loss of energy. [56, 85] Materials scientists, who saw potential in synchrotron radiation, were allowed by particle physicists to sometimes tap into radiation that went lost otherwise and operate beam ports in “parasitic” mode. The first generation synchrotrons were born. From nuisance synchrotron radiation evolved to one of the most powerful tools for the study of matter. The next evolutionary step was the construction of what became known as the second generation synchrotron sources, of the

1980s. These were properly dedicated facilities and not merely attachments to particle accelerators. The second generation synchrotron sources were composed of two straight sections with a wiggler or an undulator and connected by two semi-circular ends with bending magnets.[56, 85] Third generations sources, such as the Advanced Photon Source Argonne national Laboratory (Argonne, IL, USA), were built in the 1990s. They are composed of many straight sections connected in to a polygon and optimized to supply very bright radiation from far UV to hard X-rays depending on the synchrotron.

2.5.2. Bending Magnets, Undulators, Wigglers

Synchrotron radiation goes from far infrared to hard X-rays. Highly parallel radiation originates from a very small source (0.01-0.1 mm). It is linearly polarized in the plane of the electron orbit and elliptically polarized above and below the plane.

Accelerated charged particles emit radiation in the well-known sine squared angular pattern of dipole radiation. The synchrotron makes use of the fact that centripetal acceleration of charged particles causes transverse emission of electromagnetic radiation in the tangential direction of the ring where electrons circulate (due to an applied magnetic field). If, in addition the particles travel at relativistic speeds, the radiation is emitted in a narrow cone, tangent to the path and in the forward direction, mimicking a sweeping searchlight or a train on a circular track. [56, 86]

In a third generation synchrotron source the circular motion of a tightly confined beam of relativistic electrons is insured by bending magnets. End-stations that follow only a bending magnet are characterized by wide spectrum of radiation sometimes referred to as a synchrotron light bulb. Undulators can be found between two bending magnets and they are periodic magnetic structures with a large number of cycles (ex: 100). The relatively weak magnetic field of undulators causes the electrons to have a small harmonic oscillation which is also called undulation. The electrons experience additional acceleration in a direction which is perpendicular to their circular motion. Due to the fact that the amplitude of oscillation is small the resultant radiation cone is narrow. Also since the original electron beam was already tightly confined, the end result is highly directional radiation with small angular divergence, small cross-section and narrow spectral width. The undulator radiation is quasi-monochromatic and approximates many of the desired properties of an X-ray laser. Wigglers are also periodic magnetic structures that can be found between two bending magnets, but with fewer periods than undulators and with a much stronger magnetic field. Here the amplitude of oscillation is larger, and as the electron is jolted up and down, the resultant radiation cone is wider in space and angle. Stronger magnetic field also translates into larger radiated power. As a result the radiation from a wiggler has a wide spectrum much like for a bending magnet, but the spectrum is shifted towards higher energies and the photon flux is larger.[56, 86]

Synchrotron radiation is the best tool for the study matter enclosed in a high-pressure cell. Synchrotron radiation is characterized by a very penetrating high-energy beam. High-brilliance and low-emittance of the beam permit to focus it down to micron sized spots, which are ideal when the sample chamber is itself a few tens of microns in diameter. The brilliance of X-rays at a third generation synchrotron source also reduces the data collection time down to a few minutes or a few seconds depending on the beamline versus hours or more for a standard X-ray diffractometer. [56, 86]

2.5.3. The Advanced Photon Source at Argonne National Laboratory

There exists today only about a dozen synchrotron facilities in the world that possess high-pressure-dedicated beamlines: APS (US), ESFR (FR), Spring-8 (JP), Soleil (FR), NSLS (US), ALS (US), BSRL (China), HasyLab (DE), DESY-PETRAIII (DE), CHESS (US), KEK-PF (JP), SERC (UK), ELETTRA (IT), Australia, Korea). The portion of experimental work related to high-pressure x-ray diffraction presented in this work was carried out at the U.S. Department of Energy's Advanced Photon Source of Argonne National Laboratory (Figure 17). Electrons are first emitted from a cathode ray tube and accelerated by high-voltage alternating electric fields in a linear accelerator. Selective phasing of the electric field accelerates the electrons to 450 MeV. At 450 MeV, (>99.999% of the speed of light).

Figure 17. Aerial view of the Advanced Photon Source (APS).
The APS is a third generation synchrotron, at Argonne National Laboratory in Argonne (Chicago), IL, and it is the brightest source of radiation in the northern hemisphere. [87]

Electrons are injected into the booster synchrotron (a ring of electromagnets), and accelerated from 450 MeV to 7 GeV in one-half second (>99.999999% of the speed of light).[87] The accelerating force is supplied by electrical fields in four radio frequency cavities.

In order to maintain the orbital path of the electrons, bending and focusing magnets increase the electron field strength in synchronization with the radio frequency field. The 7-GeV electrons are injected into the 1,104-m (3,622 ft or ~0.7 mi) circumference storage ring, a circle of more than 1,000 electromagnets and associated equipment, located in a concrete enclosure inside the experimental hall. A powerful electromagnetic field focuses the electrons into a narrow beam that is bent on a circular path as it orbits within aluminum-alloy vacuum chambers running through the centers of the electromagnets.[87]

There are 40 straight sections, or sectors, in the storage ring of this 3rd generation synchrotron. Five sectors are used for beam injection and radio frequency equipment. The remaining 35 are equipped with insertion devices. Each sector has a least 2 beamlines which extend up to 75 meters from ring across the experimental hall floor. One of the beamlines begins at a bending magnet. The other beamline begins at an insertion device (undulator or wiggler).

The work described in the experimental part of this Thesis was carried out at sector 16, the High-pressure Collaborative Access Team (HPCAT). HPCAT is a sector dedicated to high-pressure research and it has three BM (BMA, BMB, BMD) and two ID operational beamlines (IDB, IDD) as well as one ID beamline under construction (ID-E). The maintenance and operations costs for an 8-hour shift at a beamline amount to ~$10K. The annual budget of the APS is of about $2 billion. That is why experimental time (or beamtime) is very valuable and experiments need to be carefully designed to make the most of the allotted time. Hence the time variable has a crucial influence in the already challenging aspects of a high-pressure experiment.

CHAPTER 3 – EXPERIMENTAL

3.1. Samples

3.1.1. Alumino-Silicate Mullite and Sillimanite

Mullite with composition of 75.2 wt.% Al_2O_3, 24.5 wt.% SiO_2 (designated as 2:1-mullite) is a commercial product (Duramul, Washington Mills Electro Minerals Ltd, UK). The material was produced by electric arc furnace fusion above 2000°C of Bayer processed Al_2O_3 and high purity SiO_2, and cool-down to room temperature. The starting materials contained ~0.20 wt.% Na_2O and minor traces of TiO_2, Fe_2O_3, K_2O, CaO and MgO. Mullite with a composition of 72.0 wt.% Al_2O_3 and 28.0 wt.% SiO_2 (designated as 3:2-mullite) was synthesized from aluminum sec-butoxide ($C_{12}H_{27}AlO_3$) and tetraethyloxysilane $Si(OC_2H_5)_4$. The starting materials were diluted in isopropanol, homogenized and heat-treated at 1600°C for 2 h. Sillimanite was provided by CSIRO (Melbourne, Australia) and originates from Australia. According to visual inspection, the XRD-derived lattice parameters, its white color and its fibrous character, it has a composition of ideal sillimanite.

3.1.2. Boron Mullites

The samples of 7:4 mullite and of the alumino-silicate mullite with 3.5(4) mol% B_2O_3 were synthesized by the sol-gel procedure and follow the nitrate decomposition method using aluminum-nitrate nonahydrate, tetraethoxysilane and boric acid as reactants. The chemicals were dissolved in pure ethanol and heated at 60°C in a water bath to form transparent sols followed by gelation at 60°C and subsequent drying at 150°C. The resulting yellowish, spongy glass was ground and calcined at 350°C with subsequent mullitization in corundum crucibles at 1200°C. For more details refer to Lührs.[29]

3.1.3. $PbAlBO_4$, $PbFeBO_4$ and $PbMnBO_4$ Mullites

Polycrystalline $PbFeBO_4$ was prepared by the glycerin method.[88] More details can be found in the reference. Stoichiometric amounts of $Pb(NO_3)_2$, $Fe(NO_3)_2{\bullet}6H_2O$ with 5% excess of $B(OH)_3$ were mixed with 10 wt.% of glycerin. The mixture was stirred at 353 K till it solidified upon release of NO_x. It was dried at 473 K for 2 hours followed by mixing in an agate mortar and then heated at 973 K in a corundum crucible for 24 h. For more details refer to Gesing et al. [88]

3.2. Raman Spectroscopy at Ambient and High Pressure

The pressure-dependent Raman spectra were measured in a backscattering configuration with a Horiba Jobin-Yvon T64000 triple-grating confocal Raman spectrometer using micro-mode. The 514.532 nm line of a Spectra Physics Stabilite 2018 Ar-Kr laser was used for sample excitation less than 10 mW power at the sample to avoid burning. A liquid nitrogen cooled CCD detector (Symphony, 2048 x 512 pixels) was used for recording the spectra. The incoming and scattered light was focused and collected with an Olympus microscope objective (20× LWD), leading to a theoretical 1.7 µm diameter focal spot and a length of the focal region of a few µm. Raman spectra were collected in the range between 10 cm^{-1} and 1500 cm^{-1} with a spectral resolution of approximately 1 cm^{-1}, using three gratings of 1800 grooves/mm working in *Subtractive Mode*. Signal integration times were 20 – 600s, with multiple acquisitions per pressure point, and with longer acquisition times for increasing pressure measurements.

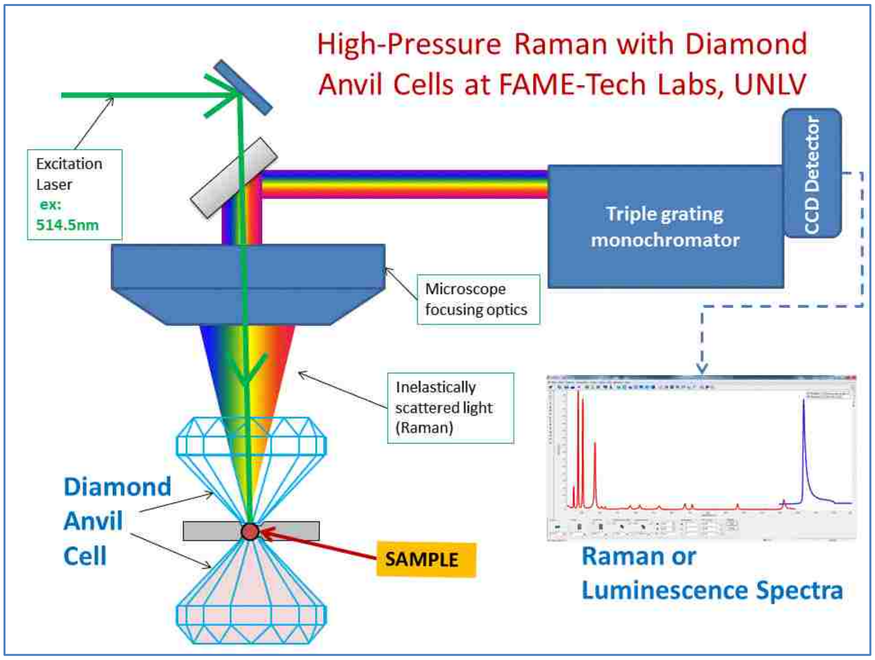

Figure 18. Overview of the experimental Raman setup at FAME-Tech Labs, UNLV.
The setup was used for the presented in situ high-pressure Raman spectroscopy experiments.

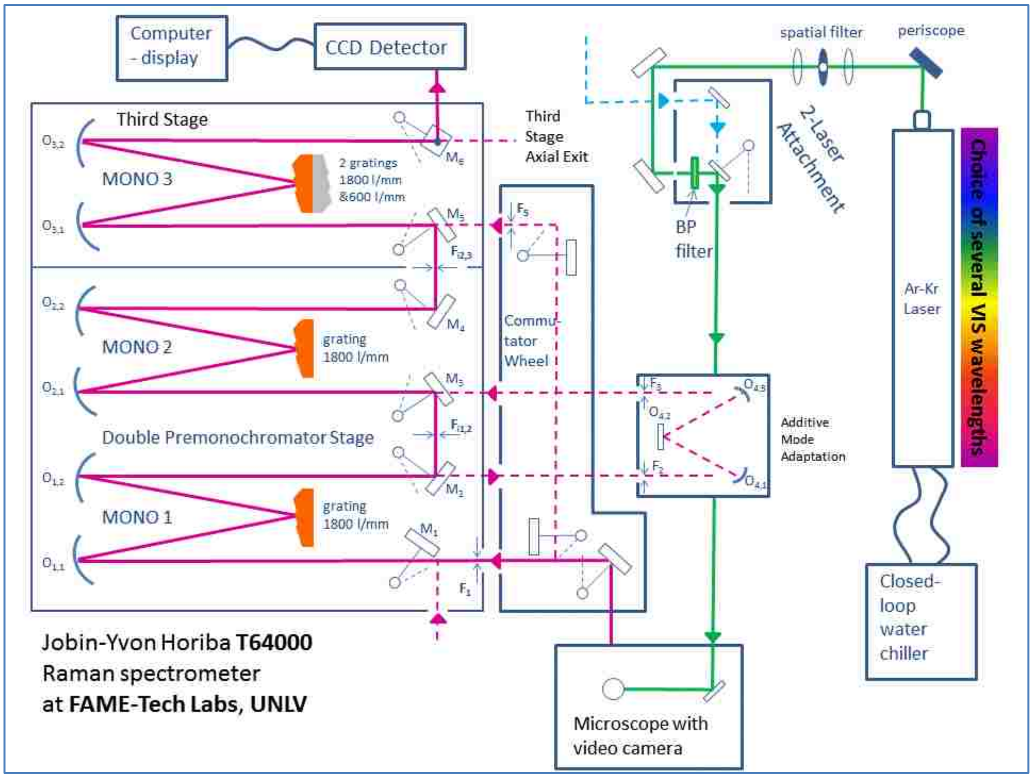

Figure 19. Sketch of the optical setup of the experimental Raman at FAME-Tech Labs, UNLV.
The sketch shows the optical path and various optical elements used for in situ high-pressure Raman spectroscopy experiments. The triple spectrometer contains three gratings used in tandem in the pre-monochromator and spectrometer.

Band positions, determined from peak fitting are accurate to ±4 cm^{-1} for broad/overlapped bands and ±1 cm^{-1} for the sharper bands. Micro grains of the sample were compressed in a symmetric type diamond anvil cell (DAC), in numerous pressure steps at ambient temperature.

3.2.1. Alumino-Silicate Mullites and Sillimanite

The 514.532 nm line of a Spectra Physics Stabilite 2018 Ar-Kr laser was used for sample excitation. Micro grains of sample were compressed in a symmetric type diamond anvil cell (DAC), from ambient pressure up to 33 GPa for 2:1 mullite and from ambient pressure up to 25.5 for sillimanite, in several pressure steps at ambient temperature. A Rhenium gasket was pre-indented to a thickness of ~50 μm using diamonds with 250 μm diameter culets. The sample chamber consisted of a 90 μm diameter hole, drilled in the pre-indented rhenium gasket. To ensure quasi-hydrostatic pressure conditions, compression was carried out with Ne as pressure transmitting medium, which was loaded into the sample chamber at about 138 MPa (20,000 psi), using the gas loading setup of Sector 13 of APS, ANL.[89]. For accurate pressure readings during compression ruby microspheres were placed in the sample chamber and used to measure pressure using the Mao pressure scale.[90] A second method for pressure determination was based on the shift of the high-frequency edge of the Raman band of diamond, which corresponds to the Raman shift of the anvil culet due to the normal stress.[91] The interval between a pressure increase and the measurement of spectra was kept at several minutes allowing for the pressure inside the sample chamber to equilibrate. Spectra were decomposed into individual Lorentzian or mixed Gaussian-Lorentzian bands using LabSpec 5.78.24 software (Jobin-Yvon Horiba).

3.2.2. $PbAlBO_4$ Mullite

The 514.532 nm line of a Spectra Physics Stabilite 2018 Ar-Kr laser was used for sample excitation. Micro grains of the sample were compressed in a symmetric type diamond anvil cell (DAC), from ambient pressure up to 88 GPa in several pressure steps at ambient temperature. A Rhenium gasket was pre-indented to a thickness of ~50 μm using diamonds with 250 μm diameter culets. The sample chamber consisted of a 90 μm diameter hole, drilled in the pre-indented rhenium gasket. To ensure quasi-hydrostatic pressure conditions, compression was carried out with Ne as pressure transmitting medium, which was loaded into the sample chamber at about 138 MPa (20,000 psi), using the gas loading setup of Sector 13 of APS, ANL.[89]. For accurate pressure readings during compression ruby microspheres were placed in the sample chamber and used to measure pressure using the Mao pressure scale. [90] A second method for pressure determination was based on the shift of the high-frequency edge of the Raman band of diamond, which corresponds to the Raman shift of the anvil culet due to the normal stress.[91] The interval between a pressure increase and the measurement of spectra was kept at several minutes allowing for the pressure inside the sample chamber to equilibrate. Spectra were decomposed into individual Lorentzian or mixed Gaussian-Lorentzian bands using LabSpec 5.78.24 software (Jobin-Yvon Horiba).

3.2.3. $PbFeBO_4$ Mullite

The 514.532 nm line of a Spectra Physics Stabilite 2018 Ar-Kr laser was used for sample excitation with less than 10 mW power at the sample to avoid burning.. Micro grains of the sample were compressed in a symmetric type diamond anvil cell (DAC), from ambient pressure up to 20.4 GPa in several pressure steps at ambient temperature. A Rhenium gasket was pre-indented to a thickness of ~50 μm using diamonds with 250 μm diameter culets. The sample chamber consisted of a 90 μm diameter hole, drilled in the preindented rhenium gasket. To ensure quasi-hydrostatic pressure conditions, compression was carried out with a 4:1 methanol-ethanol mixture. For accurate pressure readings during compression ruby microspheres were placed in the sample chamber and used to measure pressure using the Mao pressure scale. [90] A second method for pressure determination was based on the shift of the high-frequency edge of the Raman band of diamond, which corresponds to the Raman shift of the anvil culet due to the normal stress.[91] The interval between a pressure increase and the measurement of spectra was kept at several minutes allowing for the pressure inside the sample chamber to equilibrate. Spectra were decomposed into individual Lorentzian or mixed Gaussian-Lorentzian bands using LabSpec 5.78.24 software (Jobin-Yvon Horiba).

3.3. High Pressure XRD at the Advanced Photon Source, Argonne National Laboratory

3.3.1. Experimental Conditions

All high-pressure, *in situ,* angle-dispersive synchrotron X-ray diffraction (ADXRD) measurements were performed at the 16-IDB beamline of the High Pressure Collaborative Access Team (HPCAT), Advanced Photon Source (APS), Argonne National Laboratory (ANL). For the geometry of the experimental setup see Figure 20. A monochromatic X-ray beam, with a wavelength λ=0.3-0.4Å (depending on the experimental run) was focused down to a ~7 x 5 μm^2 spot using Kirkpatrick-Baez 200 mm mirrors. Diffraction images were recorded with a MAR345 imaging plate and were integrated and corrected for distortion using the FIT2D software. [92, 93] Any overexposed spots on the image plate, due to sample texture, were masked, and hence excluded, prior to image integration. The acquisition time was between 30s and 5 min (depending on the specific sample). The sample-detector distance and geometric parameters were calibrated at the beginning of each high pressure run, using a CeO_2 standard reference material from the National Institute of Standards and Technology.

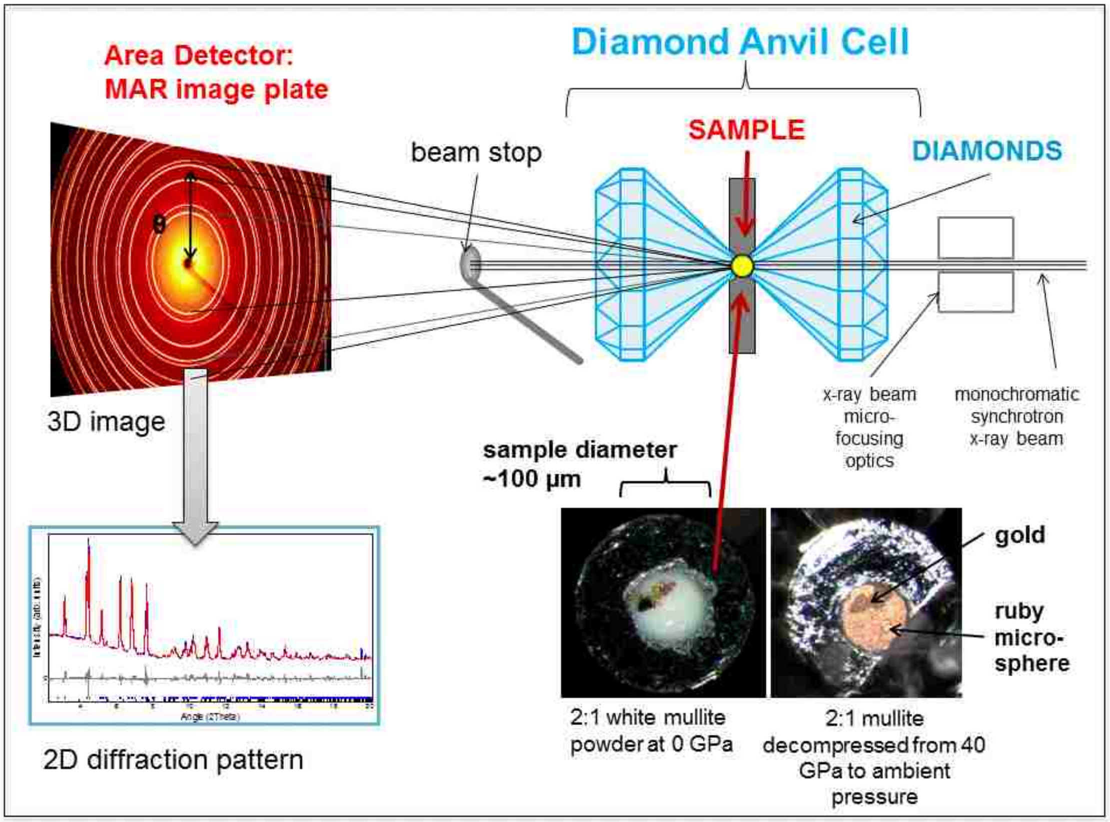

Figure 20. Setup for in-situ high-pressure synchrotron x-ray diffraction experiments in a DAC.
The schematic is not to scale. The synchrotron x-ray beam – focused down to a few microns – enters the DAC and, after passing through one diamond anvil, reaches the sample chamber. The x-rays diffract on the sample and Debye diffraction rings are intercepted by an imaging plate. The 3-dimensional Debye rings are integrated to yield a 2-dimensional diffraction pattern.

The samples consisting of very fine powders were compressed in a symmetric type diamond anvil cell (DAC). Rhenium gaskets were pre-indented to a thickness of ~40 μm, using diamonds with 250 or 300 μm diameter culets (depending on the specific sample). A 90-130 μm diameter hole (depending on the compressibility of pressure media), was drilled by electrical discharge machining in the pre-indented rhenium gasket and served as the sample chamber. For accurate pressure determination during compression experiments, fragments of gold foil were mixed-in with the samples and used to measure pressure using the equation of state of gold by Anderson *et al.*[94] For the gas loading procedure, a ruby microsphere was placed in the sample chamber and used to measure pressure using the pressure scale of Mao.[90] All compression runs were carried out with either Ne or He as a quasi-hydrostatic pressure transmitting medium,[95] which was loaded into the sample chamber at about 138 MPa (20,000 psi), using the gas loading setup of Sector 13 of APS, ANL.[89] All diffraction patterns were collected at ambient temperature. The time interval between a pressure increase and the subsequent X-ray measurement was kept at several minutes, especially at lower pressures, in order to allow for the pressure inside the sample chamber to stabilize. Pressure increase was controlled remotely using a motorized mechanical pressure control device. The Topas 4.2 program [96] was used to index diffraction patterns and to perform Rietveld full-profile structural refinements. The Diamond 3.2 program [97] was used to draw and examine crystal structures.

3.3.2. Alumino-Silicate Mullite and Sillimanite

The structural stability of 2:1-mullite, 3:2-mullite and sillimanite was investigated in separate compression runs, up to 40.8 GPa, 27.3 GPa and 44.6 GPa, respectively. High-pressure, in situ, angle dispersive, synchrotron X-ray diffraction measurements were performed at the 16-IDB beamline of the High Pressure Collaborative Access Team, Advanced Photon Source, Argonne National Laboratory (see section 3.3.1). The monochromatic X-ray beam, had a wavelength λ = 0.398039 Å, λ = 0.398160 Å or λ = 0.407530 Å (depending on the day of the experimental run). To insure quasi-hydrostatic pressure conditions, all compression runs were carried out with either Ne (2:1-mullite) or He (3:2-mullite and sillimanite) as a quasi-hydrostatic pressure transmitting medium, [98, 99] (gas loading setup of Sector 13, APS, ANL[89]). The number of pressure points analyzed for each sample was: 24 for 2:1-mullite, 27 for 3:2-mullite and 21 for sillimanite.

3.3.3. Boron Mullite

The structural stability of 7:4 mullite and B-mullite was investigated in separate compression runs, up to 28.2, and 28.8 GPa, respectively. High-pressure *in situ* angle-dispersive synchrotron X-ray diffraction measurements were performed at the 16-IDB beamline of the High Pressure Collaborative Access Team, Advanced Photon Source, Argonne National Laboratory (see section 3.3.1). The monochromatic X-ray beam, had a wavelength λ= 0.373790Å. The number of pressure points acquired and analyzed for each sample was: 20 for 7:4 mullite and 29 for B-mullite. All compression runs were carried out with Ne as a quasi-hydrostatic pressure transmitting medium,[95] (gas loading setup of Sector 13, APS, ANL[89]). The monochromatic X-ray beam, had a wavelength λ = 0.398160 Å, λ = 0.398137 Å or λ = 0.398175 Å (depending on the day of the experimental run).

3.3.4. $PbMBO_4$ Mullites

The structural stability of PbMBO4 was investigated in separate compression runs, up to 71.7 GPa ($PbFeBO_4$), and 111.8 GPa ($PbAlBO_4$). High-pressure, in situ, angle dispersive, synchrotron X-ray diffraction measurements were performed at the 16-IDB beamline of the High Pressure Collaborative Access Team, Advanced Photon Source, Argonne National Laboratory (see section 3.3.1). All patterns were collected between 21°C and 23°C. All compression runs were carried out with Ne or He as a quasi-hydrostatic pressure transmitting medium [95] (gas loading setup of Sector 13, APS, ANL[89]).

3.3.5. Ambient Pressure X-ray Diffraction

Conventional angle dispersive X-ray diffraction patterns were collected in Θ-2Θ Bragg-Brentano geometry, using a D8 Advance Bruker X-ray diffractometer with CuK_α radiation and a LynxEye point detector. The sample was placed in low background Si sample holder. The patterns were recorded with step size of 0.008^o 2Θ in the range 10^o to 120^o 2Θ and variable time per step. A very fine powder of Si standard reference material was mixed with the samples to calibrate the instrument parameters during Rietveld refinements.

CHAPTER 4 – RESULTS AND DISCUSSION

4.1. Crystal Structure of Crystal Structures of Mullites

4.1.1. Crystal Structure of Alumino-Silicate Mullite

The chemical composition of the mullite samples was verified by using the well-known linear relationship between the *a*-lattice parameter and the molar Al_2O_3 content of the $Al_{4+2x}Si_{2-2x}O_{10-x}$ phases. [100] The mullite sample with a = 7.58154 (6) Å, was determined to have a chemical composition of 65.3 mol% Al_2O_3 which corresponds to that of 2:1-mullite with x = 0.4 (designated as 2:1-mullite). The mullite sample with a = 7.55707(6) Å, was determined to have a chemical composition of 61.6 mol% Al_2O_3 which corresponds to that of 3:2-mullite with x = 0.25 (designated as 3:2-mullite). According to its cell dimensions (a = 7.4840 (2) Å) and its white color, sillimanite is near the ideal composition $Al_2O_3 \cdot SiO_2$.

At ambient pressure and temperature all the phases of the $Al_{4+2x}Si_{2-2x}O_{10-x}$ system studied in this work all have an orthorhombic crystal lattice: mullite crystallizes in the space group Pbam (55) whereas sillimanite crystallizes in the space group Pbnm (62). The crystal structures of mullite-type alumino-silicates of $Al_{4+2x}Si_{2-2x}O_{10-x}$ composition may best be described by means of sillimanite. The key features of the crystal structure of sillimanite (Figure 21a) are edge-sharing octahedral AlO_6 chains, forming single Zweier chains, [101] running parallel to the **c**-axis. [1, 102] These octahedral chains are linked by double chains of corner-sharing MO_4 tetrahedra (also parallel **c**), with an ordered distribution of the tetrahedral cations Al^{3+} and Si^{4+}. Perpendicular to the **c**-axis the situation is different, with a sequence of AlO_6 octahedra and AlO_4 and SiO_4 tetrahedra occurring parallel to the **a**- and **b**-axis (Figure 21a). The average structure of mullite can be derived from the closely related, but structurally more simple sillimanite by the coupled substitution $Si^{4+}_{tet} + O^{2-} = 2Al^{3+}_{tet}$ + vacancy □ (where tet = tetrahedral) and simultaneous Al^{3+} and Si^{4+} disordering over the tetrahedral sites (Figure 21b). The "fictitious" reaction involves removal of oxygens bridging two adjacent tetrahedra in the sillimanite structure (O(C) oxygen atoms) and the formation of oxygen vacancies (this being needed to maintain the overall charge neutrality), with the number of vacancies corresponding to the x-value of the general formula of the mullite-type alumino silicates $Al_{4+2x}Si_{2-2x}O_{10-x}$.

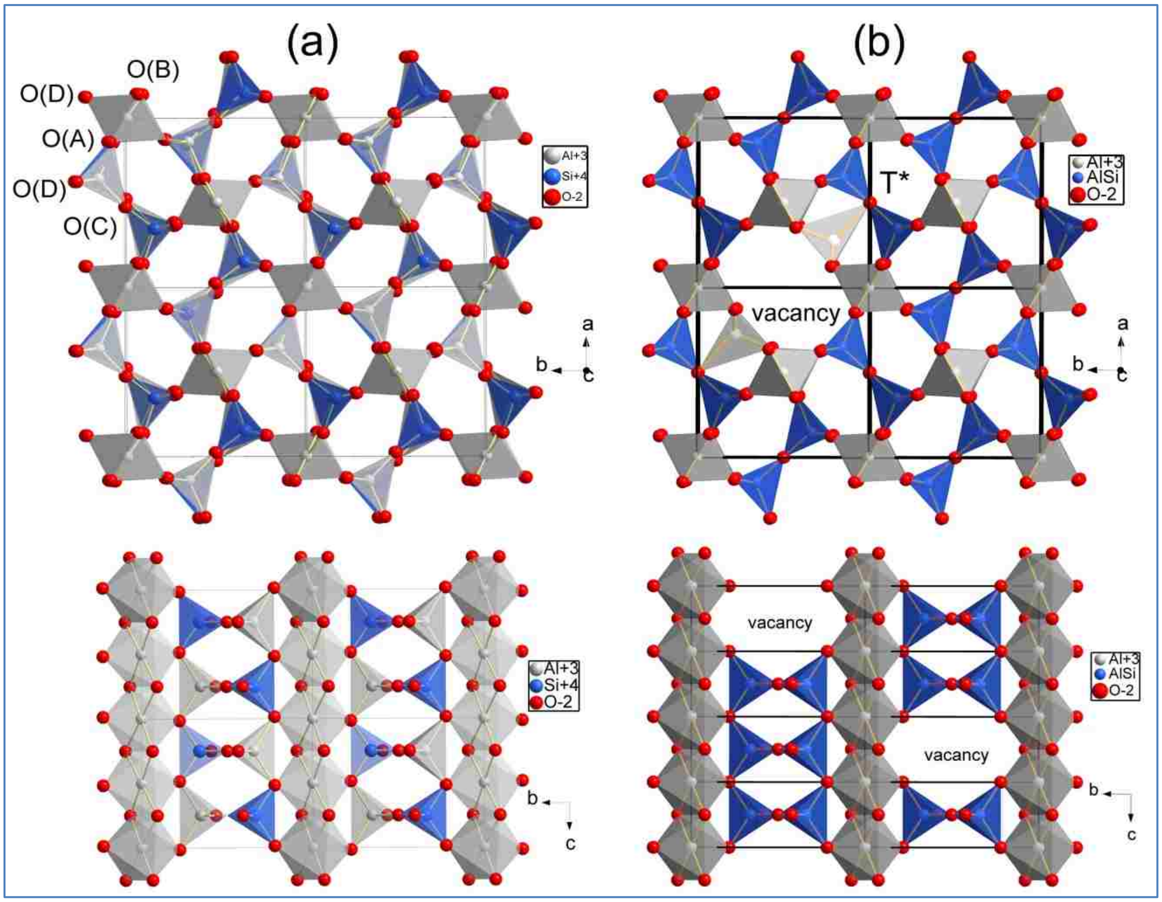

Figure 21. Comparison of the structures of sillimanite (a) and of mullite (b).
In order to illustrate oxygen vacancies, while maintaining the same number of octahedral units along the c-axis, eight unit cells are displayed. Crystal structures were drawn with Diamond 3.2 software. [97]

The formation of vacancies causes associated tetrahedral sites T to be displaced to positions designated as T^*, and the formerly bridging O(C) oxygen atoms become threefold coordinated and form T_3O groups (the so-called tetrahedral triclusters, T^* according to literature is favorably Al, see Figure 21). The excess positive charge in mullite produced by the formation of oxygen vacancies is compensated by substitution of Si^{4+} by Al^{3+}.

The mullite-type $Al_{4+2x}Si_{2-2x}O_{10-x}$ phases investigated in this study differ in the amount of oxygen vacancies in going from 2:1-mullite ($x = 0.4$, or 0.4 oxygen vacancies per unit cell), to 3:2-mullite ($x = 0.25$ or 0.25 oxygen vacancies per unit cell) and to sillimanite ($x = 0$, no vacancy). The main motivation of this portion of the present study was to understand the role of oxygen vacancies on the high-pressure behavior and structural integrity of the mullite-type alumino silicates.

4.1.2. Crystal Structure of Boron Mullite

At ambient pressure and temperature the 7:4 mullite and B-mullite systems studied in this work have an orthorhombic crystal lattice and crystallize in the same space group as conventional mullite (*Pbam* (55)). The crystal structures of mullite-type alumino–silicates of $Al_{4+2x}Si_{2-2x}O_{10-x}$ composition were described in section 4.1.1 above.

Another $Al_{4+2x}Si_{2-2x}O_{10-x}$ mullite-type phase investigated in this study is the 7:4 mullite ($Al_{4.66}Si_{1.33}O_{9.66}$) with x=0.333 (or about one oxygen vacancy per three unit cells). Its high pressure behavior was compared to that of an alumino-silicate mullite with 3.5(4) mol% B_2O_3, where B substitutes some of the Si atoms. [29] The boron-substituted mullite is hereafter referred to as B-mullite. The Si→B substitution leads to formation of additional oxygen vacancies, according to the coupled substitution $2Si^{4+} + O^{2-} \rightarrow 2B^{3+} + \square$, as well as to formation of BO_3 triangles connecting the octahedral AlO_6 chains (Figure 22). [29] The goal of this portion of the present study was the investigation of the structural behavior and phase stability of 7:4 mullite in comparison to B-mullite, including a possible description of pressure-induced structural rearrangements at the atomic scale, and the role of oxygen vacancies, upon compression and decompression.

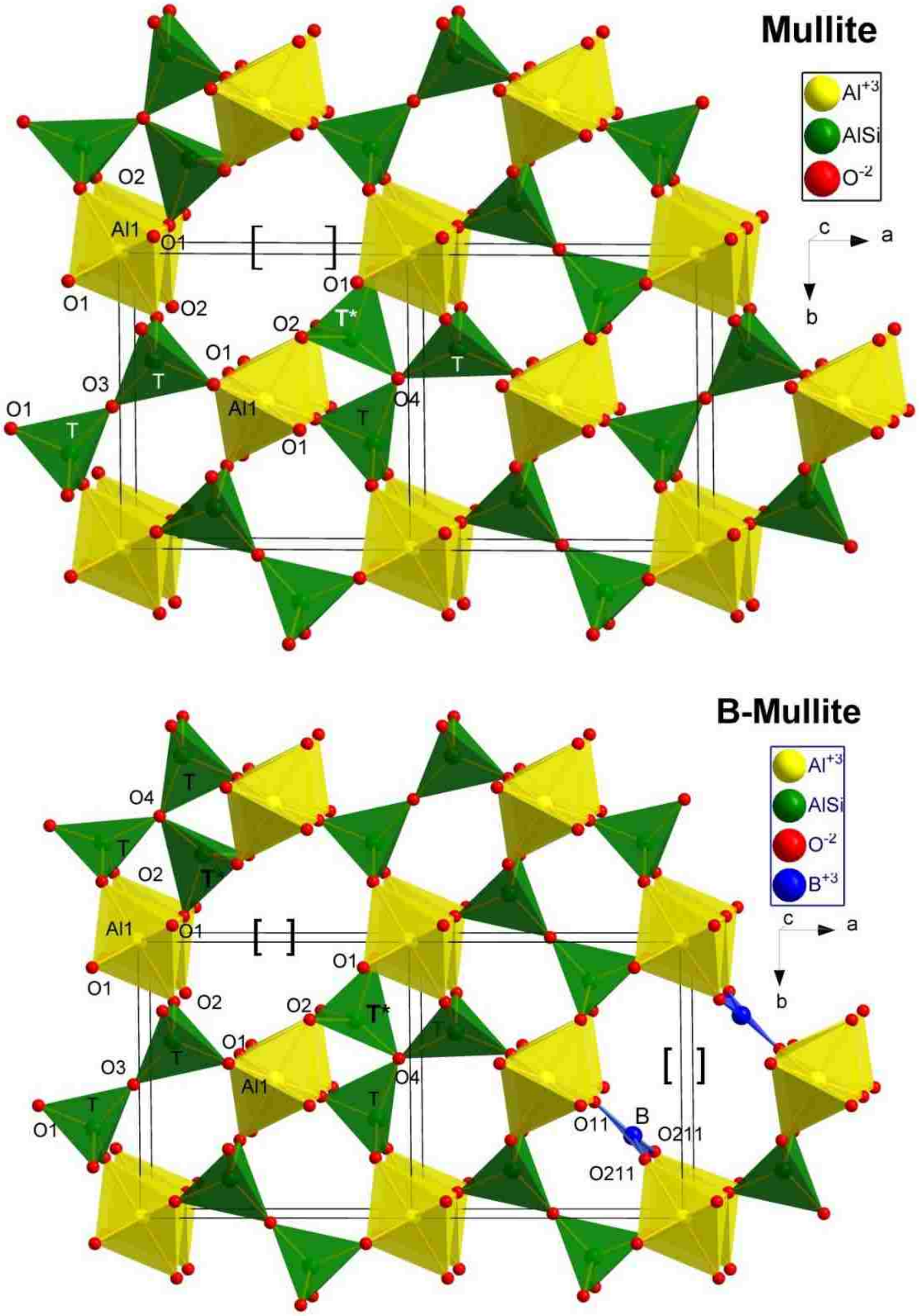

Figure 22. Ambient pressure crystal structures of mullite [103] and B-substituted mullite. [29]
The schematic substitution mechanisms are shown. Tetrahedral triclusters are found near T* sites, while oxygen vacancies are indicated by [ ]. Crystal structures were drawn with Diamond 3.2 software. [97]

Additionally, the thermal behavior of various B-mullites mullite was recently reported. [29] The thermal expansion, along with the volume compression in response to the applied pressure, allows to provide, given some assumptions, a P–T–V Equation-of-State for B-mullite.

4.1.3. Crystal Structure of $PbMBO_4$ Synthetic Mullites

The crystal structure of mullite-type $PbAlBO_4$, $PbFeBO_4$ and $PbMnBO_4$ has been known since Park et al. [36] who described it in space group Pnma. The $PbMBO_4$ (M= Al, Mn, Fe and $Al_{1-x}Mn_x$) compounds have been recently reported [38, 104] with the space group set to Pnam in order to ensuing their conformity to the mullite family while better understanding their physical properties. [1]

Figure 23 shows the crystal structure of $PbAlBO_4$ and Figure 24 that of $PbFeBO_4$. The (infinite) chains of edge-sharing AlO_6/FeO_6 octahedra run parallel to the c-axis. The octahedra chains are bridged by boron forming a trigonal planar BO_3 group.

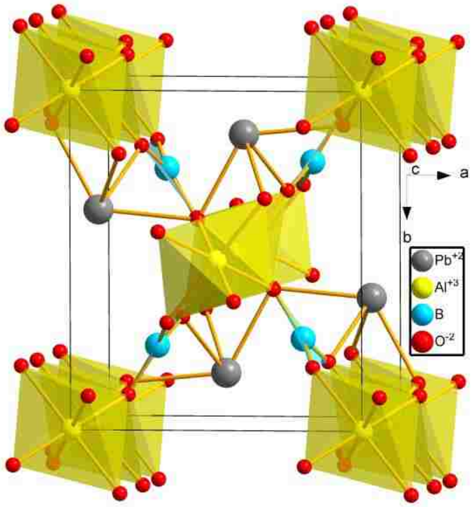

Figure 23. The ambient pressure and temperature crystal structure of $PbAlBO_4$.
The structure is drawn in the mullite setting. Both individual atoms and the polyhedral outlines can be seen. The parallel with the mullite family of materials can be readily observed, among others, by the edge-sharing octahedral chains running along the *c* crystallographic axis. The difference is in the fact that the octahedral chains are cross-linked with BO_3 triangles and PbO_4E distorted square pyramids instead of AlO_4 and SiO_4 tetrahedra, as in aluminosilicate mullites. 'E' stands for the lone electron pair.

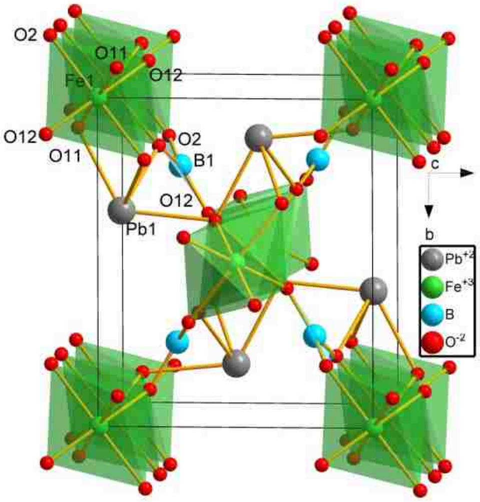

Figure 24. The ambient pressure and temperature crystal structure of $PbFeBO_4$.
The structure is drawn in the mullite setting. Both individual atoms and the polyhedral outlines can be seen. The parallel with the mullite family of materials can be readily observed, among others, by the edge-sharing octahedral chains running along the *c* crystallographic axis. The difference is in the fact that the octahedral chains are cross-linked with BO_3 triangles and PbO_4E distorted square pyramids instead of AlO_4 and SiO_4 tetrahedra, as in aluminosilicate mullites. 'E' stands for the lone electron pair.

Between two BO_3 groups a Pb^{2+} cation locates at the apex of a distorted PbO_4 square pyramid, where the $6s^2$ lone electron pair (LEP) of Pb^{2+} cations is stereochemically active.As in other mullite-type materials, in lead-boron contacting mullites the characteristic building units are edge sharing MO_6 octahedra, forming single Zweier chains [1] running parallel to the crystallographic c-axis. A well-known Pb containing compound of the Pbam structural family is the mineral minium Pb_3O_4, (used in anticorrosion paint for years [105]). In minium the octahedral chains are made of Pb^{4+} cations surrounded by oxygens, and the chains are interconnected by Pb^{2+} cations, which stabilize the structure using their stereochemically active $6s^2$ lone electron pair (LEP, E in formula). In the orthorhombic arrangement the Pb^{4+} cations could be replaced by Sn^{4+},[105] as well as cations having a lower valence, resulting in the same orthorhombic crystal structure which is, with this chemical composition, stable at room temperature.[38] If we replace the Pb^{4+} ions by M^{3+} ions, then for the purpose of charge balance one of the Pb^{2+} cations must also be replaced by a trivalent cation. Such a mutual combination is found in $PbMBO_4$ phases (M = Ga, Al, Cr, Mn, Fe) where Pb^{4+} is replaced for example by Al^{3+} while Pb^{2+} is replaced by B^{3+}; this was first reported by Park et al. [34, 35, 36]

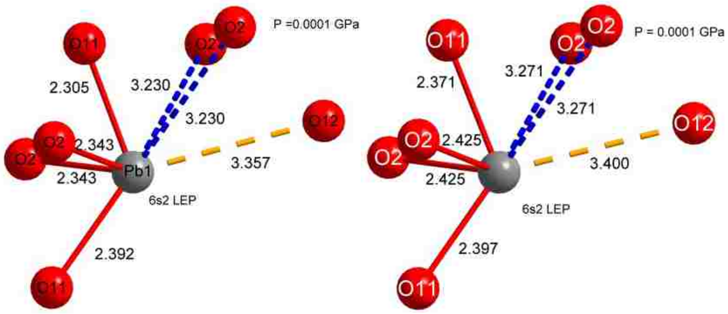

Figure 25. The first coordination sphere of the Pb^{2+} cation.
Left: $PbAlBO_4$ and *right*: $PbFeBO_4$. The spatial distribution of the bonding oxygens illustrates the stereochemical activity of the lone electron pair. Dotted lines indicate non-bonding oxygens.

Comparing these two structure types, the Pb1 atom in Pb_3O_4 is replaced for example by Al, the Pb2 atom remains as Pb and the Pb3 atom is replaced by B. If we consider that the average B‒‒O bond length is 137.6(7) pm [35] while average Pb‒‒O bond length is much longer with 237.6(7) pm [34] then we can see that the resulting BO_3 group in the $PbMBO_4$ structure significantly increases the strength of the interconnection between octahedral chains.[38]

In $PbMBO_4$ the 6 s2 lone electron pair of Pb^{2+} with a nido-like trigonal bipyramidal coordination (PbO_4/LEP) is also stereochemically active, [106] thus not influenced by the trigonal planar BO_3 group. [38] The $Bi_2Fe_4O_9$ synthetic mullite also possesses such a coordination of the LEP for the bismuth atoms, [106] but the closely related $Bi_2Mn_4O_{10}$ phase does not.[107] The BO_3 group greatly influences the properties of the $PbMBO_4$ phases and indeed Park et al. [35] reported it to be the driving force for the temperature-driven $\alpha \rightarrow \beta$ phase-transition of $PbAlBO_4$. Moreover, in the $PbMBO_4$ mullites the strong B‒‒O bonds were found to be the origin of negative thermal expansion of the *a* lattice parameter, whereas a positive thermal expansion of the *b* and *c* lattice parameters was observed.[38, 108]

4.2. High-Pressure Behavior of Alumino-Silicate Mullites and Sillimanite

4.2.1. High-Pressure Synchrotron XRD

High-pressure ADXRD patterns of the three mullite-type $Al_{4+2x}Si_{2-2x}O_{10-x}$ phases were collected in-situ in a DAC, on compression from 0.9 GPa up to 44.6 GPa for sillimanite, from 1.3 GPa to 27.3 GPa for 3:2-mullite and from 0.45 GPa to 40.8 GPa for 2:1-mullite. Figure 26 shows selected x-ray diffraction patterns. As pressure is increased all diffraction lines shift towards higher 2θ angles i.e. lower *d*-spacings. According to the ADXRD patterns the compression appears to be continuous up to ~30 GPa for sillimanite, and up to ~25 GPa in the case of the two mullites (Figure 26). The discontinuous change of the *d*-spacings goes along with a dramatic intensity loss and important broadening of x-ray diffraction lines. This finally leads to complete x-ray amorphization of both mullites at above ~ 30 GPa, while amorphization of sillimanite is observed at much higher pressure, above ~40 GPa. High-pressure, synchrotron ADXRD patterns of the three $Al_{4+2x}Si_{2-2x}O_{10-x}$ phases were also collected in situ (DAC), during decompression runs from the highest pressures investigated down to ambient conditions. Comparative x-ray diffraction patterns of sillimanite and 2:1-mullite decompressed to ambient pressure are shown in Figure 27. Sillimanite retains most of its crystallinity upon decompression from 44.6 GPa to ambient pressure. On the contrary in the 2:1-mullite decompressed from 28.5 GPa to ambient pressure the amorphized phase is metastably retained reverting gradually to a highly disordered, parent-like phase. upon decompression from 43 GPa the 2:1-mullite appears mostly x-ray amorphous (Figure 27).

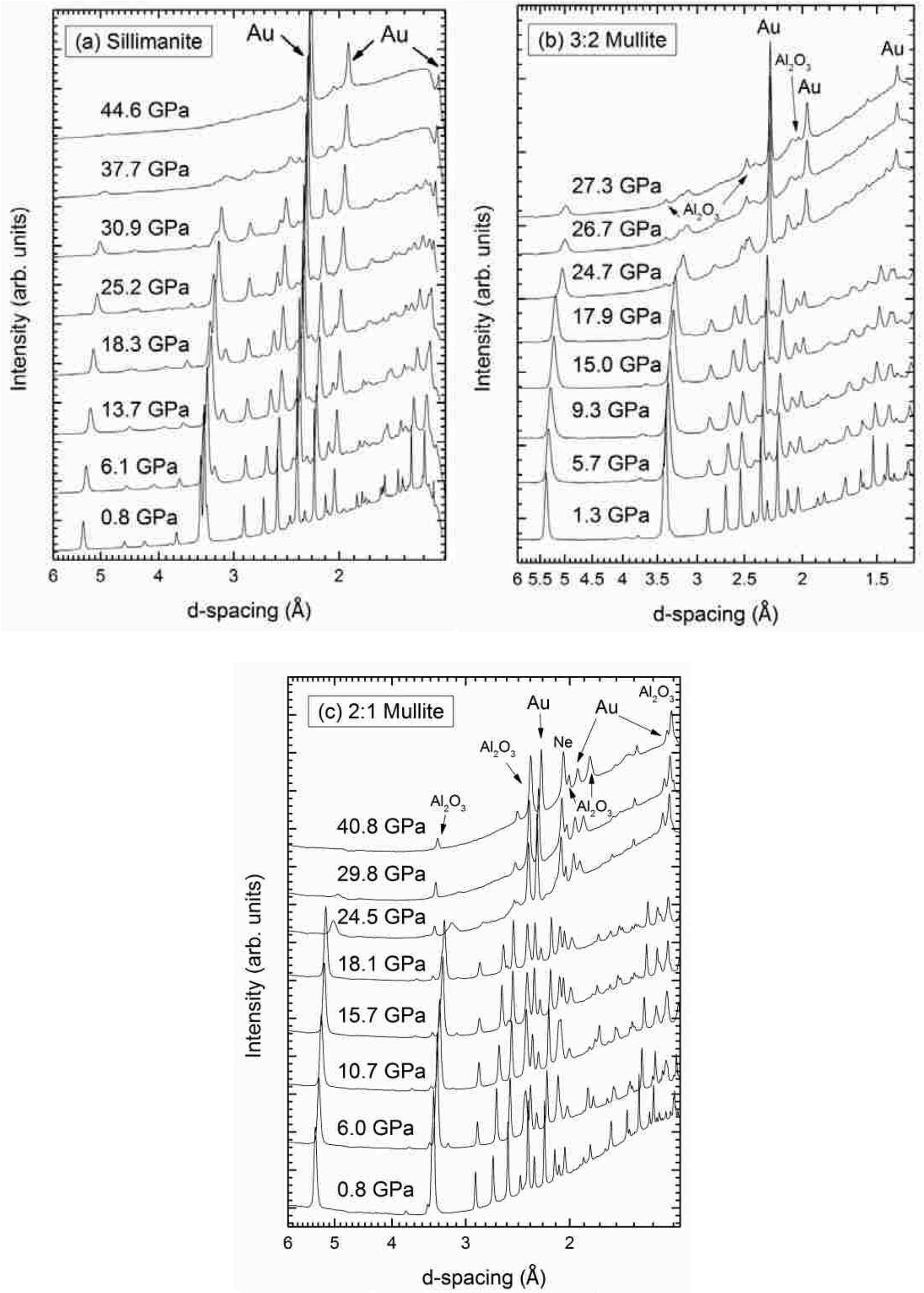

Figure 26. Selected high pressure XRD patterns of: (a) sillimanite, (b) 3:2- and (c) 2:1-mullite. Lines of the gold pressure indicator, Ne pressure medium and Al_2O_3 impurity are marked.

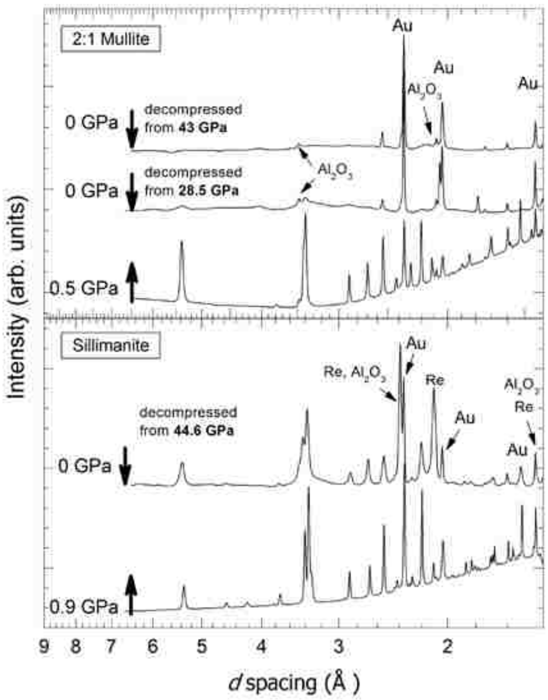

Figure 27. High-pressure XRD patterns of 2:1-mullite and sillimanite on decompression.
Compression (arrows up) and the subsequent decompression to ambient pressure (arrows down).
For 2:1-mullite two patterns are shown: decompression from 28.5 GPa and from 43 GPa while for sillimanite decompression from 44.6 GPa is shown. Diffraction lines of Re gasket, ruby pressure indicator and of gold, are marked.

In order to follow the pressure evolution of unit cell parameters and unit cell volumes, of 2:1- and 3:2-mullite and of sillimanite, Rietveld full-profile structural refinements were performed on all x-ray diffraction patterns collected. Pressure-induced broadening and intensity loss of ADXRD lines limited the structural refinements to 37.7 GPa for sillimanite, 27.3 GPa for 3:2-mullite and 24.5 GPa for 2:1-mullite.

At ambient pressure and temperature all the phases of the $Al_{4+2x}Si_{2-2x}O_{10-x}$ system studied in this work all have an orthorhombic crystal lattice: mullite crystallizes in the space group Pbam (55) whereas sillimanite crystallizes in the space group Pbnm (62). For starting the ambient pressure refinements of 2:1-mullite we used the initial structure of Voll *et al.*, [109] for 3:2-mullite the initial structure of Brunauer *et al.* [8] was used and sillimanite was refined with the initial structure of Winter and Ghose. [95] The pressure-induced evolution of unit cell parameters *a*, *b*, and *c* and of cell volumes *V* are given in Figure 28, while relative fractional changes of these parameters are shown in Figure 29. A detailed comparison of the fractional evolution of the **c-**axis of all the samples investigated in this work compared with available literature data are shown in Figure 30. The lattice compression is anisotropic for all samples studied, with the **c**-axis being much less compressible than the **a**-axis and the **b**-axis (Figure 28, Figure 29, Figure 30). On compression below ~20 GPa sillimanite and both mullites display nearly identical fractional pressure evolution (Figure 29).

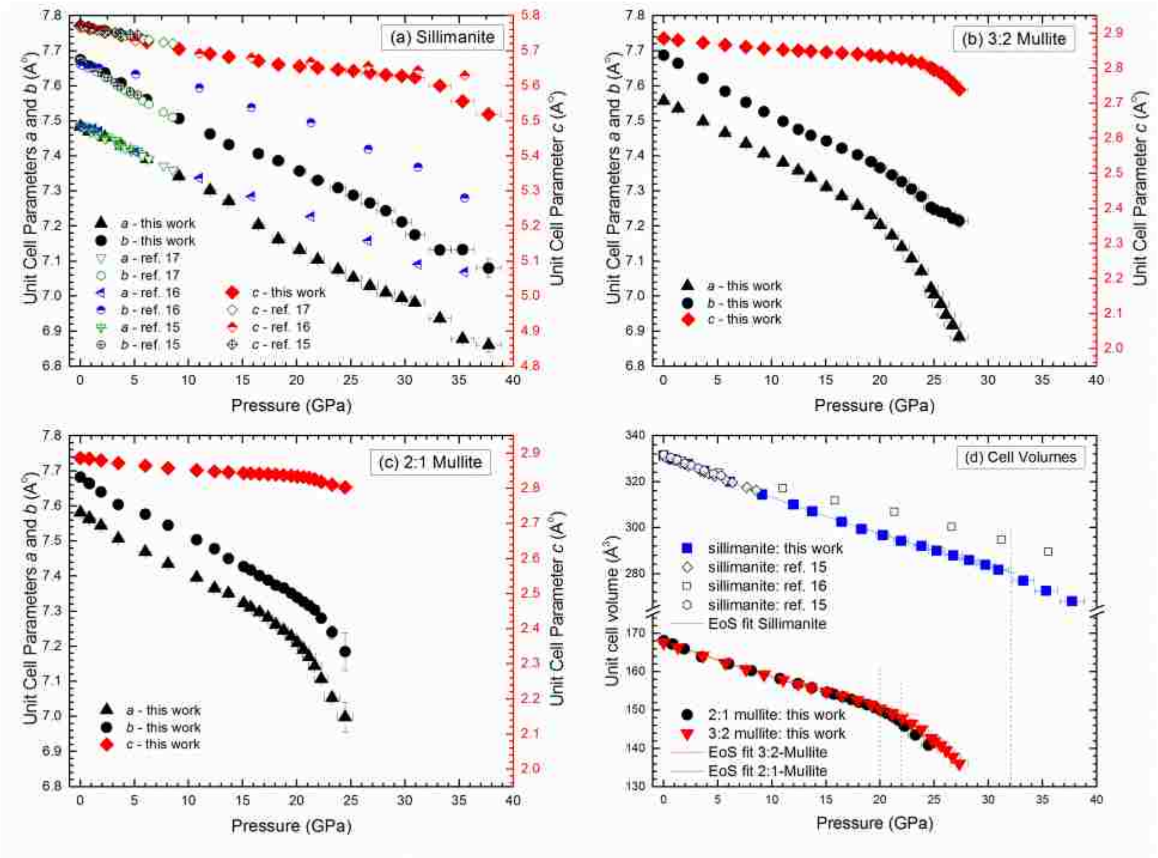

Figure 28. Cell parameters *vs*. pressure.
Pressure evolution of the unit cell parameters of: (a) sillimanite, (b) 3:2-mullite and (c) 2:1-mullite as well as the pressure evolution of their unit cell volumes (d) obtained from ADXRD data.
In (d) the solid lines represent 3rd order Birch-Murnaghan EoS fits. For graphs (a) through (c) the left-side axes refer to *a* and *b* while the right-hand axes refer to *c*. All vertical axes span 1 Å for easy comparison. For sillimanite, the evolution, as a function of pressure, is compared with available literature data.

However, for sillimanite the **a**- and **b**-axis compression appears linear up to ~30 GPa, while for both mullites the linearity of the **a** and **b** compression is limited only to ~22

GPa for 3:2-mullite and ~20 GPa for 2:1-mullite (Figure 28, Figure 29). It is interesting to note that for the **c**-axis there exists a slight, but characteristic discontinuity of compression (decrease of the **c**-axis slope with increasing pressure) above ~20 GPa for sillimanite and above ~10 GPa for both mullites (Figure 30).

On compression above ~20 GPa the lattice constants and correlated cell volumes of 2:1 and 3:2-mullites decrease rapidly. This discontinuity is slightly stronger for 2:1- than for 3:2-mullite. A similar, though less pronounced discontinuity in lattice constants and cell volume can be observed for sillimanite, but at much higher pressures, namely above ~30 GPa (Figure 28, Figure 29, Figure 30).

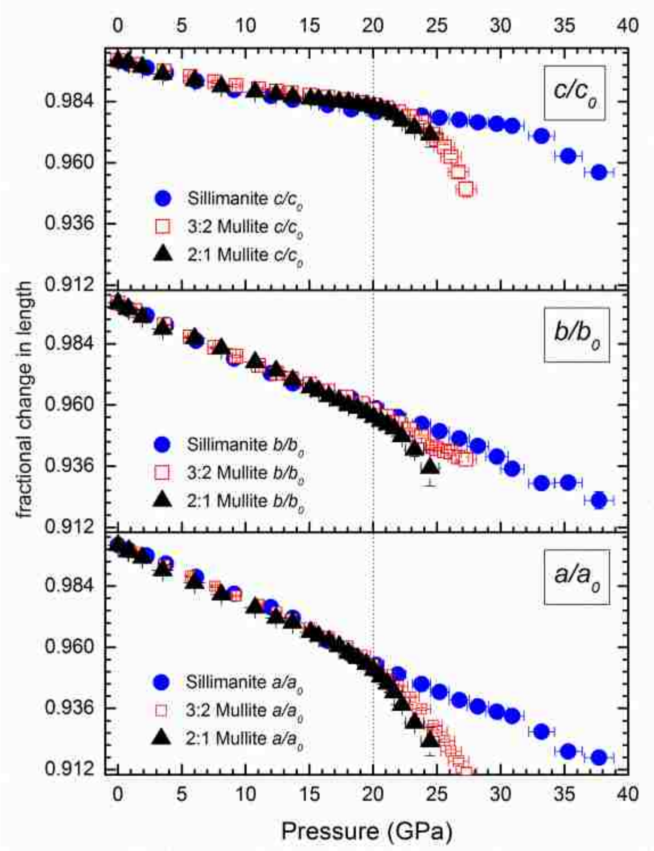

Figure 29. Fractional pressure evolution cell parameters.
Fractional pressure evolution of the *a*, *b* and *c* unit cell parameters for sillimanite, 3:2- and 2:1-mullite.
Fractional changes are shown by grouping the *a*, *b* and *c* parameters of all three materials together, to illustrate similarities and differences in their pressure behavior along the three crystallographic axes. For easy comparison all axes span the same vertical range.

No compression data for mullite have been reported in the literature up to now. For compression of sillimanite, our results of pressure-evolution of cell parameters (Figure 28, Figure 30) agree well with data reported by Yang *et al.* [17] on compression up to 5.3 GPa and with data of Burt *et al.* up to 8.5 GPa. [19] In the sillimanite data of Friedrich *et al*. [18] the pressure evolution of the **c**-axis appears to follow the same trend as our data, with a discontinuity, but this evolution is slightly slower above ~15 GPa and significantly slower above ~30 GPa (Figure 30). This can be attributed to different pressure-transmitting media used and different methods for pressure measurement, especially since the observed differences increase steadily with pressure. Data of sillimanite in reference [18] were obtained with a 4:1 methanol-ethanol mixture as pressure-transmitting medium, which is hydrostatic only up to 10 GPa, [95] while pressure measurements were done using the ruby luminescence scale, which gives inaccurate pressure readings in non-hydrostatic conditions (above 10 GPa). On the other hand, in the present work the pressure-transmitting medium was helium, which gives excellent hydrostatic conditions up to at least 50 GPa, [98, 99] covering

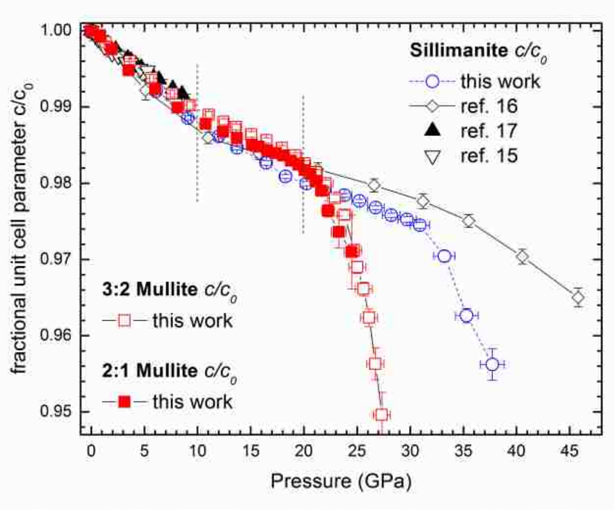

Figure 30. Zoom on the fractional pressure-evolution of the *c* lattice parameter.
Zoom on the fractional pressure-evolution of the *c* lattice parameter of 2:1-mullite, 3:2-mullite and of sillimanite. Results for sillimanite are compared with literature data. It is interesting to note that sillimanite displays a similar behavior to mullite, with a discontinuity in the compression of the *c*-axis, but at higher pressure (~10 GPa for both mullites and at ~20 GPa for sillimanite).

our entire experimental range of pressure. Also our pressure readings were done using the equation of state of gold, mixed-in with the sample thus allowing, together with hydrostatic conditions, for more realistic pressure readings.

4.2.1.1. Compression Mechanisms

Based on our results it appears that the changes of lattice parameters above ~20 GPa in 2:1-mullite, 3:2-mullite and sillimanite probably represent processes taking place in several steps, which we describe as follows.[75] Below ~20 GPa, 2:1-mullite, 3:2-mullite and sillimanite behave quite similarly on compression. The pressure-evolution of cell parameters and cell volumes of all phases are given in Figure 28. The fractional compression (Figure 29) between ambient pressure and 20 GPa along the crystallographic **a**-axis (≈ 5%) is similar to that along the **b**-axis (≈ 4%). The significantly lower compression along the **c**-axis (≈ 2%) - observed in both mullites and in sillimanite - is reasonable, because of the occurrence of the firmly bound, edge-connected octahedral chains in this lattice direction, which are cross-linked by rigid tetrahedral double chains (see structure in Chapter 2). In fact, in sillimanite at low pressures (below 8 GPa), it was found [17, 19] that the main compression mechanism is the shortening of bonds within the AlO_6 octahedra, whereas the tetrahedra behave as rigid units. So compression along the **c**-axis can only take place through the compression of the edge-sharing AlO_6 octahedra. Clearly the arrangement of the firmly bound octahedral and tetrahedral chains in the mullite-type alumino-silicate structures results in the high resistance against elastic compression in the **c**-direction observed for all three phases. The situation is different perpendicular to the **c**-axis, in the *(001)* plane, where a sequence of rigid AlO_4 and SiO_4 tetrahedra and the more compliant AlO_6 octahedra are corner-sharing (see structure in Chapter 2).

In corner sharing systems the inter-polyhedral angles can change more easily as the result of compression and this can justify the higher compressibility observed in **a** and **b** directions for both mullites and for sillimanite. It is interesting to have a closer look at the influence of the compliant AlO_6 octahedra on the compressibility of the investigated phases. The longest and most elastic Al-O(D) bond of the octahedron should display the largest pressure-induced shortening. Since Al-O(D) encloses an angle of about 30° with the **b**-axis and of about 60° with the **a**-axis (see structure in Chapter 2), it can be expected that the fractional compression is higher parallel to **b** than parallel **a**. However this is not observed and the fractional compression is even slightly higher parallel to the **a**-axis than it is parallel to **b** (Fig.5). One simple explanation could be that the octahedral chains are rotated in a way that the angle between Al-O(D) and the **b**-axis becomes larger with pressure. The similar high-pressure compressibility of sillimanite and of both mullites up to ~20 GPa implies that the observed behavior is mainly controlled by pressure-induced compression of the three-dimensional structural networks of sillimanite and mullite. Obviously the absence – in sillimanite – or presence – in mullite – of oxygen vacancies does not play a significant role on their pressure response below ~20 GPa. [75]

Comparison of the compressibilities β_j of sillimanite and of the mullites with the linear elastic stiffnesses c_{ij} provides further understanding. Sillimanite displays a slightly higher mean linear stiffness of 303 GPa (from Brillouin scattering [10]), than does 2:1-mullite with 292 GPa (from resonant ultrasound spectroscopy [12]), which explains the higher resistance of sillimanite against mechanical load. In both phases the high stiffnesses along the **c**-axis (c_{33}) reciprocally correspond to the low compressibilities (β_c) in this lattice direction, found in the present work. Actually our experimental data support the idea that alumino-silicates with mullite structure display their highest mechanical stability along the **c**-axis. The situation is less clear perpendicular to the **c**-axis, where the highest compressibility is expected along **b** (see above). Actually the compressibilities along the **a** and **b**-axes are quite similar (Figure 29). [75]

Below 20 GPa, it is worthwhile to have a closer look on the high-pressure behavior of 3:2-mullite, 2:1-mullite and sillimanite. Figure 30 compares the fractional pressure evolution of the *c*-parameter of both mullites and of sillimanite obtained in this work with published data of sillimanite. [17, 18, 19] At ~10 GPa in both mullites and at ~20 GPa in sillimanite, a small discontinuity of the *c*-parameter compression occurs and is seen as a decrease in the slope, indicating a slowdown of the *c*-parameter's compression. A similar discontinuity in sillimanite can be seen in literature data of sillimanite, [18] at slightly different pressures (Figure 30). No such discontinuity is observed in the compression along the *a*- and *b*-parameters up to 20 GPa neither in sillimanite nor in mullite (Figure 28, Figure 29). One possible explanation of the observed slowdown is that the rigid tetrahedral double chains and the cross-linked, edge-connected octahedral chains are close to reaching a lower-limit of cation-oxygen bond lengths and of oxygen-cation-oxygen angles. Yet, the polyhedral network along the **c**-axis is still strong enough to support further compression load up to ~20 GPa for 2:1-mullite, up to ~22 GPa for 3:2-mullite and up to~30 GPa for sillimanite. On the other hand, the polyhedral network perpendicular to **c**, with its sequences of rigid tetrahedra and compliant octahedra, allows for further, steady compression parallel to the **a** and **b**-axes up to ~20 GPa (Figure 28, Figure 29). At this compression stage the number of oxygen vacancies and the substitution and disordering of tetrahedrally bound Si^{4+} by Al^{3+}, with the associated weakening of the tetrahedral Si(Al)-O bonds, do not seem to have significant influence on the high-pressure behavior of both mullites and of sillimanite. [75]

Above ~20 GPa for 2:1-mullite, and ~ 22 GPa for 3:2-mullite, an important increase of pressure-induced compression, manifested by a significant decrease in the unit cell volume is observed (Figure 28). The strong discontinuity of the volume compression together with a dramatic intensity loss and important broadening of ADXRD lines (Figure

26) is interpreted in terms of a gradual and irreversible structural decomposition of both mullites. This is consistent with a work by Braue *et al.* [23] that reported a shock-wave induced amorphization of mullite above 35 GPa. A displacive or reconstructive phase transformation is excluded, since the diffraction patterns of the decompressed materials (recovered from high-pressure loading), display a very low degree of crystallinity (Figure 27). The structural decomposition in our data for both mullites and for sillimanite (Figure 26, Figure 28, Figure 29), in turn, strongly reduces the resistance of the crystal lattices against compression, which drives the volume discontinuity further. Moreover, it is found that 2:1-mullite, containing more oxygen vacancies (0.4 per unit cell) than 3:2-mullite (0.25 per unit cell), displays a larger and somewhat faster structural decomposition effect than the latter, especially in **a** and **b** (but not **c**) directions (Figure 29). Oxygen vacancies in both mullites obviously play a significant role in lowering their mechanical stability. Interestingly, in both mullites the *b* parameter is the most resistant against the discussed decomposition at pressures above 20 GPa (Figure 29). Possibly the longer and more elastic octahedral Al-O(D) bonds lying at about 30° to the **b**-axis allow for a better support of the pressure-induced stress along **b**, whereas the shorter and less elastic octahedral Al-O(A,B) bonds lying closer to the **a**-axis are less flexible (see structure in Chapter 2). In the **c**-direction, for both mullites, the mechanical stability limit is reached at about 20 GPa for 2:1-mullite and 22 GPa for 3:2-mullite, and both structures collapse upon further pressure increase (Figure 26, Figure 29). [75]

A pressure-driven discontinuity of lattice parameters and unit cell volume similar to that of both mullites is also observed for sillimanite. It is attributed to an early onset of a pressure-induced amorphization. However, the observed volume discontinuity is much less marked and occurs at ~30 GPa for sillimanite compared to ~20 GPa for the mullites (Figure

28, Figure 29, Figure 30), again demonstrating the higher mechanical stability of sillimanite with respect to mullite. [75]

The lower structural stability of both mullites in comparison to sillimanite is attributed to the presence of oxygen vacancies in mullites. The more open and disordered crystal structures of mullites are not able to support as high pressures as the sillimanite structure does. This statement is consistent with the fact that sillimanite forms in low-pressure metamorphic rocks, whereas mullite is a typical high-temperature phase. Finally, it is the presence of oxygen vacancies in both mullite structures that leads to an irreversible, pressure-driven structural decomposition. [75]

Using theoretical simulations Oganov *et al.* [15] predicted a phase transition in sillimanite at ~35 GPa. This is in the same pressure range where we observe the onset of structural amorphization. Oganov *et al.* [15] proposed the formation of a metastable high-pressure phase of sillimanite with fivefold coordinated Al^{3+} and fivefold coordinated Si^{4+}. Our Rietveld refinements of sillimanite above 30 GPa, however, yielded no match to a metastable [15] sillimanite structure. In this study of 2:1 and 3:2 mullite and sillimanite there is no evidence of formation of a metastable high-pressure phase of sillimanite with fivefold coordinated Al^{3+} and Si^{4+}. [75]

4.2.1.2. Equation of State of Alumino-Silicate Mullites and Sillimanite

The pressure-volume plot shown in Figure 28(d) is a good illustration of the threshold at which discontinuities in the pressure-evolution of unit cell parameters appear. The following sequence of pressure-induced discontinuity onsets can be identified: ~30 GPa for sillimanite, ~22 GPa for 3:2-mullite and ~20 GPa for 2:1-mullite. A third order Birch-Murnaghan [110, 111, 112, 113, 114] equation of state (EoS) was fitted to the experimental pressure-volume data (Figure 28(d)) in order to determine the bulk modulus K_0 and its pressure derivative K_0' at ambient conditions for sillimanite, for 3:2-mullite and for 2:1-mullite:

$$P = \frac{3}{2}K_0\left[\left(\frac{V_0}{V}\right)^{\frac{7}{3}} - \left(\frac{V_0}{V}\right)^{\frac{5}{3}}\right]\left\{1+\frac{3}{4}(K_0'-4)\left[\left(\frac{V_0}{V}\right)^{\frac{2}{3}}-1\right]\right\}$$

The bulk moduli (K_0) obtained from the Birch-Murnaghan fits are summarized in Table 1, together with literature data obtained by other methods. For each sample, the EoS was fitted only up to the early onset of the pressure-induced discontinuities, beyond which the EoS breaks down (Figure 28(d)). [75]

Table 1. Comparison of: bulk moduli for mullites and for sillimanite.
Comparison of: bulk moduli (K_0), their pressure derivatives (K_0') and unit cell volumes at ambient pressure (V_0) obtained in the present work with available literature data. [75]

	K₀ **(GPa)**	***K₀'***	***V₀*** **(Å³)**	**method**
2:1-Mullite	169.2	-	-	acoustic resonance spectroscopy [11]
	169.1	-	168.13	resonance ultrasound spectroscopy [12]
	166.5	-	168.13	resonance ultrasound spectroscopy [12]
	171.0 [2]	-	168(1)	Brillouin spectroscopy [115]
	167.6	-	332.0738	theoretical (VASP) [116]
	162(7)	2.2(6)	168.13(2)	powder XRD - this work
3:2-Mullite	174	-	167.335(2)	ultrasonic [7]
	172.4	-	167.335(2)	ultrasonic [117]
	190	-	167.335(2)	theoretical (ionic-model) [7]
	173.2	-	329.6418	theoretical (VASP) [116]
	173(6)	2.3(2)	167.580 (1)	powder XRD - this work
Sillimanite	166.4	-	-	Brillouin (Reuss) [10]
	175.1	-	-	Brillouin (Voigt) [10]
	164(1)	5.0(3)	331.208(18)	single crystal XRD [19]
	171(7)	4(3)	331.81(5)	single crystal XRD [17]
	176(11)	4 (fixed)	331.0(3)	powder XRD [18]
	160.1	2.69	339.57	theoretical (VASP) [15]
	161.4	2.99	319.11	theoretical (GULP) [15]
	174.9	-	325.3389	theoretical (VASP) [116]
	159	-	-	theoretical DFT [16]
	167(7)	2.1(4)	331.459(3)	powder XRD - this work

Data in Table 1 show that the bulk moduli (K_0) of the two mullites and of sillimanite obtained in this work are in good agreement with averaged literature data. The higher value of the pressure derivative K_0' obtained for sillimanite by Burt *et al.* [19] can be explained by

---

[2] Data available only for 2.5:1 mullite.

the fact that the EoS was fitted in a much smaller pressure range (up to 8.5 GPa) as compared to the present work (up to 30.5 GPa). Contrary to expectations, it is not possible to establish a trend of bulk modulus value versus the amount of oxygen vacancies. Our experimental values of K_0 are too close to each other to allow for such differentiation. Moreover the pressure-evolution of unit cell parameters and of unit cell volume of the two mullites and of sillimanite is very similar below ~20 GPa, which helps to illustrate that the bulk modulus values are so comparable. [75]

4.2.2. Laser Raman Spectroscopy at High Pressures

Measuring the pressure dependence of the Raman vibrational modes gives information on bonding and crystal chemical properties. Raman spectra contain characteristic signatures of structural phase transitions, phase transitions involving subtle changes in symmetry of the crystal lattice and transitions to disordered and amorphous state. The mechanisms involved in the phase transitions and what happens to the structural building blocks can be inferred by analyzing of the features as Raman spectra evolve versus pressure. One of the most active areas in high pressure research in recent years has been pressure-induced amorphization, and in this field Raman spectroscopic studies have played an important role.

4.2.3. High-Pressure Raman Spectroscopy of Mullites and of Sillimanite

4.2.3.1. Predicting Vibrations using Group Theory

In Chapter 2 we obtained an expression for the intensity of Raman scattering, but that expression does not show whether the key terms, the α_{ij}'s are non-zero for a particular vibrational mode. Group theory allows to predict whether these terms can be non-zero, with information about the symmetry of a molecule (crystal). In each case *group theory* predicts whether a *transition moment integral* can be non-zero. These integrals contain the product of three terms – the wavefunctions for the ground and excited states, and the operator (in this case the components of the polarizability derivatives) that connects these two states. For a transition to occur the product of these three terms must be totally symmetric, which means it must leave the original molecule totally unchanged.

When a crystal is composed of single atoms at each lattice site in the crystal structure then all vibrations can be considered as EXTERNAL (or lattice) vibrations. For the case of EXTERNAL (or lattice) vibrations: we need to correlate only Site Group → Factor Group. When a crystal is composed of molecules or sub-units such as polyhedra at some lattice sites in the crystal structure then one needs to consider two types of vibrations:

- Vibrations within the polyhedron are INTERNAL vibrations (n)
- Vibrations of the polyhedron as a unit are EXTERNAL (or lattice) vibrations and are composed of:
    - Translatory (T') and
    - Rotatory (R') vibrations

In this case we need to predict external vibrations for the polyhedron by correlating:

Site Group → Factor Group

We also need to predict internal vibrations for the polyhedron by correlating:

Point Group → Site Group → Factor Group

This correlations needs to be executed for each atom that is on a different crystallographic Wyckoff site.

Sillimanite or Al_2O_3 - SiO_2 belongs to Space Group #62 – Pbnm – D_{2h}^{16} and has a Primitive unit cell (P) with Z=4. Sillimanite is built of:

- AlO_6 octahedra – which have a center of inversion so are optically inactive

- SiO_4 tetrahedra consisting of atoms Si1 O1, O3 and O4 (Table 2)
- AlO_4 tetrahedra and Al2, O2, O3, O4 (Table 2)

To predict vibrational modes we need to analyze the following units:

- The SiO_4 tetrahedron which involves Si1 O1, O3 and O4 and
- the remaining O2 atom and
- two aluminum atoms Al1 and Al2 which have different Wyckoff positions (Table 2).

Table 2. Atomic sites and atomic parameters for sillimanite.

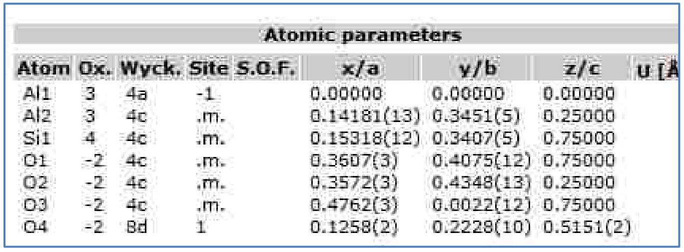

Atomic parameters								
Atom	Ox.	Wyck.	Site	S.O.F.	x/a	y/b	z/c	U [Å
Al1	3	4a	-1		0.00000	0.00000	0.00000	
Al2	3	4c	.m.		0.14181(13)	0.3451(5)	0.25000	
Si1	4	4c	.m.		0.15318(12)	0.3407(5)	0.75000	
O1	-2	4c	.m.		0.3607(3)	0.4075(12)	0.75000	
O2	-2	4c	.m.		0.3572(3)	0.4348(13)	0.25000	
O3	-2	4c	.m.		0.4762(3)	0.0022(12)	0.75000	
O4	-2	8d	1		0.1258(2)	0.2228(10)	0.5151(2)	

According to Wyckoff's Tables for determining proper site correlation (appendix 5 in Ferraro [44]) space group SG #62 (D_{2h}^{16}) only states that site c = $\sigma_{zx.}$ So it needs to be determined what site symmetry are the other Wyckoff sites in space group #62, D_{2h}^{16}. Wyckoff's nomenclature of site *i* can be deduced from the site symmetries of space group #62 by listing the site positions in alphabetical order (Appendix 4 in Ferraro [44]) as shown in Table 3 and Table 4. For the SiO_4 tetrahedron we need therefore to find internal vibrations (n) by correlating: Point Group → Site Group → Factor Group. For the SiO_4 polyhedron we also need to find External vibrations by correlating: Site Group → Factor Group. As part of External vibrations the tetrahedron will have both Translatory (T') and Rotatory (R') vibrations. For Al1, Al2 and O2 we only need to correlate: Site Group → Factor Group. These atoms will only have External vibrational modes. What is the expected number of vibrational modes for sillimanite? Sillimanite or $Si_1Al_2O_5$ has Z=4. The total number of vibrational modes expected is:

$$3nZ = 3x(1+2+5)x4 = 3x8x4 = \mathbf{96}$$

If the primitive cell contains σ molecules, each with ρ atoms: Z=4 so σ =4 SiO_4 molecules, with ρ =5 atoms.

Table 3. Site correlation for space group #62, D_{2h}^{16}

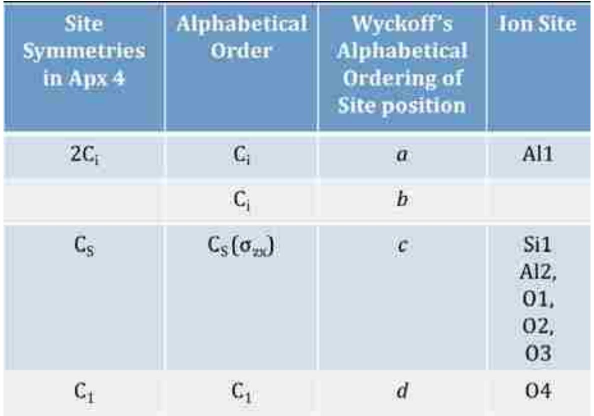

Site Symmetries in Apx 4	Alphabetical Order	Wyckoff's Alphabetical Ordering of Site position	Ion Site
$2C_i$	C_i	*a*	Al1
	C_i	*b*	
C_S	$C_S(\sigma_{zx})$	*c*	Si1 Al2, O1, O2, O3
C_1	C_1	*d*	O4

Table 4. Finding Factor Group, Site Group and Point Group Symmetries for Sillimanite

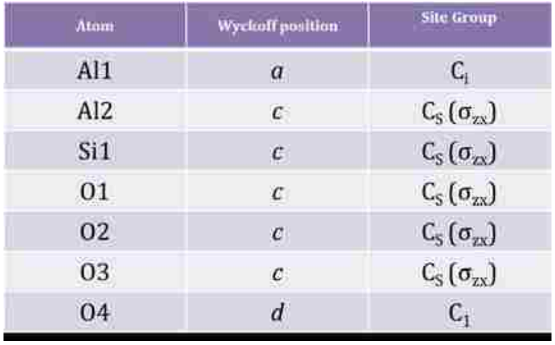

Atom	Wyckoff position	Site Group
Al1	*a*	C_i
Al2	*c*	$C_S(\sigma_{zx})$
Si1	*c*	$C_S(\sigma_{zx})$
O1	*c*	$C_S(\sigma_{zx})$
O2	*c*	$C_S(\sigma_{zx})$
O3	*c*	$C_S(\sigma_{zx})$
O4	*d*	C_1

The number of acoustic modes is **3.** Number of optical modes is 3σρ-3 = 3x4x5 – 3 = **57.** Optical modes are divided into:

- Internal modes = (3 ρ-6) σ = (3x5 – 6)x4 = **36**
- Eternal (Lattice) modes = 6 σ-3 = 6x4 – 3 = **21**

Al1 is on Wyckoff site 2*a*. According to Wyckoff's Tables for determining proper site correlation (appendix 5 in Ferraro [44]) SG #62 (D^{16}_{2h}) indicates that site *a* → = C_i. A calculation of degrees of freedom gives DOF = (3n, Z) = 3x1xZ = 3x1x4 = 12 DOF (Translatory only).

Table 5. Expected number of vibrational modes for sillimanite.

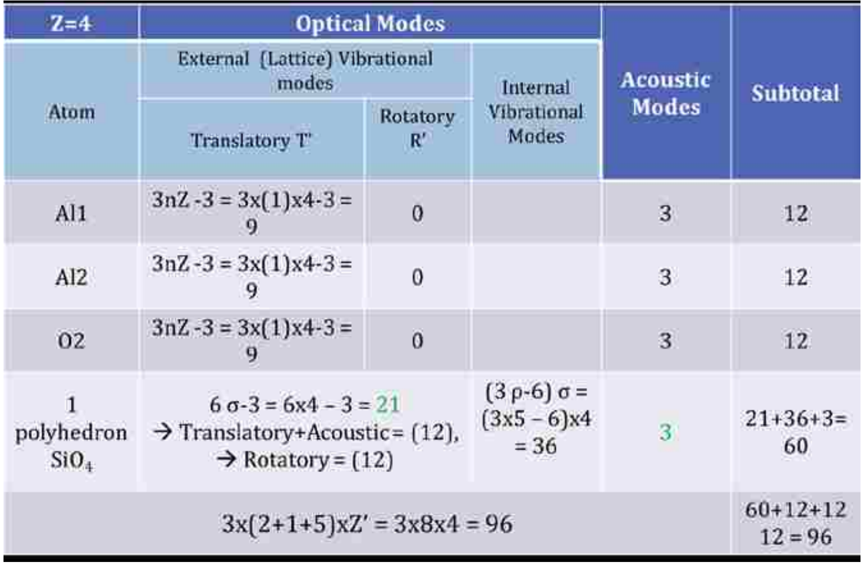

Z=4	Optical Modes			Acoustic Modes	Subtotal
Atom	External (Lattice) Vibrational modes		Internal Vibrational Modes		
	Translatory T'	Rotatory R'			
Al1	3nZ -3 = 3x(1)x4-3 = 9	0		3	12
Al2	3nZ -3 = 3x(1)x4-3 = 9	0		3	12
O2	3nZ -3 = 3x(1)x4-3 = 9	0		3	12
1 polyhedron SiO_4	6 σ-3 = 6x4 – 3 = 21 → Translatory+Acoustic= (12), → Rotatory = (12)		(3 ρ-6) σ = (3x5 – 6)x4 = 36	3	21+36+3= 60
3x(2+1+5)xZ' = 3x8x4 = 96					60+12+12 12 = 96

So we need to set up correlation table between the Factor Group (space group) 62 – D^{16}_{2h} and Site Group C_i (Table 6). The C_i site group has 2 characters, A_g and A_u. According to Character Tables of Point Groups A_u (Appendix 1 in [44]) possesses all three translation vectors, T_x, T_y and T_z while A_g has three rotational vectors only. Therefore all 12 DOFs go under Au, Table 6 (there are no site rotations for single atoms).

We fill out the correlation table between the Factor Group (D^i_{2h}) and Site Group $\mathbf{C_i}$ by consulting the Correlation Tables (Appendix 6 in [44]) under space group D^i_{2h}, which shows which species from C_i "correlate" (connect) to which species of D_{2h} (Table 7). Once the species under Factor Group are filled out, we note from Point Groups and their Character Tables (Appendix 1 in [44]), that B_{1u} has translation vector T_z, B_{2u} has T_y, and B_{3u} has T_x (Table 7). Now we need to distribute equally the DOFs from the left side (Site Group) to the right side (Factor group). All four species correlated to A_u get 12/4=3 DOFs. The species with a translatory vector get 1 acoustic and 2 translatory DOFs, while the species without a translatory vector get all 3 DOFs under the Translatory (T') modes.

Table 6. Filling out the Site Group → Factor Group Correlation Table for Al1 in sillimanite.

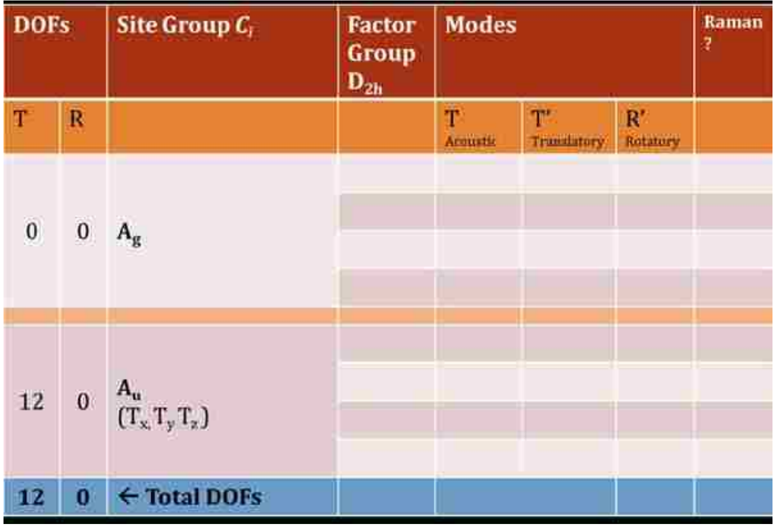

DOFs		Site Group C_i	Factor Group D_{2h}	Modes			Raman ?
T	R			T Acoustic	T' Translatory	R' Rotatory	
0	0	A_g					
12	0	A_u (T_x, T_y, T_z)					
12	**0**	**← Total DOFs**					

Table 7. Site Group → Factor Group Correlation Table for Al1 in sillimanite.

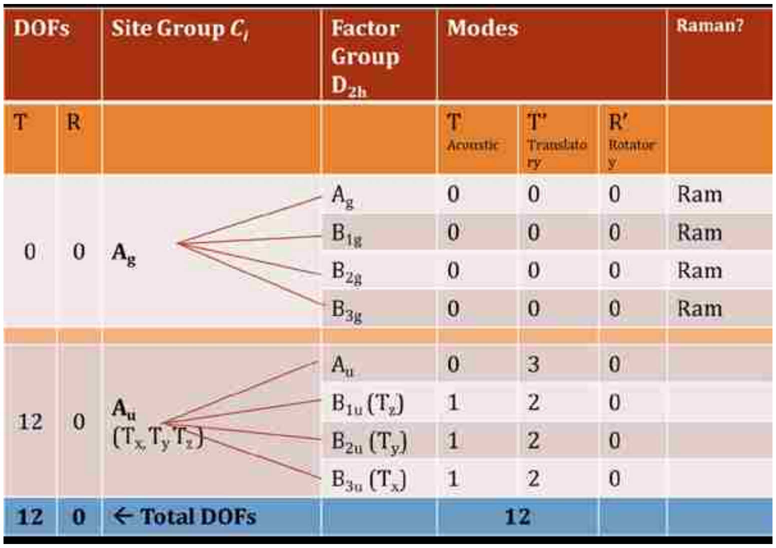

DOFs		Site Group C_i	Factor Group D_{2h}	Modes			Raman?
T	R			T Acoustic	T' Translatory	R' Rotatory	
0	0	A_g	A_g	0	0	0	Ram
			B_{1g}	0	0	0	Ram
			B_{2g}	0	0	0	Ram
			B_{3g}	0	0	0	Ram
12	0	A_u (T_x, T_y, T_z)	A_u	0	3	0	
			B_{1u} (T_z)	1	2	0	
			B_{2u} (T_y)	1	2	0	
			B_{3u} (T_x)	1	2	0	
12	**0**	**← Total DOFs**		**12**			

There were no Rotatory (R') DOFs on the left under Site Group and hence zero R' in the Factor Group. Raman activity (none in this case) can be read from the Point Groups and their Character Tables (Appendix 1 in [44]).

Now this procedure is repeated for the other atoms/molecules/sites.

Table 8. Site Group → Factor Group Correlation Table for Al2

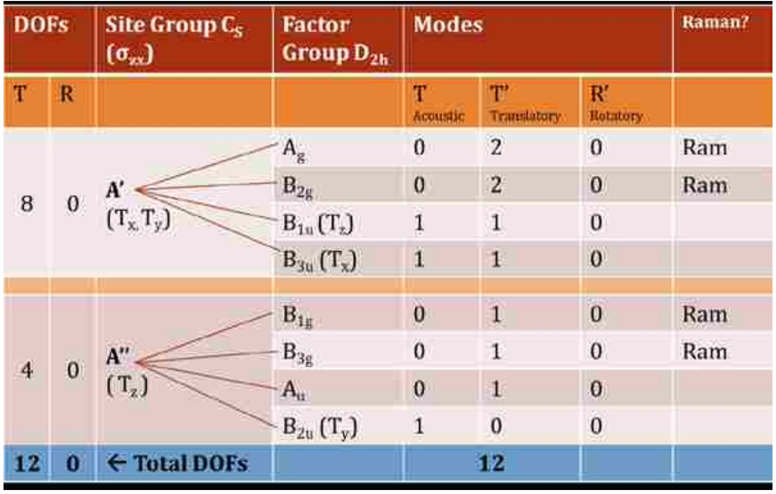

DOFs		Site Group C_S (σ_{zx})	Factor Group D_{2h}	Modes			Raman?
T	R			T Acoustic	T' Translatory	R' Rotatory	
8	0	A' (T_x, T_y)	A_g	0	2	0	Ram
			B_{2g}	0	2	0	Ram
			B_{1u} (T_z)	1	1	0	
			B_{3u} (T_x)	1	1	0	
4	0	A'' (T_z)	B_{1g}	0	1	0	Ram
			B_{3g}	0	1	0	Ram
			A_u	0	1	0	
			B_{2u} (T_y)	1	0	0	
12	0	← Total DOFs			12		

Table 9. Factor Group Correlation Table for O2

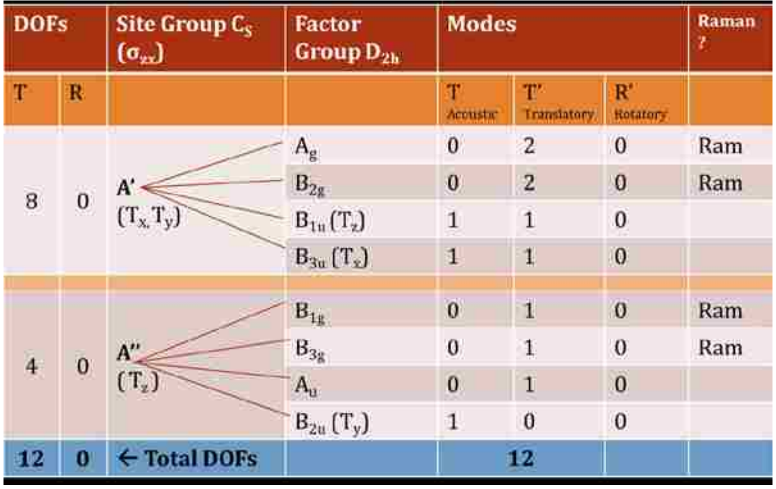

DOFs		Site Group C_S (σ_{zx})	Factor Group D_{2h}	Modes			Raman ?
T	R			T Acoustic	T' Translatory	R' Rotatory	
8	0	A' (T_x, T_y)	A_g	0	2	0	Ram
			B_{2g}	0	2	0	Ram
			B_{1u} (T_z)	1	1	0	
			B_{3u} (T_x)	1	1	0	
4	0	A'' (T_z)	B_{1g}	0	1	0	Ram
			B_{3g}	0	1	0	Ram
			A_u	0	1	0	
			B_{2u} (T_y)	1	0	0	
12	0	← Total DOFs			12		

Next, we need to find out the species and their number of normal vibrations for the SiO_4 tetrahedron, which is on the molecular Point Group T_d. (Appendix 2 in [44]). The number of vibrations is calculating knowing that:

- m = 0 = # of sets of nuclei not on any symmetry elements.
- m_0 = 1 = # of sets of nuclei on all symmetry elements.
- m_d = 0 = # of sets of nuclei on σ_d plane but not on any other element of symmetry.

- m_2 = 0 = # of sets of nuclei on a C_2 axis but not on any other symmetry element that does not wholly coincide with that axis.
- m_3 = 1 = # of sets of nuclei on a C_3 axis but not on any other symmetry element that does not wholly coincide with that axis.

Table 10. Correlation Table for SiO_4 Tetrahedron – Internal Modes.

Molec Point Grp	Total # of Atoms	Species	Number of Vibrations	Number of Vibrational species of GaO_4
T_d	$24_m + 12m_d + 6m_2 + 4m_3 + m_0 = 4x1 + 1 = 5$	A_1	$3m + 2m_d + m_2 + m_3 = 1$	1 A_1
		A_2	$3m + m_d = 0$	–
		$E_{(\text{doubly degenerate})}$	$6m + 3m_d + m_2 + m_3 = 1$	1 E
		$F_{1\ (\text{triply degenerate})}$	$9m + 4m_d + 2m_2 + m_3 - 1 = 1 - 1 = 0$	–
		$F_{2(\text{triply degenerate})}$	$9m + 5m_d + 3m_2 + 2m_3 + m_0 - 1 = 2x1 + 1 - 1 = 2$	2 F_2

We then set up a correlation table between the Molecular Point Group T_d and Site Group C_s and Factor Group (62) D_{2h}^{16}. The molecular point group column gets the vibrational species found in Table 10. Translation and rotation vectors are obtained from the Point Groups and their Character Tables (Appendix 1 in [44]). The SiO_4 tetrahedron is on Wyckoff site *c* so its Site Group is C_s. The C_s site group has 2 characters A' and A'' and these go under the Site Group column. The correlation between Site Group C_s and Point Group T_d is obtained from the Correlation Tables (Appendix 6 in [44]). Under Site group we count the number of lines connecting to each species and also include the number in front of a given molecular point group: this is how species A' has 4 lines but two of those count as 2 each so we get 1+1+2+2=6 A'. The D_{2h}^{16} Factor Group has 8 characters: A_g, A_u, B_{1g}, B_{2g}, B_{3g}, B_{1u}, B_{2u}, B_{3u} and these go under the Factor Group column (Appendix 1 in [44]). We then correlate the D_{2h}^{16} Factor Group with the Site Group C_s. The SiO_4 tetrahedron has 36 internal modes (Table 5) and 2/3 of them are correlated to species A' while 1/3 is correlated to A'

Table 11. Correlation table for internal modes of SiO_4 tetrahedron.

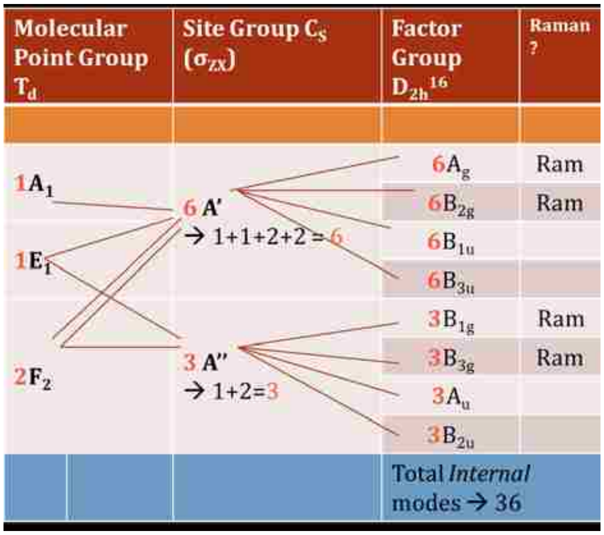

Molecular Point Group T_d	Site Group C_S (σ_{ZX})	Factor Group D_{2h}^{16}	Raman ?
$1A_1$	$6A'$ $\rightarrow 1+1+2+2=6$	$6A_g$	Ram
		$6B_{2g}$	Ram
$1E_1$		$6B_{1u}$	
		$6B_{3u}$	
	$3A''$ $\rightarrow 1+2=3$	$3B_{1g}$	Ram
$2F_2$		$3B_{3g}$	Ram
		$3A_u$	
		$3B_{2u}$	
		Total *Internal* modes → 36	

Table 12. Correlation table for external modes of SiO_4 tetrahedron.

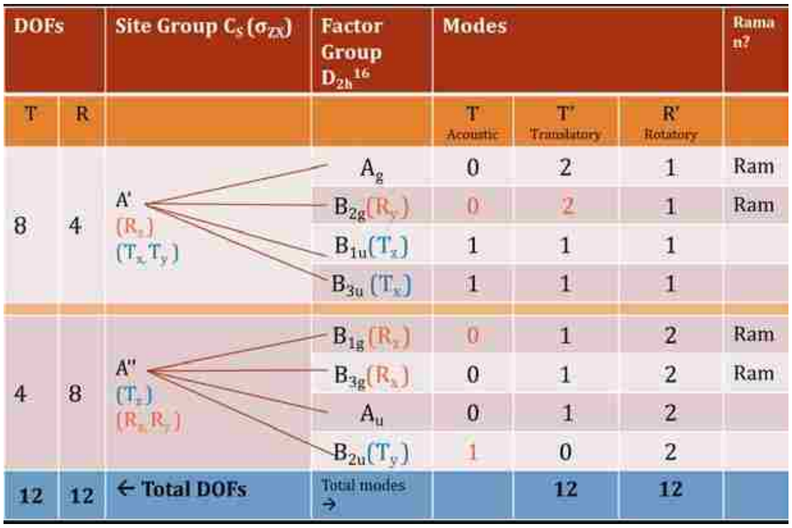

DOFs		Site Group C_S (σ_{ZX})	Factor Group D_{2h}^{16}	Modes			Raman?
T	R			T Acoustic	T' Translatory	R' Rotatory	
8	4	A' (R_z) ($T_x T_y$)	A_g	0	2	1	Ram
			$B_{2g}(R_y)$	0	2	1	Ram
			$B_{1u}(T_z)$	1	1	1	
			$B_{3u}(T_x)$	1	1	1	
4	8	A'' (T_z) ($R_x R_y$)	$B_{1g}(R_z)$	0	1	2	Ram
			$B_{3g}(R_x)$	0	1	2	Ram
			A_u	0	1	2	
			$B_{2u}(T_y)$	1	0	2	
12	12	← Total DOFs	Total modes →		12	12	

Finally for the external vibrational modes of SiO_4 we set up a correlation table between the Factor Group (space group 62) D_{2h}^{16} and Site Group C_s. From Table 5 we know that there are 24 DOFs, 12 are translatory + acoustic and 12 are rotatory. The C_s site group has 2 characters A' and A'' and these go under the Site Group column. A' possesses two translation vectors, T_x and T_y and rotation R_z while A'' has vector T_z and rotation R_x and R_y. For translatory DOFs: put ⅔ under A' (=8) and ⅓ under A'' (=4). For rotatory DOFs: put ⅓ under A' (=4) and ⅔ under A'' (=8). We then correlate The correlation between Site Group

C_s and Factor Group D_{2h} is obtained from the Correlation Tables (Appendix 6 in [44]). Now we distribute equally the DOFs from the Site Group to the Factor group.

Table 13. Complete Character Table and Correlation Scheme

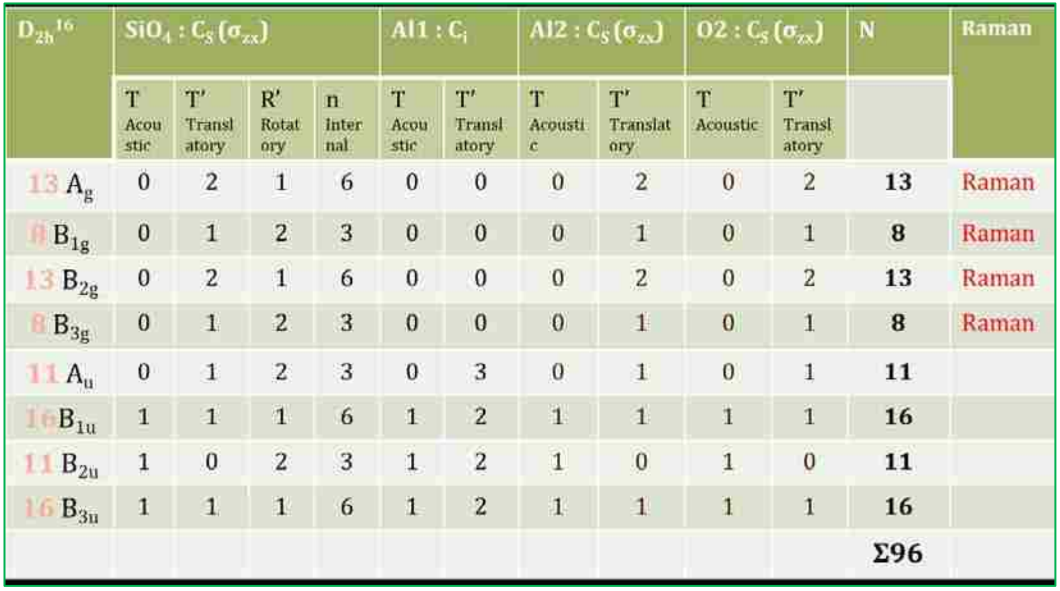

D_{2h}^{16}	$SiO_4 : C_S (\sigma_{zx})$				Al1 : C_i		Al2 : $C_S (\sigma_{zx})$		O2 : $C_S (\sigma_{zx})$		N	Raman
	T Acoustic	T' Translatory	R' Rotatory	n Internal	T Acoustic	T' Translatory	T Acoustic	T' Translatory	T Acoustic	T' Translatory		
13 A_g	0	2	1	6	0	0	0	2	0	2	**13**	Raman
8 B_{1g}	0	1	2	3	0	0	0	1	0	1	**8**	Raman
13 B_{2g}	0	2	1	6	0	0	0	2	0	2	**13**	Raman
8 B_{3g}	0	1	2	3	0	0	0	1	0	1	**8**	Raman
11 A_u	0	1	2	3	0	3	0	1	0	1	**11**	
16 B_{1u}	1	1	1	6	1	2	1	1	1	1	**16**	
11 B_{2u}	1	0	2	3	1	2	1	0	1	0	**11**	
16 B_{3u}	1	1	1	6	1	2	1	1	1	1	**16**	
											Σ96	

In summary the irreducible representations corresponding to the sillimanite lattice are derived from the character table, under the assumption that all vibrations can be separated into internal modes of SiO_4-tetrahedra and external modes in which these tetrahedra act as rigid molecules. The set of irreducible representations corresponding to the lattice of sillimanite is:

$\Gamma = 13A_g + 8B_{1g} + 13B_{2g} + 8B_{3g} + 11A_u + 16B_{1u} + 11B_{2u} + 16B_{3u}$

including the acoustic modes

$\Gamma_{acoust.} = B_{1u} + B_{2u} + B_{3u}$

Therefore, there are 42 Raman active modes ($13A_g + 8B_{1g} + 13B_{2g} + 8B_{3g}$) and 40 infrared active modes ($15B_{1u} + 10B_{2u} + 15B_{3u}$) for sillimanite. This is in agreement with the correlation scheme shown by Salje and Werneke. [118]

By following the same procedure we derive the irreducible representations corresponding to the mullite lattice but assuming an 'ideal' mullite without vacancies (x=0):

$\Gamma = 6A_g + 6B_{1g} + 3B_{2g} + 3B_{3g} + 5A_u + 5B_{1u} + 10B_{2u} + 10B_{3u}$

including the acoustic modes:

$\Gamma_{acoust.} = B_{1u} + B_{2u} + B_{3u}$

There are 18 Raman active modes ($6A_g + 6B_{1g} + 3B_{2g} + 3B_{3g}$) and 22 infrared active modes ($4B_{1u} + 9B_{2u} + 9B_{3u}$) for mullite.

Four different modes of vibration occur in free SiO_4 according to the point group T_d: ν_1(A_1-type), ν_2 (E_1-type), ν_3 and ν_4 (T_2-type).

4.2.3.2. Raman Spectra at High Pressures

It is interesting to note that in the present work Raman spectroscopy was used to spotlight the local disorder of 2:1 mullite: in fact Raman spectra of mullite contrast starkly with those of the ordered sillimanite structure.

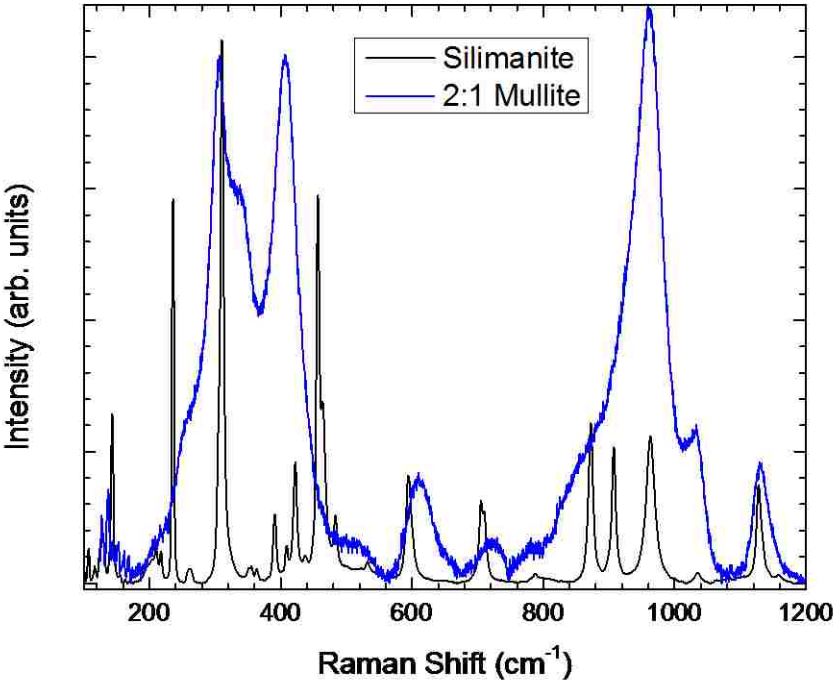

Figure 31. Comparison of Raman spectra of 2:1 mullite and sillimanite at ambient pressure.

The key differences between the structure of mullite and sillimanite are the oxygen vacancies as well as the disorder in the tetrahedral sites. On the level of "long range order" both materials present crystalline x-ray diffraction patterns where the above mentioned differences cannot be perceived. On the other hand when looking at a comparison of Raman spectra of sillimanite and 2:1 mullite (Figure 31) the large structural differences are very readily apparent.

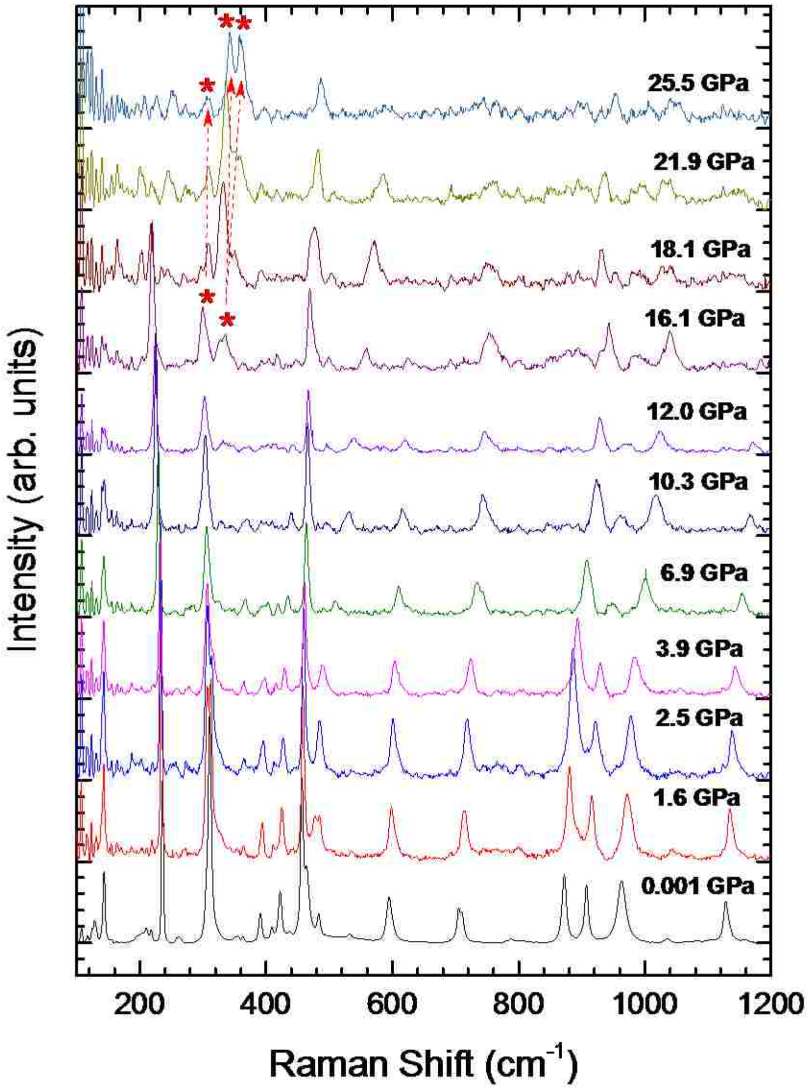

Figure 32. Pressure-driven evolution of Raman spectra of sillimanite measured in the DAC. Stars mark new vibrations.

Sillimanite has a set of very narrow vibrations and 2:1 mullite has instead several wide and overlapping bands, illustrating that the "short range order" of these materials is indeed very different. Many strong peaks of sillimanite can be identified as bands in mullite, some of them shifted by a few wavenumbers and some having very different intensities.

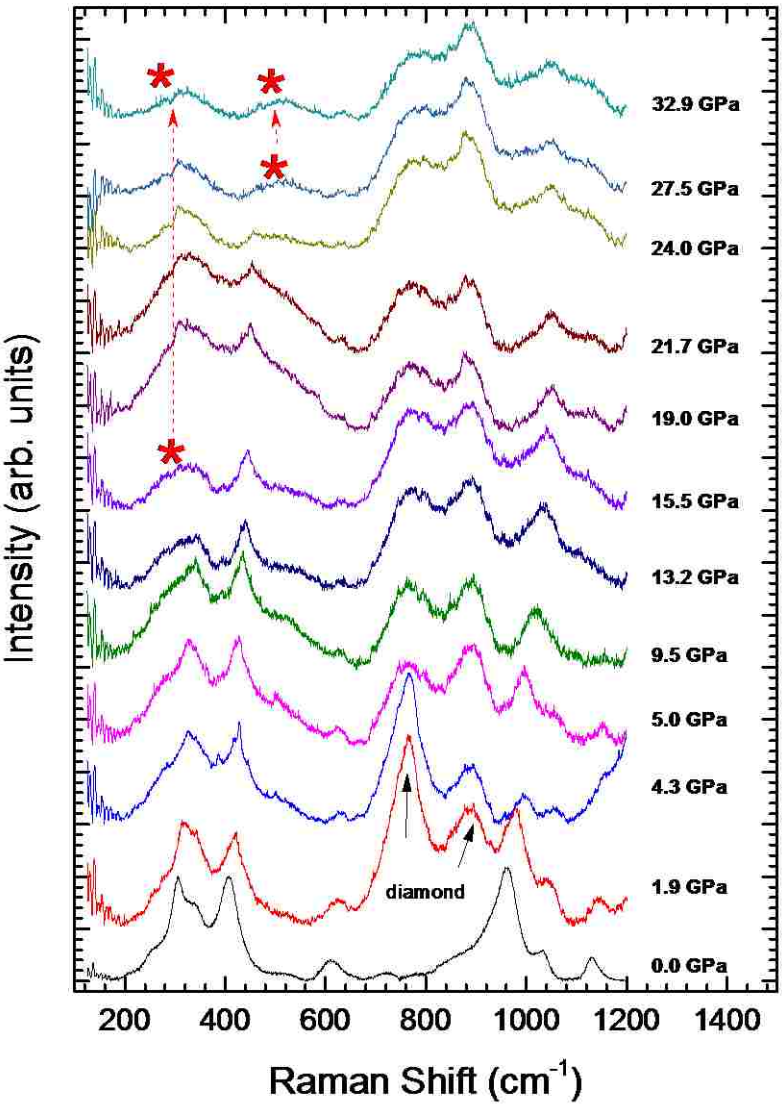

Figure 33. Pressure-driven evolution of Raman spectra of 2:1 mullite measured in the DAC. Stars mark suspected new peaks.

Figure 32 presents the Raman spectra of sillimanite as a function of pressure from ambient condition to 25.5 GPa. At ambient pressure 28 Raman bands are observed, out of the 42 predicted ones. Figure 33 presents the Raman spectra of 2:1 mullite acquired as a function of pressure from ambient conditions up to 32.9 GPa. 12 Raman bands are observed out of the 18 predicted ones. To the best of the author's knowledge a high-pressure Raman spectroscopy investigation of alumino-silicate mullite has not been published before.

A Raman spectroscopy study of sillimanite examining the effect of pressure on compression up to 15 GPa was discussed by Mernagh and Liu. [119] It was reported that 11 Raman bands were observed, but no spectra of sillimanite as a function were published in that work. [119] No phase changes were observed.

Peak broadening in sillimanite and the shift of bands towards broad features in 2:1 mullite reveal the progress of amorphization in the two samples. The Raman spectroscopy results coincide with the results of in situ high pressure X-ray diffraction studies. In amorphization, the sharp X-ray diffraction lines disappear.

On release of pressure, the amorphized phase is metastably retained down to ambient pressure, reverting gradually to a highly disordered, parent-like phase (see Chapter on results of XRD).

4.2.3.3. Mode Grüneisen Parameters

The Grüneisen parameter, γ, named after Eduard Grüneisen, describes the effect that changing the volume of a crystal lattice has on its vibrational properties, and, as a consequence, the effect that changing temperature has on the size or dynamics of the lattice. The term is usually reserved to describe the single thermodynamic property γ, which is a weighted average of the many separate parameters γ_i entering the original Grüneisen's formulation in terms of the phonon nonlinearities.

The Debye model estimates the contribution of phonons to specific heat.[54] Thermal expansion (coefficient α) is proportional to specific heat and the proportionality is the average Grüneisen constant γ_{AV}:

$$\alpha = \frac{\gamma_{AV} C_V}{3 V_M K_0}$$

where V_M is the molar volume, K_0 is the bulk modulus, and C_V is the molar specific heat at constant volume and may be written as:

$$C_V = \sum_i \frac{p_i C_i}{4}$$

The mode Grüneisen parameter is the logarithmic derivative of vibrational frequency over volume:

[redacted]

A value of $\gamma_i = 1$ means that there is a 1% change in frequency over a 1% change in volume. The typical values of γ_i are 0.5 – 2. If we transform the equation for gamma to a pressure derivative we obtain:

[redacted]

Measurements of Raman spectroscopy at high pressures allows to obtain mode Grüneisen parameters for each vibration: it is the relative change in vibrational frequency over the change in pressure multiplied by the bulk modulus (which is obtained in this work from analysis of high-pressure x-ray diffraction).

Raman modes for sillimanite (experimental and theoretical) and 2:1 mullite (experimental) are shown in Table 14 along with the experimental and calculated mode Grüneisen parameters for sillimanite as well as the experimental ones for 2:1 mullite. Also indicated are the mode type and symmetry for all modes of sillimanite. The correspondence between calculated and experimental mode Grüneisen parameters is good, with a few exceptions.

Table 14. Raman modes and Grüneisen parameters for 2:1 mullite and sillimanite below 350cm^{-1}. Experimentally obtained Raman modes for sillimanite (experimental and theoretical) and 2:1 mullite (experimental) as well as their mode Grüneisen parameters. Raman modes marked with * appear at higher pressures, so for those the ν_i value is derived from an extrapolation to ambient pressure. Theoretical values are issued from calculations carried out by Prof. D. Többens, Helmholtz Zentrum Berlin (private communication). Also included are the type and symmetry of each mode: b=bending, s=stretching, o=other; (o)=octahedra, (t)=tetrahedra.

Sillimanite – this work – K_0 = 167(7)GPa								**2:1 Mullite – this work – K_0=162(7)GPa**		
Irreducible Representation and Assignment		**Theoretical**			**Experimental**			**Experimental**		
		ν_i (cm^{-1})	**$d\nu_i$/dP**	**γ_i**	**ν_i (cm^{-1})**	**$d\nu_i$/dP**	**γ_i**	**ν_i (cm^{-1})**	**$d\nu_i$/dP**	**γ_i**
A_g	b(Al(o)-O-Si) b(O-Al(o)-O) b(O-Si-O)	139.251	0.40	0.48	143(1)	0.17	0.20(1)	-	-	-
B_{1g}	b(Al(o)-O-Si) b(O-Al(o)-O)	155.854	-1.03	-1.1	-	-		-	-	-
B_{1g}	b(O-Al(o)-O)	186.067			-	-		-	-	-
B_{3g}	o(O-Al(o)-O) o(O-Si-O)	208.603	0.33	0.26	-	-		-	-	-
B_{2g}	o(O-Al(o)-O)	216.113			-	-		-	-	-
A_g	b(O-Al(o)-O)	234.65	-0.86	-0.61	236(1)	-0.99	-0.70(5)	-	-	-
B_{3g}	o(O-Al(o)-O)	249.626			-	-		-	-	-
B_{1g}	b(O-Al(t)-O)	259.257	0.31	0.20	*262 (5)	0.41	0.26(2)	257.0(50)	0.56	0.35
B_{2g}	o(O-Al(o)-O) o(O-Si-O)	260.361			-	-		-	-	-
A_g	o(O-Al(t)-O) b(O-Si-O)	301.857	-0.62	-0.34	-	-		-	-	-
A_g	b(Al(o)-O-Si) b(O-Al(o)-O)	309.786	0.81	0.44	311(2)	0.52	0.28(2)	-	-	-
B_{1g}	b(Al(o)-O-Si) b(O-Al(o)-O)	310.179	-0.51	-0.27	309(1)	-0.59	-0.32(2)	-	-	-
-	-	-	-	-	-	-		-	-	-
-	-	-	-	-	*303 (2)	1.55	0.85(6)	-	-	-
-	-	-	-	-	*303 (5)	2.28	1.30(8)	307(2)	2.0	1.1
-	-	-	-	-	309*(5)	0.11	0.06(1)	*313 (5)	-0.15	-0.078
-	-	-	-	-	-	-	-	333(5)	3.67	1.8

Table 15. Raman modes and Grüneisen parameters for 2:1 mullite and sillimanite above 350cm^{-1}. Experimentally obtained Raman modes for sillimanite (experimental and theoretical) and 2:1 mullite (experimental) as well as their mode Grüneisen parameters. Raman modes marked with * appear at higher pressures, so for those the ν_i value is derived from an extrapolation to ambient pressure. Theoretical values are issued from calculations carried out by Prof. D. Többens, Helmholtz Zentrum Berlin (private communication). Also included are the type and symmetry of each mode: b=bending, s=stretching, o=other; (o)=octahedra, (t)=tetrahedra.

Sillimanite – this work – K_0 = 167(7)GPa								**2:1 Mullite – this work – K_0=162(7)GPa**		
Irreducible Representation and Assignment		**Theoretical**			**Experimental**			**Experimental**		
		ν_i (cm^{-1})	**$d\nu_i$/ dP**	**γ_i**	**ν_i (cm^{-1})**	**$d\nu_i/dP$**	**γ_i**	**ν_i (cm^{-1})**	**$d\nu_i/dP$**	**γ_i**
B_{3g}	o(O-Al(t)-O) b(O-Al(o)-O) b(O-Si-O)	350.692	1.78	0.85	-	-	-	-	-	-
A_g	b(O-Al(t)-O) b(O-Al(o)-O)	354.529	1.34	0.63	-	-	-	-	-	-
B_{2g}	o(O-Al(t)-O) b(O-Al(o)-O) b(O-Si-O)	381.059	0.64	0.28	364(1)	0.4	0.18(1)	-	-	-
B_{1g}	b(O-Al(o)-O)	387.469	1.73	0.75	391(1)	1.78	0.76(5)	*384.2 (10)	0.72	0.30
A_g	b(O-Al(t)-O) b(O-Si-O)	406.23	1.47	0.60	409(1)	1.34	0.55(4)	*412.2 (30)	1.23	0.48
B_{1g}	b(O-Al(t)-O)	417.411	1.64	0.66	422(1)	1.68	0.66(4)	411(2)	1.69	0.67
B_{2g}	s(O-Al(t)-Al(t)) s(Al(o)-O-Al(t)) b(Si-O-Al(t))	437.331	-	-	-	-	-	-	-	-
B_{3g}	s(O-Al(t)-Al(t)) s(Al(o)-O-Al(t)) b(Si-O-Al(t))	444.704	-	-	-	-	-	-	-	-
A_g	b(Si-O-Al(o)) b(O-Si-O)	445.774	0.66	0.25	457(1)	0.93	0.34(2)	-	-	-
B_{1g}	b(Si-O-Al(o)) b(O-Si-O)	447.883	1.15	0.43	464(1)	0.87	0.31(2)	-	-	-
B_{3g}	s(O-Al(t)-Al(t)) o(O-Si-O)	479.461	1.06	0.032	483(1)	1.26	0.44(3)	-	-	-
-	-	-	-	-	-	-	-	*515 (1)	0.04	0.013
B_{2g}	s(O-Al(t)-Al(t))	529.346	-	-	-	-	-	-	-	-
A_g	b(O-Al(o)-O) b(O-Si-O)	592.75	1.81	0.51	594(1)	1.96	0.55(4)	-	-	-
B_{2g}	s(O-Al(t)) s(Al(o)-O-Al(t)) b(Si-O-Al(t)) b(O-Si-O)	601.77	3.12	0.87	*600(1)	3.44	0.96(6)	612(5)	0.86	0.23
B_{3g}	b(Al(o)-O-Al(t)) b(Si-O-Al(t))	647.001	-	-	-	-	-	-	-	-
B_{1g}	b(O-Al(o)-O) b(O-Si-O)	648.36	-	-	-	-	-	-	-	-
B_{3g}	s(O-Al(o))	688.511	-	-	-	-	-	-	-	-
B_{2g}	b(Al(o)-O-Al(t)) s(O-Al(o))	706.297	4.16	0.98	705(1)	3.74	0.89(6)	-	-	-
A_g	s(O-Al(o)-O)	710.859	3.17	0.74	710(1)	3.87	0.91(6)	720(2)	-	-
B_{1g}	s(O-Al(o)-O)	773.62	-	-	-	-	-	-	-	-
B_{1g}	s(O-Al(o))	780.399	-	-	-	-	-	-	-	-
A_g	s(O-Al(o))	788.799	-	-	-	-	-	-	-	-
A_g	s(O-Si)	874.665	3.27	0.62	872(1)	3.02	0.58(4)	-	-	-
B_{3g}	s(O-Si)	903.423	5.25	0.97	907(1)	4.95	0.91(6)	-	-	-
B_{1g}	s(O-Si-O)	910.971	-	-	-	-	-	-	-	-
B_{2g}	s(O-Si)	913.75	-	-	-	-	-	-	-	-
A_g	s(O-Si)	957.902	4.19	0.73	963(1)	4.32	0.75(5)	962(2)	4.53	0.76
B_{1g}	s(O-Si)	1035.69	4.89	0.79	1035(1)	4.57	0.74(5)	1034(5)	4.39	0.69
A_g	s(O-Si)	1130.15	3.37	0.50	1128(2)	3.45	0.51(3)	1131(2)	2.55	0.37
B_{1g}	s(O-Si)	1136.31	3.39	0.50	*1137 (3)	3.26	0.48(3)	-	-	-

4.2.3.4. Comparison of Pressure Evolution.

To focus the analysis, it was decided to follow the pressure-induced evolution of selected, strong Raman modes of sillimanite and compare them with all bands of 2:1 mullite.

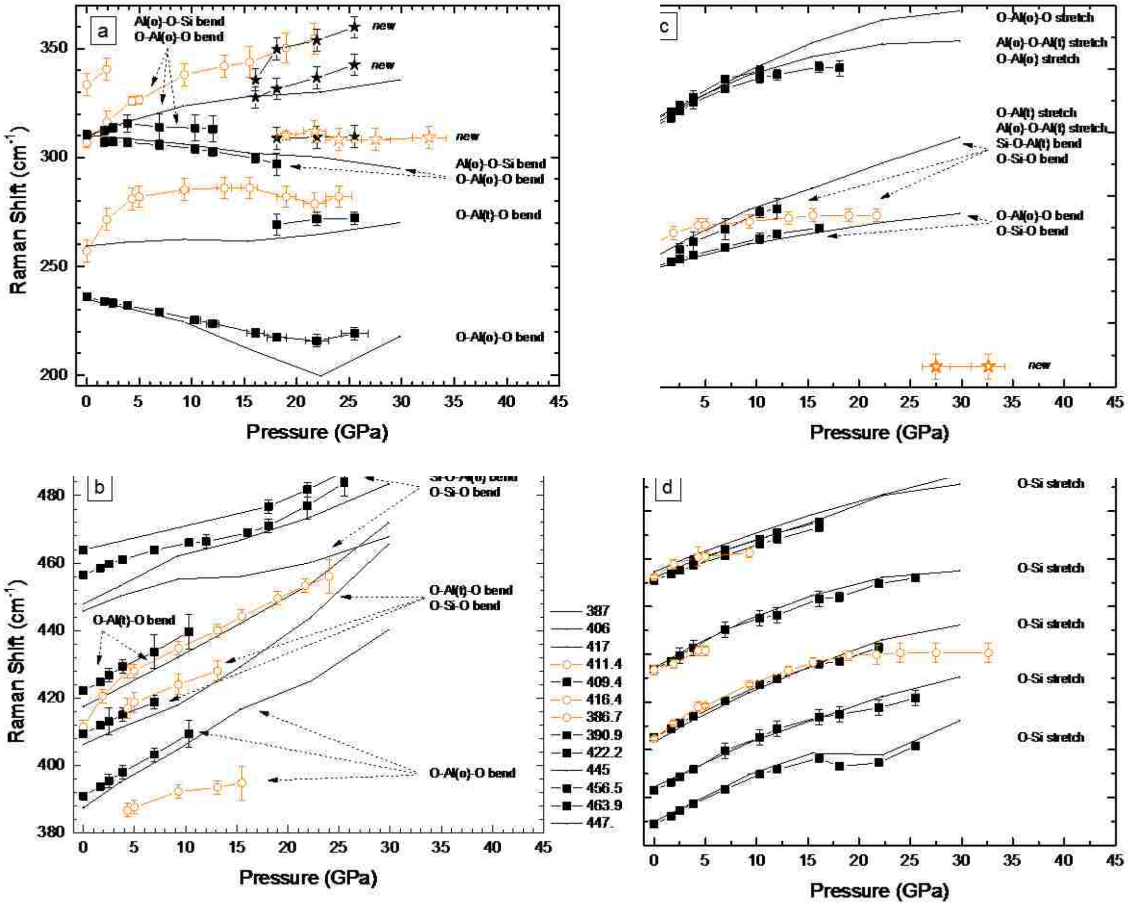

Figure 34. Pressure-evolution of experimental vibrational modes of 2:1 mullite and sillimanite.
Comparison of pressure-evolution of experimental vibrational modes of 2:1 mullite (orange) and those of sillimanite (black). Continuous lines (no symbols) represent calculated sillimanite, full squares represent experimental sillimanite and open circles represent experimentally measured 2:1 mullite. Stars mark new vibrations of 2:1 mullite (orange) and sillimanite (black) found experimentally. Numbers in the legend correspond to a given peak's position at lowest pressure in which it appears.

The shift of Raman peak positions (vibrational frequencies) vs. pressure for experimental data of 2:1 mullite is illustrated together with experimental and calculated data of sillimanite in Figure 34. Some trends can be identified. In sillimanite all vibrations above 850cm^{-1}, which corresponds to pure stretching modes of SiO_4 tetrahedra agree very well with calculations (Figure 34d). When experimental vibrations of 2:1 mullite are superimposed on those of sillimanite the agreement is very good (Figure 34d), with the exception of the vibration at 256cm^{-1}. Finally, 2:1 mullite does not present any strong vibrations below 250cm^{-1} (Figure 34a).

Vibrations in sillimanite are sharp and narrow, but in 2:1 mullite they correspond to wide bands. So vibrations which are localized in ordered sillimanite are much more spread in 2:1 mullite, due to both site disorder and oxygen vacancies.

Within the crystal lattice of both 2:1 mullite and sillimanite, the vibrations around 700-800 cm^{-1} are attributed to internal motions of AlO_4 (O-Al stretching modes,) and those above 800 cm^{-1} are attributed to SiO_4 and tetrahedra (O-Si stretching). These modes show a large pressure dependence of over 3cm^{-1}/GPa. This was also observed for sillimanite by Mernagh and Liu. [119] When considering the crystal structure of sillimanite the AlO_6 octahedral chains are linked by double chains of corner-sharing MO_4 tetrahedra (also parallel **c**), with an ordered distribution of the tetrahedral cations Al^{3+} and Si^{4+}. In this configuration there are open tunnels running along the c-axis. With increasing pressure, such open tunnels permit minor rotations of the tetrahedral chains to occur, which leads to a general increase in energy of the tetrahedral vibrations. The Raman modes above 700cm^{-1} are also in excellent agreement with their calculated pressure evolution over the entire pressure range, which implies that tetrahedral vibrations are well isolated form the rest of the lattice. On the other hand all other vibrations (below 700 cm^{-1}) present some degree of variation from their calculated counterparts, implying that that they are much less isolated and the whole lattice has a greater influence on their high-pressure behavior.

In a few instances, an increase in pressure makes vibrations more localized, and decouples them. For example, where theoretically calculated sillimanite presents two vibrations (ex. 592cm^{-1} and 601cm^{-1}), for experimental sillimanite only one corresponding peak can be identified (594 cm^{-1}). However above 2.5 GPa a second peak appears as a shoulder (at 608cm^{-1}). This is also seen for the sillimanite peak at 1127cm^{-1} (one experimentally measured peak but two calculated vibrations), which splits into two at 4GPa and above. The same behavior is observed in the corresponding peak of mullite (ex: peak at 611cm^{-1} and shoulder appearing above 4GPa at 636cm^{-1}; or the peak at 406cm and two shoulders appearing above 4GPa).

The vibrational mode at 483cm^{-1} was attributed to the free SiO_4 ion due to its very high Grüneisen parameter value (1.93). In this work however it is found the 483^{-1} mode has a small Grüneisen parameter (0.44) and can be attributed to both a vibrational mode of O-Si-O and to a stretching mode of the aluminum tetrahedra O-Al(t)-Al(t).

Vibrations with lower mode-Grüneisen parameters are indicative of more ionic bonding and may correspond to vibrations of the aluminate tetrahedra. However there is only one instance of isolated aluminate tetrahedra vibration: bending of O-Al(t)-O at 262cm^{-1} with a Grüneisen parameter of 0.2.

The low wavenumber modes show very little pressure dependence, and a couple even have a negative slope. Vibrations with negative mode Grüneisen parameters (235cm^{-1} and 309cm^{-1}) indicate lengthening of bonds and involve the aluminate octahedra, in the form of intra-octahedral bending or inter-polyhedral bending with SiO_4 tetrahedra. The low wavenumber modes are mostly rotational or translational lattice modes and are strongly mixed as indicated in Table 14. As pressure is increased, they are not very influenced by the rotation of the tetrahedral chains and the corresponding decrease in cell volume. In both sillimanite and 2:1 mullite, starting from ~15 GPa we also observe the appearance of new vibrational bands between 300 and 350 cm^{-1}. In sillimanite there are 3 rather sharp peaks, while in mullite there is one band around 310 cm^{-1}, which coincides very well with the position of the sharp feature in sillimanite (Figure 34 (a)) as well as another broad band

~510 cm^{-1}. These new features persist up to the highest pressure of the experiment in both materials. New vibrational modes could point towards the beginning of a phase transition as was proposed by Oganov et al. [15]

Table 16. Correspondence of sillimanite and mullite Raman modes and Grüneisen parameters.
This Table is limited to the correspondence between modes of sillimanite (experimental and theoretical) and 2:1 mullite (experimental) found in Figure 34. Vibrations marked with * appear at higher pressures so ν_i is derived from an extrapolation to ambient pressure. Theoretical values are issued from calculations carried out by D. Többens, Helmholtz Zentrum Berlin (private communication). Also shown are Raman modes obtained by Mernagh and Liu,[119] in a study of sillimanite only, on compression up to 15 GPa.

Sillimanite – this work – K_0 = 167(7)GPa				2:1 Mullite – this work – K_0=162(7)GPa		Sillimanite – Mernagh&Liu [119]	
Theoretical		**Experimental**		**Experimental**			
ν_i (cm^{-1})	γ_i	ν_i (cm^{-1})	γ_i	ν_i (cm^{-1})	γ_i	ν_i (cm^{-1})	γ_i
139.251	0.48	143.4(10)	0.20(1)	-	-	143	0.023(2)
234.65	-0.61	235.9(10)	-0.70(5)	-	-	236	-0.92(9)
259.257	0.20	262.1 * (50)	0.26(2)	257.0(50)	0.35	-	-
309.786	0.44	310.6(20)	0.28(2)	-	-	311	-0.48(5)
310.179	-0.27	309.0(10)	-0.32(2)	-	-	-	-
-	-	302.9*(20)	0.85(6)	-	-	-	-
-	-	303.3*(50)	1.30(8)	306.7(20)	1.1	-	-
-	-	306.8*(50)	0.06(1)	313.2*(50)	-0.078	-	-
387.469	0.75	391.0(10)	0.76(5)	384.2*(10)	0.30	-	-
406.23	0.60	409.4(10)	0.55(4)	412.2*(30)	0.48	-	-
417.411	0.66	422.1(10)	0.66(4)	411.4(20)	0.67	421	0.83(8)
445.774	0.25	456.5(10)	0.34(2)	-	-	456	0.29(3)
447.883	0.43	463.8(10)	0.31(2	-	-	-	-
479.461	0.032	483.0(10)	0.44(3)	-	-	483	1.93(19)
-	-	-	-	514.8*(10)	0.013	-	-
592.75	0.51	594.2(10)	0.55(4)	-	-	594	0.70(7)
601.77	0.87	600.2 *(13)	0.96(6)	612.0(50)	0.23	-	-
706.297	0.98	704.7(10)	0.89(6)	-	-	708	0.75(7)
710.859	0.74	710.4(10)	0.91(6)	720.0(20)	-	-	-
874.665	0.62	872.3(10)	0.58(4)	-	-	871	0.96(9)
903.423	0.97	907.3(10)	0.91(6)	-	-	-	-
957.902	0.73	963.1(10)	0.75(5)	961.5(20)	0.76	962	0.97(10)
1035.688	0.79	1035.0(10)	0.74(5)	1033.6(50)	0.69	-	--
1130.151	0.50	1127.6(20)	0.51(3)	1130.9(20)	0.37	1126	0.62(6)
1136.308	0.50	1136.8*(30)	0.48(3)	-	-	-	-

As shown in x-ray diffraction investigations earlier in this text, unit cell volumes of 7:4 mullite display a collapse with pressure and within the structure, the distortion of octahedra, coupled with the motion of tetrahedral sites towards the edge of the tetrahedra causes the tetrahedral sites and the O(1) oxygen sites to move closer. This could ultimately lead to formation of SiO_5 and AlO_5 distorted bipyramids, sharing an edge with the AlO_6 octahedra (Figure 38). A structural evolution of 7:4 mullite towards a possible formation of

AlO_5 or SiO_5 would be consistent with the pressure/coordination rule, which suggests that increasing pressure (or decreasing temperature) leads to formation of higher coordination groups. Oganov [15] proposed that in sillimanite there exists a critical bonding distance, for the Si–O bond, above which atomic interactions cannot be considered as bonding. Our structural refinements show the T–O1 distance in 7:4 mullite at 24.7 GPa to be greater than the distance that would be necessary for the capture of a fifth oxygen (bonding interaction) and creation of AlO_5 and SiO_5. Nevertheless it can be thought that the crystal structure of mullite, under the influence of pressure, is evolving in the direction of a possible phase transition, with motion towards the formation of five-coordinated silica and alumina. However, the transition does not ultimately take place, because the process of amorphization takes over as seen with the disappearance of Raman bands in mullite and in sillimanite. Table 16 lists and attempts to match the vibrations found in 2:1 mullite with the experimental and calculated vibrations of sillimanite, and compares the values obtained in this work with those reported Mernagh and Liu. [119] The correspondence between theoretical and experimental mode Grüneisen parameters is very good above 380cm^{-1} and excellent above 500cm^{-1}. There is also good agreement, for most values, with the data reported by Mernagh and Liu. [119]

4.3. High-Pressure Synchrotron XRD of Boron Mullites

The samples of 7:4 mullite and B-mullite were compressed, in small pressure steps, up to 28.2 GPa and 28.8 GPa respectively, and then decompressed back to ambient pressure. Figure 35 shows X-ray diffraction patterns collected *in situ* in a DAC. As pressure is increased, all diffraction lines shift toward higher 2Θ angles or lower *d*-spacings.

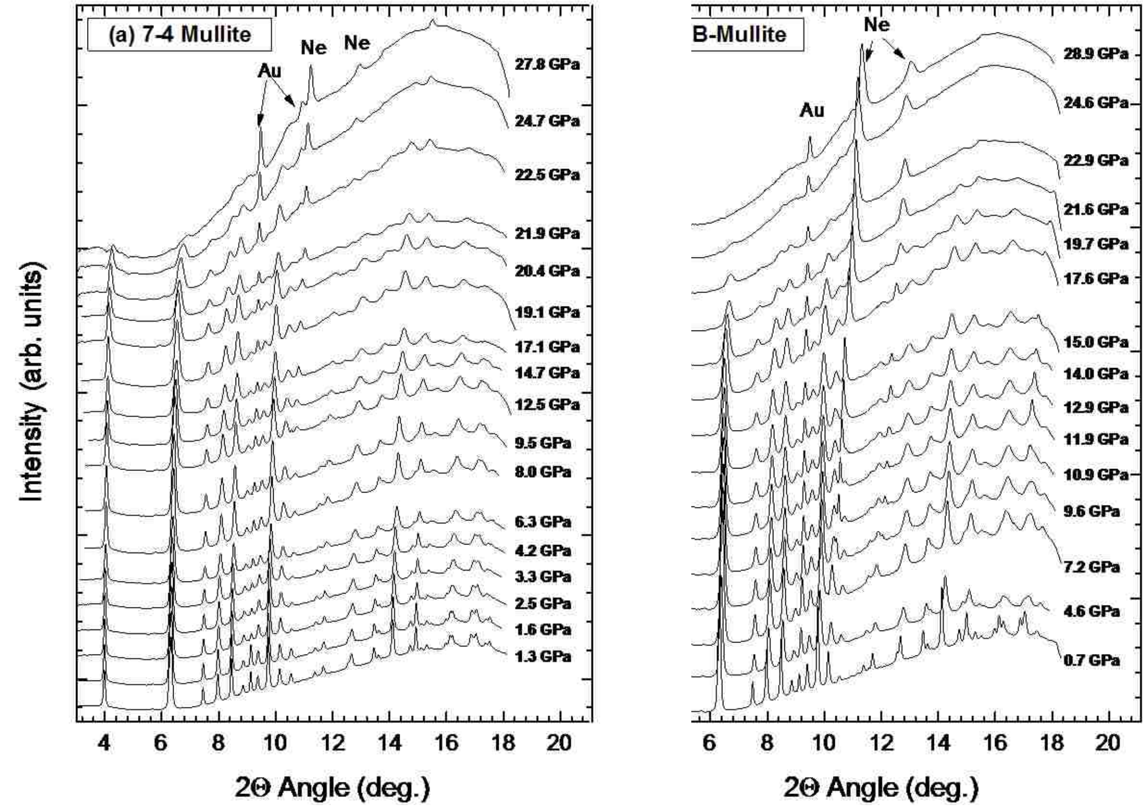

Figure 35. 7:4 mullite and B-mullite X-ray diffraction at high-pressures.
Selected patterns of *in situ* synchrotron X-ray diffraction of 7:4 mullite and B-mullite in diamond anvil cell, for various values of increasing pressure.

All along the compression both samples' patterns were indexable in the mullite space group *Pbam*. Compression data were smooth up to about 19 GPa (~17 GPa for B-mullite), from which point the diffraction peaks appeared to broaden, and the refined unit cell parameters deviated significantly down from the compressional trend. At 24.7 GPa (24.6 GPa for B-mullite) the diffraction patterns were not indexable anymore, suggesting X-ray amorphization or a phase transition underway.

To follow the pressure evolution of unit cell parameters and unit cell volumes of 7:4 mullite and B-mullite, Rietveld full-profile structural refinements were performed on X-ray diffraction patterns (see examples in Figure 36 and Table 17). Refinements were done starting from the structure of 3:2 mullite of Saalfeld and Guse, [103] which was transformed into the standard mullite setting.

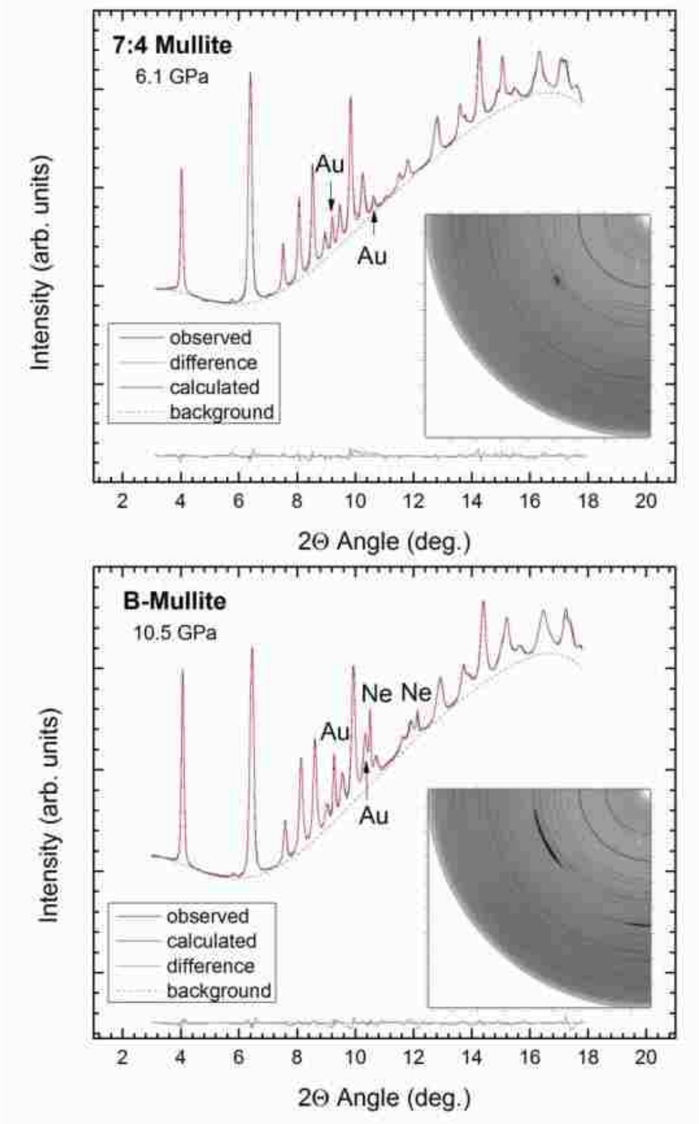

Figure 36. Rietveld refinements of 7:4 mullite and B-mullite.
Representative Rietveld refinements of 7:4 mullite and B-mullite at pressure 6.1 GPa and 10.5 GPa.
Insets show portions of the original synchrotron X-ray diffraction images to illustrate the good quality of high pressure powder X-diffraction data.

The structure was further adapted to reflect the 7:4 ratio of Al_2O_3:SiO_2 composition. Since boron has a low scattering factor and hence its positions cannot be determined in using X-rays, the same starting structure was used for refinements of both samples. The displacement parameters of atoms forming the octahedra and those forming tetrahedra were refined in two groups.

Pressure-induced broadening and intensity loss of ADXRD lines limited the refinement of displacement parameters to 24.7 GPa for 7:4 mullite and 22.9 GPa for B-mullite. Figure 36 shows representative Rietveld refinements at high pressures and insets show snapshots of portions of the original diffraction images with Debye rings. Table 17 shows the data of the Rietveld refinements from Figure 36. The statistically good quality of high-pressure X-ray diffraction data allowed us to extract reasonable trends in the pressure-driven evolution of atom positions and consequently trends concerning polyhedral distortion and tilting. [120]

Table 17. Results of Rietveld structural refinements of B-Mullite and 7:4 mullite from Figure 36.

7:4 Mullite

Crystal system	orthorhombic	***a** (Å)*	7.452(1)	***p** (GPa)*	6.3(2)
Space group	Pbam (55)	***b**(Å)*	7.581(2)	***V** (Å^3)*	161.0(1)
Z	2	***c**(Å)*	2.851(2)	***Rwp***	0.371

Label	***Site***	***x***	***y***	***z***	***Atom***	***Occ.***	***B (temp.)***
Al1	2a	0.00000	0.00000	0.00000	Al+3	1	0.93(3)
TAl	4h	0.1453(4)	0.3371(4)	0.50000	Al+3	0.5	0.93(3)
TSi	4h	0.1453(4)	0.3371(4)	0.50000	Si+4	0.334	0.93(3)
T*	4h	0.274(2)	0.198(2)	0.50000	Al+3	0.167	0.93(3)
O1	4h	0.3487(5)	0.4192(4)	0.50000	O-2	1	0.93(3)
O2	4g	0.1356(6)	0.2156(3)	0.00000	O-2	1	0.93(3)
O3	2d	0.00000	0.50000	0.50000	O-2	0.501	0.93(3)
O4	4h	0.428(4)	0.040(4)	0.50000	O-2	0.137	0.93(3)

B-Mullite

Crystal system	orthorhombic	***a** (Å)*	7.380(1)	***p**(GPa)*	10.9(3)
Space group	Pbam (55)	***b**(Å)*	7.526(1)	***V** (Å^3)*	156.78(9)
Z	2	***c**(Å)*	2.824(1)	***Rwp***	0.311

Label	***Site***	***x***	***y***	***z***	***Atom***	***Occ.***	***B (temp.)***
Al1	2a	0.00000	0.00000	0.00000	Al^{+3}	1	0.74 (3)
TAl	4h	0.1506(2)	0.3356(3)	0.50000	Al^{+3}	0.5	0.74 (3)
TSi	4h	0.1506(2)	0.3356(3)	0.50000	Si^{+4}	0.334	0.74 (3)
T*	4h	0.267(1)	0.202(1)	0.50000	Al^{+3}	0.167	0.74 (3)
O1	4h	0.3606(4)	0.4172(3)	0.50000	O^{-2}	1	0.74 (3)
O2	4g	0.1301(3)	0.2113(2)	0.00000	O^{-2}	1	0.74 (3)
O3	2d	0.00000	0.50000	0.50000	O^{-2}	0.501	0.74 (3)
O4	4h	0.439(2)	0.071(2)	0.50000	O^{-2}	0.167	0.74 (3)

The pressure-induced evolution of unit cell parameters *a*, *b*, and *c* and the relative fractional changes of these parameters are shown in Figure 37. For both 7:4 mullite and B-mullite the lattice compression is anisotropic (Figure 37(a) and (b)). The lowest compressibility along the *c* axis is explained by firmly-bound, edge-sharing octahedra and corner-sharing tetrahedra running along this direction.

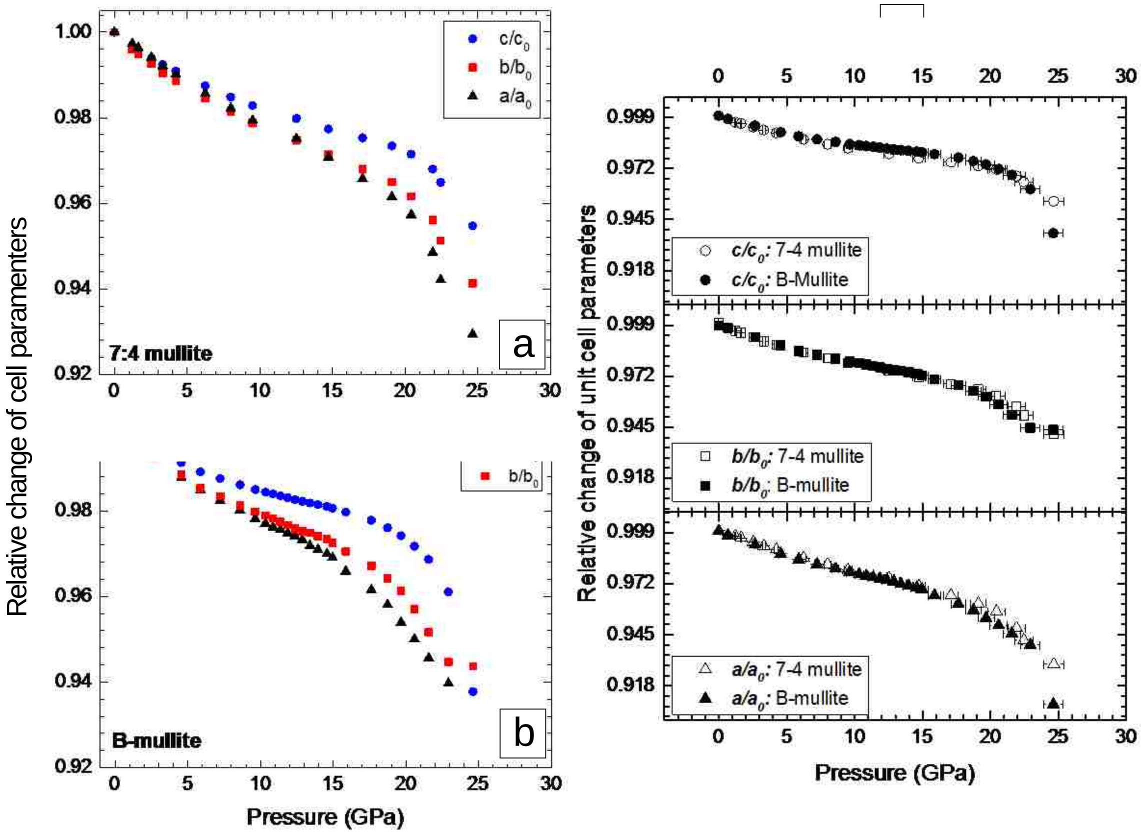

Figure 37. Pressure-driven change of unit cell parameters.
Relative, pressure-driven change of unit cell parameters of (a) 7:4 mullite and (b) B-mullite: comparison of all cell parameters for each sample. (c): Comparison of normalized unit cell parameters for the two samples.

Further, the compression appears very slightly more anisotropic in B-mullite when compared to 7:4 mullite (Figure 37(a) and (b)). It has been shown that in borates the BO_3 and BO_4 polyhedra change little upon heating, much like tetrahedra in silicates.[97] In many borates this can lead to highly anisotropic thermal expansion or to negative thermal expansion. [121] We can then assume that the replacement of some of the SiO_4 by BO_3 in B-mullite also increases the anisotropic nature of compression in this material. On compression below ~15 GPa both mullites display nearly identical fractional pressure evolution (Figure 37(c)). On compression above ~20 GPa the lattice parameters (and correlated cell volumes) deviate significantly down from the compressional trend (Figure 37(c)). This discontinuity is slightly stronger for B-mullite than for 7:4-mullite. [120]

4.3.1. Compression Mechanisms

The pressure driven evolution of AlO_6 octahedra may shed some light on the compression mechanisms. In any mullite structure the angle defined by octahedra in the *a*-*b* plane, constructed by drawing lines through the terminating oxygen atoms of the octahedra (O2 oxygen sites), is called the inclination angle ω. Figure 38(a) shows the location of ω within the mullite structure. Figure 39 shows, for both samples, the pressure-driven change of the inclination angle ω (Figure 39(c)) as well as the indices of distortion (Figure 39(a) and (b)) of angles and distances within the AlO_6 octahedra and SiO_4/AlO_4 tetrahedra, calculated after Baur. [121] For example, following Baur, the distortion index for distances within a tetrahedron is calculated as:

$$DI(TO) = \left(\sum_{i=1}^{4}|TO_i - TO_m|\right)/4TO_m$$

where TO_i is an individual distance from tetrahedral cation to an oxygen atom and m signifies the mean value for the polyhedron. Similar calculations are done for the octahedral distances and angles. [120]

It is observed that up to ~18 GPa for B-mullite (20 GPa for 7:4 mullite) the octahedral distances are almost not distorted, while angles present a greater, but rather constant distortion (Figure 39(a) and (b)). Minimal and constant distortion in octahedral distances and a constant distortion of angles in both samples implies that the increase in the angle ω, below ~18 GPa for B-mullite (20 GPa for 7:4 mullite), is related to the rotation of

AlO$_6$ octahedra away from each other, in the *a*-*b* plane (Figure 38, Figure 39), rather than a distortion of the octahedra. [120]

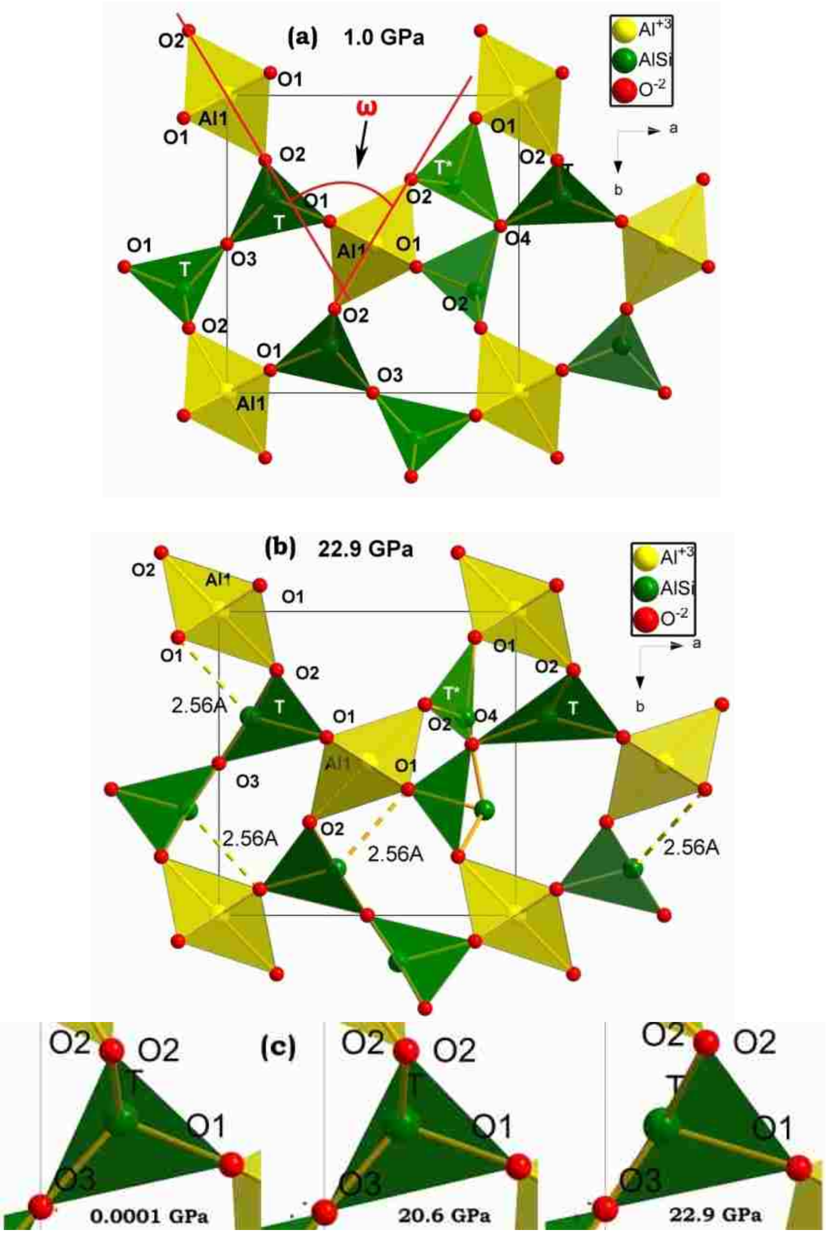

Figure 38. The crystal structure of B-mullite at different pressures.
(a) The crystal structure of B-mullite at 1 GPa. Also shown is the inclination angle ω, which illustrates the rotation of the AlO$_6$ octahedra with respect to each other. (b): The crystal structure of B-mullite at 22.9 GPa illustrating the distortion of octahedra, the increase in the inclination angle ω and the evolution of AlO$_4$ or SiO$_4$ tetrahedra towards distorted AlO$_5$ or SiO$_5$ bipyramids. (c): The pressure driven evolution of the tetrahedral site.

Above ~18 GPa for B-mullite (20 GPa for 7:4 mullite) the dramatic increase in ω (Figure 39(c)) can no longer be interpreted in terms of rotation of octahedra, but rather in terms of more pronounced distortion of octahedral angles and octahedral distances (Figure 39(a) and (b). The dramatic increase of ω (Figure 39(c)), corresponds to the pressure range where the refined unit cell parameters of both B-mullite and 7:4 mullite deviate significantly down from the compressional trend (Figure 37(a) and (b)). The more significant deviation of ω in B-mullite can be correlated with the higher compressibility of B-mullite (see chapter below) and the earlier onset of pressure-induced amorphization in this sample. [120]

The compression along *a* and *b* is overall greater than along *c*. At lower pressures *b* is slightly more compressible than *a*, but this is only true up to ~15 GPa for 7:4 mullite and up to ~7 GPa for B-mullite (Figure 37(a) and (b)). Above this threshold pressure the compressibilities cross-over and the *a* axis becomes progressively more compressible, indicating a change in the mechanism of compression. [120]

Yang *et al.* [17] investigated sillimanite on compression up to 5.29 GPa and proposed that the greater compressibility along *b*, in that low pressure range, is due to the compression of the long octahedral bonds, which are oriented closer to the *b* axis and therefore influence more its compressibility than that of the *a* axis. In the present work, in the case of both 7:4 mullite and B-mullite, it is observed that at pressures below 5 GPa the octahedral bonds Al1-O1 oriented closer to the *a* axis increase slightly under compression, while those oriented closer to the *b* axis, Al1-O2 decrease slightly (Figure 38(a) and Figure 40). This is consistent with the fact that, at low pressures, *b* is more compressible than *a*. However with increasing pressure the octahedra rotate away from each other, as shown by the evolution in the inclination angle ω (Figure 39(c)), and this rotation makes the Al1-O2 bonds to orient more in the middle between the *a* and the *b* axes. [120]

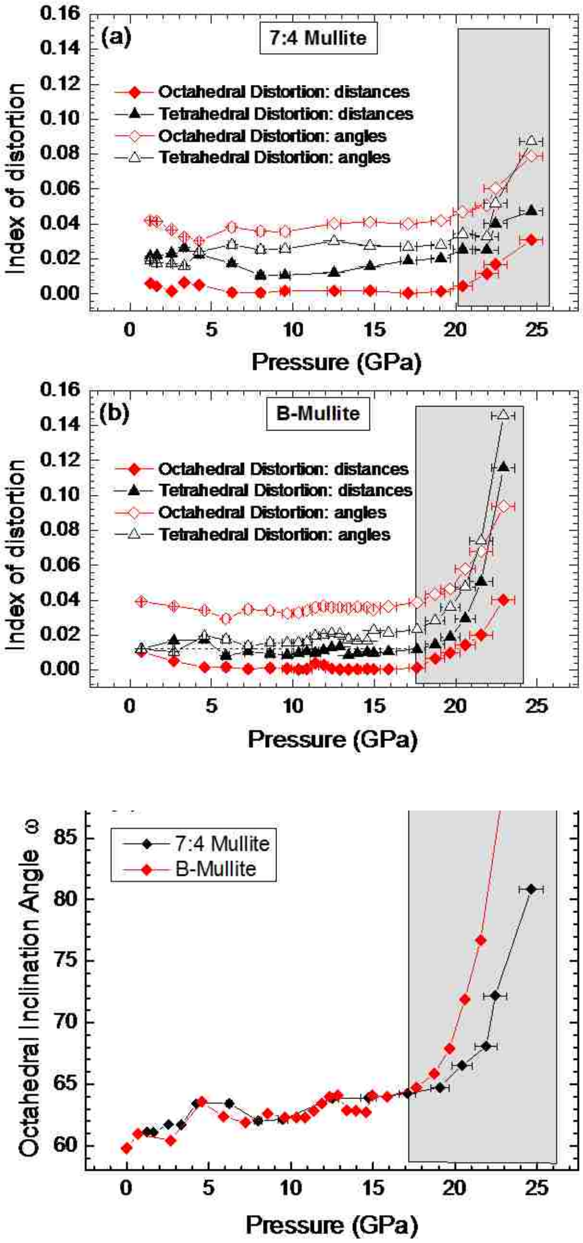

Figure 39. Indices of distortion in in 7:4 mullite and B-mullite.
(a) and (b) The pressure-driven change in the index of distortion of distances and angles in the polyhedra and (c) of the inclination angle ω, in 7:4 mullite and B-mullite.

Also under further compression the Al1-O1 and Al1-O2 bonds become approximately equal (Figure 40). Starting from 20 GPa in 7:4 mullite and 18 GPa in B-mullite, the octahedral angles become distorted (Figure 39(a) and (b)), which makes the octahedral distance Al1-O1 decrease, while Al1-O2 increases (Figure 40). Since Al1-O1 is oriented closer to the *a* axis this could explain the greater compressibility of *a* at higher pressures (above ~18 GPa). There can exist other mechanisms, at lower pressures, related to changes in inter-polyhedral bonds and angles that could shed further light on the difference in compressibility of *a* and *b*. [120]

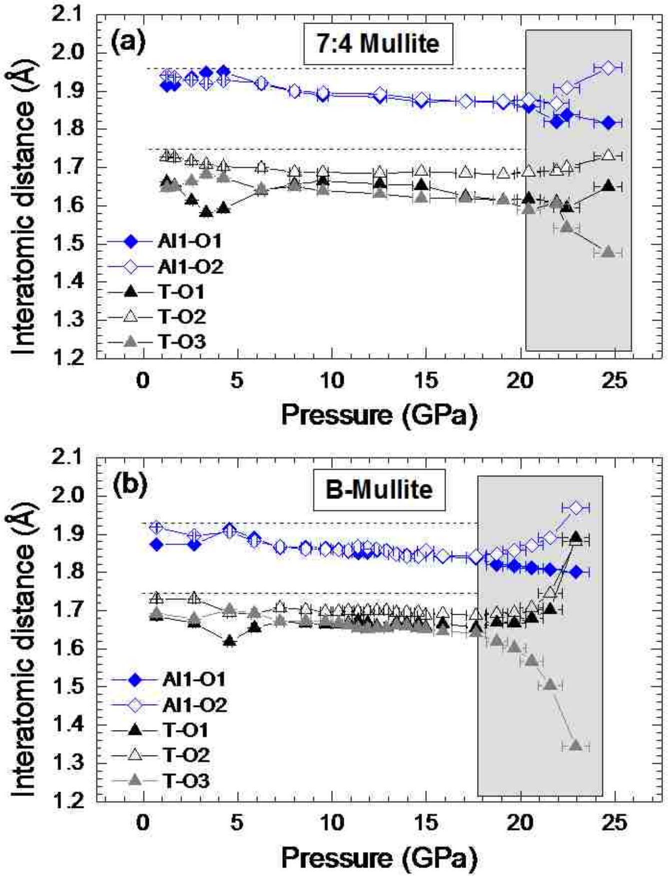

Figure 40. Bond lengths in 7:4 mullite and B-mullite.
Evolution of octahedral and tetrahedral bond lengths versus pressure, in 7:4 mullite and B-mullite. The location of specific atoms and bonds can be found in Table 17.

In summary, compression in B-mullite and 7:4 mullite can be thought of as occurring in steps. Initially compression is dominated by a decrease in the longest (octahedral) bonds, coupled with a small rotation of octahedra away from each other (increase in ω). Octahedral distances are almost not distorted, while angles present some approximately constant distortion. In tetrahedra bond lengths decrease more slowly than in the octahedra, and distortion in bond lengths and angles is present, but remains approximately constant, so the tetrahedra can be considered to behave as more rigid units, compared to octahedra, which is expected. As octahedra rotate under pressure, the *b* axis, initially more compressible, gives way to the *a* axis to became the most compressible, above ~13 GPa for 7:4 mullite and ~7 GPa for B-mullite. The region above ~18 GPa for B-mullite (20 GPa for 7:4 mullite) can be thought of as the last stage of compression, with significant increase in distortion of all polyhedral bond lengths and angles, which causes a dramatic increase in the inclination angle ω. These changes are accompanied by a progressive, pressure-induced X-ray amorphization, discussed below. [120]

4.3.2. Mechanisms of Pressure-Induced Amorphization

Above ~15 GPa we observe a gradual loss of long range order due to distortion (Figure 35), leading to pressure-driven X-ray amorphization at the highest pressures of compression, in both samples. It is found that B-mullite becomes almost completely X-ray amorphous at at ~25 GPa while 7:4 mullite still has some residual crystallinity at 27.8 GPa. We previously observed X-ray amorphization in 2:1 mullite and 3:2 mullite above ~30 GPa and in the structurally similar sillimanite above ~40 GPa.[122] The mullite-type Al_5BO_9 was also found to undergo complete X-ray amorphization, at ~26.7 GPa. [123]

Several factors appear to lead towards amorphization. At 24.7 GPa for 7:4 mullite and 22.9 GPa for B-mullite (last pressure where structural refinements were carried out) AlO_6 octahedra are distorted, and the distortion appears most prominent in the *ab*-plane (Figure 38(b)). The inclination angle ω, which was, initially, increasing slowly, experiences a dramatic upturn starting from around 20 GPa (Figure 39). The most striking change occurs in the tetrahedra (Figure 38(b) and (c)), where the central atom (Si or Al) moves in the direction outward from the tetrahedron volume, all the while the O1 atom sites move closer to the tetrahedral sites, due to the increase in distortion of octahedra (or of the inclination angle ω). It was proposed by Oganov [15] that the crystal structure of sillimanite can undergo a pressure-induced phase transition at ~35 GPa, having the same symmetry and similar structure, but characterized by the formation of AlO_5 and SiO_5 distorted bipyramids, which share an edge with the AlO_6 octahedra. The formation of five coordinated Si and Al is achieved by pulling an extra O atom, initially not bonded to Si and Al inside the first coordination sphere of Si and Al2. Compression of silica glass was reported to increase the coordination number of silica [124] and fivefold coordination was reported starting around 12 GPa. [125] Five-coordinated silica is also found in silicate and aluminate glasses [126, 127] and in calcium silicate $CaSi_2O_5$.[128] AlO_5 bipyramids are found in numerous crystal structures, e.g. in mullite-type Al_5BO_9 [123] and $Al_4B_2O_9$, [123] and in andalusite.

In the present case of 7:4 mullite and B-mullite, it is observed that pressure appears to drive the crystal structures in the direction of what could ultimately become a phase transition. Unit cell volumes display a collapse with pressure and within the structure, the distortion of octahedra, coupled with the motion of tetrahedral sites towards the edge of the tetrahedra causes the tetrahedral sites and the O(1) oxygen sites to move closer. This could ultimately lead to formation of SiO_5 and AlO_5 distorted bipyramids, sharing an edge with the AlO_6 octahedra (Figure 38). A structural evolution of B-mullite and of 7:4 mullite towards a possible formation of AlO_5 or SiO_5 would be consistent with the pressure/coordination rule, which suggests that increasing pressure (or decreasing temperature) leads to formation of higher coordination groups. Further, one could assume that in the case of B-mullite pressure would tend to create BO_4 groups in place of the BO_3 groups observed at ambient pressure and temperature conditions. Oganov [15] proposed that in sillimanite there exists a critical bonding distance, of 2.25 Å, for the Si–O bond, above which atomic interactions cannot be considered as bonding. Our structural refinements put the T–O1 distance at

~2.70 Å in 7:4 mullite at 24.7 GPa and ~2.56 Å in B-mullite at 22.9 GPa (compared to 3.0 Å at ambient pressure), which is greater than the distance that would be necessary for the capture of a fifth oxygen (bonding interaction) and creation of AlO_5 and SiO_5. Nevertheless it can be thought that the crystal structure of B-mullite and that of 7:4 mullite, under the influence of pressure, is evolving in the direction of a possible phase transition, with motion towards the formation of five-coordinated silica and alumina. However, the transition does not ultimately take place, because the process of amorphization takes over. It can also be thought that process of shifting towards five-coordinated silica and alumina actually creates instabilities in the structure and contributes to the amorphization. However sillimanite, which does not have oxygen vacancies, also undergoes pressure driven amorphization above ~40 GPa. [122] So instabilities around oxygen vacancies are only one of the factors that contribute to an earlier pressure-induced amorphization in mullite. [120]

In recent shock experiments Atou *et al.* [122] proposed that oxygen vacancies in mullite act as initiation points for amorphization. In the present work it is found that B-mullite ($x \approx 0.4$), which has more oxygen vacancies than 7:4 mullite ($x=0.33$), also undergoes amorphization at a lower pressure than 7:4 mullite, while the previously investigated sillimanite, [122] which does not have any oxygen vacancies, undergoes amorphization above ~40 GPa. This is consistent with the idea the amorphization of mullite could be triggered by phase instability around these oxygen vacancies, which would then result in a crystallographically uncontrolled crystal collapse and localized amorphization. [120]

High-pressure, Synchrotron ADXRD patterns of 7:4 mullite and B-mullite were also collected *in situ* (DAC), during decompression runs from the highest pressures investigated down to ambient conditions. Comparative X-ray diffraction patterns of both samples decompressed to ambient pressure are shown in Figure 41. [120] It appears that B-mullite and 7:4 mullite behave somewhat differently upon complete release of pressure. B-mullite remains mostly X-ray amorphous upon decompression from 28 GPa (no diffraction lines visible, other than Al_2O_3 and Au).

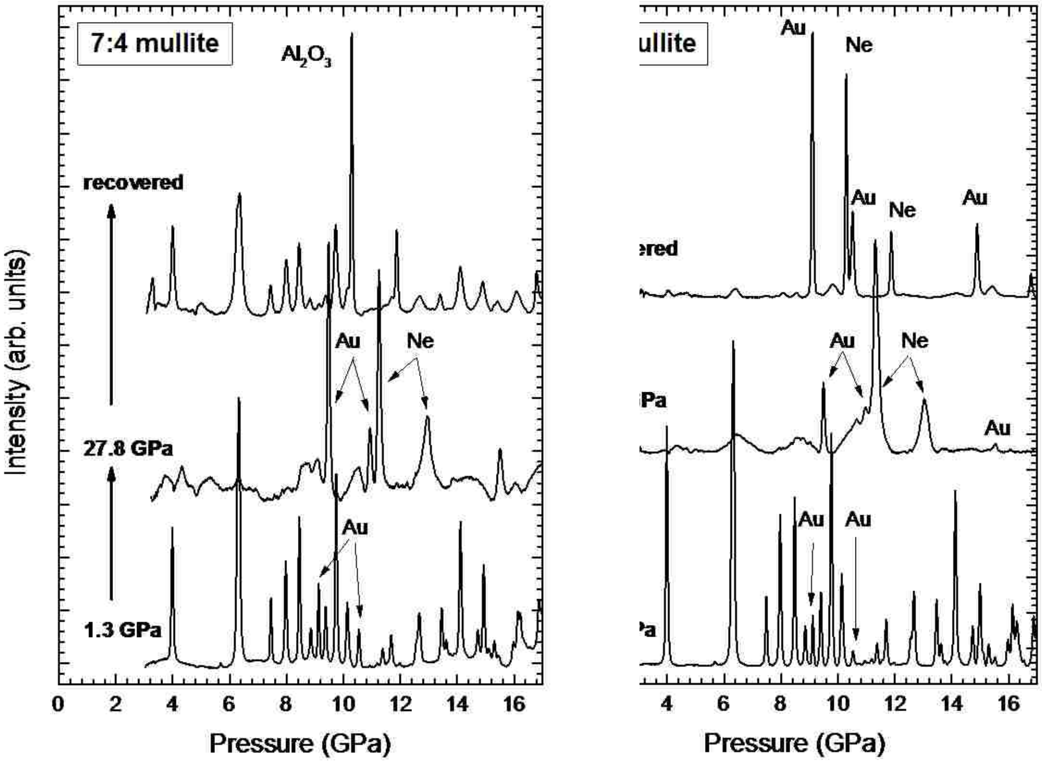

Figure 41. Decompression of 7:4 mullite and B-mullite.
Comparison of XRD patterns of 7:4 mullite and B-mullite recovered after decompression with: the highest compression pressure pattern and the beginning of compression pattern. All patterns are background subtracted to facilitate comparison. Also visible are diffraction lines of Au and Al_2O_3 (pressure indicators), and Ne pressure transmitting medium. The recovered sample of B-mullite still displays diffraction lines of Ne due to residual stresses in the gasket.

7:4 mullite however appears to partially recover some of its crystallinity upon decompression down from 28 GPa as is evidenced by a few diffraction lines attributable to the mullite structure. Figure 41 suggests that depending on the amount of oxygen vacancies and the top compression pressure, amorphization is partially reversible**.** In this light, the pressure driven amorphization can be thought of as an extreme distortion of bond distances and angles, or temporary loss of long range order (preserving at least a portion of the bonds), which upon pressure release allows the crystal structure to partially recover (and in this sense recovery does not involve recrystallization). [120]

4.3.3. Equation of State and Axial Compressibilities

When comparing the axial compression between 7:4 mullite and B-mullite, the evolution appears almost identical along c in the entire compression range, while along a and b the B-mullite is slightly more compressible above ~15 GPa (Figure 37). The overall similarity in compression is then observed in the volume evolution versus pressure (Figure 42). The unit cell volume of B-mullite appears a little more compressible. A third order Birch-Murnaghan [110, 111, 113] equation of state (EoS) was fitted to the experimental pressure-volume data (Figure 42) to determine the bulk modulus K_0 and its pressure derivative K_0' at ambient conditions for 7:4-mullite and for B-mullite:

$$P = \frac{3}{2}K_0\left[\left(\frac{V_0}{V}\right)^{\frac{7}{3}} - \left(\frac{V_0}{V}\right)^{\frac{5}{3}}\right]\left\{1 + \frac{3}{4}(K_0' - 4)\left[\left(\frac{V_0}{V}\right)^{\frac{2}{3}} - 1\right]\right\}$$

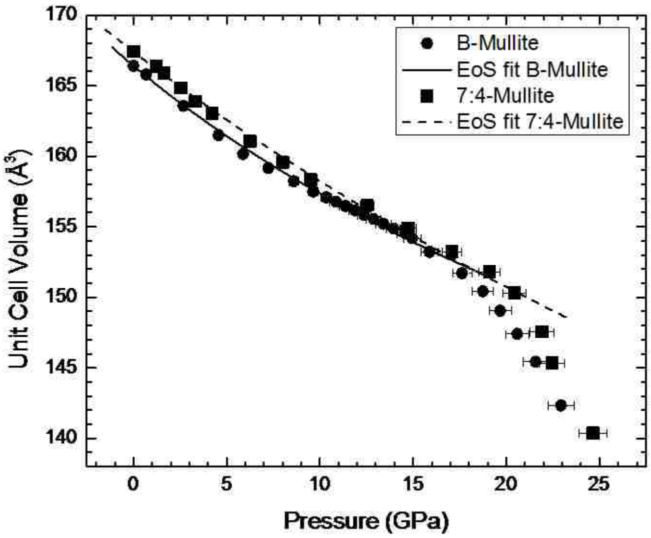

Figure 42. Pressure-volume plot and equation of state fits for 7:4 mullite and B-mullite.

The bulk moduli obtained from the Birch-Murnaghan fits, accounting for uncertainties in P and volume, are summarized in Table 18, together with our previous data for 3:2 and 2:1 mullite, as well as literature data for synthetic boron-mullite Al_5BO_9 and sillimanite. For each sample, the EoS was fitted only up to the early onset of the pressure-induced discontinuities, beyond which the EoS breaks down (Figure 42). [120] It is possible to establish a trend of bulk modulus value versus the amount of oxygen vacancies. In fact we observe a slight decrease in bulk modulus with increasing number of oxygen vacancies x in the structure: sillimanite (x=0) ≥ 3:2 mullite (x=0.25) > 7:4 mullite (x=0.33) > 2:1 mullite (x=0.4) ≥ B-mullite (x≈0.4). Such ordering was suggested in first-principles modelling by Aryal [116] for sillimanite and several mullites. Interestingly, the inclusion of boron in the mullite structure makes the structure more compressible, probably due to the structurally less resilient BO_3 triangles, which replace some of the SiO_4 tetrahedra in B-mullite and the higher number of oxygen vacancies. [120]

Table 18. Bulk moduli of various mullites.
Comparison of: bulk moduli (*K_0*), their pressure derivatives (*K_0'*) and unit cell volumes at ambient pressure (*V_0*) obtained in the present work with available literature data. For a comprehensive list of bulk moduli of various mullite and of sillimanite, obtained by different methods, see Kalita et al. [75]

	K_0 **(GPa)**	***K_0'***	***K_0''***	***V_0*** **(Å^3)**	***Space Group***
3:2 Mullite - this work	173(6)	2.3(2)	–	167.580 (1)	*Pbam (55)*
3:2 Mullite [116]	173.2				*Pbam (55)*
7:4 Mullite - this work	164(7)	2.7(1.7)	–	167.401(1)	*Pbam (55)*
	160(5)	*4 (fixed)*	–	167.401(1)	
2:1 Mullite - this work	162(7)	2.2(6)	–	168.13(2)	*Pbam (55)*
2:1 Mullite [116]	167.6				*Pbam (55)*
B-Mullite - this work	148(7)	6.7(1.7)	–	166.402(1)	*Pbam (55)*
	159(4)	4 *(fixed)*	–	166.401(1)	
4:1 Mullite [116]	151.3				*Pbam (55)*
Al_5BO_9 (mullite-type)[123]	164(1)	4	–	657.3(2)	*$Cmc2_1$ (36)*
Sillimanite - this work	167(7)	2.1(4)	–	331.459(3)	*Pbnm (62)*
Sillimanite [116]	174.9				*Pbnm (62)*

The elastic anisotropy of B-mullite and 7:4 mullite can be described in terms of axial bulk moduli, which are obtained by applying a linearized Birch-Murnaghan EoS, [24] where virtual volumes a^3, b^3, or c^3 must be used. The axial compressibilities, described as linearized bulk moduli obtained from the EoS fits are summarized in Table 19.

Table 19. Axial compressibilities of various mullites.
Axial compressibilities, described as linearized bulk moduli obtained from the EoS fits, obtained in the present work and compared with literature data.

	K_{a0} (GPa)	K_{a0}'	K_{b0} (GPa)	K_{b0}'	K_{c0} (GPa)	K_{c0}'
7:4 Mullite - this work	139(3)	2.7(5)	138(4)	*5.3(9)*	173(6)	8.3(1.0)
B-Mullite - this work	109(4)	8.0(1.0)	147(8)	*5.1(9)*	198(15)	8.8(1.0)
Al_5BO_9 (mullite-type)[123]	244(9)	4.6(9)	120(4)	2.5(4)	166(11)	6.9(9)
Sillimanite - this work	163(1)	2.1(3)	113.1(7)	5.1(2)	297(1)	11.1(4)

The anisotropic scheme thus obtained is for 7:4 mullite: K_{a0}:K_{b0}:K_{c0} = 1.007:1:1.254; $\beta_{(a)}$:$\beta_{(b)}$:$\beta_{(c)}$ = 1:245:1.254:1 (where $\beta_{(n)}$ = $1/(K_{0(n)})$); and for B-mullite: K_{a0}:K_{b0}:K_{c0} = 1:1.349:1.817; $\beta_{(a)}$:$\beta_{(b)}$:$\beta_{(c)}$ = 1.817:1.347:1. [120]

In situ high-temperature X-ray diffraction experiments performed by Lührs [29] on B-mullite from 300°C up to 1000°C yielded the following thermoelastic anisotropy: $\alpha(a)$:$\alpha(b)$:$\alpha(c)$ = 1:1.29:1.18 with $\alpha(a)$=4.5(1), $\alpha(b)$=5.8(1) and $\alpha(c)$=5.3(1)x10^{-6} °C^{-1} (where $\alpha(i) = 1/li(\partial li/\partial T)$ is the axial expansion coefficient). We can obtain a first approximation P–T–V EoS of B-mullite by combining the elastic parameter obtained in this study with the thermal parameters of Lührs et al.: [29]

$$V(P,T) \cong V(P_{0,}T_0)[1-\beta\Delta P+\alpha\Delta T] = V(P_{0,}T_0)[1-0.0067(1)\Delta P+5.2(1)\times10^{-6}\Delta T]$$

where $\beta=1/K_{T0}$ is in GPa^{-1} and α is in K^{-1}. This equation is based on the assumptions that both thermal expansion and K' are constant with pressure. It should also be noted that bulk modulus data are associated with a ~10% volume compression whilst the thermal parameters area derived from a ~1% volume change. [120]

4.4. High-Pressure Behavior of $PbMBO_4$ Synthetic Mullites

4.4.1. High-Pressure Synchrotron XRD of $PbFeBO_4$

High-pressure ADXRD patterns of mullite-type $PbFeBO_4$ phases were collected in-situ in a DAC, on compression from 1.4 GPa up to 71.7 GPa. Figure 43 shows x-ray diffraction patterns measured for $PbFeBO_4$. As pressure is increased all diffraction lines shift towards higher 2θ angles i.e. lower d-spacings. According to the ADXRD patterns the compression appears to be continuous up to the highest pressure investigated, although the diffraction lines display pressure-broadening and some changes in relative intensities.

In order to follow the pressure evolution of unit cell parameters and unit cell volumes of mullite-type $PbFeBO_4$, Rietveld full-profile structural refinements were performed on all x-ray diffraction patterns collected. At ambient pressure and temperature $PbFeBO_4$ has an orthorhombic crystal lattice and crystallizes in the space group Pnam (62). For starting the ambient pressure refinements we used the initial structure of Murshed et all, [104] which is in the usual mullite setting, i.e. with the octahedral chains running along the c crystallographic axis. The pressure-induced evolution of unit cell parameters a, b, and c and of cell volumes V are given in Figure 44, while relative fractional changes of unit cell parameters are shown in Figure 45.

Rietveld refinements of high-pressure X-ray diffraction data combined with analysis of Raman spectra helped to reveal some unexpected and interesting features of the process of compression.

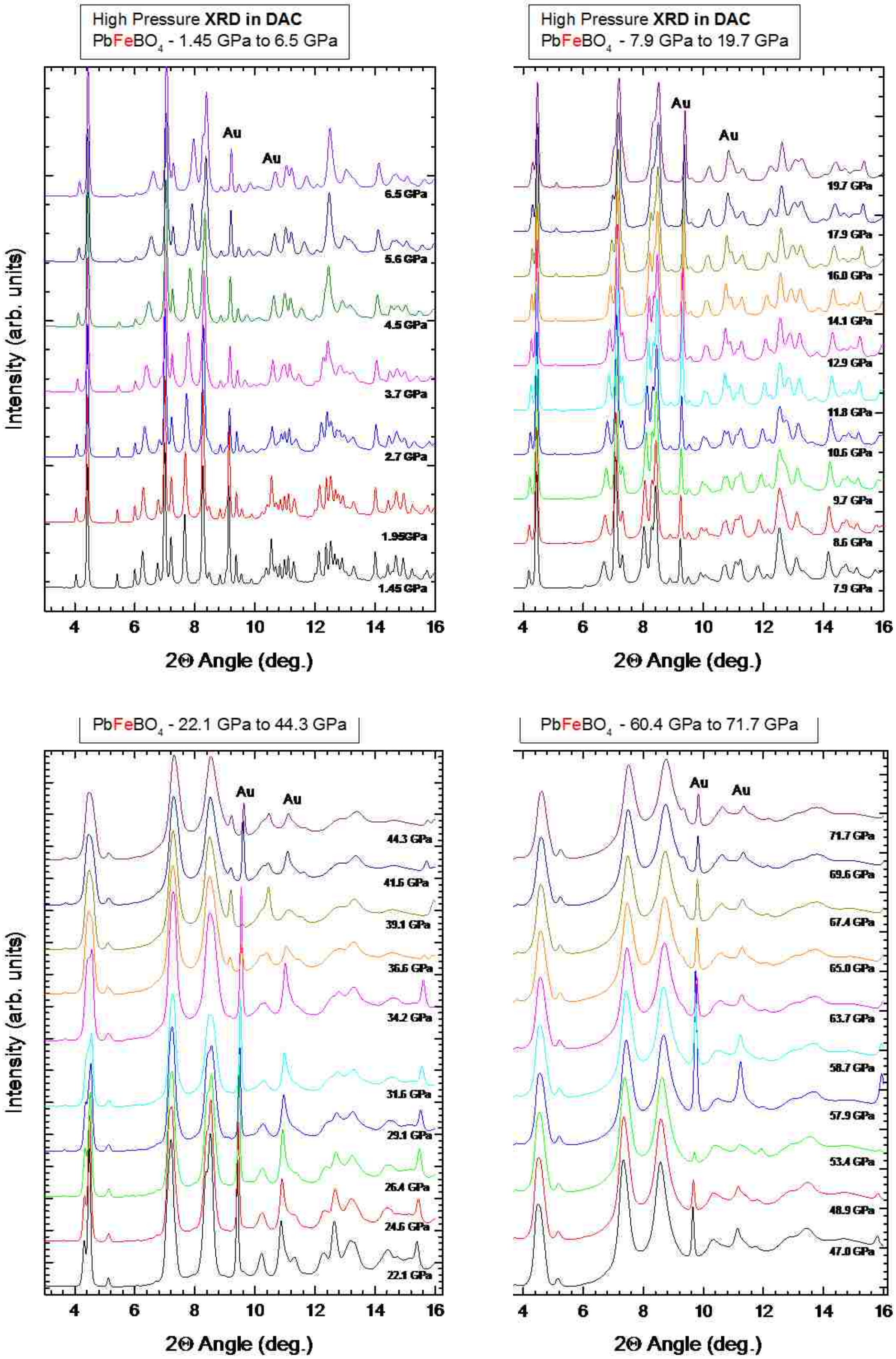

Figure 43. High-pressure ADXRD patterns of the mullite-type $PbFeBO_4$.
The ADXRD patterns were measured in-situ in a DAC on compression from ambient pressure up to 71.7 GPa.

First of all, as the $PbFeBO_4$ structure is compressed between ambient pressure and ~8GPa and while the *a* and *c* unit cell parameters decrease, on the contrary the *b* unit cell parameter increases. This expansion under pressure or negative axial compressibility is ~ 1.5% (Figure 45). This feature, also referred to as negative linear compressibility (NLC), is discussed in detail in a section below. With pressure increase above ~8 GPa the *b* parameter slowly decreases by ~3.7% on compression up to 71 GPa.

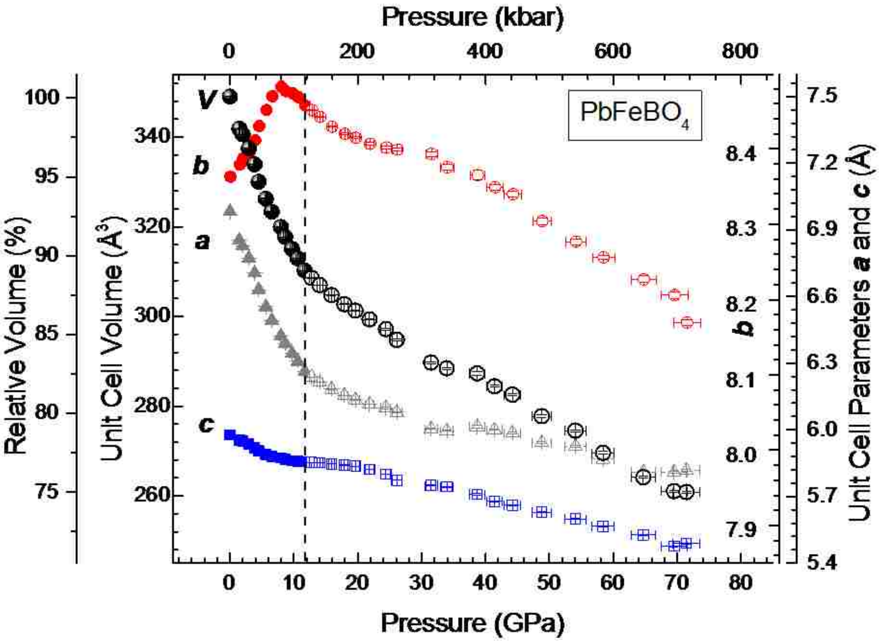

Figure 44. Pressure-driven evolution of unit cell parameters and volume of $PbFeBO_4$. Open symbols refer to the high-pressure phase.

The *c* unit cell parameter decreases by ~8% in the entire compression range, but displays a temporary slowdown in compression (between 8 and 18 GPa). The most compressible is the *a* parameter, decreasing by ~11% between ambient pressure and 11.8 GPa. Above this pressure the compression of the *a* parameter slows down noticeably and it is only ~6% between 11.8 GPa and 71 GPa. Since compressibility along the *a*-axis is much higher as compared to the *b*-axis, it points to the fact that any major pressure-induced changes in the crystal structure of $PbFeBO_4$ are likely to occur along the *a*- and *c*-axes.

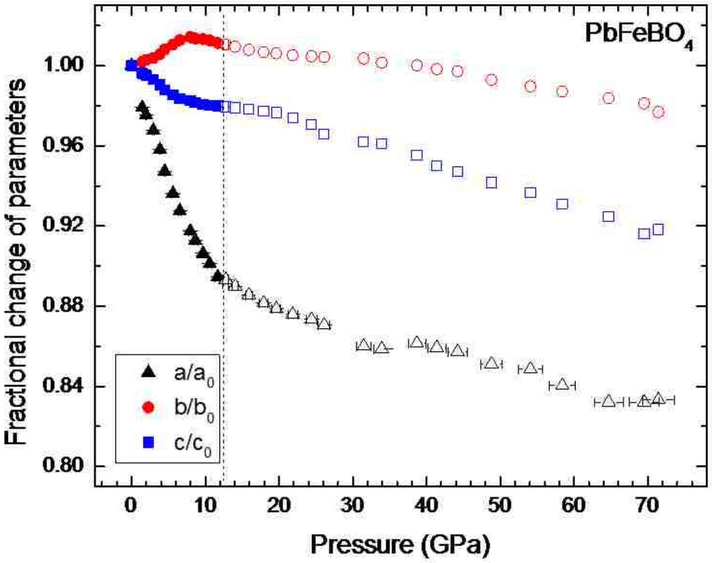

Figure 45. Pressure-driven fractional change of unit cell parameters in PbFeBO$_4$. Open symbols refer to the high-pressure phase.

11.8 GPa is also the pressure threshold from which the unit cell volume curve appears to markedly change its rate of compression, all of which points to a structural rearrangement. *In situ* high pressure Raman spectroscopy studies carried out for this compound also indicate changes in vibrational modes around 12 GPa and the appearance of new vibrational modes (see the chapter on Raman spectroscopy studies).

4.4.2. High-Pressure Synchrotron XRD of PbAlBO$_4$

High-pressure ADXRD patterns of mullite-type PbAlBO$_4$ phases were collected in-situ in a DAC, on compression from 0.5 GPa to 111.8 GPa. Figure 46 shows x-ray diffraction patterns measured for PbAlBO$_4$. As pressure is increased all diffraction lines shift towards higher 2θ angles i.e. lower d-spacings. According to the ADXRD patterns the compression appears to be continuous up ~54 GPa. Above this pressure we observe some changes in relative intensities and the appearance of new diffraction lines in the low 2θ region (Figure 46). The new lines appear to persist up to the highest pressure investigated, 111.8 GPa.

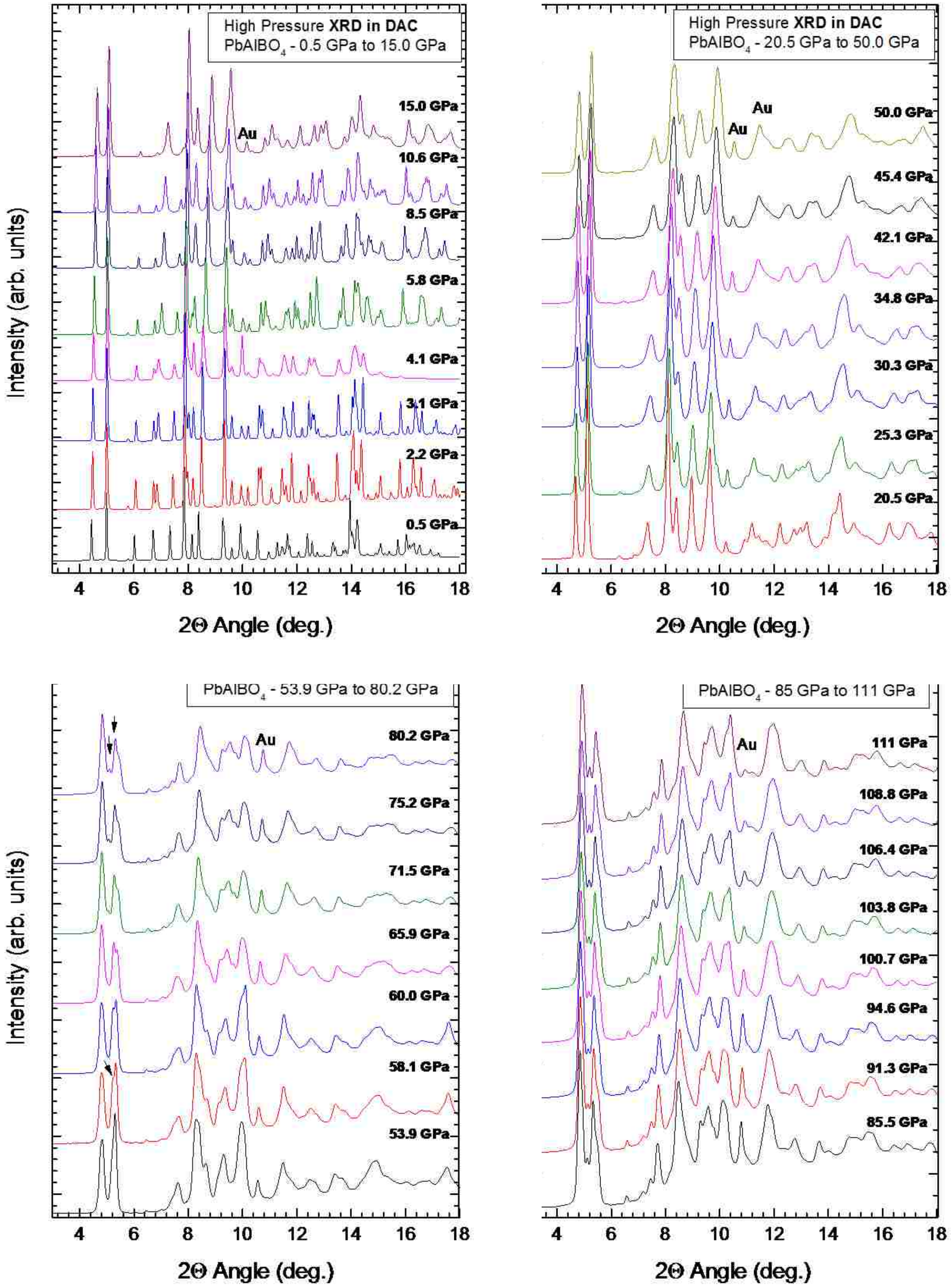

Figure 46. High-pressure ADXRD patterns of the mullite-type PbAlBO$_4$.
The ADXRD patterns were measured in-situ in a DAC on compression from ambient pressure up to 111 GPa.

In order to follow the pressure evolution of unit cell parameters and unit cell volumes of mullite-type $PbAlBO_4$, Rietveld full-profile structural refinements were performed on all x-ray diffraction patterns collected. At ambient pressure and temperature $PbAlBO_4$ has an orthorhombic crystal lattice and crystallizes in the space group *Pnam* (62). For starting the ambient pressure refinements we used the initial structure of Murshed *et al.*, [104] which is in the usual mullite setting, i.e. with the octahedral chains running along the *c* crystallographic axis.

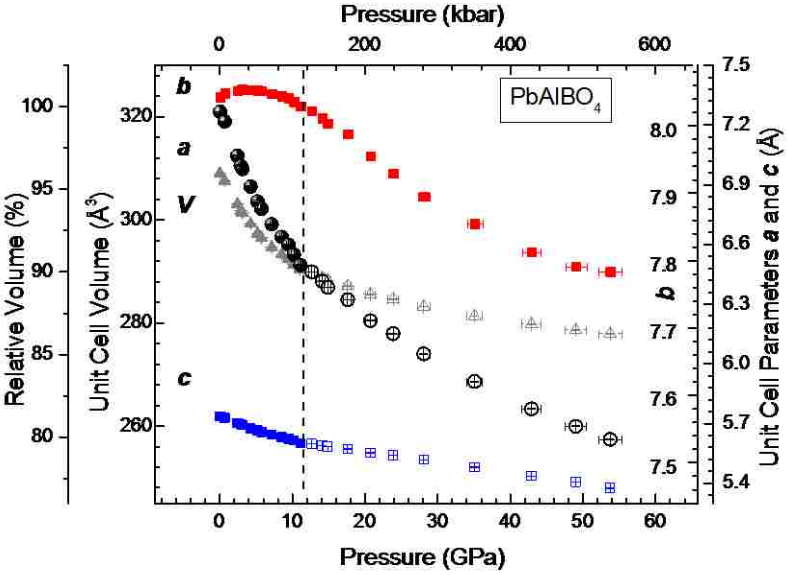

Figure 47: Pressure-driven evolution of unit cell parameters and volume of $PbAlBO_4$.

The pressure-induced evolution of unit cell parameters *a*, *b*, and *c* and of cell volumes *V* are given in Figure 47, while relative fractional changes of unit cell parameters are shown in Figure 48. As with $PbFeBO_4$, the Rietveld refinements of high-pressure X-ray diffraction data of $PbAlBO_4$ helped to reveal some unexpected and interesting features of the process of compression. As the $PbAlBO_4$ structure is compressed between ambient pressure and ~3GPa, the *a* and *c* unit cell parameters decrease, but the *b* unit cell parameter increases. This expansion under pressure or negative axial compressibility is ~ 0.15% up to

3 GPa (Figure 47). As with the previous sample, $PbAlBO_4$ shows evidence of negative linear compressibility (NLC, discussed in detail in a section below), but in a smaller pressure range (up to 3 GPa vs. up to 8 GPa as observed for $PbFeBO_4$).

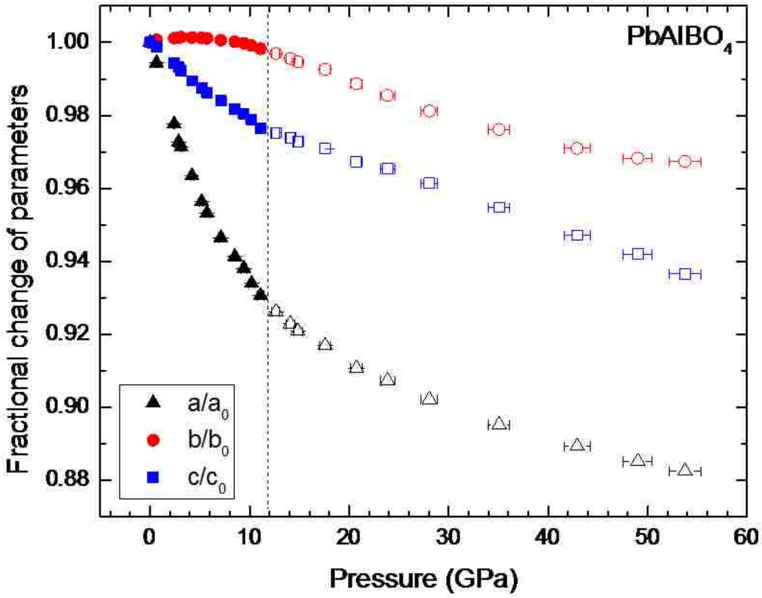

Figure 48: Pressure-driven fractional change of unit cell parameters in $PbAlBO_4$.

With pressure increase above ~3 GPa the *b* parameter slowly decreases by ~3.3% on compression up to 54 GPa. The *c* unit cell parameter displays a small discontinuity and decreases by ~2.3% up to 11 GPa and by ~4% from 11 up to 54 GPa. The most compressible is again the *a* parameter, decreasing by ~7% between ambient pressure and 11 GPa. Above this pressure the compression of the *a* parameter slows down noticeably and it is only ~4.7% between 11 GPa and 54 GPa. Since compressibility along the *a*-axis is much higher as compared to the *b*-axis, it points to the fact that any major pressure-induced changes in the crystal structure of $PbFeBO_4$ are likely to occur along the *a*- and *c*-axes.

11 GPa is also the pressure threshold from which the unit cell volume curve appears to change its rate of compression, all of which points to a structural rearrangement. *In situ* high pressure Raman spectroscopy studies carried out for this compound also indicate

changes in vibrational modes around 11 GPa and the appearance of new vibrational modes (see the chapter on Raman spectroscopy studies).

4.4.3. High-Pressure Raman Spectroscopy of $PbFeBO_4$

Figure 49 shows the progression of Raman spectra of $PbFeBO_4$ measured as a function of increasing pressure between ambient and 20.4 GPa. Figure 50 shows the pressure dependent shift of frequencies and the assignment of those frequencies to vibrations of specific groups. Raman (and infrared) mode assignment was previously published by the author and collaborators. [37] In the following discussion vibrational modes are referred by their ambient pressure position or by their position at the lowest pressure they become visible.

Vibrations due to heavy molecular groups are located at lowest frequencies: Pb-O vibrations are between 50 and 280 cm^{-1} (Figure 50, panels a, b, c, and d); vibrations of the lighter Fe-O groups are located between 260 and 560 cm^{-1} and finally vibrations of the lightest B-O groups are clustered above 600 cm^{-1} and up to 1250 cm^{-1}. Therefore the vibrations due to different molecular groups are rather well separated from each other.

A phase transition is indicated by changes in vibrational modes prior to 12 GPa. Three modes disappear at 10 GPa: the O—Pb—O rocking at 191 cm^{-1} and at 193 cm^{-1} at ~8GPa, the O—Fe—O symmetric stretching and the O—Pb—O asymmetric stretching at 264 cm^{-1} at ~11 GPa and finally the B—O asymmetric stretch at 1220 cm^{-1} at 11 GPa. Some vibrational energies decrease under applied pressure. Remarkably, the Pb-O stretching mode at 55 cm^{-1} softens up to ~8 GPa, but above that pressure it steadily increases towards higher frequencies.

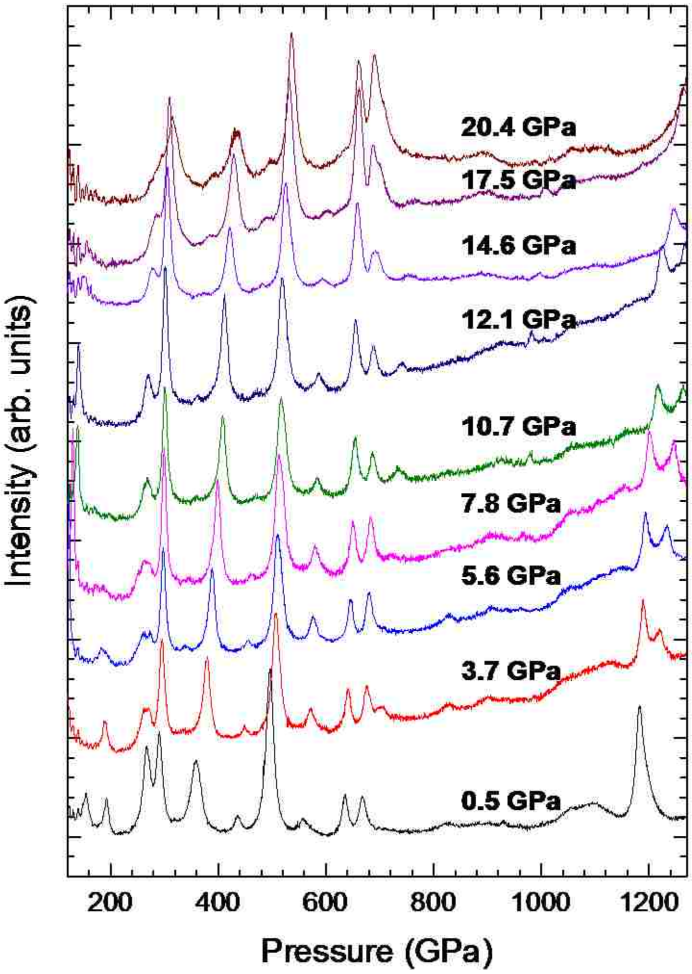

Figure 49. Selected Raman spectra of $PbFeBO_4$ measured as a function of increasing pressure.
The range was between ambient pressure up to 20 GPa. Vibrational bands below 100cm^{-1} (not shown) were fitted after subtraction of peaks due to scattering from air.

Another indication of structural changes around 12 GPa is given by the O-Pb-O wagging mode at 65 cm^{-1}, which first experiences softening up to ~8 GPa and then above this pressure it linearly increases in frequency. The theoretical calculations of mode behavior versus pressure, and particularly the non-linear behavior of some modes, are consistent with experimental observations.

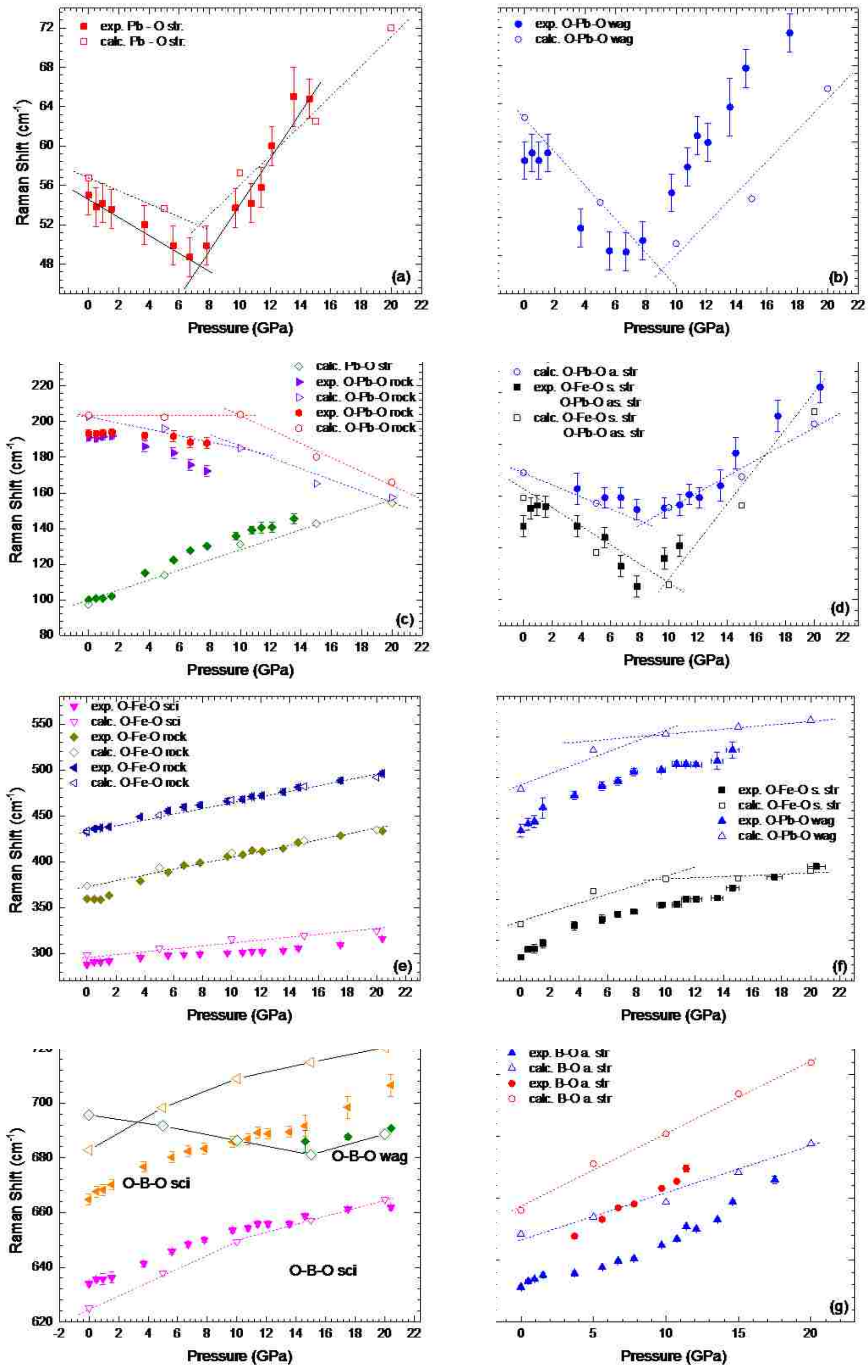

Figure 50. Pressure-dependence of Raman modes of PbFeBO$_4$.
Vibrations assumed new (due to the phase transition) are marked with star symbols.

The softening of vibrational mode frequencies reflects the expected symmetry lowering at the transition pressure. The pressure dependencies of the phonon frequencies revert to positive values in the high pressure phase. No new vibrational modes are observed in the pressure range up to 20.4 GPa.

It is interesting to note that most changes in vibrational mode behavior are associated with changes around the Pb^{2+} cation. These point to the fact that Pb^{2+} plays an important role in the phase transition.

Experimental and theoretical Raman modes for $PbFeBO_4$ are shown in Table 20 along with the experimental and theoretical mode-Grüneisen parameters. Also indicated are the mode type and symmetry for all modes. For the bulk modulus the experimental value of 73(3) GPa (derived later in this work) was used. The values for v_i were obtained from the Raman spectrum at ambient pressure or, in the case of non-linear modes, from the extrapolation of the linear fits of the pressure dependences of the Raman shifts to ambient pressure. In the case of non-linear modes two values of mode Grüneisen parameters are reported. Calculations for the mode Grüneisen parameter of any modes that appears above 12 GPa (or changes its slope above 12 GPa) use the bulk modulus of the high pressure phase. The correspondence between calculated and experimental mode-Grüneisen parameters is good. With increasing pressure most Raman bands shift towards higher frequencies, i.e. show positive mode-Grüneisen parameters. However all the modes describing Pb—O vibrations (with one exception) show a negative value of mode-Grüneisen parameter before 12 GPa, which is the assumed pressure of phase transition. Except for modes which display softening ($-1.6< \gamma < -0.2$), the mode-Grüneisen parameters range from $0.1 < \gamma < 0{:}8$ with three modes having $\gamma \sim 2$ or 3. Most mode-Grüneisen parameters values are comparable to with typical values of alumino-silicate mullite and sillimanite.

Table 20. Raman modes for $PbFeBO_4$ and its mode Grüneisen parameters.
Experimentally obtained Raman modes for $PbFeBO_4$ and mode Grüneisen parameters on compression to 88 GPa. Raman modes marked with * appear at higher *p*, so for those the ω_i value is derived from an extrapolation to ambient *p*. Errors in refer to the last significant figure. Theoretical values are from calculations by Prof. Mendive and M. Curti. [37]

$(\omega_i)_{DFT}$	$(\omega_i)_P$ P=0.0001 GPa T = 298 K	Pressure range for γ_i /GPa	$(d\gamma_i/dp)_{EXP}$	$(d\gamma_i/dp)_{DFT}$	$(\gamma_i)_P$	$(\gamma_i)_{DFT}$	Irr. Rep.	Assignment
56.8	55(2)	0.0 – 7.8	-0.75(9)	-0.62	-1.0(1)	-0.91(6)	A_g	Pb-O stretch
56.8	55(2)	9.7 - 17.5	2.8(4)	1.5(2)	3.7(6)	2.2(3)	A_g	Pb-O stretch
70.5	68(2)	0.0 – 7.8	-1.5(2)	-1.79	-1.6(2)	-2.1(1)	B_{2g}	O-Pb-O wagg
70.5	68(2)	9.7 - 17.5	2.2(2)	1.6(4)	2.4(3)	1.9(5)	B_{2g}	O-Pb-O wagg
97.4	100(1)	0 - 17.5	3.5(1)	2.9(2)	2.6(1)	2.5(2)	A_g	Pb-O stretch
202.9	191(2)	0 - 7.8	-2.5(3)	-1.8(2)	-1.0(1)	-0.74(9)	B_{3g}	O-Pb-O scissor
202.9	–	10.0 – 20.0	–	-2.8(7)	–	-1.2(3)		
203.7	193(2)	0-7.8	-0.7(1)	-0.2	-0.26(4)	-0.08(1)	B_{1g}	O-Pb-O rock
203.7	–	10.0 – 20.0	–	-3.8(6)	–	-1.6(3)		
269.7	264(2)	0.0 – 7.8	-1.7(3)	-1.7(3)	-0.47(9)	-0.5(1)	B_{1g}	O-Fe-O s. stretch + O-Pb-O a. stretch
269.7	264(2)	9.7 – 10.8	2.7(1)	3.3(2)	0.75(4)	1.02(9)	B_{1g}	O-Fe-O s. stretch + O-Pb-O a. stretch
274.5	275(1)*	3.7 – 7.8*	-0.9(2)*	-1.2*	-0.24(5)	-0.36(2)	B_{2g}	O-Pb-O a. stretch
274.5	275(1)*	9.7 – 20.4*	2.4(2)*	1.6(2)*	0.64(6)	0.48(7)	B_{2g}	O-Pb-O a. stretch
298.5	288(1)	0.0 - 20.4	1.15(6)	1.3(1)	0.29(2)	0.36(4)	A_g	O-Fe-O scissor
373.8	360(2)	0.0 - 20.4	4.1(2)	3.0(2)	0.83(5)	0.67(6)	B_{1g}	O-Fe-O rock
433.7	432(2)	0.0 - 20.4	3.04(8)	3.0(2)	0.51(3)	0.57(5)	B_{3g}	O-Fe-O rock
507.9	492(1)	0.0 - 20.4	2.1(1)	2.2(6)	0.31(2)	0.4(1)	A_g	O-Fe-O s. stretch
507.9	–	10.0 – 20.0	–	0.80(1)	–	0.13(1)	A_g	O-Fe-O s. stretch
574.4	554(3)	0.0 – 14.6	2.4(2)	2.7(6)	0.32(3)	0.39(9)	B_{1g}	O-Pb-O wagg
574.4	–	10.0 – 20.0	–	0.672(2)	–	0.10(1)	B_{1g}	O-Pb-O wagg
625.1	634(1)	0 - 20.4	1.55(9)	2.0(1)	0.18(1)	0.27(2)	B_{1g}	O-B-O scissor
682.8	665(2)	0 - 20.4	1.82(7)	1.8(2)	0.20(1)	0.22(3)	B_{2g}	O-B-O scissor
695.6	675(2)*	14.3 – 20.4	0.8(1)*	1.51*	0.23(4)	0.42(4)	A_g	O-B-O wagg
1221.0	1178(1)	0 – 17.5	4.8(3)	3.6(3)	0.30(2)	0.24(3)	A_g	B-O a. stretch
1240.2	1244(3)*	3.7 - 11.4	6.8(3)*	5.9(2)*	0.40(2)	0.39(3)	B_{1g}	B-O a. stretch

In fact, the structurally related 2:1 mullite and sillimanite, an Al_2SiO_5 polymorph, show mode-Grüneisen parameter values $0.06 < \gamma < 1.3$ (sillimanite) and $0.01 < \gamma < 1.8$ (mullite) with typical values from 0.2 to 0.9 with the exception of some *negative* parameters at frequencies of 236 cm^{-1} and 311 cm^{-1}.

Mode Grüneisen parameters were previously published by the author and collaborators. [37] However, that work did not take into consideration the phase transition taking place ~12 GPa (and the associated high-pressure bulk modulus) as well as the non-linear behavior of some modes.. Here any mode Grüneisen parameters with non-linear behavior were updated to display two values, one for each pressure range (see for example the first two entries of Table 20).

4.4.4. High-Pressure Raman Spectroscopy of $PbAlBO_4$

Figure 51 shows the progression of Raman spectra of $PbAlBO_4$ measured as a function of increasing pressure between ambient and 88 GPa. Figure 52 shows the pressure dependent shift of frequencies and the assignment of those frequencies to vibrations of specific groups. Raman (and infrared) mode assignment was previously published by the author and collaborators.[38] In the following discussion vibrational modes are referred by their ambient pressure position or by their position at the lowest pressure they become visible. As expected the vibrations of heavy molecular groups are located at lowest frequencies: Pb-O vibrations are between 50 and 280 cm^{-1}; vibration of the lighter Al-O groups are located between 300 and 550 cm^{-1} and finally vibration of the lightest B-O groups are above 500 cm^{-1}. Vibrations due to different molecular groups are rather well separated from each other, which allows a more certain attribution of new vibrational modes appearing at during compression. The first phase transition is indicated by changes in vibrational modes around 10 GPa. Three modes disappear at 10 GPa: the Pb-O stretching at 230 cm^{-1}, O-B-O scissoring at 675 cm^{-1}, B-O stretching at 1224 cm^{-1}. Some vibrational energies decrease under applied pressure. Interestingly the Pb-O stretching mode at 55 cm^{-1} softens slightly up to 10 GPa, but above that pressure it moves linearly towards higher frequencies.

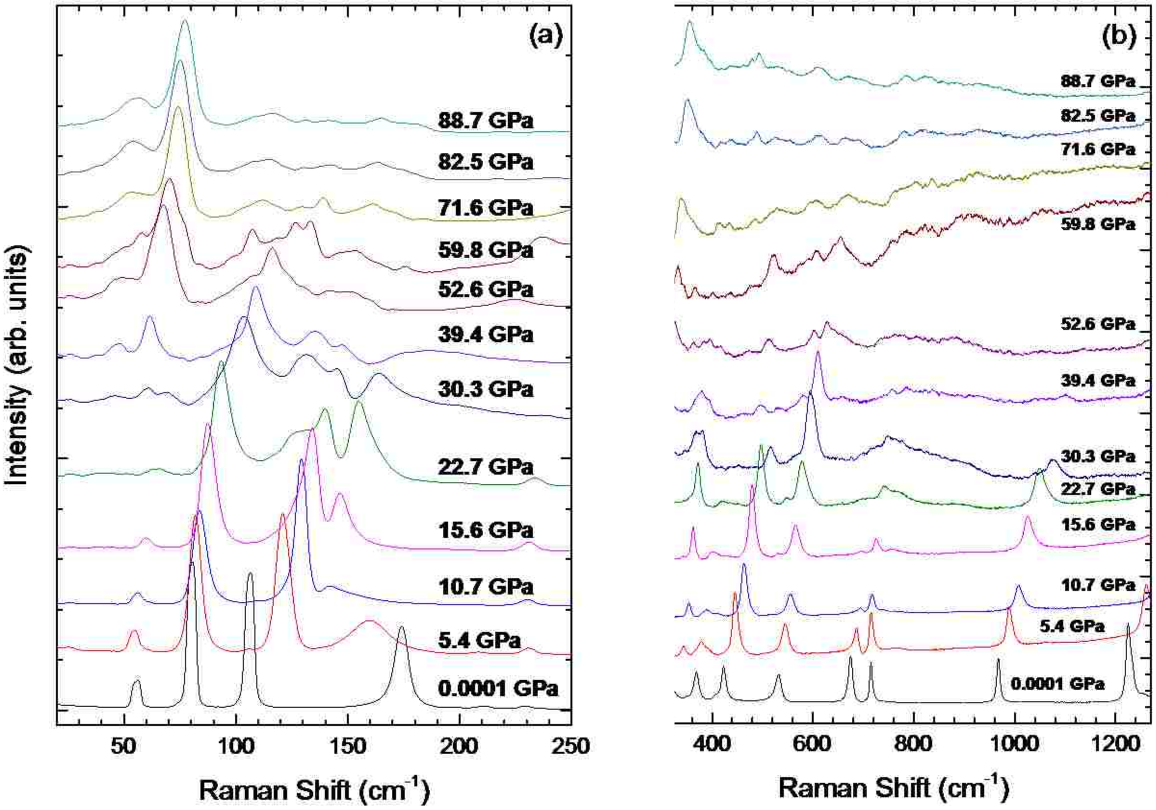

Figure 51. Raman spectra of $PbAlBO_4$ measured as a function of pressure from ambient and 88 GPa.

Another indication of structural changes around 10 GPa is given by the O-Pb-O scissoring mode at 174 cm^{-1}, which first experiences softening between ambient pressure and 10 GPa and above this pressure linearly increases in frequency. Mode splitting is observed to occur for a few vibrations at different pressures: the 106 cm^{-1} Pb—O stretch splits into two modes ~18 GPa, the 80 cm^{-1} O—Pb—O wag splits into two at ~54 GPa, the Al—O stretch at 325 cm^{-1} splits at ~26 GPa.

It is interesting to note that most changes in vibrational mode behavior are associated with changes around the Pb^{2+} cation. This points to the fact that Pb^{2+} plays an

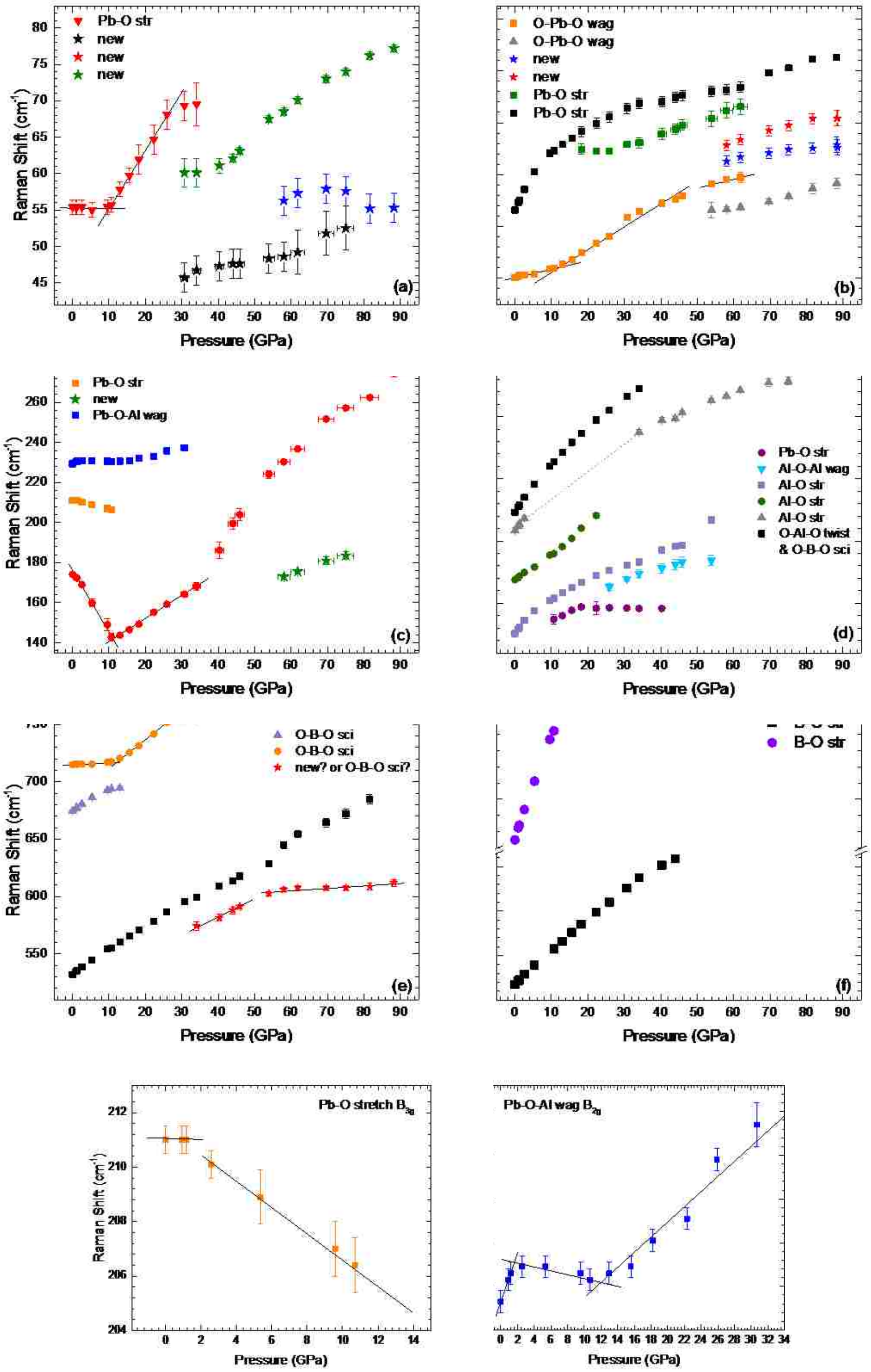

Figure 52. Pressure-dependence of Raman modes of $PbAlBO_4$.
Vibrations assumed new (due to the phase transition) are marked with star symbols.

important role in the phase transition. The softening of vibrational mode frequencies together with mode splitting reflects the expected symmetry lowering at the transition pressure. The pressure dependencies of the phonon frequencies revert to positive values in the high pressure phase.

As shown earlier in high-pressure X-ray diffraction data a second structural phase transition occurs between 50 and 60 GPa. This is supported by several features observed in high-pressure Raman spectra. It is interesting to note that again the majority of new vibrational bands are associated with changes around the Pb^{2+} cation. These point to the fact that Pb^{2+} plays an important role in the phase transition. The phase transition is evidenced by the appearance of 7 new vibrational modes that are present all the way to 88 GPa. Three new vibrational modes are observed as early as ~30GPa: 46 cm^{-1}, 60 cm^{-1} in the region of Pb—O stretching and a mode ~574 cm^{-1} in the O—B—O scissoring region.

New distinct Raman bands are also observed ~58GPa: a band at ~ 55 cm^{-1} (most probably a Pb-O stretching), bands at 125 cm^{-1} and 131 cm^{-1} (which could be Pb—O stretching or wagging modes) and a mode at 173 cm^{-1} (in the Pb—O scissoring region). The band at 574 cm^{-1} could also be the result of pressure-driven splitting of Raman peaks composed of more than one vibration into separate peaks. With the second phase transition several modes disappear as well: the Pb—O stretch at 130 cm^{-1} disappears at ~62 GPa, the Pb—O—Al wag at 229 cm^{-1} disappears ~30 GPa, the Al—O stretch at 325 cm^{-1} and the Al—O—Al wag at 363 cm^{-1} both disappear ~54 GPa, and finally the B—O stretch at 967 cm^{-1} disappears ~44 GPa.

Experimental and theoretical Raman modes for $PbAlBO_4$ are shown in Table 21 along with the experimental mode Grüneisen parameters. Also indicated are the mode type and symmetry for all modes. For the bulk modulus the experimental value of 79(6) GPa (derived later in this work) was used.

Table 21. Raman modes for $PbAlBO_4$ and its mode Grüneisen parameters.
Experimentally obtained Raman modes for $PbAlBO_4$ as well as corresponding mode Grüneisen parameters obtained from compression to 88 GPa. Raman modes marked with ***** appear at higher pressures, so for those the ν_i value is derived from an extrapolation to ambient pressure. Errors in parenthesis refer to the last significant figure. Theoretical values at ambient *p* and *T* are from calculations by C. Mendive and M. Curti. [38]

$(\omega_i)_{DFT}$ P = 0.0001GPa T = 0 K	$(\omega_i)_P$ P = 0.0001GPa T = 298 K	Pressure range for γ_i /GPa	$d\gamma_i/dp$	$(\gamma_i)_P$	Irr. Rep.	Assignment
–	41.2(8)*	30.7 – 75.0*	0.14(1)	0.66(8)	–	*new*
–	49.1(7)*	30.7 – 88.2*	0.32(1)	1.3(1)	–	*new*
59.54	55.4(9)	0.0 – 10.7	0.01(2)	0.01(1)	A_g	Pb-O stretch
59.54	55.4(9)	13.0 – 34.0	0.65(5)	2.3(3)	A_g	Pb-O stretch
–	60(3)*	58.0 – 88.2*	-0.06(4)	-0.19(4)	–	*new*
77.42	80.3(2)	0.0 – 10.7	0.31(3)	0.32(4)	B_{1g}	O-Pb-O wagg
77.42	80.3(2)	13.0 – 25.9	0.86(2)	2.1(2)	B_{1g}	O-Pb-O wagg
77.42	80.3(2)	30.7 – 61.8	0.50(2)	1.2(1)	B_{1g}	O-Pb-O wagg
79.32	89(1)*	53.9 – 88.2*	0.31(2)	0.68(7)	B_{2g}	O-Pb-O wagg
104.33	106.3(2)	0.0 – 10.7	2.0(1)	1.6(1)	B_{3g}	Pb-O stretch
104.33	106.3(2)	13.0 – 81.6	0.39(2)	0.71(7)	B_{3g}	Pb-O stretch
–	113(3)*	58.0 – 88.2*	0.33(3)	0.57(7)	–	*new*
–	115(2)*	58.0 – 88.2 *	0.18(2)	0.30(4)	–	*new*
119.65	119(1)*	18.2 – 61.8	0.42(3)	0.68(8)	B_{3g}	Pb-O stretch
–	137(3)*	58.0 – 75.0*	0.63(4)	0.9(1)	–	*new*
180.79	174.1(5)	0.0 – 10.7	-2.9(1)	-1.4(1)	A_g	O-Pb-O scissor
180.79	174.1(5)	13.3 – 34.1	1.17(2)	1.3(1)	A_g	O-Pb-O scissor
180.79	174.1(5)	40.3 – 88.2	1.8(1)	2.0(2)	A_g	O-Pb-O scissor
217.88	211.0(5)	0.0 – 10.7	-0.45(1)	-0.18(1)	B_{3g}	Pb-O stretch
234.86	229.3(5)	0.0 – 30.7	0.22(3)	0.08(1)	B_{2g}	Pb-O-Al wagg
315.72	322.6(9)*	10.7 – 18.2	1.35(6)	0.35(3)	B_{3g}	Al-O-Al wagg
315.72	322.6(9)*	22.3 – 40.3	-0.02(1)	-0.01(1)	B_{3g}	Al-O-Al wagg
349.81	346(4)*	25.9 – 53.9	0.76(9)	0.43(6)	A_g	Al-O-Al twist
334.66	326(1)	0.0 – 10.7	2.6(2)	0.66(6)	A_g	Al-O stretch
334.66	326(1)	13.0 – 53.9	1.33(7)	0.79(8)	A_g	Al-O stretch
366.19	368.9(2)	0.0 – 22.3	2.40(7)	0.54(4)	B_{2g}	Al-O-Al twist
409.74	408.5(2)	0.0 – 2.6	3.8(3)	0.77(8)	B_{1g}	Al-O stretch
409.74	408.5(2)	34.1 – 75.0	1.02(6)	0.21(2)	B_{1g}	Al-O stretch
415.57	423.1(2)	0.0 – 34.1	2.81(8)	0.55(4)	A_g	Al-O-Al twist & O-B-O sci
–	525(3)	34.1 – 53.9	1.44(6)	0.53(5)	–	*new*
–	525(3)	58.0 – 88.2	0.16(4)	0.06(2)	–	*new*
536.09	531.9(2)	0.0 – 53.9	1.75(4)	0.27(2)	A_g	O-B-O scissor
536.09	531.9(2)	58.0 – 81.6	1.61(8)	0.59(6)	A_g	O-B-O scissor
669.50	674.6(2)	0.0 – 13.0	1.5(1)	0.18(2)	A_g	O-B-O scissor
712.33	714.9(2)	0.0 – 10.7	0.24(3)	0.03(1)	B_{2g}	O-B-O scissor
712.33	714.9(2)	13.0 – 25.9	2.47(9)	0.67(6)	B_{2g}	O-B-O scissor
712.33	714.9(2)	30.7 – 44.0	0.37(7)	0.10(2)	B_{2g}	O-B-O scissor
975.06	967.4(2)	0.0 – 44.0	3.11(9)	0.27(2)	A_g	B-O symm stretch
1261.78	1225.1(2)	0.0 – 10.7	6.2(1)	0.42(3)	B_{2g}	B-O assym stretch

The values for v_i were obtained from the Raman spectrum at ambient pressure or, in the case of non-linear modes, from the extrapolation of the linear fits of the pressure dependences of the Raman shifts to ambient pressure. In the case of non-linear modes two values of mode Grüneisen parameters are reported. Calculations for the mode Grüneisen parameter of any modes that appear above 12 GPa (or changes its slope above 12 GPa) use the bulk modulus of the high pressure phase.

With increasing pressure most Raman bands shift towards higher frequencies, i.e. show positive mode-Grüneisen parameters. However all the modes describing Pb—O vibrations (with one exception) show a negative value of mode-Grüneisen parameter before 12 GPa, which is the assumed pressure of the phase transition. Except for modes which display softening, the mode-Grüneisen parameters range from $0.01 < \gamma < 1.5$ with three modes having $\gamma \sim 2$. Most mode-Grüneisen parameters values are comparable to with typical values of alumino-silicate mullite and sillimanite and are also comparable to the mode-Grüneisen parameters obtained for $PbFeBO_4$.

The structurally related 2:1 mullite and sillimanite, an Al_2SiO_5 polymorph, show mode-Grüneisen parameter values between 0.06 and 1.3 (sillimanite) and between 0.01 and 1.8 (mullite) with typical values from 0.2 to 0.9 with the exception of some negative parameters at frequencies of 236 cm^{-1} and 311 cm^{-1}. Such values are comparable to the ones found for $PbAlBO_4$ and $PbFeBO_4$.

4.4.5. Phase transition in $PbMBO_4$

4.4.5.1. Structural Phase Transition in $PFeBO_4$

The combination of the observations from results of high-pressure Raman spectroscopy and high-pressure X-ray diffraction of $PbFeBO_4$ and a detailed analysis of

Rietveld structural refinements led the author to propose a new pressure-driven phase transition in $PbFeBO_4$.

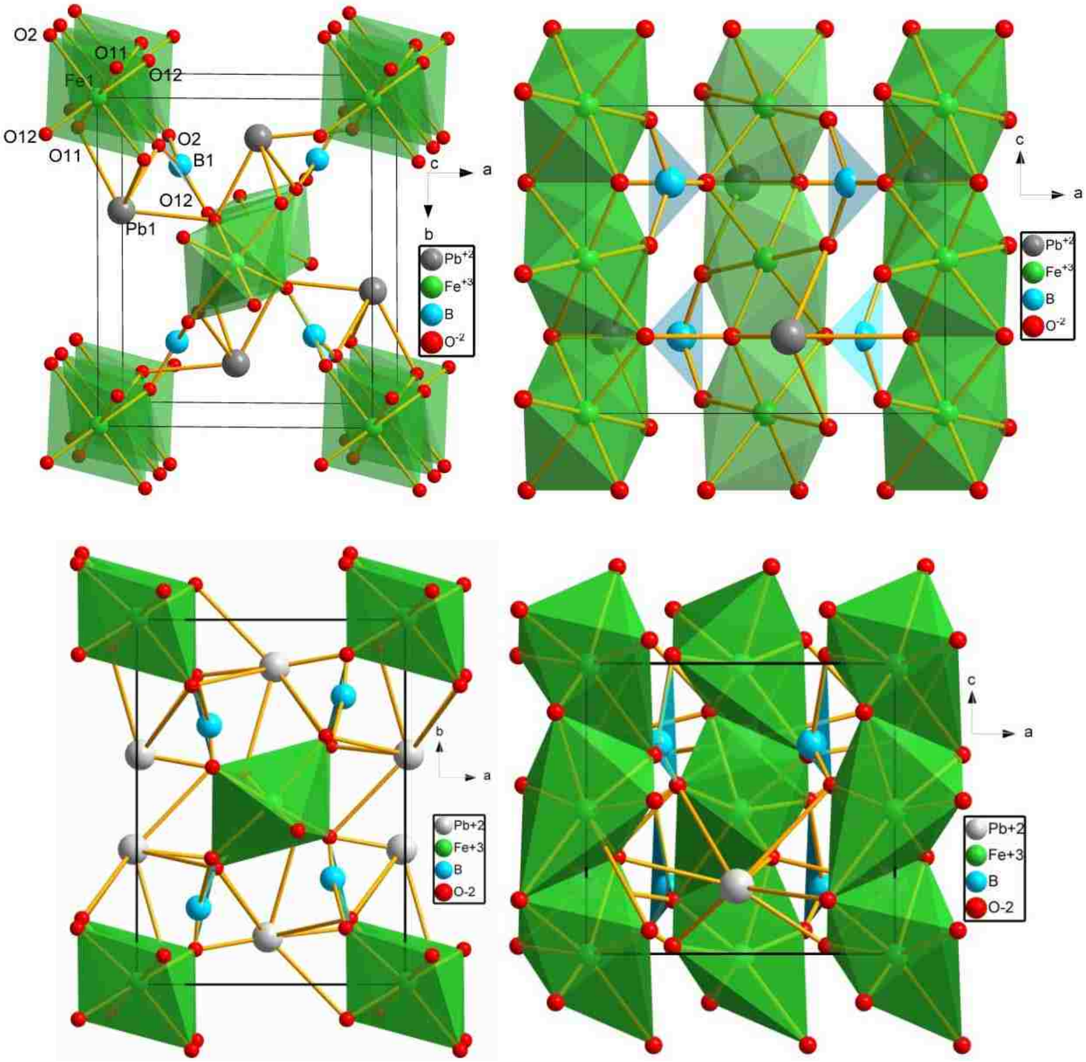

Figure 53. Crystal structure of $PbFeBO_4$ at 0.0001GPa and ~14 GPa.
The top structures are for 0.0001 GPa and the bottom structures are for 14 GPa. Two orientations are shown: in the *a*-*b* plane and in the *c*-*a* plane.

The crystal structure of $PbFeBO_4$ at ~14 GPa is shown in Figure 53 and examples of results of Rietveld refinements for both phase-I and phase-II are shown in Table 22 and Figure 54 and Figure 55. Around 11.8 GPa $PbFeBO_4$ mullite undergoes a phase transition from the orthorhombic *Pnma* phase (space group #62) to another phase with orthorhombic symmetry: the proposed space group for this transition is *Pna*2₁ (#33). *Pna*2₁ (referred to, from now on, as phase-II) is a maximal non-isomorphic subgroup of *Pnma* (referred to, from now on, as phase-I). The high pressure phase *Pna*2₁ remains stable up to at least 71 GPa. On pressure decrease the phase transition is fully reversible.

Table 22. Results of Rietveld structural refinements of $PbFeBO_4$ at high pressures.

$PbFeBO_4$ - 9.7							
Crystal system	orthorhombic		***a** (Å)*	6.344 (1)		***p** (GPa)*	9.7(3)
Space group	*Pnam* (62)		***b**(Å)*	8.474 (2)		***V (Å^3)***	315.1(1)
Z	2		***c**(Å)*	5.861 (2)		***Rwp***	3.44
Label	***Site***	***x***	***y***	***z***	***Atom***	***Occ.***	***B (temp.)***
Pb1	4a	0.01896(63)	0.63423(28)	0.25	Pb^{+2}	1	0.23(8)
Fel	4c	0	0	0	Fe^{+3}	1	0.23(8)
B	4c	0.276(16)	0.269(11)	0.25	B	1	0.23(8)
O11	4c	0.3598(37)	0.5867(34)	0.25	O^{-2}	1	0.23(8)
O12	4c	0.2016(38)	0.0861(37)	0.25	O^{-2}	1	0.23(8)
O2	8d	0.2816(39)	0.3148(31)	0.0324(23)	O^{-2}	1	0.23(8)

$PbFeBO_4$ - 14 GPa							
Crystal system	orthorhombic		***a** (Å)*	6.215(1)		***p**(GPa)*	14.0(4)
Space group	*Pna*2_1 (33)		***b**(Å)*	8.443(2)		***V (Å^3)***	307.0(1)
Z	2		***c**(Å)*	5.851(2)		***Rwp***	2.77
Label	***Site***	***x***	***y***	***z***	***Atom***	***Occ.***	***B (temp.)***
Pb1	4a	0.0131(60)	0.6296(23)	0.7325(30)	Pb^{+2}	1	0.7 (1)
Fel	4a	0.003(10)	0.0047(58)	-0.009(6)	Fe^{+3}	1	0.7 (1)
B	4a	0.230(11)	0.2101(82)	0.722(37)	B	1	0.7 (1)
O11	4a	0.4(1)	0.5788(32)	0.8326(51)	O^{-2}	1	0.7 (1)
O12	4a	0.2178(30)	0.0958(35)	0.6851(81)	O^{-2}	1	0.7 (1)
O2a	4a	0.2789(53)	0.3460(53)	1.0270(38)	O^{-2}	1	0.7 (1)
O2a	4a	0.7045(46)	0.6804(45)	0.0802(37)	O^{-2}	1	0.7 (1)

The crystal structure of phase II can derived from phase-I by moving the atomic sites of Pb1, Fe1, B1, O11 and O12 from special positions to free positions, while the O2 position is split into O2a and O2b. The coordination of the Pb^{2+} cation increases around the phase transition from [4] to [6 + 1]: three additional bonds are formed with O2a, O2b and O12 atoms.

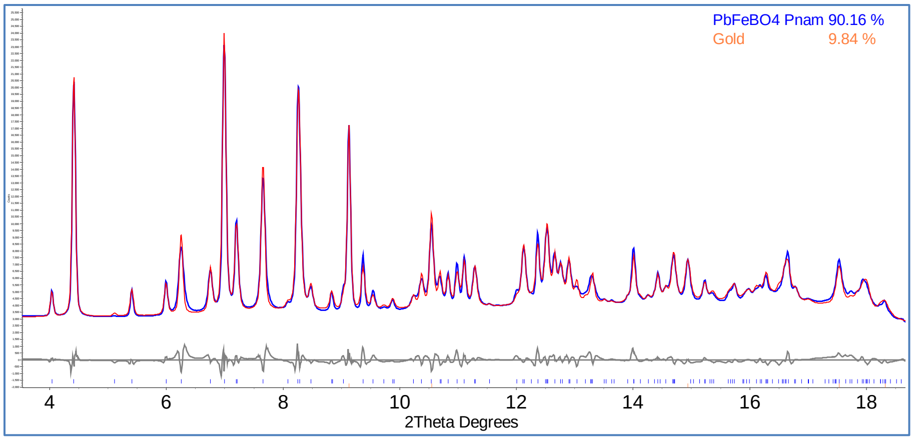

Figure 54 Example of Rietveld refinements: the low-pressure structure of $PbFeBO_4$ at ~9.7GPa.

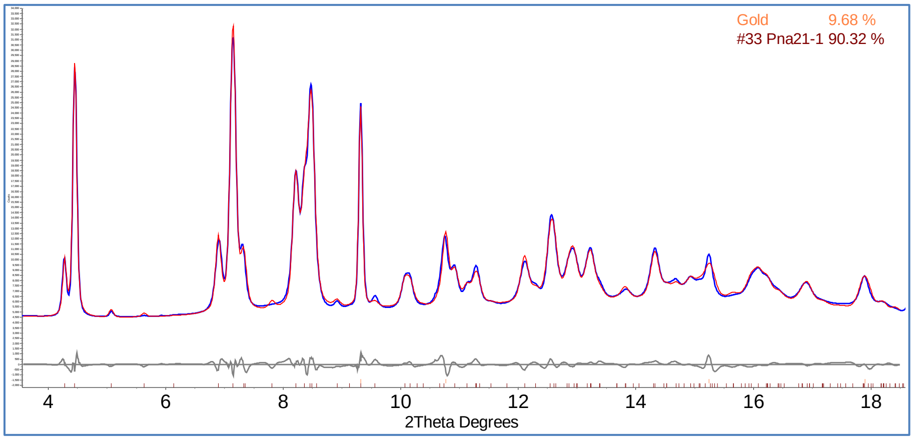

Figure 55. Example of Rietveld refinements: the high-pressure structure of $PbFeBO_4$ at ~14GPa.

In pressure dependent Raman spectroscopy measurements the softening of vibrational mode frequencies also reflects the expected symmetry lowering (mode splitting) at the transition pressure and it is accompanied by the appearance of new modes. The pressure dependencies of the phonon frequencies revert to positive values in the high pressure phase.

4.4.5.2. Two Structural Phase Transitions in $PAlBO_4$

The combination of the observations from results of high-pressure Raman spectroscopy and high-pressure X-ray diffraction of $PbAlBO_4$ and a detailed analysis of

Rietveld structural refinements led the author to propose this time not one, but two new pressure-driven phase transition in $PbAlBO_4$.

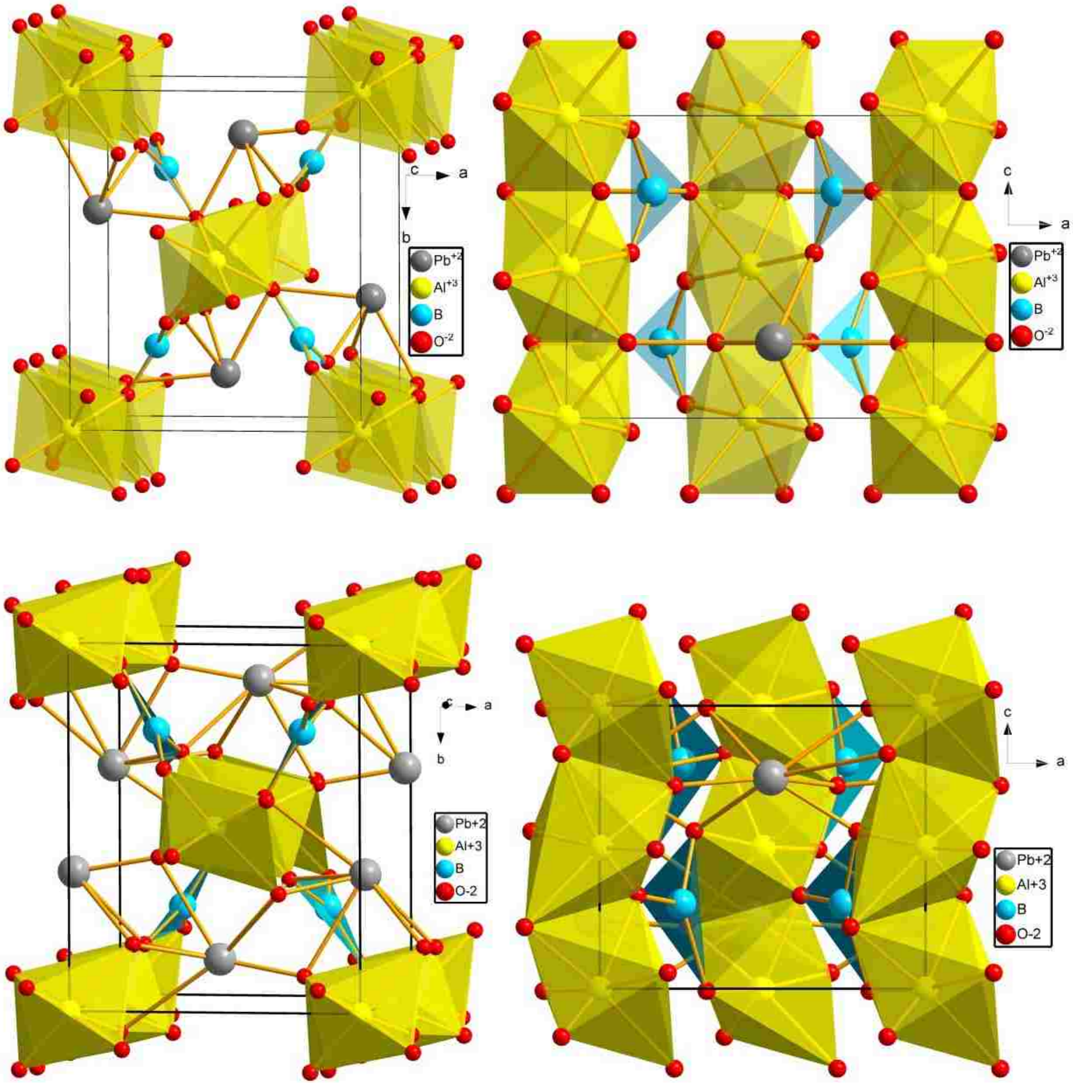

Figure 56. Crystal structure of $PbAlBO_4$ at 0.0001GPa and ~14 GPa.
The top structures are for 0.0001 GPa and the bottom structures are for 14 GPa. Two orientations are shown: in the ab-plane and in the ca-plane.

Just as was the case for $PbFeBO_4$ above, around 11.8 GPa $PbAlBO_4$ mullite undergoes a phase transition from the orthorhombic *Pnma* phase (space group #62) to another phase with orthorhombic symmetry: the proposed space group is $Pna2_1$ (#33). $Pna2_1$ (referred to, from now on, as phase-II) is a maximal non-isomorphic subgroup of *Pnma* (referred to, from now on, as phase-I). The high pressure phase $Pna2_1$ remains stable up to ~54 GPa. The crystal structure of phase II can derived from phase-I by moving the atomic sites of Pb1, Al1, B1, O11 and O12 from special positions to free positions, while the O2 position is split into two: O2a and O2b. The structure of phase-II is illustrated in Figure 56 and examples of Rietveld refinements for both phase-I and phase-II are shown in Figure 57 and Figure 58. Compared to ambient pressure the octahedral chains of phase-II structure have more of a zigzag-like shape. On pressure decrease both phase transition are fully reversible.

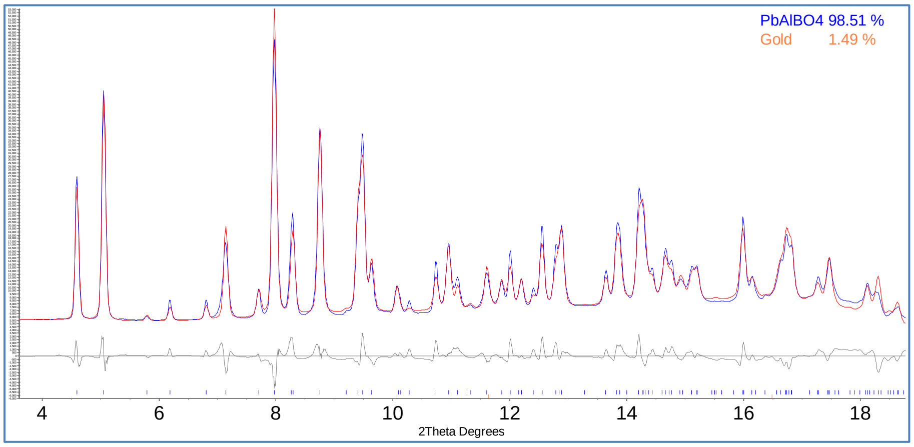

Figure 57. Example of Rietveld refinements: the low-pressure structure of $PbAlBO_4$ at ~9.7GPa.

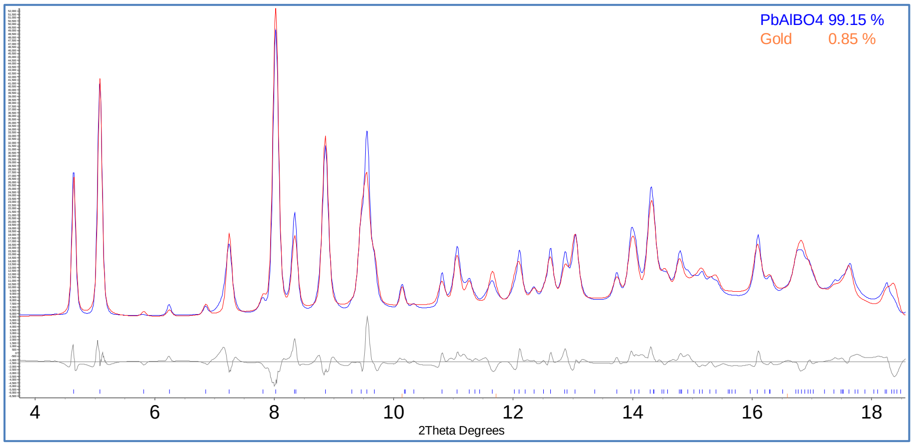

Figure 58. Example of Rietveld refinements: the high-pressure structure of $PbAlBO_4$ at ~14GPa.

The phase transition in $PbAlBO_4$ at ~12 GPa appears identical to the one observed in $PbFeBO_4$ at ~12 GPa. Due to these similarities in the pressure-dependent behavior, the compression of the asymmetric environment of the Pb^{2+} ion and its $6s^2$ lone electron pair can be thought to be reason for the phase transition. The mechanisms and characteristics of the phase-I → phase-II transition are discussed further in a section below.

In pressure dependent Raman spectroscopy measurements the softening of vibrational mode frequencies also reflects the expected symmetry lowering (mode splitting) at the transition from phase-I to phase-II and it is accompanied by the appearance of new modes. The pressure dependencies of the phonon frequencies revert to positive values in phase-II.

As shown earlier, $PbFeBO_4$ mullite compressed smoothly up to 77 GPa after the phase transition. On the other hand $PbAlBO_4$ undergoes a second pressure-driven phase transition at ~54 GPa, which can be readily seen from the change in relative intensity of diffraction lines and the appearance of new diffraction lines in the low 2θ region (Figure 46). In phase-II, there are only 2 *hkl* reflections in the 2θ region between 4 and 6 degrees, but upon phase transition the appearance of new peaks suggests that the new phase should have a larger number of reflections than 2 in order to account for the observed peak profile. The significant line broadening makes it very difficult to propose a candidate structure for the second high pressure phase. However profile indexing results suggest that the new high-pressure phase – referred to as phase-III – has most probably a monoclinic Bravais lattice (or possibly triclinic). Phase-III persists up to the highest pressure investigated, 111.8 GPa. Upon decompression to ambient pressure phase phase-II reverts back to phase-I, but with a slightly reduced unit cell.

In pressure dependent Raman spectroscopy measurements the transition from phase-II to phase-III is accompanied by the disappearance of some vibrational modes and the appearance of several new modes. For some modes the pressure dependencies of the phonon frequencies show a visibly different slope starting from, or even a few GPa prior to, the transition into phase-III.

Dinnebier *et al.* [129] reported the occurrence of two phase transitions in minium Pb_3O_4 upon compression to relatively low pressures. At ambient conditions the crystal structure of minium consists of infinite chains of distorted $Pb^{4+}O_6$ octahedra with a twist angle in the base plane of almost 20°. Within the chain, the polyhedra are connected via common edges of their base planes. Each chain of octahedra is surrounded by four neighboring chains which are rotated by 90° with respect to the central chain, corresponding to an expanded rutile structure. All Pb^{2+} ions are located in the planes spanned by the shared edges of neighboring chains of octahedra, thus forming bridges between the chains which run in a zigzag manner along the c-axis. The Pb^{2+} ions are coordinated by four O atoms forming an irregular $Pb^{2+}O_4$ pyramid with the four O atoms forming the non-planar base and the lead atoms sitting at the vertex.

Minium is therefore similar to $PbMBO_4$ mullites, because of its $Pb^{2+}O_4$ polyhedra carrying a lone electron pair at the Pb^{2+} cation and because of the octahedral chains running along c, although the chains are PbO_6 in minium but AlO_6 or FeO_6 in $PbMBO_4$ mullite. At ambient pressure Pb_3O_4 crystallizes in space group $P4_2/mbc$ (phase 1). Between 0.11 and 0.3 GPa it exhibits a displacive second order phase transition to a structure with space group *Pbam* (phase 2). A second displacive phase transition occurs between 5.54 and 6.6 GPa to another structure with space group *Pbam* (phase 3) but halved *c* dimension.

4.4.6. The Influence of LEP on High-Pressure Behavior of $PbMBO_4$

The $PbMBO_4$ mullite-type compounds are characterized by the presence of a “lone”, i.e., non-bonding electron pair (LEP) at the Pb^{2+} atom. At ambient conditions the coordination of the Pb^{2+} ion is highly asymmetric due to the existence of the localized LEP. The free electron pair can be considered as an additional ligand, causing severe distortions of the coordination polyhedra. In compounds with significant covalent bonding contributions, the LEP can be strongly *stereochemically active*. Gillespie and Nyholm [130] state that a lone pair repels electron pairs more than a bonding pair of electrons and that the tendency of the electrons pairs in a valence shell to keep apart is mainly due to the exclusion principle.

LEPs are considered as pseudo-ligands, able to replace one or more of the regular ligands in a given coordination sphere.[131, 132] In many crystalline solids with cation-centered lone pairs, the lone pair occupies the same volume as an oxide or fluoride ion. However the cation-lone pair distance (in Å) is much shorter than the cation-anion distance; Pb^{2+} -- LEP = 0.86Å ($5d^{10}$ $6s^{2}$). [133] Atoms with a LEP in the valence shell have an *anisotropic* local environment which leads to the formation of acentric or even polar crystal structures and influences dielectric properties. [134] The strong *anisotropy* of the Pb^{2+} coordination (due to the LEP) affects not only the geometry but is often the origin of interesting physical properties. For example, more than half of all non-centrosymmetric oxides contain lone electron pairs, [135] and the non-centrosymmetry is a precondition for ex. piezoelectricity, for optical activity and for optical second-harmonic generation.

Cations with a LEP, such as Pb^{2+}, display high polarizabilities and form relatively open structures, which makes them predisposed to pressure-driven phase transitions. Since in solids there is strong correlation between geometry and electronic structures, a pressure-driven change to a higher density structure should involve substantial changes in the electronic structure as well.

Some of the following discussion singles out $PbFeBO_4$ for the sake of simplicity, but all conclusions are also valid for $PbAlBO_4$. The pressure dependence of the lattice parameters of $PbFeBO_4$ shows a distinct anisotropy, which could be related to the changes in the space requirements of the free electron pair of Pb^{2+}. The abrupt changes in slope of compression of *a*, *b* and *c* (of more than an order of magnitude) are one more piece of evidence pointing to the phase-I→II transition. Specifically lattice parameter *a* decreases rapidly (–0.06 Å/GPa) with increasing pressure, with an abrupt decrease in slope at the phase I/II border (–0.006 Å/GPa). The *b* parameter first rapidly increases with increasing pressure (0.017 Å/GPa) with an abrupt sign change before the phase I/II border (–0.005 Å/GPa). Lattice parameter *c* decreases (-0.01 Å/GPa) with increasing pressure up to about 8, stays stable until 18 GPa, and then again decreases slowly (–0.007Å/GPa).

Similarly in $PbAlBO_4$ the lattice parameter *a* decreases rapidly (–0.04 Å/GPa) with increasing pressure, with an abrupt decrease in slope at the phase I/II border (–0.007 Å/GPa). The *b* parameter first rapidly increases with increasing pressure (0.0027 Å/GPa) with an abrupt sign change before the phase I/II border (–0.006 Å/GPa). Lattice parameter *c* decreases (-0.01 Å/GPa) with an abrupt decrease in slope at the phase I/II border (–0.005 Å/GPa). As aside note, the above mentioned temporary “slowdown” of compression appears to be a characteristic feature of the compression of the *c*-axis of mullite materials under compression and it was observed in this work for 2:1 mullite, 3:2 mullite and B-mullite. In general, for phase-II an almost uniform decrease of *a*, *b*, and *c* with increasing pressure up to 71 GPa is observed.

The interest of the this project in examining the effect of pressure on the crystal structures Pb^{2+} compounds like $PbMBO_4$, stems from the fact that the lone electron pair is much more compressible and mobile with respect to space requirements of the lead coordination when compared to the large anions surrounding the Pb^{2+} cation. *In phase-I* of $PbMBO_4$ mullites the Pb^{2+} ions are coordinated by four O atoms forming an irregular $Pb^{2+}O_4$ pyramid.

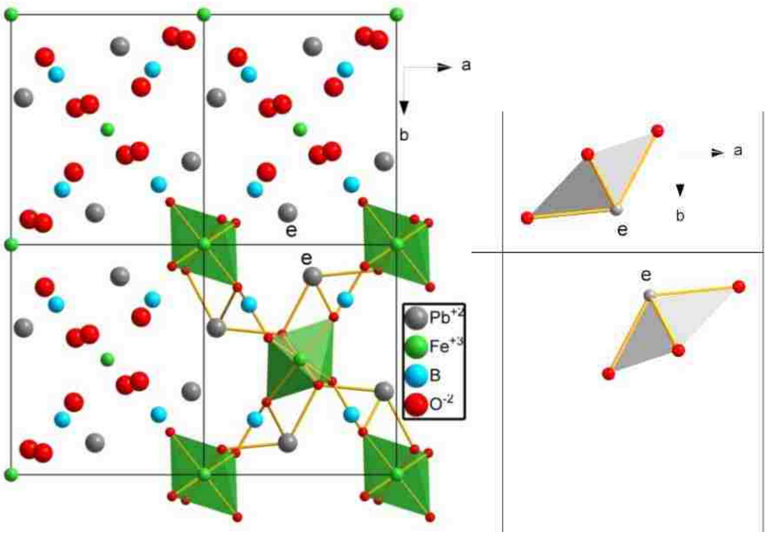

Figure 59. Supercell of $PbFeBO_4$ at ambient pressure
The detail picture shows two neighboring Pb atoms with the orientation of their lone electron pairs (marked with 'e'). The supercell is made of 2x2x2 unit cells.

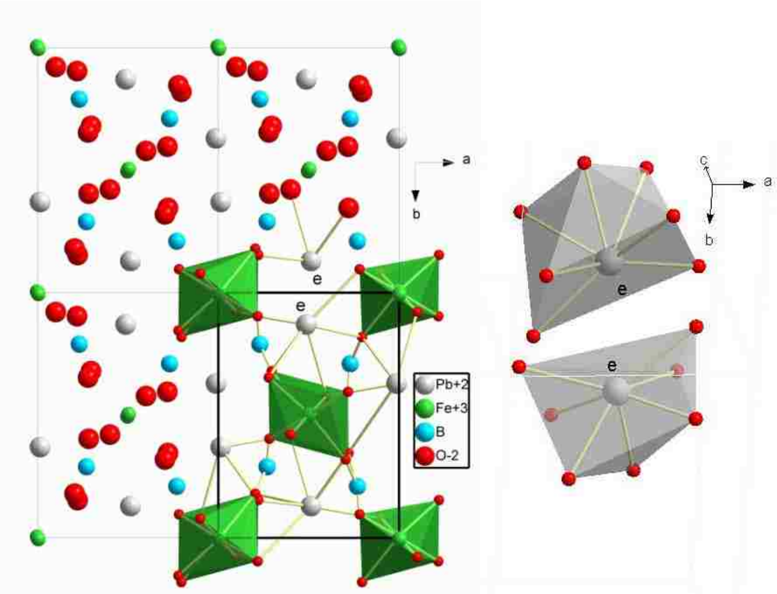

Figure 60. Supercell of $PbFeBO_4$ at 14 GPa.
The detail picture shows two neighboring Pb atoms with the orientation of their lone electron pairs (marked with 'e'). The $Pb^{2+}O_7$ polyhedra are shown in grey. The supercell is made of 2x2x2 unit cells.

The base of this pyramid is *non-planar* and is formed *by* the four O atoms while the lead atom sits at the vertex, showing that the LEP is stereochemically active. Three of the coordinating O atoms belong to the same octahedral (FeO_6) chain; the fourth one belongs to a neighboring chain of octahedra. The free electron pair of the Pb^{2+} ion *points away* from the four coordinating O atoms, thus forming large empty channels. It was reported [136] that a LEP cannot have purely *s*-character when it is stereochemically active and can be well understood by a mixing of *s* and *p* orbitals. The lack of inversion symmetry at the M-sites allows mixing between occupied metal 6*s* states and unoccupied 6*p* states thus lowering the internal electronic energy of the metal cations through a second order Jahn-Teller mechanism, and results in a directional *sp* hybrid orbital. Assuming a similar configuration in our $PbMBO_4$ system the stereoactivity of the $6s^2$ LEP of the Pb^{2+} cation is *directional*, pointing towards the void of the structural channel. [104] According to the valence shell electron pair repulsion model (VSEPR) model, [137] a nonbonding LEP requires more space on the surface of the central atom forming the ligand than a bonding pair. Abnormal displacement parameters of the ligands may be associated with the crystal-chemical characteristics as long as LEPs are concerned. [104, 138] In the same way the orientation of the LEP and its large displacement may account for a larger displacement parameter of O2 atoms which represent two apexes of the PbO_4E polyhedron. The stereoactivity of the LEP affects the PBO_4E geometry leading to an asymmetric PbO_4E polyhedron with three types of Pb—O bond lengths.

It was proposed above that the distinct anisotropy of the pressure dependence of the lattice parameters can be related to the changes in the space requirements of the free electron pair of Pb^{2+}. In fact in phase-I the rapid decrease of the *a* parameter can be explained by the fact that decreasing *a* does not bring the Pb atoms much closer together so most of the compression occurs along *a*, instead of being shared by *a* and *b*, since compression along b would be countered by electrostatic repulsion of the LEPs (also see Figure 61). On the contrary, expansion instead of compression takes place along *b* since the Pb atoms and their LEPs - which are facing each other along *b*- fight against compression in this direction. Along the c-axis the significantly lower compression is reasonable, because of the occurrence of the firmly bound, edge-connected octahedral chains in this lattice direction, which are cross-linked by rigid BO_3 groups.

In general it is anticipated that the application of pressure will lead to an increase of the symmetry of the coordination sphere and a simultaneous increase in symmetry of the electron distribution around the Pb^{2+} cation. This effect goes along with a decrease of the stereochemical activity of the LEP (as seen for example in the case [139] of $CsGeCl_3$ or in the case [129] of Pb_3O_4). A high enough pressure can compel the lone electron pair into the *s* state,[129] or semiconducting or metallic behavior can be observed, if a broadening or overlap of the valence and the conduction band occurs. [140]

In phase-II the basic crystal packing of phase-I is preserved. The key difference in the crystal structure of $PbMBO_4$ at pressures above ~12 GPa is the increase of the coordination number of Pb^{2+} from 4 to 6+1, forming distorted $Pb^{2+}O_7$ trigonal prisms with a pyramidal vertex “sitting upside-down” on a rectangular plane. The notation of ‘6+1’ is used instead of 7 because one of the oxygens is farther away from the Pb atom and contributes less than the other 6 to the bond valence sum. The now irregular $Fe^{3+}O_6$ octahedra still form infinite chains running along *c*, interconnecting consecutive layers of $Pb^{2+}O_7$ polyhedra. Each $Pb^{2+}O_7$ polyhedron shares two pyramidal edges with two consecutive $Fe^{3+}O_6$ octahedra. The large deviation of the Pb^{2+} central cation from the center of gravity of the trigonal prism indicates that the *stereochemistry* of Pb^{2+} in phase-II is similar to that of phase-I and thus that Pb^{2+} remains stereochemically active in the high-pressure structure, at least at up to 14 GPa (Figure 59 and Figure 60).

4.4.7. Bond Valence Model and Eccentricity Parameter

Since Pauling's electrostatic valence rule [141] the bond valence model (BVM) has been successfully used as an empirical method to interpret crystal structures. According to BVM an inorganic structure is considered as an arrangement of atoms linked by bonds between atoms with opposite signs of valences. The bond valence sum (BVS) of an atom A_i can be calculated from:

$$BVS_i = \sum_j \left[\frac{exp\left(r_0 - D_{ij}\right)}{b}\right]$$

Where D_{ij} is the distance from atom A_i to its neighbor X_j, and r_0 and b are empirical parameters derived from well refined structures. b=37 pm is considered to be independent of bond types and r_0 is the bond valence parameter for each A—X pair. [142] [143]

Furthermore bond valences can be corrected for pressure [144] by recognizing that the bond-valence parameter, r_0 changes with pressure according to the equation:

$$\frac{dr_o}{dp} = \frac{10^{-4} r_0^4}{\frac{1}{B} - \frac{2}{r_0}} \text{ Å } GPa^{-1}$$

where r_0 is the ambient pressure bond valence parameter and b (usually 0.37 Å) is the softness constant, and both values can be found in Brown (2002). [143, 144]

For most inorganic structures the calculated BVS are close to the integer valence of the atom concerned. Any large deviations of BVS between the observed value and the formal value can be attributed to chemical or steric reasons. [145] However systematic deviations of BVS from formal valences have been observed for cations with a lone electron pair. In fact Wang and Liebau [146, 147, 148, 149, 150, 151] observed that the BVS calculated around a LEP cation increases as the cation's coordination sphere experiences more distortion when the LEP is stereochemically active. To express the LEPs influence on BVS, Wang-Liebau devised a vector term eccentricity parameter $\boldsymbol{\Phi}_i$. The absolute value $|\boldsymbol{\Phi}_i|$ measures the deformation density of the LEP and the direction is considered along the along the line from the cation nucleus to the approximate center of the deformation density of the LEP. The absolute value of the eccentricity parameter $|\boldsymbol{\Phi}_i|$ can be found from:

$$\boldsymbol{\Phi}_i = -\sum_j \boldsymbol{\varphi}_{ij}$$

where

$$\varphi_{ij} = exp\left[-\frac{D_{ij}}{g}\right]$$

and where D_{ij} is the distance from atom A_i to its neighbor X_j, and g=20pm is an empirical constant used by Wang and Liebau. The direction of $\boldsymbol{\Phi}_i$ is along the line from the cation nucleus to the approximate center of the deformation density of the LEP. Following Wang and Liebau the structural bond valence sum for a cation with one LEP can be calculated using:

$$^{struc}BVS = \sum_j \frac{E|\boldsymbol{\Phi}_i| + F - D_{ij}}{b}$$

where E and F are fit parameters which can be found in Wang and Liebau (2007). [149]

Table 23. Calculations of bond valence sums for $PbFeBO_4$ and $PbAlBO_4$. Errors are standard deviation values.

$PbFeBO_4$			**$PbAlBO_4$**		
Pressure (GPa)	**BVS*** (v. u.)	**BVS$^\&$** (v. u.)	**Pressure** (GPa)	**BVS*** (v. u.)	**BVS$^\&$** (v. u.)
0.0	2.10(3)	1.82(3)	0.0	2.47(5)	2.13(4)
1.5	2.28(8)	1.96(7)	2.2	2.56(2)	2.20(2)
8.6	2.1(4)	1.8(3)	8.3	2.11(8)	1.78(7)
14.0	2.5(3)	2.1(2)	14.1	3.0(3)	2.5(2)

* Corrected for LEP eccentricity

$^\&$ corrected for the effect of pressure

As shown in Table 23 the correction for eccentricity gives larger BVS values than the correction for pressure. As expected the bond valence sum of Pb increases with pressures.

With increasing pressure the four coordinated Pb^{2+} cation increases its coordination to 7 – as demonstrated by the increasing BVS values – and it is therefore reasonable to propose that pressure increase leads to the formation of a $Pb^{2+}O_7$ polyhedron in $PbMBO_4$. The formation of a similar polyhedron was observed in minium on compression above 6.6 GPa.

4.4.8. Large Negative Linear Compressibility in $PbMBO_4$

For nearly all known materials, an increase in hydrostatic pressure results in a shortening of their linear dimensions. This means that the volume compressibility, area compressibilities, and linear compressibilities are all positive. However, there are rare reports of crystals having negative linear compressibilities (NLC). A solid increases density when stretched along an axis of negative linear compressibility, so it is equivalent either to say that a solid has the property of being stretch densified or that it has a negative linear compressibility.

The magnitude of shortening of linear dimensions under pressure can be compared by means of the isothermal compressibilities:

$$K_l = -\frac{\partial \ln(L/L_0)}{\partial p}$$

which uses the relative rate of change of length L/L_0 with respect to pressure.

Typical linear compressibilities for engineering materials such as metals, alloys and ceramics are K~5 TPa^{-1}. [152] This means that there occurs a 0.5% reduction in length for each 1 GPa increase in pressure.

In contrast, for the handful of materials known to exhibit NLC, one or more of the compressibilities actually takes a negative value. For many years, only 13 NLC compounds had been identified. [153] Amongst these long-established, canonical NLC systems, the strongest effect observed [154] was for trigonal Se with K_{NLC} = - 1.2 TPa^{-1}. So in general NLC is much weaker than the typical positive compressibilities of ordinary materials. Two recent reports of stronger NLC effects exploit structures with `wine-rack' topologies: methanol monohydrate [155] (K_{NLC} = -2.6 TPa^{-1}) and ammonium zinc formate [156] (K_{NLC} = -1.8 TPa^{-1}). Very recently it was reported that the molecular framework material zinc(II) dicyanoaurate(I), $ZnTAu(CN)_2U_2$, exhibits the most extreme and persistent NLC behavior yet reported: K_{NLC} =-45 TPa^{-1}. [157] Under increasing hydrostatic pressure its crystal structure expands in one direction at a rate that is an order of magnitude greater than both the typical contraction observed for common engineering materials [158] and also the anomalous expansion in established NLC candidates. [153]

In NLC systems with "wine-rack" topologies, volume reduction is accommodated by simultaneous compression and expansion of the crystal lattice in orthogonal directions (that is, folding-up of the wine-rack). [153] Consequently the existence of NLC implies stronger positive linear compressibility (PLC) in directions perpendicular to the NLC axis.

Remarkably the two $PbMBO_4$ mullites are among the ~20 or so materials known to display NLC (Table 24), which is important not only because the NLC effect is very rare, but also because examples of inorganic materials are even fewer. In $PbBFeO_4$ we observe a *large* NLC effect parallel to the *b* crystal axis (K_{NLC} = -2.02(1) TPa^{-1}) coupled with a strong positive compressibility along the *a* crystal axis (K_a = +26.90(1) TPa^{-1}). The NLC effect persist throughout the stability field up to 8 GPa (within the stability field of phase-I) but ends abruptly ~8 GPa where it into PLC. The author proposes to use the term "*large*" to distinguish the NLC behavior of $PbFeBO_4$ observed here, that is ~70% larger than that of the canonical systems described above (where the biggest was selenium with K_{NLC} = -1.2 TPa^{-1}), and which persists for the approximately 8 GPa, well over the range associated with typical high-pressure applications.

Table 24. About 20 materials known to possess negative linear compressibility.

#	Material	K_{NLC} (TPa^{-1})	Notes	Year
1	Silver(I) hexacyanocobaltate(III) $Ag_3[Co(CN)_6]$,	**-75**	‘wine-rack type’ [159]	2008
2	zinc dicyanoaurate $Zn[Au(CN)_2]_2$	~-45	Metal-organic framework ‘molecular honeycomb’ [157]	2013
3	MIL-53(Al) and NH_2-MIL-53(Al)	-27	Metal-organic framework, [160] ‘wine-rack type’	2015
4	methanol monohydrate deuterated 1:1 methanol-water	-2.6(3)	simple molecular crystal [155]	2011
5	**$PbMBO_4$**	**-2.0(1)**	**inorganic oxide! stable solid (this work)**	2015
6	α-cristobalite structured $BAsO_4$ (also BPO_4)	-2	oxide [161]	2003
7	Minium Pb_3O_4	~-2.0(5)	inorganic oxide! [129]	2003
8	α’ – NaV_2O_5	-1.8	inorganic oxide, spin-Peierls compound [162]	1999
9	ammonium zinc formate, $[NH_4][Zn(HCOO)_3]$	-1.8(8)	Metal-organic framework, [156] ‘wine-rack type’	2012
10~22	Selenium (trigonal) Tellurium Mercurous iodide, Hg_2I_2 Mercurous bromide, Hg_2Br_2 3-Methyl 4-nitropyridine 1-oxide, $C_6N_2O_3H_6$ Cadmium formate, $Cd(COOH)_2$ Calcium formate, $Ca(COOH)_2$ m-Dihydroxybenzene, $C_6H_4(OH)_2$ Cesium biphthalate, $C_6H_4COOHCOOCs$ Tris-sarcosine calcium chloride, $(CH_3NHCH_2COOH)_3CaCl_2$ Lanthanum niobate, $LaNbO_4$ Cesium dihydrogen phosphate, CsH_2PO_4 Ethylene diamine tartrate, $C_6H_{14}N_2O_6$	≦ -1.2 -0.2 to - 1	canonical materials [153]	Up to 1998

In $PbBAlO_4$ we observe strong positive compressibility along the *a* crystal axis (K_a = +9.36 TPa^{-1}) together with a *small* NLC effect parallel to the *b* crystal axis (K_{NLC} = -0.47 TPa^{-1}). The NLC effect persist throughout the stability field up to 8 GPa (within the stability field of phase-I), but ends abruptly ~8 GPa where it turns into PLC. Thermodynamically, the NLC we observe in $PbMBO_4$ is not sustainable indefinitely. What limits the NLC along *b* to 8 GPa in $PbFeBO_4$? Two factors could interplay synergically to create ideal conditions for negative linear expansion: (i) a mechanism that opposes compression along *b*, together with (ii) a structural mechanism that allows expansion along *b*.

Firstly, there is a factor opposing compression along b. At ambient pressure the Pb—Pb distance is 3.88Å and the LEPs of two neighboring Pb atoms face each other. At 14 GPa the Pb—Pb distance is 3.66Å, but the LEPs point away from each other. It is proposed that up to 8 GPa the configuration of two neighboring Pb atoms is such that their respective LEPs face each other (Figure 59). Thus the stereochemical activity of the LEPs opposes compression in the *b* direction, because compression in *b* would bring them closer together. 8 GPa is the threshold pressure starting from which the two neighboring Pb atoms and the orientation of their respective LEPs is such that further compression does not reduce significantly the distance between them (Figure 60 and Figure 61). Also the stereochemical activity is believed to decrease with pressure (Figure 61). Therefore the persistent (but weakened) stereochemical activity of the LEPs does not oppose as much the compression along the *b* direction any longer – albeit the compression along *b* is sluggish. Note that all along the compression in *a* is positive since shortening *a* does not change the distance between the two LEPs. The compression in *c* is also positive since along this direction single layers of Pb atoms are separated by layers containing the BO_3 triangles.

There is then a second factor, which is needed to create expansion along *b*. As pressure is applied the octahedral chains rotate towards each other in the a-b plane (thus decreasing the inclination angle ω). As the chains rotate, the longest bonds inside the octahedra align more and more with the b-axis (Figure 61). This causes the lengthening of *b* as the octahedra become more horizontal or aligned with the *b*. At higher pressures (> ~10 GPa) the stereochemical activity of LEPs decreases and the opposition to compression along *b* disappears. It is also reasonable to assume that there is some limit up to which the structure can accommodate this effect and at some point it will be more energetically favorable shorten bonds to accommodate compression. As the *b* axis switches form negative to the standard positive compressibility, we also observe and increase in coordination of the Pb^{2+} cation and a phase transition around 12 GPa (discussed in section 4.4.5). The same structural reasoning can be extended to the NLC effect observed in $PbAlBO_4$.

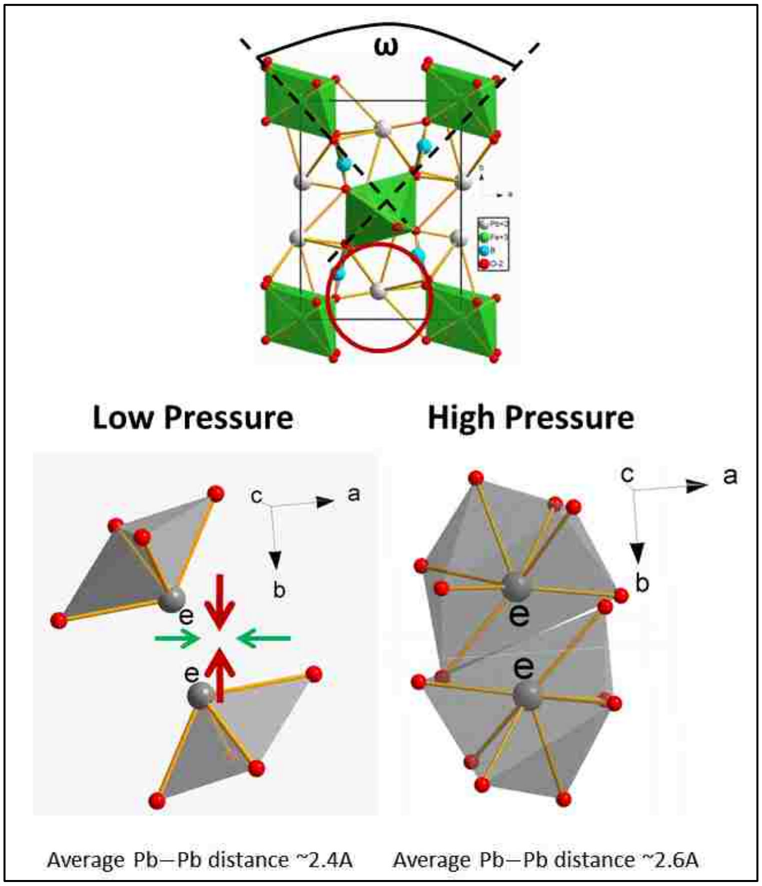

Figure 61. Synergical interplay of factors leading to negative linear compressibility along *b*.
Top: crystal structure of $PbMBO_4$ showing the inclination angle ω. Bottom: respective location of two neighboring lead oxide polyhedra within the crystal structure. A mechanism that opposes compression along b (LEPs of neighboring Pb atoms facing each other - red arrows) together with a structural mechanism that allows expansion along *b* (the rotation of octahedral chains). At higher pressures the stereochemical activity of LEPs decreases and the opposition to compression along *b* disappears.

$PbMBO_4$ mullites bear some structural similarity with minium (Pb_3O_4, see section 4.1.3). NLC was also observed in a study of static compression of minium by Dinnebier *et al.* [129] Negative compressibility was observed along both the *a* and *b* lattice directions (as can be seen in the figure of the referenced paper), but it was not discussed by the authors. By analogy to the mechanisms of NLC proposed here for $PbMBO_4$ mullites, NLC in minium can be explained by the fact that in minium there are not two, but four Pb atoms in the interstices between the octahedral chains. They are located so that either compression along *a* or along *b* would tend to bring two of the opposing Pb atoms closer together. Therefore a negative linear compressibility is observed in minium both along *a* and along *b* up to a pressure threshold.

4.4.8.1. Implications of the Large NLC Effect in $PbMBO_4$ Compounds

$PbMBO_4$ mullites are negative thermal expansion materials (NTE). [37, 38] From a physics point of view it is rational to search for unusual pressure-dependent behavior in NTE materials (and NLC certainly qualifies as unusual). In fact, NTE materials, possess phonon modes with negative Grüneisen parameters (as it is the case of $PbMBO_4$ - see results of high-pressure Raman studies above) and often have low-density structures. Although NTE and NLC are not thermodynamically required to coexist, it has been proposed that there exists a general correspondence between strong NTE materials and a strong NLC effect. [159]

Regardless of its rarity, NLC is a highly attractive mechanical property, with a key application being the development of effectively incompressible optical materials. [153, 163] Applications would be centered on high-pressure working environments: (i) optical telecommunications devices that must function at deep-sea pressures >1,000 atm. (ii) ultrasensitive pressure detectors, such as interferometric optical sensors for sonar and aircraft altitude measurements. The NLC effect has also been found alongside the "auxetic" behavior, which is itself being used to improve shock resistance for ex. in body armor. [164]

Cation-centered lone pairs (often with Pb^{2+} as the central cation, but also Sn^{2+} and Bi^{3+}) are tremendously important for applications requiring off-centered polyhedra and their associated dipoles: ferroelectric and piezoelectric materials, actuators, multiferroic materials, *non-linear optical materials*, ionic conductors, high-refractive index materials (lead crystal), semiconductor/semimetal to insulator transitions. Conceivably the most direct application of NLC in $PbMBO_4$ mullite-type materials is as the optical component in interferometric pressure sensors. Such sensors operate based on two effects: the rate of variation in refractive index, which is a function of volume compressibility and also the macroscopic path length, which is a function of linear compressibility. In *conventional optical materials* these two factors have an opposed relationship. Large volume compressibility in a material usually implies large PLCs, so that pressure increasing corresponds to the increase of the refractive index. Increase of refractive index produces an increase optical path length, but concurrently the material dimensions also decrease, which decreases optical path length. Therefore in conventional materials, the overall variation in optical path length is greatly reduced with pressure. The combination of large volume compressibility with a negative linear compressibility – as observed in $PbMBO_4$ mullites - however, means that NLC materials become more dense while their length increases in one direction. Now the relationship between these two effects becomes synergistic and gives an increase in pressure sensitivity.[153] For applications this effect would of course have to be associated with optical transparency in the desired optical region.

From a fundamental physics point of view there are strong implications associated with understanding mechanisms of NLC. There are biological species thought to use NLC to translate variations in internally generated hydrostatic pressure into appendage contraction, analogous to muscular response. Examples include the arms and tentacles of squid, octopus limb movement, and even elephant trunk contraction. [165] Mechanical amplification gained from linking small changes in cross-sectional diameter to large variations in length means that these are widely considered to be very efficient biological structures.

4.4.9. Equation of State

A third order Birch-Murnaghan [110, 111, 112, 113, 114] equation of state (EoS) was fitted to the experimental pressure-volume data (Figure 62 and Figure 63) in order to determine the bulk modulus B_0 and its pressure derivative B_0' at ambient conditions for $PbFeBO_4$ and $PbAlBO_4$:

$$P = \frac{3}{2}B_0\left[\left(\frac{V_0}{V}\right)^{\frac{7}{3}} - \left(\frac{V_0}{V}\right)^{\frac{5}{3}}\right]\left\{1 + \frac{3}{4}(B_0' - 4)\left[\left(\frac{V_0}{V}\right)^{\frac{2}{3}} - 1\right]\right\}$$

The bulk moduli (B_0) obtained from the Birch-Murnaghan fits are summarized in Table 25, [37, 38, 75, 120] together with literature data for similar materials. For each sample, the EoS was fitted for phase-I and for phase-II, in their respective pressure ranges.

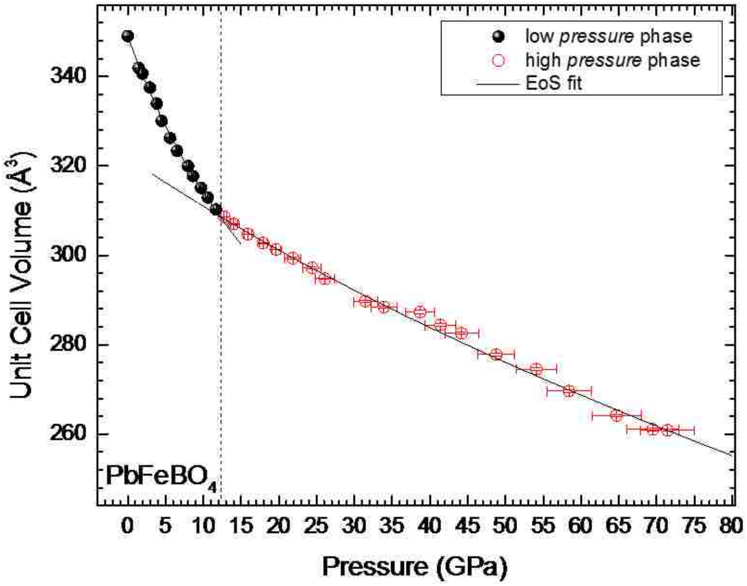

Figure 62. Pressure-driven change of unit cell volume in $PbFeBO_4$.
The solid line is a 3rd order Birch-Murnaghan equation of state fit. The vertical dashed line separates the low pressure and high pressure phases and indicates the pressure at which the phase transition occurs.

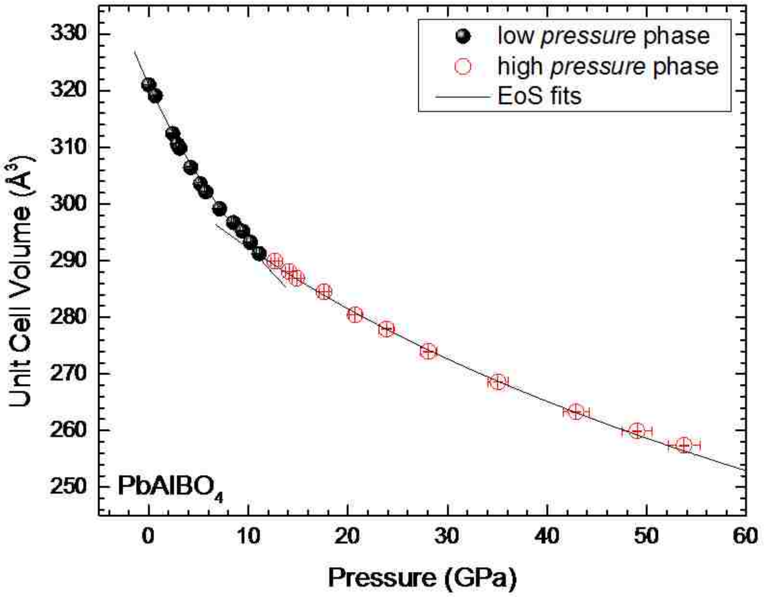

Figure 63. Pressure-driven change of unit cell volume in PbAlBO$_4$.
The solid line is a 3rd order Birch-Murnaghan equation of state fit. The vertical dashed line separates the low pressure and high pressure phases and indicates the pressure at which the phase transition occurs.

Table 25. Comparison of bulk moduli for PbMBO$_4$.
Comparison of: bulk moduli (B_0), their pressure derivatives (B_0') and unit cell volumes at ambient pressure (V_0) obtained in the present work for PbFeBO$_4$ and PbAlBO$_4$.

Sample	B_0	B_0'	V_0	Method
PbFeBO$_4$ phase-I	73(3)	5.0(9)	349.0(4)	exp., this work
	75(2)	4	349.0(3)	exp., this work
	62	-	351.23	DFT [37]
	70(7)	-	-	exp., author's previous work [37]
PbFeBO$_4$ phase-II	190(19)	3.8(9)	326(2)	exp., this work
PbAlBO$_4$ phase-I	83(5)	5.7(9)	321.0(3)	exp., this work
	87(3)	4	321.0(3)	exp., this work
	77.35	6.51	321.95	DFT [38]
	79(6)	4.2(22)	320.0	exp., author's previous work [38]
PbAlBO$_4$ phase-II	194(17)	5.1(9)	306 (6)	exp., this work
	215(6)	4	305.2 (6)	exp., this work
Pb_3O_4 phase II	20.8(4)	4	511(1)	exp. [129]
Pb_3O_4 phase III	98(3)	4	222(2)	exp. [129]

The correlation between the unit-cell volume and the bulk modulus of PbMBO$_4$ synthetic mullites and of structurally related compounds is illustrated in Figure 64. A comparison with sillimanite and mullite shows that these compounds are less compressible than the Pb-based compounds of the mullite-type family. This difference can be related to the higher compressibility of the larger and stereochemically active Pb^{2+} cation when compared to the other cations in the structure.

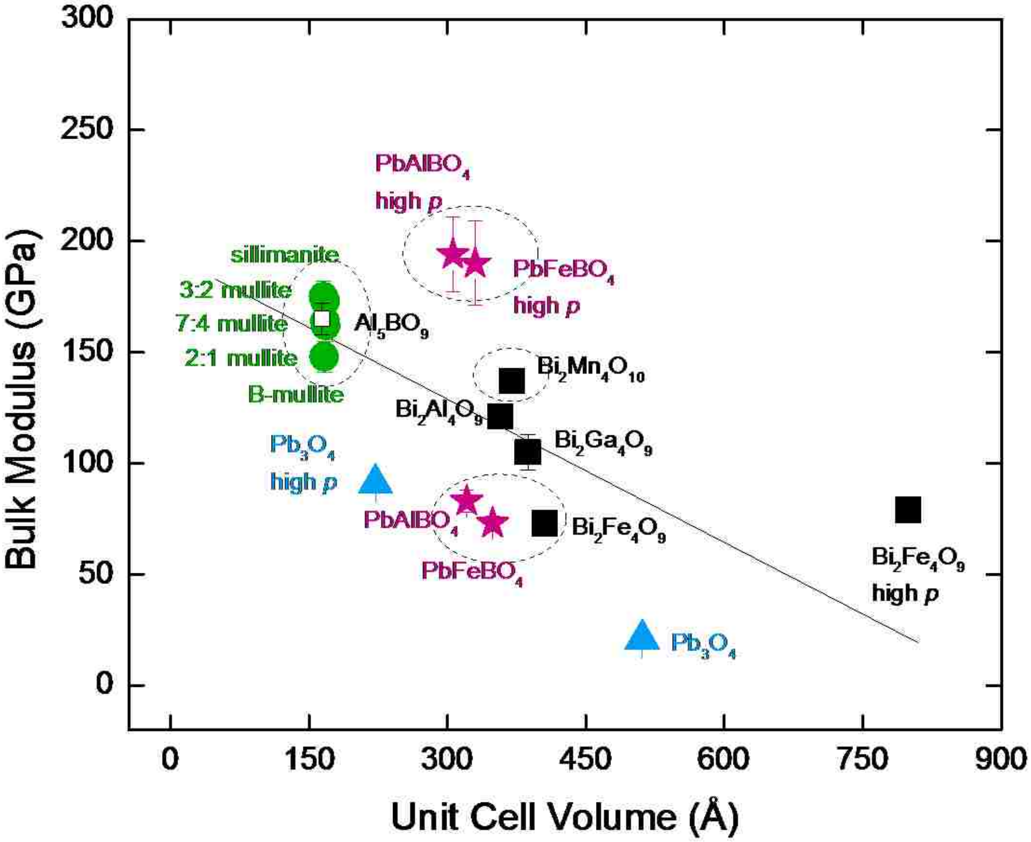

Figure 64. Correlation between bulk moduli of $PbMBO_4$ and of other mullite materials.
Correlation (solid line) between the unit-cell volume and the bulk modulus of $PbMBO_4$ synthetic mullites and of isotypic or structurally related compounds. Values for $PbMBO_4$, 2:1 mullite., 3:2 mullite, B-mullite and sillimanite are from this work (dashed ovals). Values for Pb_3O_4 are from Dinnebier *et al.* [129] Values for $Bi_2M_4O_9$ mullites are from Friedrich et al. [166] Values for Al_5BO_9 are from Gatta *et al.*

One generally anticipates a reduction in magnitude of compressibilities at increased pressure and this is indeed shown by data in Figure 64: bulk moduli for the $PbMBO_4$ samples increase in phase-II with respect to phase-I. The bulk modulus of phase-I in comparison to the corresponding values of phase-II is about 3 times lower, indicating a much higher compressibility. This behavior can be related to packing effects of the Pb^{2+} polyhedra at low pressure due to a change in space requirements of the free electron pair.

In phase-I the free electron pair of the Pb^{2+} ion points away from the four coordinating O atoms, thus forming large empty channels in the structure, which also lead to a low space filling at ambient conditions. Space filling is increased upon compression to phase-II - see for example Figure 53 or Figure 56, where space filling is visibly larger comparing to the ambient pressure structure.

A comparison of the bulk moduli and the unit-cell volumes of the two isotypic $PbMBO_4$ compounds agrees with the expected tendency that the *lower bulk modulus* is observed for the isostructural oxides with *larger unit-cell volumes*. [167] Following this trend $PbFeBO_4$ is more compressible than $PbAlBO_4$. The increase in unit-cell volumes is determined by the substitution of the metal cations Al^{3+} and Fe^{3+}, which have increasing ionic radii (Shannon 1976).[168] The same trends can be identified in Figure 64 for the $Bi_2M_4BO_9$ mullite family and for the low and high-pressure phases of minium.

CHAPTER 5 – CONCLUSIONS

5.1. Alumino-Silicate mullites and Sillimanite

The main motivation for this part of the study was to understand the role of oxygen vacancies on the high-pressure behavior and structural integrity of mullite-type alumino-silicates. Comparative studies were performed on mullite-type phases of general formula $Al_{4+2x}Si_{2-2x}O_{10-x}$ and differing in the amount of oxygen vacancies: 2:1-mullite (x = 0.4, i.e. 0.4 oxygen vacancies per unit cell), 3:2-mullite (x = 0.25, i.e. 0.25 oxygen vacancies per unit cell) and sillimanite (x = 0, no oxygen vacancy). The structural stability of 2:1-mullite, 3:2-mullite and sillimanite was investigated as a function of pressure using *in situ* angle-dispersive, synchrotron x-ray diffraction and diamond anvil cells, in quasi-hydrostatic compression conditions. The structural stability was also investigated using *in situ* high-pressure Raman spectroscopy. To the best of the author's knowledge this work presents the first Raman spectroscopy results of alumino-silicate mullite at high-pressures. Our studies show that the pressure-induced structural changes in 2:1-mullite, 3:2-mullite and sillimanite take place in several steps. The almost identical high-pressure compressibility of both mullites and of sillimanite on compression from ambient pressure up to 20 GPa implies that the observed behavior is mainly controlled by compression of the three-dimensional structural networks with compression of octahedra and inter-polyhedral angle distortion as probable main mechanisms.

The pressure-driven evolution of vibrational modes was analyzed and mode-Grüneisen parameters were obtained for 2:1 mullite and for sillimanite. Raman spectroscopy allows spotlighting of the local disorder of 2:1 mullite: in fact Raman spectra of mullite contrast starkly with those of the ordered sillimanite structure. The key differences between the structure of mullite and sillimanite are the oxygen vacancies as well as the disorder in the tetrahedral sites. On the level of "long range order" both materials present very crystalline x-ray diffraction patterns where the above mentioned differences cannot be perceived. On the other hand when comparing Raman spectra of sillimanite and 2:1 mullite, the great structural differences are very readily apparent. Sillimanite has a set of very narrow vibrations and 2:1 mullite has instead several wide and overlapping bands, illustrating that the "short range order" of these materials is indeed very different. Close analysis of compression data below 20 GPa along the crystallographic c-axis of both mullites and of sillimanite, shows that the presence of oxygen vacancies does not have significant influence on the behavior of both mullites. Above 20 GPa 2:1 and 3:2-mullite show a strong discontinuity of the volume compression, together with a dramatic intensity loss and important broadening of ADXRD lines which is attributed to a gradual and irreversible amorphization. The degree of x-ray amorphization of sillimanite above 30 GPa is only small, on the other hand, since the crystalline structure of sillimanite is mostly recovered upon decompression. Raman peak broadening in sillimanite and the shift of bands towards broad features in 2:1 mullite confirm the progress of amorphization in the two samples. The Raman spectroscopy results coincide with the results of in situ high pressure X-ray diffraction studies. In amorphization, the sharp X-ray diffraction lines disappear. On release of pressure, the amorphized phase is metastably retained down to ambient pressure, reverting gradually to a highly disordered, parent-like phase. The absence - in sillimanite or the presence - in mullites of oxygen vacancies does play a dual role on their pressure response on compression. First, pressure-induced effects, such as the slowdown of the compression of the c-axis (~10 GPa), appear at much lower pressures in both mullites than they do in sillimanite (~20 GPa), and are attributed to oxygen vacancies in the former. Second, the pressure-driven structural decomposition or amorphization is strong in both mullites and occurs at lower pressures (~20 GPa) than in sillimanite (~30 GPa). The lower stability of mullite in comparison to that of sillimanite is ascribed to the presence of oxygen vacancies in mullite, but not in sillimanite.

5.2. Boron Mullites

The high-pressure behavior, phase stability and mechanisms of amorphization of 7:4 mullite and B-mullite, were investigated *in situ* by synchrotron powder X-ray diffraction with a diamond anvil cell in quasi-hydrostatic conditions. The samples were compressed, in small pressure steps, up to 27.8 GPa and 28.9 GPa respectively, and then decompressed back to ambient pressure. All along the compression both samples' patterns are indexable with a modified 3:2 mullite structure. Compression data are smooth up to ~15 GPa, from which point the diffraction lines broaden, and subsequently refined unit cell parameters deviate significantly down from the compressional trend. Above ~15 GPa the distortion of the mullites and the proportion of amorphous phase progressively increases and above ~23GPs diffraction patterns are not indexable anymore, suggesting X-ray amorphization. The *c* axis is the stiffest one due to edge-sharing firmly bound AlO_6 octahedra and the tetrahedral double chains, which control the compression along that direction. The other two directions display greater compressibility. The compression along the *a* and *b* axes are similar, however with *b* being slightly more compressible at lower pressures and *a* becoming more compressible at higher pressures. Compression is dominated by a reduction in octahedral bonds and an increasing in the inclination of AlO_6 octahedra away from each other in the *a*-*b* plane, while tetrahedra behave as rigid units. Above ~18 GPa for B-mullite (20 GPa for 7:4 mullite) distortion of all polyhedra becomes the main compression mechanism. Amorphization is driven by a significant increase in distortion of octahedra and a dramatic increase in the octahedral inclination angle. It can be thought that the crystal structure of B-mullite and that of 7:4 mullite, under the influence of pressure, is evolving in the direction of a possible phase transition, with motion towards the formation of five-coordinated silica and alumina, or very distorted AlO_5 and SiO_5 bipyramids sharing one edge with the AlO_6 octahedra. However, the transition does not ultimately take place, because the process of amorphization appears to take over. Alternatively it can be thought that the process of going towards five-coordinated silicon and aluminum actually creates instabilities in the structure and helps to bring about the amorphization. For B-mullite amorphization upon compression is permanent, even upon return to ambient conditions. Even though 7:4 mullite appears mostly X-ray amorphous at 28 GPa, it is able to partially recover some crystallinity, indicating that the distortion-driven amorphization is at least somewhat reversible. A third-order Birch Murnaghan equation of state is fitted to the P-V data and experimental bulk moduli as well as axial bulk moduli are obtained for both mullites. A P-V-T equation of state is also proposed for B-mullite by combining compressibility data with thermal expansion results.

5.3. $PbMBO_4$ Synthetic Mullites

To the best of the author's knowledge this works present the first high-pressure x-ray diffraction results, and the first high-pressure Raman spectroscopy results of $PbMBO_4$ mullite at high-pressures including: evidence of multiple phase transitions, evidence of significant negative linear compressibility and persistence of stereochemical activity of the Pb^{2+} lone electron pair and high pressures.

ADXRD patterns of mullite-type $PbFeBO_4$ phase were collected in-situ in a DAC, on compression from 1.4 GPa up to 71.7 GPa, and for the $PbAlBO_4$ phase on compression from

0.5 GPa to 111.8 GPa. Raman spectra of $PbFeBO_4$ were measured as a function of increasing pressure between ambient and 20.4 GPa, while Raman spectra of $PbAlBO_4$ were measured between ambient pressure and 88 GPa. Rietveld refinements of high-pressure X-ray diffraction data combined with analysis of high-pressure Raman spectra helped to reveal some unexpected and interesting features of the process of compression. Also the pressure-driven evolution of vibrational modes was analyzed and mode-Grüneisen parameters were obtained for both $PbMBO_4$ mullites. Mode assignment is was presented.

Changes in vibrational modes around 12 GPa, the appearance of new vibrational modes and the change in the rate of compression in the unit cell volume points to a phase transition in both $PbMBO_4$ mullites. The combination of the observations from results of high-pressure Raman spectroscopy and high-pressure X-ray diffraction of $PbFeBO_4$ and a detailed analysis of Rietveld structural refinements led the author to propose a new pressure-driven phase transition in $PbFeBO_4$. Around 11.8 GPa $PbFeBO_4$ mullite undergoes a phase transition from the orthorhombic *Pnma* phase (space group #62) to another phase with orthorhombic symmetry: the proposed space group for this transition is $Pna2_1$ (#33). The high pressure phase $Pna2_1$ remains stable up to at least 71 GPa.

$PbAlBO_4$ undergoes two new pressure-driven phase transition in $PbAlBO_4$. Just as was the case for $PbFeBO_4$, around 11.8 GPa $PbAlBO_4$ mullite undergoes a phase transition from the orthorhombic *Pnma* phase (space group #62) to another phase with orthorhombic symmetry: the proposed space group is $Pna2_1$ (#33).$PbAlBO_4$ undergoes a second pressure-driven phase transition at ~54 GPa which can be readily seen from the change in relative intensity of diffraction lines and the appearance of new diffraction lines in the low 2θ region. The significant line broadening makes it very difficult to propose a candidate structure for the second high pressure phase. However profile indexing results suggest that the new high-pressure phase has most probably a monoclinic or possibly triclinic Bravais lattice. The new persists up to the highest pressure investigated, 111.8 GPa. In both $PbMBO_4$ mullites the disappearance of some Raman modes and appearance of new ones, as well as softening of vibrational mode frequencies together with mode splitting reflect the occurrence of phase transitions on one side and, on the other side, the expected symmetry lowering at the transition pressure. It is interesting to note that most changes in vibrational mode behavior are associated with changes around the Pb^{2+} cation. These point to the fact that Pb^{2+} plays an important role in the phase transition. On pressure decrease all phase transition in $PbMBO_4$ are fully reversible.

The pressure dependence of the lattice parameters of $PbFeBO_4$ shows a distinct anisotropy, which could be related to the changes in the space requirements of the free electron pair of Pb^{2+}. The abrupt changes in slope of compression of *a*, *b* and *c* (of more than an order of magnitude) are one more piece of evidence pointing to the phase-I→II transition.

Due to the similarities in the pressure-dependent behavior, the compression of the asymmetric environment of the Pb^{2+} ion and its $6s^2$ lone electron pair can be thought to be the reason for the phase transition. *In phase-I* of $PbMBO_4$ mullites the Pb^{2+} ions are coordinated by four O atoms forming an irregular $Pb^{2+}O_4$ pyramid with the lead atom at the vertex, showing that the LEP is stereochemically active. In both $PbMBO_4$ mullites the coordination of the Pb^{2+} cation increases around the phase transition from [4] to [6 + 1]. In phase-II the large deviation of the Pb^{2+} central cation from the center of gravity of the trigonal prism indicates that the *stereochemistry* of Pb^{2+} in phase-II is similar to that of phase-I and thus that Pb^{2+} remains stereochemically active in the high-pressure structure, at least at up to 14 GPa.

A third-order Birch Murnaghan equation of state was fitted to the P-V data and experimental bulk moduli for the low- and the high-pressure phases of $PbMBO_4$ were obtained. The high-pressure phases display much smaller compressibility, most likely due to a change in space requirements of the free electron pair. There is a good correlation between the unit-cell volume and the bulk modulus of $PbMBO_4$ synthetic mullites and of isotypic or structurally related compounds.

The compression of $PbMBO_4$ lattice parameters is highly anisotropic with *a* being the most compressible cell parameter and with *b* displaying expansion under pressure or negative axial compressibility at low pressures. Remarkably the two $PbMBO_4$ mullites are among the ~20 or so materials known to display negative linear compressibility, which is important not only because the NLC effect is very rare, but also because examples of inorganic materials are even fewer. Negative linear compressibility in $PbMBO_4$ is explained with two mechanisms, which interplay synergically: (i) the stereochemical activity of the LEPs opposes compression in one direction; (ii) the expansion of the lattice parameter (along the same direction where LEPs oppose compression) is due to the rotation of MO_6 octahedra and BO_3 groups and the alignment of their longest bonds in one direction, leading to NLC. From a fundamental physics point of view there are strong implications associated with understanding mechanisms of NLC. In practice NLC is a highly attractive mechanical property, with a key application being the development of effectively incompressible optical materials.

5.4. Global Conclusions

Even though mullite occurs rarely in nature, it is perhaps one of the most important phases in both traditional and advanced ceramics. Existing and emerging applications of mullite and mullite-type materials include: high-temperature composites, aerospace materials, ballistic shielding for military applications and even non-linear optical materials.

There are many uncertainties regarding the basic physical properties of mullite-type materials, particularly in terms of their high-pressure structural stability and mechanical behavior that are important to address for emerging applications of mullites as engineering materials. Application of pressure provides a powerful way to produce a wide range of physical phenomena in a controlled environment.

This work is the first reported comprehensive investigation of the high –pressure structural behavior of several different mullites and synthetic mullite-type oxides. The materials investigated are representatives of different structural and chemistry branches of the mullite family. The goal was to elucidate how the most fundamental building blocks of mullite oxides accommodate high pressure compression. Mullites and mullite-type oxides were investigated at extreme pressures using synchrotron x-ray diffraction and laser Raman spectroscopy. These experiments enable the extraction of the materials' structure and its modifications in a function of increasing pressure: deformation of polyhedra, phase transitions, formation and breaking of bonds. The experimental techniques used here are ideally suited to provide a synergical interplay in the study of oxides under high-pressure conditions: Raman spectroscopy is a technique for investigating short range order phenomena while x-ray diffraction accesses structural changes occurring at the long range order.

Among the variety of findings the following phenomena were discussed: phase transitions, equations of state, pressure-driven amorphization, and the very rare effect of negative linear compressibility. The unprecedented discovery of negative linear compressibility in mullite-type oxides presented here opens the door to military applications as incompressible optical materials.

REFERENCES

1. H. Schneider and S. Komarneni, "Mullite." Wiley-VCH: Germany, (2005).
2. H. Schneider, J. Schreuer, and B. Hildmann, "Structure and properties of mullite--A review," *J. Euro. Ceram. Soc.,* **28**, 329-44 (2008).
3. E. Medvedovski, "Alumina-mullite ceramics for structural applications," *Ceram. Int.,* **32**, 369-75 (2006).
4. W. F. Brace, C. H. Scholz, and P. N. Lamori, "Isothermal compressibility of kyanite, andalusite and sillimanite from synthetic aggregates," *J. Geophys. Res.,* **74**, 2089-& (1969).
5. J. K. Winter and S. Ghose, "Thermal expansion and high-temperature crystal chemistry of the Al_2SiO_5 polymorphs," *America Mineralogist,* **64**, 573 - 86 (1979).
6. H. Schneider and E. Eberhard, "Thermal-Expansion of Mullite," *J. Am. Ceram. Soc.,* **73**, 2073-76 (1990).
7. D. Balzar and H. Ledbetter, "Crystal-structure and compressibility of 3-2 mullite," *Am. Miner.,* **78**, 1192-96 (1993).
8. G. Brunauer, H. Boysen, F. Frey, T. Hansen, and W. Kriven, "High temperature crystal structure of a 3:2 mullite from neutron diffraction data," *Z Kristallogr,* **216**, 284-90 (2001).
9. G. Brunauer, F. Frey, H. Boysen, and H. Schneider, "High temperature thermal expansion of mullite: an in situ neutron diffraction study up to 1600^{O}C," *J. Europ. Ceram. Soc.,* **21**, 2563-67 (2001).
10. M. T. Vaughan and D. J. Weidner, "Relationship of elasticity and crystal structure in andalusite and sillimanite," *Physics and Chemistry of Minerals,* **3**, 133-44 (1978).
11. B. Hildmann, H. Ledbetter, S. Kim, and H. Schneider, "Structural control of elastic constants of mullite in comparison to sillimanite," *J. Am. Ceram. Soc.,* **84**, 2409-14 (2001).
12. J. Schreuer, B. Hildmann, and H. Schneider, "Elastic properties of mullite single crystals up to 1400^{o}C," *J. Am. Ceram. Soc.,* **89**, 1624-31 (2006).
13. M. Schmücker, H. Schneider, and W. M. Kriven, "Indentation-Induced Amorphization in Mullite Single Crystals," *J. Am. Ceram. Soc.,* **86**, 1821-22 (2003).
14. M. Schmücker, H. Schneider, and K. J. D. MacKenzie, "Mechanical amorphization of mullite and thermal recrystallization," *J Non-Cryst Solids,* **226**, 99-104 (1998).
15. A. R. Oganov, G. D. Price, and J. P. Brodholt, "Theoretical investigation of metastable Al_2SiO_5 polymorphs," *Acta Cryst.,* **A57**, 548-57 (2001).
16. B. Winkler, M. Hytha, M. C. Warren, V. Milman, J. D. Gale, and J. Schreuer, "Calculation of the elastic constants of the Al_2SiO_5 polymorphs andalusite, sillimanite and kyanite.," *Z Kristallogr,* **216**, 67-70 (2001).
17. H. Yang, R. M. Hazen, L. W. Finger, C. T. Prewitt, and R. T. Downs, "Compressibility and crystal structure of sillimanite, Al_2SiO_5, at high pressure," *Phys. Chem. Miner.,* **25**, 39-47 (1997).
18. A. Friedrich, M. Kunz, B. Winkler, and T. Le Bihan, "High-pressure behavior of sillimanite and kyanite: compressibility, decomposition and indications of a new high-pressure phase," *Z Kristallogr,* **219**, 324-29 (2004).
19. J. B. Burt, N. L. Ross, R. J. Angel, and M. Koch, "Equations of state and structures of andalusite to 9.8 GPa and sillimanite to 8.5 GPa," *Am. Miner.,* **91**, 319-26 (2006).
20. H. Schneider, W. E. Klee, and U. Horneman, "Shock-induced transformations of andalusite and kyanite powders.," *J Mater Sci,* **15**, 154-60 (1980).
21. H. Schneider and U. Hornemann, "Disproportionation of andalusite (Al_2SiO_5) to Al_2O_3 and SiO_2 under shock compression. ," *Phys. Chem. Miner.,* **1**, 257-64 (1977).

22. N. Kawai, K. G. Nakamura, and K.-i. Kondo, "High-pressure phase transition of mullite under shock compression," *J. Appl. Phys.,* **96**, 4126-30 (2004).
23. W. Braue, B. Hildmann, H. Schneider, and U. Hornemann, "The crystalline-to-amorphous transition in shock-loaded mullite $Al_{(2)}^{(VI)}(Al_{(2+2x)}Si_{(2-2x)})^{(IV)}O_{(10-x)}$ in the light of shear modulus anisotropy," *J. Europ. Ceram. Soc.,* **29**, 3135-46 (2009).
24. R. J. Angel, "Equation of State," pp. 35-59. in High-Temperature and High-Pressure Crystal Chemistry**.** *Reviews in Mineralogy and Geochemistry, Vol. 41.* Mineralogical Society of America and Geochemical Society, Washington, 2000.
25. R. J. Angel, N. L. Ross, F. Seifert, and T. F. Fliervoet, "Structural characterization of pentacoordinate silicon in a calcium silicate," *Nature,* **384**, 441-44 (1996).
26. L. M. Anovitz and E. S. Grew, "Mineralogy, petrology and geochemistry of boron: An introduction.," pp. 1-40. in Boron. Mineralogy, petrology and geochemistry*,* Vol. 33**.** *Reviews in Mineralogy.* Edited by E. S. Grew and L. M. Anovitz. Mineralogical Society of America, Washington, D.C., 1996.
27. G. Werding and W. Schreyer, "Alkali-free tourmaline in the system $MgO-Al_2O_3-B_2O_3-SiO_2-H_2O$. ," *Geochim Cosmochim Ac,* **48**, 1331-44 (1984).
28. K. J. Griesser, A. Beran, D. Voll, and H. Schneider, "Boron incorporation into mullite," *Miner Petrol,* **92**, 309-20 (2008).
29. H. Lührs, "The Influence of Boron on the Crystal Structure and Properties of Mullite - Investigations at Ambient, High-Pressure, and High-Temperature Conditions." in Fachbereich Geowissenschaften*,* Vol. Ph.D. Universität Bremen, Bremen, Germany, 2013.
30. Bruker-AXS, "Topas 4.2." in. Bruker-AXS, Germany, 2009.
31. M. Garsche, E. Tillmanns, H. Almen, H. Schneider, and V. Kupcik, "Incorporation of chromium into aluminum borate $9Al_2O_3{\cdot}2B_2O_3$ (A_9B_2)," *Eur J Mineral,* **3**, 793-808 (1991).
32. H. Lührs, R. X. Fischer, and H. Schneider, "Boron mullite: Formation and basic characterization," *Mat. Res. Bull.,* **47**, 4031-42 (2012).
33. H. Lührs, A. Senyshyn, S. P. King, J. V. Hanna, H. Schneider, and R. X. Fischer, "Neutron diffraction and B-11 solid state NMR studies of the crystal structure of B-doped mullite," *Z Kristallogr,* **228**, 457-66 (2013).
34. H. Park and J. Barbier, "$PbGaBO_4$, an orthoborate with a new structure-type," *Acta Crystallogr E,* **57**, i82-I84 (2001).
35. H. Park, J. Barbier, and R. P. Hammond, "Crystal structure and polymorphism of $PbAlBO_4$," *Solid State Sci,* **5**, 565-71 (2003).
36. H. Park, R. Lam, J. E. Greedan, and J. Barbier, "Synthesis, crystal structure, crystal chemistry, and magnetic properties of $PbMBO_4$ (M = Cr, Mn, Fe): A new structure type exhibiting one-dimensional magnetism," *Chem Mater,* **15**, 1703-12 (2003).
37. M. M. Murshed, C. B. Mendive, M. Curti, G. Nenert, P. E. Kalita, K. Lipinska, A. L. Cornelius, A. Huq, and T. M. Gesing, "Anisotropic lattice thermal expansion of $PbFeBO_4$: A study by X-ray and neutron diffraction, Raman spectroscopy and DFT calculations," *Mat. Res. Bull.,* **59**, 170-78 (2014).
38. T. M. Gesing, C. B. Mendive, M. Curti, D. Hansmann, G. Nenert, P. E. Kalita, K. E. Lipinska, A. Huq, A. L. Cornelius, and M. M. Murshed, "Structural properties of mullite-type $Pb(Al_{1-x}Mn_x)BO_4$," *Z Kristallogr,* **228**, 532-43 (2013).
39. R. X. Fischer and H. Schneider, "Crystal chemistry of borates and borosilicates with mullite-type structures: a review," *Eur J Mineral,* **20**, 917-33 (2008).
40. H. J. Koo and M. H. Whangbo, "Density functional investigation of the magnetic properties of $PbMBO_4$ (M = Cr, Mn, Fe)," *Solid State Commun,* **149**, 602-04 (2009).

41. C. T. Chen and G. Z. Liu, "Recent Advances in Nonlinear Optical and Electrooptical Materials," *Annu Rev Mater Sci,* **16**, 203-43 (1986).
42. H. Bärnighausen, "Group-subgroup relations between space groups: A useful tool in crystal chemistry," pp. 139-75. in Communications in mathematical chemistry”*,* Vol. 9**.** Edited by A. T. Balaban, A. S. Dreiding, A. Kerber, and O. E. Polansky. Institut für Strahlenchemie im Max-Planck-Institut für Kohlenforschung,, Mülheim, 1980.
43. D. Long, "The Raman Effect: A Unified Treatment of the Theory of Raman Scattering by Molecules.*"* John Wiley & Sons, Ltd: England, (2002).
44. J. R. Ferraro, K. Nakamoto, and C. Brown, "Introductory Raman Spectroscopy.*"* Academic Press, (2003).
45. E. Smith and G. Dent, "Modern Raman Spectroscopy: A Practical Approach.*"* John Wiley & Sons, Ltd: England, (2005).
46. J. G. Grasselli and B. J. Bulkin, "Analytical Raman Spectroscopy.*"* Wiley Interscience (1991).
47. G. W. King, "Spectroscopy and Molecular Structure.*"* Holt, Rinehart and Winston: New York, (1964).
48. C. V. Raman and K. S. Krishnan, "A new type of secondary radiation," *Nature,* **121**, 501-02 (1928).
49. G. Landsberg and L. Mandelstam, "A new occurrence in the light diffusion of crystals.," *Naturwissenschaften,* **16**, 557-58 (1928).
50. G. Placzek, "Rayleigh-Streuung und Raman Effekt." in Handbuch der Radiologie*,* Vol. VI**.** Edited by E. Marx. Akademische Verlagsgesellschaft, Leipzig 1934.
51. Y. Nishimura, A. Y. Hirakawa, and M. Tsuboi, *Adv. Infrared Raman Spectrosc.,* **5**, 217 (1978).
52. A. F. Goncharov, "Raman Spectroscopy at High Pressures," *Int. J. Spectroscopy,* **2012**, 16 (2012).
53. H. Ibach and H. Luth, "Solid State Physics,*"* 2nd ed. Springer-Verlag Berlin Heidelberg, (1996).
54. C. Kittel, "Intorduction to Solid State Physics.*"* John Wiley & Sons: New York, (1996).
55. P. Atkins, "Physical Chemistry,*"* sixth edition ed. Oxford University Press, (1998).
56. D. Attwood, "Soft X-rays and Extreme Ultraviolet Radiation.*"* Cambridge University Press: New York, NY, (2000).
57. M. R. Wehr, J. A. Richards, and T. W. Adair, "Physics of the Atom,*"* third edition ed. Addison-Wesley Publishing Company: Reading, MA, (1978).
58. K. Kirschner, "Einfuhrung in die Rontgenfeinstrukturanalyse,*"* 3rd ed. Veiweg: Braunschweig/Wiesbaden, (1987).
59. K. N. Trueblood, H.-B. Burgi, H. Burzlaff, D. Dunitz, C. M. Gramaccioli, H. H. Schulz, U. Shmueli, and S. C. Abrahams, "Atomic Displacement Parameter Nomenclature: Report of a Subcommittee on Atomic Displacement Parameter Nomenclature.," *Acta Cryst. ,* **A52**, 770-81 (1996).
60. A. Mujica, A. Rubio, A. Muñoz, and R. J. Needs, "High-pressure phases of group-IV, III-V, and II-VI compounds," *Reviews of Modern Physics,* **75**, 863 (2003).
61. R. J. Hemley and N. Ashcroft, "The revealing role of pressure in the condensed matter sciences," *Physics Today,* **51/8**, 26 (1998).
62. W. Paszkowicz, "X-Ray Diffraction at the Turn of the Century," (2002).
63. K. E. Lipinska, B. Chen, M. B. Kruger, Y. Ohki, J. Murowchick, and E. P. Gogol, "High-pressure x-ray diffraction studies of the nanostructured transparent vitroceramic medium K2O-SiO2-Ga2O3," *Phys Rev B,* **68**, 035209 (2003).

64. K. E. Lipinska, S. A. Gramsch, P. E. Kalita, and R. J. Hemley, "In situ Raman scattering studies of high-pressure stability and transformations in the matrix of a nanostructured glass–ceramic composite," *J. Raman Spectr.,* **36**, 938-45 (2005).
65. K. E. Lipinska, G. Mariotto, P. E. Kalita, and Y. Ohki, "Effects of high pressure on stability of the nanocrystalline LiAlSi2O6 phase of a glass-ceramic composite: A synchrotron X-ray diffraction study," *Physica B,* **365**, 155-62 (2005).
66. K. E. Lipinska, P. E. Kalita, D. M. Krol, R. J. Hemley, C. L. Gobin, and Y. Ohki, "Spectroscopic properties of Cr3+ ions in nanocrystalline glass-ceramic composites," *J Non-Cryst Solids,* **352**, 524-27 (2006).
67. K. E. Lipinska, M. Pravica, G. Mariotto, P. E. Kalita, and Y. Ohki, "Core/shell ZrTiO4/LiAlSi2O6 nanocrystals: A synchrotron X-ray diffraction study of high-pressure compression," *J Phys Chem Solids,* **67**, 2072-76 (2006).
68. M. Pravica, K. Lipinska, Z. Quine, E. Romano, Y. Shen, M. F. Nicol, and W. J. Pravica, "Studies of phase transitions in PETN at high pressures," *J Phys Chem Solids,* **67**, 2159-63 (2006).
69. P. E. Kalita, A. L. Cornelius, K. E. Lipinska, C. L. Gobin, and H. P. Liermann, "In situ observations of temperature- and pressure-induced phase transitions in TiH2: Angle-dispersive and synchrotron energy-dispersive X-ray diffraction studies," *J Phys Chem Solids,* **69**, 2240-44 (2008).
70. K. E. Lipinska, O. A. Hemmers, P. E. Kalita, G. Mariotto, S. Gramsh, R. J. Hemley, and T. Hartmann, "High-pressure structural integrity and structural transformations of glass-derived nanocomposites: A review," *J Phys Chem Solids,* **69**, 2268-73 (2008).
71. K. E. Lipinska, P. E. Kalita, C. Gobin, O. A. Hemmers, T. Hartmann, and G. Mariotto, "Stability and equation of state of a nanocrystalline Ga-Ge mullite in a vitroceramic composite: A synchrotron x-ray diffraction study," *Phys Rev B,* **77**, (2008).
72. K. E. Lipinska, P. E. Kalita, O. A. Hemmers, and T. Hartmann, "Equation of state of gallium oxide to 70 GPa: Comparison of quasihydrostatic and nonhydrostatic compression," *Phys Rev B,* **77**, (2008).
73. P. E. Kalita, S. V. Sinogeikin, K. Lipinska-Kalita, T. Hartmann, X. Z. Ke, C. F. Chen, and A. Cornelius, "Equation of state of TiH2 up to 90 GPa: A synchrotron x-ray diffraction study and ab initio calculations," *Journal of Applied Physics,* **108**, (2010).
74. K. Lipinska, P. E. Kalita, O. Hemmers, S. Sinogeikin, G. Mariotto, C. Segre, and Y. Ohki, "Exploring New Routes for the Development of Functional Nanomaterials using Extreme Pressure," *Ceramic Transactions,* **220**, 6 (2010).
75. P. E. Kalita, H. Schneider, K. Lipinska, S. Sinogeikin, O. A. Hemmers, and A. Cornelius, "High-Pressure Behavior of Mullite: An X-Ray Diffraction Investigation," *J. Am. Ceram. Soc.,* **96**, 1635–42 (2013).
76. B. Buras, J. S. Olsen, L. Gerward, G. Will, and E. Hinze, "X-ray energy-dispersive diffractometry using synchrotron radiation " *J.Appl. Cryst.,* **10**, 431-510 (1977).
77. R. J. Hemley, "Effects of High Pressure on Molecules," *Annual Rev. Phys. Chem.,* **51**, 763-800 (2000).
78. E. Wigner and H. B. Huntington, *J. Chem. Phys.*764 (1935).
79. A. Jayaraman, "Diamond anvil cell and high-pressure physical investigations," *Rev. Mod. Phys.,* **55**, 65 (1983).
80. J. C. Jamieson, A. W. Lawson, and N. D. Nachtrieb,, *Rev. Sci. Instrum.,* **30**, 1016 (1959).
81. C. E. Weir, E. R. Lippincott, A. van Valkenburg, and E. N. Bunting, *J. Res. Natl. Bur. Stand.,* **63**, 55 (1959).

82. M. I. Eremets, "High-Pressure Experimental Methods." Oxford University Press: Oxford, (1996).
83. W. B. Holzapfel, Isaacs N. S. , "High-Pressure Techniques in Chemistry and Physics." Oxford University Press: Oxford/New York/Tokyo, (1997).
84. H. K. Mao, pp. 221. in Simple Molecular Systems at Very High Density**.** Edited by A. Polian, P. Loubeyre, and N. Boccara. Plenum, New York, 1989.
85. R. J. Hemley, "Ultrahigh-Pressure Mineralogy: Physics and Chemistry of the Earth Deep Interior." in Reviews in Mineralogy*,* Vol. 37. Edited by P. H. Ribbe. The Mineralogical Society of America, Washington, DC, 1998.
86. G. Margaritondo, "Introduction to synchrotron radiation ". Oxford University Press: New York, (1988).
87. Advanced Photon Source, http://www.aps.anl.gov/ (2008).
88. T. M. Gesing, R. X. Fischer, M. Burianek, M. Muhlberg, T. Debnath, C. H. Ruscher, J. Ottinger, J. C. Buhl, and H. Schneider, "Synthesis and properties of mullite-type (Bi1-xSrx)(2)((M1-yMy2)-M-1)(4)O9-x (M = Al, Ga, Fe)," *J Eur Ceram Soc,* **31**, 3055-62 (2011).
89. M. Rivers, V. B. Prakapenka, A. Kubo, C. Pullins, C. M. Holl, and S. D. Jacobsen, "The COMPRES/GSECARS gas-loading system for diamond anvil cells at the Advanced Photon Source," *High Pressure Res,* **28**, 273-92 (2008).
90. H. K. Mao, P. M. Bell, J. W. Shaner, and D. J. Steinberg, "Specific volume measurements of Cu, Mo, Pd, and Ag and calibration of the ruby R1 fluorescence pressure gauge from 0.06 to 1 Mbar," *J. Appl. Phys.,* **49**, 3276-83 (1978).
91. Y. Akahama and H. Kawamura, "Pressure calibration of diamond anvil Raman gauge to 310 GPa," *Journal of Applied Physics,* **100**, 043516 (2006).
92. A. P. Hammersley, Svensson, S. O., Hanfland M., Fitch, A. N. and Häusermann, D., "Two-Dimensional Detector Software: From Real Detector to Idealised Image or Two-Theta Scan," *High Pressure Res,* **14**, 235-48 (1996).
93. R. X. Fischer, H. Schneider, and D. Voll, "Formation of aluminum rich 9:1 mullite and its transformation to low alumina mullite upon heating," *J Eur Ceram Soc,* **16**, 109-13 (1996).
94. O. L. Anderson, D. G. Isaak, and S. Yamamoto, "Anharmonicity and the Equation of State for Gold," *J. Appl. Phys.,* **65**, 1534-43 (1989).
95. R. J. Angel, M. Bujak, J. Zhao, G. D. Gattac, and S. D. Jacobsen, "Effective hydrostatic limits of pressure media for high-pressure crystallographic studies," *J. Appl. Cryst.,* **40**, 26-32 (2007).
96. Bruker-AXS, "Topas." in. Bruker-AXS, 2005.
97. S. K. Filatov and R. S. Bubnova, "Structural mineralogy of borates as perspective materials for technological applications.." in Minerals as Advanced Materials I**.** Edited by S. V. Krivovichev. Springer-Verlag, Berlin Heidelberg, 2008.
98. K. Takemura, "Evaluation of the hydrostaticity of a helium-pressure medium with powder x-ray diffraction techniques," *J. Appl. Phys.,* **89**, 662-68 (2001).
99. A. Dewaele and P. Loubeyre, "Pressurizing conditions in helium-pressure-transmitting medium," *High Pressure Res,* **27**, 419-29 (2007).
100. P. Rehak, G. Kunath-Fandrei, P. Losso, B. Hildmann, H. Schneider, and C. Jager, "Study of the Al coordination in mullites with varying Al : Si ratio by Al-27 NMR spectroscopy and X-ray diffraction," *Am. Miner.,* **83**, 1266-76 (1998).
101. S. K. Filatov and R. S. Bubnova, "Borate crystal chemistry.," *Phys. Chem. Glasses,* **41**, 216-24 (2000).
102. R. X. Fischer and H. Schneider, "The Mullite-type Family of Crystal Structures," pp. 1 - 46. in Mullite**.** Wiley-VCH, Germany, 2005.

103. H. Saalfeld and W. Guse, "Structure refinement of 3:2-mullite (3Al2O_3 * 2SiO_2). ," *Neues Jahrbuch für Mineralogie-Monatshefte,* **4**, 145-50 (1981).
104. M. M. Murshed, R. X. Fischer, and T. M. Gesing, "The role of the Pb^{2+} lone electron pair for bond valence sum analysis in mullite-type $PbMBO_4$ (M = Al, Mn and Fe) compounds," *Z Kristallogr,* **227**, 580-84 (2012).
105. A. Bystroem and A. Westgren, *Arkiv foer Kemi, Mineral. Geol.,* **B16**, 1-7 (1943).
106. M. M. Murshed and T. M. Gesing, "Anisotropic thermal expansion and anharmonic phonon behavior of mullite-type $Bi_2Ga_4O_9$," *Mater Res Bull,* **48**, 3284-91 (2013).
107. M. Burianek, T. F. Krenzel, M. Schmittner, J. Schreuer, R. X. Fischer, M. Muhlberg, G. Nenert, H. Schneider, and T. M. Gesing, "Single crystal growth and characterization of mullite-type Bi2Mn4O10," *Int J Mater Res,* **103**, 449-55 (2012).
108. J. R. Gavarri, D. Weigel, and A. W. Hewat, "Lead-Oxides .4. Structural Evolution of Pb_3O_4 between 240-Degree-K and 5-Degree-K and Transition Mechanism," *J Solid State Chem,* **23**, 327-39 (1978).
109. D. Voll, C. Lengauer, A. Beran, and H. Schneider, "Infrared band assignment and structural refinement of Al-Si, Al-Ge, and Ga-Ge mullites," *Eur J Mineral,* **13**, 591-604 (2001).
110. A. E. H. Love, "A Treatise on the Mathematical Theory of Elasticity," 4th ed. ed. Cambridge University Press, Cambridge, (1927).
111. F. D. Murnaghan, "Finite Deformations of an Elastic Solid," *Am. J. Math.,* **59**, 235-60 (1937).
112. F. D. Murnaghan, "The Compressibility of Media Under Extreme Pressures," *PNAS,* **30**, 244-47 (1944).
113. F. Birch, "Finite Elastic Strain of Cubic Crystals," *Phys. Rev.,* **71**, 809-24 (1947).
114. F. Birch, "Finite strain isotherm and velocities for single-crystal and polycrystalline NaCl at high pressures and 300 degrees K," *J. Geophys. Res.,* **83**, 1257-68 (1978).
115. J. W. Palko, A. Sayir, S. V. Sinogeikin, W. M. Kriven, and J. D. Bass, "Complete elastic tensor for mullite (similar to 2.5$Al_{(2)}O_{(3)}$• SiO_2) to high temperatures measured from textured fibers.," *J. Am. Ceram. Soc.,* **85**, 2005-12 (2002).
116. S. Aryal, P. Rulis, and W.-Y. Ching, "Mechanical Properties and Electronic Structure of Mullite Phases Using First-Principles Modeling," *J. Am. Ceram. Soc.,* **95**, 2075-88 (2012).
117. H. Ledbetter, S. Kim, D. Balzar, S. Crudele, and W. Kriven, "Elastic Properties of Mullite," *J. Am. Ceram. Soc.,* **81**, 1025-28 (1998).
118. E. Salje and C. Werneke, "The Phase-Equilibrium between Sillimanite and Andalusite as Determined from Lattice-Vibrations," *Contrib. Mineral. Petr.,* **79**, 56-67 (1982).
119. T. P. Mernagh and L. G. Liu, "Raman-Spectra from the Al_2SiO_5 Polymorphs at High-Pressures and Room-Temperature," *Physics and Chemistry of Minerals,* **18**, 126-30 (1991).
120. P. E. Kalita, A. Cornelius, K. Lipinska, S. Sinogeikin, R. X. Fischer, H. Lührs, and H. Schneider, "High Pressure Behavior of 7:4 Mullite and Boron-Substituted Mullite: Compressibility and Mechanisms of Amorphization," *J. Am. Ceram. Soc.,* **97**, 2980-89 (2014).
121. W. H. Baur, "The Geometry of Polyhedral Distortions. Predictive Relationships for the Phosphate Group," *Acta Cryst.,* **B30**, 1195 (1974).
122. T. Atou, N. Kawai, S. Ito, K. Yubuta, and M. Kikuchi, "Instantaneous nano-order fragmentation in mullite ceramics triggered by a shock-induced phase transition," *J. Appl. Phys.,* **108**, (2010).
123. G. D. Gatta, P. Lotti, M. Merlini, H.-P. Liermann, and M. Fisch, "High-Pressure Behavior and Phase Stability of Al_5BO_9, a Mullite-Type Ceramic Material," *J. Am. Ceram. Soc.,* **96**, 2583-92 (2013).

124. K. E. Lipinska, S. A. Gramsch, P. E. Kalita, and R. J. Hemley, "In situ Raman scattering studies of high-pressure stability and transformations in the matrix of a nanostructured glass–ceramic composite," *Journal of Raman Spectroscopy,* **36**, 938-45 (2005).
125. M. Wu, Y. Liang, J.-Z. Jiang, and J. S. Tse, "Structure and Properties of Dense Silica Glass," *Scientific Reports,* **2**, 398 (2012).
126. J. F. Stebbins and P. Mcmillan, "Compositional and Temperature Effects on 5-Coordinated Silicon in Ambient-Pressure Silicate-Glasses," *J. Non-Cryst. Solids,* **160**, 116-25 (1993).
127. P. F. Mcmillan and J. F. Stebbins, "Unusual Coordination Numbers in Silicate and Aluminate Glasses," *Abstr Pap Am Chem S,* **205**, 41-Phys (1993).
128. A. Dietzel and H. Scholze, "Untersuchungen im System B_2O_3-Al_2O_3-SiO_2," *Glastechnische Berichte,* **28**, 47-51 (1955).
129. R. E. Dinnebier, S. Carlson, M. Hanfland, and M. Jansen, "Bulk moduli and high-pressure crystal structures of minium, Pb_3O_4, determined by X-ray powder diffraction," *Am. Miner.,* **88**, 996-1002 (2003).
130. R. J. Gillespie and R. S. Nyholm, "Inorganic Stereochemistry," *Q Rev Chem Soc,* **11**, 339-80 (1957).
131. I. D. Brown, "Bond Valence as an Aid to Understanding Stereochemistry of O and F Complexes of Sn(II), Sb(III), Te(IV), I(V) and Xe(VI)," *J. Solid State Chem.,* **11**, 214-33 (1974).
132. J. Galy, G. Meunier, S. Andersson, and A. Astrom, "Stereochemistry of Elements Which Are Unbound Pairs - Ge (Ii), as (Iii), Se (Iv), Br (V), Sn (Ii), Sb (Iii), Te (Iv), I (V), Xe (Vi), Tl (I), Pb (Ii), and Bi (Iii) (Oxides, Fluorides and Oxyfluorides)," *J. Solid State Chem.,* **13**, 142-59 (1975).
133. B. G. Von Hyde and S. Andersson, "Inorganic crystal structures," Vol. XV, 430 S. John Wiley: Chichester, England and New York, (1989).
134. V. T. Avanesyan, V. A. Bordovskii, and S. A. Potachev, "Dielectric characterization of the lone pair oxide structure," *J Non-Cryst Solids,* **305**, 136-39 (2002).
135. P. S. Halasyamani and K. R. Poeppelmeier, "Noncentrosymmetric Oxides," *Chem. Mater.,* **10**, 2753-69 (1998).
136. L. E. Orgel, "The Stereochemistry of B-Subgroup Metals 2. The Inert Pair " *J. Chem. Soc.*3815 (1959).
137. R. J. Gillespie, "Molecular geometry ". Van Nostrand-Reinhold: London, (1972).
138. P. B. Moore, T. Araki, and S. Ghose, "Hyalotekite, a Complex Lead Borosilicate - Its Crystal-Structure and the Lone-Pair Effect of Pb(Ii)," *Am. Miner.,* **67**, 1012-20 (1982).
139. B. Winkler, V. Milman, and M.-H. Lee, "Pressure-induced change of the stereochemical activity of a lone electron pair " *J. Chem. Phys.,* **108**, 5506-09 (1998).
140. X. Wang, F. Zhang, I. Loa, K. Syassen, M. Hanfland, and Y.-L. Mathis, *Phys. Status Solidi. (B),* **241**, 3168-78 (2004).
141. L. Pauling, "The principles determining the structure of complex ionic crystals," *J. Am. Chem. Soc.,* **51**, 1010-26 (1929).
142. N. E. Brese and M. Okeeffe, "Bond-Valence Parameters for Solids," *Acta Crystallogr. B,* **47**, 192-97 (1991).
143. I. D. Brown, Accumulated list of bond valence parameters, http://ccp14.ac.uk/ccp/web-mirrors/i_d_brown (2002).
144. I. D. Brown, P. Klages, and A. Skowron, "Influence of pressure on the lengths of chemical bonds," *Acta Crystallogr B,* **59**, 439-48 (2003).
145. I. D. Brown, "Recent Developments in the Methods and Applications of the Bond Valence Model," *Chem. Rev.,* **109**, 6858-919 (2009).

146. X. Q. Wang and F. Liebau, "Studies on bond and atomic valences .1. Correlation between bond valence and bond angles in Sb-III chalcogen compounds: The influence of lone-electron pairs," *Acta Crystallogr. B,* **52**, 7-15 (1996).
147. X. Wang and F. Liebau, "Influence of lone-pair electrons of cations on bond-valence parameters," *Z Kristallogr,* **211**, 437-39 (1996).
148. F. Liebau and X. Q. Wang, "Stoichiometric valence versus structural valence: conclusions drawn from a study of the influence of polyhedron distortion on bond valence sums," *Z Kristallogr,* **220**, 589-91 (2005).
149. X. Wang and F. Liebau, "Influence of polyhedron distortions on calculated bond-valence sums for cations with one lone electron pair," *Acta Crystallogr B,* **63**, 216-28 (2007).
150. X. Q. Wang and F. Liebau, "On the optimization of bond-valence parameters: artifacts conceal chemical effects," *Acta Crystallogr B,* **65**, 99-101 (2009).
151. F. Liebau, X. Q. Wang, and W. Liebau, "Stoichiometric Valence and Structural Valence-Two Different Sides of the Same Coin: "Bonding Power"," *Chem-Eur J,* **15**, 2728-37 (2009).
152. H. L. Zhang, S. Lu, M. P. J. Punkkinen, Q. M. Hu, B. Johansson, and L. Vitos, "Static equation of state of *bcc* iron," *Phys Rev B,* **82**, (2010).
153. R. H. Baughman, S. Stafstrom, C. X. Cui, and S. O. Dantas, "Materials with negative compressibilities in one or more dimensions," *Science,* **279**, 1522-24 (1998).
154. D. R. Mccann, L. Cartz, R. E. Schmunk, and Y. D. Harker, "Compressibility of Hexagonal Selenium by X-Ray and Neutron-Diffraction," *J. Appl. Phys.,* **43**, 1432-& (1972).
155. A. D. Fortes, E. Suard, and K. S. Knight, "Negative Linear Compressibility and Massive Anisotropic Thermal Expansion in Methanol Monohydrate," *Science,* **331**, 742-46 (2011).
156. W. Li, M. R. Probert, M. Kosa, T. D. Bennett, A. Thirumurugan, R. P. Burwood, M. Parinello, J. A. K. Howard, and A. K. Cheetham, "Negative Linear Compressibility of a Metal-Organic Framework," *J. Am. Chem. Soc.,* **134**, 11940-43 (2012).
157. A. B. Cairns, J. Catafesta, C. Levelut, J. Rouquette, A. van der Lee, L. Peters, A. L. Thompson, V. Dmitriev, J. Haines, and A. L. Goodwin, "Giant negative linear compressibility in zinc dicyanoaurate," *Nat Mater,* **12**, 212-16 (2013).
158. R. E. Newnham, "Properties of Materials." Oxford Univ. Press, (2005).
159. A. L. Goodwin, D. A. Keen, and M. G. Tucker, "Large negative linear compressibility of $Ag_3[Co(CN)_6]$," *PNAS,* **105**, 18708-13 (2008).
160. P. Serra-Crespo, A. Dikhtiarenko, E. Stavitski, J. Juan-Alcaniz, F. Kapteijn, F.-X. Coudert, and J. Gascon, "Experimental evidence of negative linear compressibility in the MIL-53 metal-organic framework family," *Cryst. Eng. Comm.,* **17**, 276-80 (2015).
161. J. Haines, C. Chateau, J. M. Léger, C. Bogicevic, S. Hull, D. D. Klug, and J. S. Tse, "Collapsing Cristobalitelike Structures in Silica Analogues at High Pressure," *Phys. Rev. Lett.,* **91**, 015503 (2003).
162. I. Loa, K. Syassen, R. K. Kremer, U. Schwarz, and M. Hanfland, "Structural properties of NaV_2O_5 under high pressure," *Phys Rev B,* **60**, R6945-R48 (1999).
163. R. H. Baughman, "Auxetic materials: Avoiding the shrink," *Nature,* **425**, 667-67 (2003).
164. K. E. Evans and A. Alderson, "Auxetic Materials: Functional Materials and Structures from Lateral Thinking!," *Advanced Materials,* **12**, 617-28 (2000).
165. W. M. Kier and K. K. Smith, "Tongues, Tentacles and Trunks - the Biomechanics of Movement in Muscular-Hydrostats," *Zool J Linn Soc-Lond,* **83**, 307-24 (1985).
166. A. Friedrich, J. Biehler, W. Morgenroth, L. Wiehl, B. Winkler, M. Hanfland, M. Tolkiehn, M. Burianek, and M. Muhlberg, "High-pressure phase transition of $Bi_2Fe_4O_9$," *J Phys-Condens Mat,* **24**, (2012).

167. O. L. Anderson and J. E. Nafe, "The bulk modulus-volume relationship for oxide compounds and related geophysical problems," *J. Geophys. Res.,* **70**, 3951-63 (1965).

168. R. Shannon, "Revised effective ionic radii and systematic studies of interatomic distances in halides and chalcogenides," *Acta Crystallographica Section A,* **32**, 751-67 (1976).

CURRICULUM VITAE

Ph.D. in Physics, University of Nevada Las Vegas 2015

Dissertation: "High Pressure Behavior of Mullite-Type Oxides: Phase Transitions, Amorphization, Negative Linear Compressibility and Microstructural Implications"

Awards/Distinctions

Wolzinger Family Research Fellowship in Sciences: for excellence in Doctoral research 2014 & 2015

Outstanding Poster Award, National Nuclear Security Administration (NNSA) Stewardship Science Academic Programs (SSAP), 2015

Representative Student Speaker (invited) at the Bi-Annual DOE/NNSA Review of the High Pressure Science and Engineering Center, UNLV 2014

Selected Publications

1. Boron Mullite Ceramics under High Pressure: Compressibility , Crystal Chemistry and Amorphization Mechanisms, **P. E. Kalita**, K. Lipinska, H. Schneider, R. Fisher, H. Luhrs, J. American Ceramic Society, Vol. 97, 2980-2989 (2014)
2. Anisotropic lattice thermal expansion of $PbFeBO_4$: a study by X-ray diffraction, neutron diffraction and Raman spectroscopy., M. M. Murshed, C. B. Mendive, M. Curti, **P. E. Kalita**, K. Lipinska, A. L. Cornelius, A. Huq, T. M. Gesing, Materials Research Bulletin, Vol. 59, 170-178 (2014).
3. High-Pressure Behavior of Mullite: An X-Ray Diffraction Investigation, **P. E. Kalita**, H. Schneider, K. Lipinska, S. Sinogeikin, O. Hemmers, A. Cornelius, J. of American Ceramic Society, 96, 1635-1642 (2013)
4. Structural Properties of Mullite-Type Ceramics $Pb(Al_{1-x}Mn_x)BO4$, Th. M. Gesing, C.B. Mendive, M. Curti, D. Hansmann, G. Nenert, **P. E. Kalita**, K. Lipinska, A. Cornelius, M. M. Murshed, Zeitshrift fur Kristallographie, 228, 532-543 (2013)
5. New Pressure Induced Phase Transitions in Mullite-Type $Bi_2(Fe_{4-x}Mn_x)O_{10-d}$ Complex Oxides, **P. E. Kalita**, A. Cornelius, K. Lipinska, M. Lufaso, Z. Kann, S. Sinogeikin, O. Hemmers and H. Schneider, International Journal of Materials Research, 103, 4 (2012)
6. Exploring New Routes for the Development of Functional Nanomaterials using Extreme Pressure; K. Lipinska, **P. E. Kalita**, O. Hemmers, S. Sinogeikin, G. Mariotto, C. Segre and Y. Ohki, Ceramic Transactions, 220, 6 (2010)
7. Equation of State of TiH_2 up to 90 GPa: a Synchrotron X-Ray Diffraction Study and Ab Initio Calculations, **P. E. Kalita**, S. V. Sinogeikin, K. Lipinska, T. Hartmann, X. Ke, C. Chen and A. L. Cornelius, Journal of Applied Physics, 108, 043511 (2010)
8. In Situ Observations of Temperature- and Pressure-Induced Phase Transitions in TiH_2: Angle-Dispersive and Synchrotron Energy-Dispersive X-ray Diffraction Studies, **P. E. Kalita**, A. Cornelius, K. Lipinska, C. Gobin, H.-P. Liermann, J. of Phys. Chem. Solids, 69, 9, 2240 (2008)
9. Equation of State of Gallium Oxide to 70 GPa: Comparison of Quasi-Hydrostatic and Non-Hydrostatic Compression K. Lipinska, **P. E. Kalita**, O. A. Hemmers, T. Hartmann, Phys. Review. B 77, 094123 (2008),